Seismic Ground Motion Assessment

IDENTIFICATION OF KEY SITE FEATURES FOR SITE EFFECT EVALUATION: EXTENSIVE NUMERICAL SENSITIVITY STUDIES OF SEDIMENTARY BASIN STRUCTURES

AUTHORS NOM	DATE	VISA	REVIEW NOM	DATE	VISA	APPROVAL NOM	DATE	VISA
J. Kristek, P. Moczo-*CUB* P.-Y. Bard-*ISTerre* F. Hollender-*CEA* S. Stripajová-*CUB* Z. Margočová-*GPI SAS* E. Chaljub, C. Durand -*ISTerre*			R. Paolucci *Politectnico Milano*			F. Hollender		
			D. Baumont *Geoter*			G. Senfaute		

DISSEMINATION: *Authors; Steering Committee; Work Package leaders, Scientific Committee, Archiving.*

IDENTIFICATION OF KEY SITE FEATURES FOR SITE EFFECT EVALUATION: EXTENSIVE NUMERICAL SENSITIVITY STUDIES OF SEDIMENTARY BASIN STRUCTURES

Jozef Kristek [1, 2], Peter Moczo [1, 2], Pierre-Yves Bard [3], Fabrice Hollender [4], Svetlana Stripajová [1], Zuzana Margočová [2], Emmanuel Chaljub [3], Capucine Durand [3]

1. Faculty of Mathematics, Physics and Informatics, Comenius University in Bratislava (CUB), Slovakia
2. Geophysical Institute, Slovak Academy of Sciences (GPI SAS), Bratislava, Slovakia
3. ISTerre Grenoble, France
4. CEA France

Executive Summary

We performed 3D simulations for 3 3D local surface sedimentary structures, 2D simulations for 12 2D structures (some of them being selected 2D profiles in the 3D structures), and 1D simulations for local 1D models in the 2D models. Assuming a vertical plane-wave incidence for all structures, point DC sources for one 3D structure and linear behaviour, and using a set of selected reference accelerograms we investigated effects of uncertainty in the bedrock velocity, velocity in sediments, attenuation in sediments, interface geometry (border slope), simultaneous variations in velocity and thickness of sediments on 12 characteristics of earthquake ground motion. We identified the following key structural parameters affecting the investigated characteristics of earthquake ground motion:

- overall geometry of the sediment-bedrock interface; detailed geometry close to margins of the basin or valley affects mainly motions close to the margins,
- impedance contrast at the sediment-bedrock interface,
- attenuation in sediments.

Table of Contents

1 INTRODUCTION

1.1 Abbreviations

SIT	site of interest
LSGS	local surface geological structure
EGM	earthquake ground motion
SBI	sediment-basement interface

AF	amplification factor
$\overline{AF}$	average amplification factor
AGF	aggravation factor
$\overline{AGF}$	average aggravation factor
$\mathcal{F}$	Fourier transform
$\mathcal{F}^{-1}$	inverse Fourier transform
S_D	Response spectrum
α or V_P	P-wave speed
β or V_S	S-wave speed
ρ	density
Q_P	quality factor for the P wave
Q_S	quality factor for the S wave
$V_{S_{30}}$	average S-wave speed of the top 30 m in the sediments
$\overline{V_S}$	integral harmonic average of the S-wave speed in the sediments
W	width of the sediment-filled structure at the free surface
$z_{\max}$	maximum depth of the sediments
h	thickness of the sediments

$V_{S_{\text{bedrock}}}$ S-wave speed in the bedrock

f_0 fundamental resonant frequency

f_{00} minimum of the fundamental resonant frequencies over the sites

1.2 Data

There are two sets of data for the analysis:

- Basic $\{V_P, V_S, \rho, Q_P, Q_S\}$ models of the local surface geological structures (LSGS) for sites of interest (SIT).
- Set of selected recorded accelerograms representing variety of earthquake ground motions (EGM).

1.3 Goals

The main goals of the analysis may be summarized in three items:

- Quantitative characterization of effects of the local surface geological structures (LSGS) on earthquake ground motion (EGM) for the specified sites of interest (SIT).
- Identification of key parameters responsible for the effects.
- Evaluation of the numerical-modelling tools and sensitivity tests for estimating the effects.

1.4 Method

The overall methodology applied is indicated in the simplified logical tree. For a set of the nominal structural models for 7 sites of interest and set of modifications of the nominal models, all specified by the coordinator of WP3, we performed direct (forward) numerical simulations by the finite-difference (FD) method developed by the numerical-modelling team of the Comenius University in Bratislava (Moczo et al. 2014, Chaljub et al. 2010, 2015). The simulations were performed for

- 3D models assuming a vertical plane wave incidence and/or point DC source,
- 2D models representing selected 2D profiles in the 3D models and 2D nominal models assuming the vertical plane wave incidence,

- 1D models for selected theoretical receiver positions along 2D profiles.

The direct numerical simulations gave accelerations at specified theoretical receiver positions. Using the acceleration time histories and a set of selected accelerograms from the RESORCE (2012) database (Akkar et al. 2014) we calculated a set of earthquake ground motion characteristics. We then analysed the calculated characteristics.

The selected accelerograms and calculated characteristics are specified in Chapter 4. The characteristics are defined in Appendix: Methodology. Appendix also gives a detailed exposition of the theory based on which we calculated the acceleration time histories assuming a point DC source and the vertical plane wave incidence.

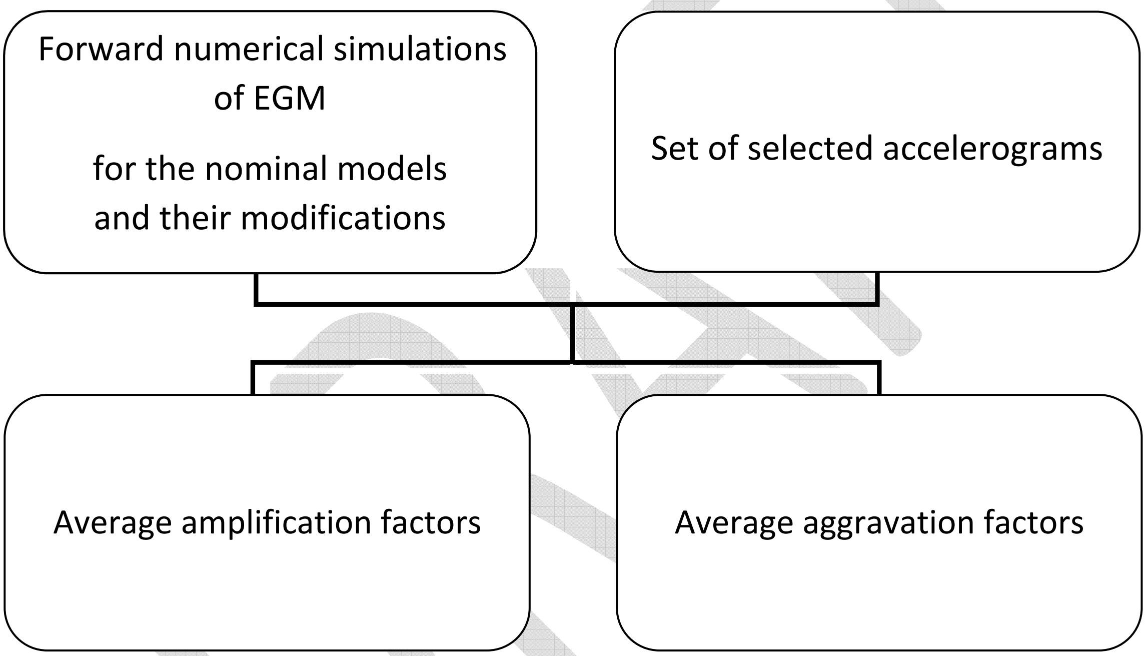

2 SITES, COMPUTATIONAL MODELS AND NUMERICAL SIMULATIONS – AN OVERVIEW

The analysis includes the following target sites:

Site 1 (Mygdonian basin) – a shallow sediment-filled basin

Site 2 (Grenoble valley) – a deep Alpine sediment-filled valley

Site 4 – a small shallow sediment-filled valley

Site 5 – a mid-size sediment-filled valley

Site 6 – a shallow sediment-filled valley, relatively small

Site 7 – a shallow sediment-filled valley, relatively large

The material parameters and geometries of the models for the 6 sites are summarized Tab 2.1 and Tab. 2.2, and Fig. 2.1. – Fig. 2.3.

Tab. 2.3 shows an overview of performed numerical simulations.

Tab. 2.1. Selected mechanical and geometrical parameters of the investigated sites.

Site	$V_{S_{30}}$	$\overline{V_S}$	W	z_{max}	$V_{S_{bedrock}}$	f_∞	z_{max}/W	$V_{S_{bedrock}}/V_{S_{30}}$
	[m/s]	[m/s]	[m]	[m]	[m/s]	[1/s]	[1]	[1]
Site 1 (Mygdonian basin)	170 - 180	400 - 520	4700 - 7450	167 - 393	2600	0.5 - 0.7	0.04 - 0.05	14.5 - 15
Site 2 (Grenoble valley)	380	590 - 680	3580 - 8750	570 - 993	3200	0.2 - 0.3	0.1 - 0.3	8.5
Site 4	400	700	920	120	2200	2.2	0.2	5.5
Site 5	410	920	3500	581	2363	0.5	0.2	6
Site 6	390 - 540	530-590	2200	161	1500	0.9	0.07	2.8 - 3.9
Site 7	400	960	6200	510	2800	0.5	0.08	7

Tab.2.2. Selected mechanical and geometrical parameters of the investigated profiles.

Site	profile	$V_{S_{30}}$	$\overline{V_S}$	W	z_{max}	$V_{S_{bedrock}}$	f_∞	z_{max}/W	$V_{S_{bedrock}}/V_{S_{30}}$
		[m/s]	[m/s]	[m]	[m]	[m/s]	[1/s]	[1]	[1]
Site 1 (Mygdonian basin)	1E	180	400	4700	167	2600	0.7	0.04	14.5
	1C	170	445	4900	266		0.5	0.05	15.4
	1W	175	520	7450	393		0.5	0.05	15
Site 2 (Grenoble valley)	2P1	380	680	3580	993	3200	0.2	0.3	8.5
	2P2		610	6590	670		0.3	0.1	
	2P3		590	4210	570		0.3	0.1	
	2P4		660	8750	844		0.2	0.1	
Site 4		400	700	920	120	2200	2.2	0.2	5.5
Site 5		410	920	3500	581	2363	0.5	0.2	5.7
Site 6	6h	540	590	2200	161	1500	0.9	0.07	2.8
	6g	390	530						3.9
Site 7		400	960	6200	510	2800	0.5	0.08	7

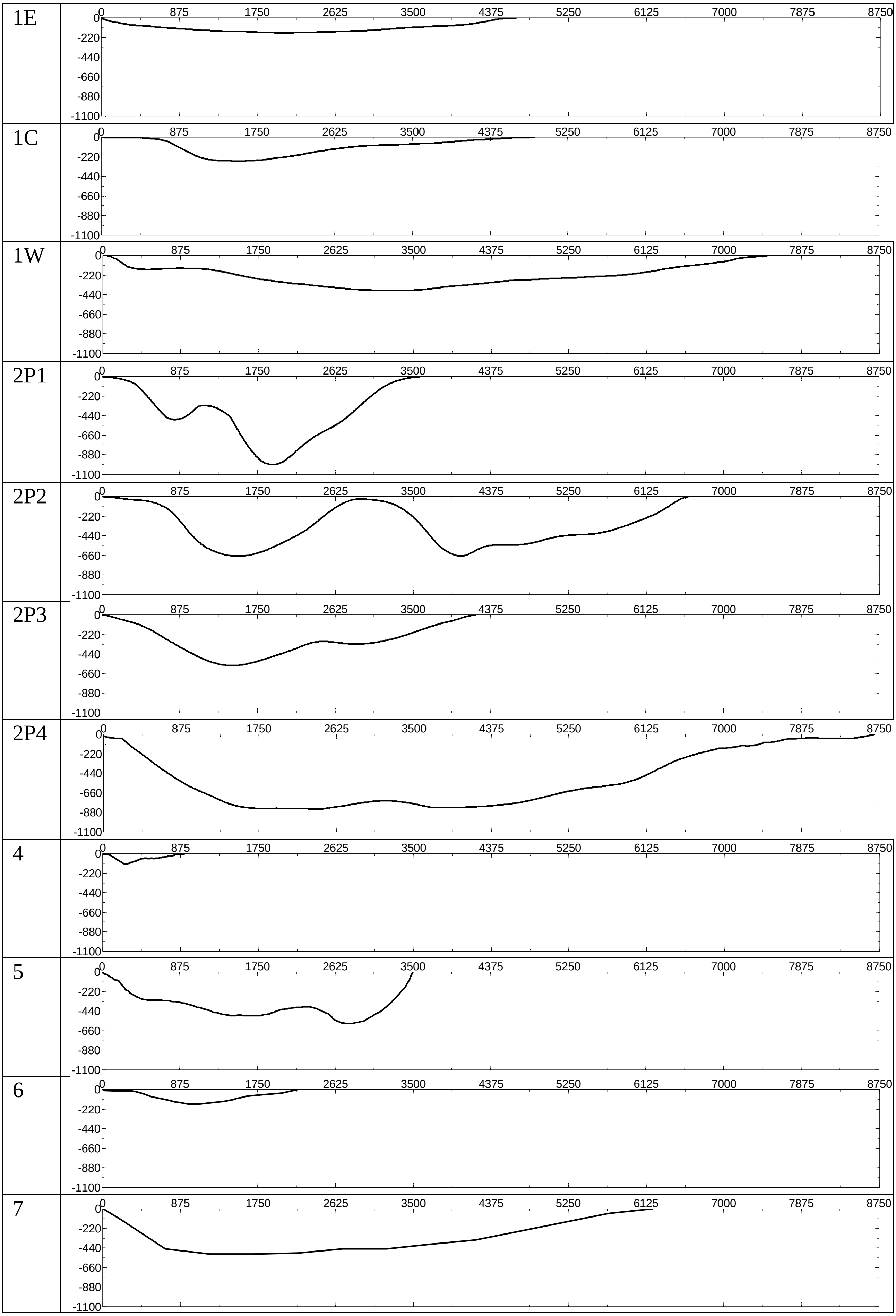

Fig. 2.1. Geometry of the sediment-basement interface in the nominal-model profiles. Both the horizontal dimension and depth shown in metres. Symbols in the left column denote profiles of the investigated nominal models. The horizontal-to-vertical scale is 1:1. All profiles are absolutely scaled.

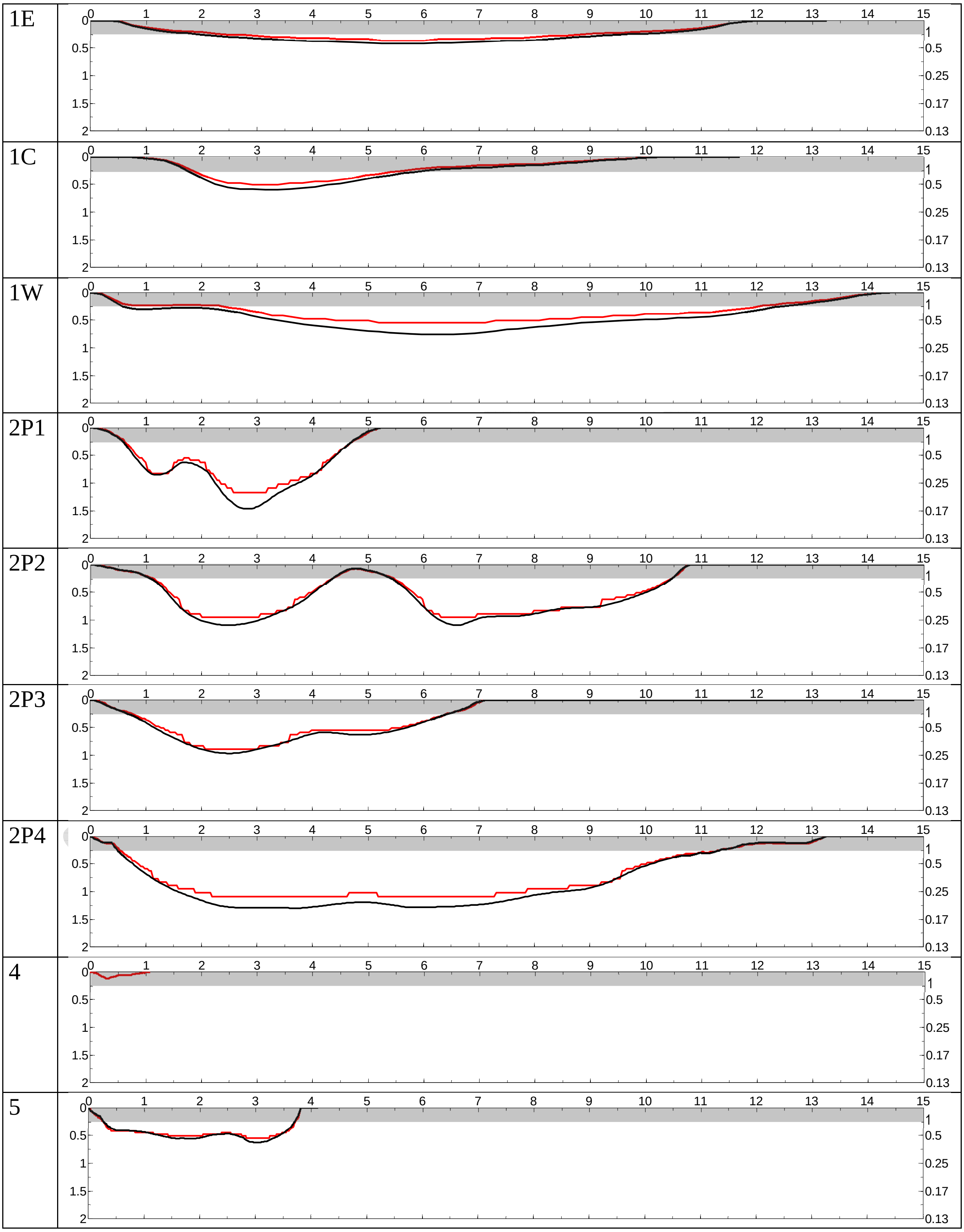
1E
1C
1W
2P1
2P2
2P3
2P4
4
5
0 1 2 3 4 5 6 7 8 9 10 11 12 13 14 15
0 0.5 1 1.5 2
1 0.5 0.25 0.17 0.13

6h

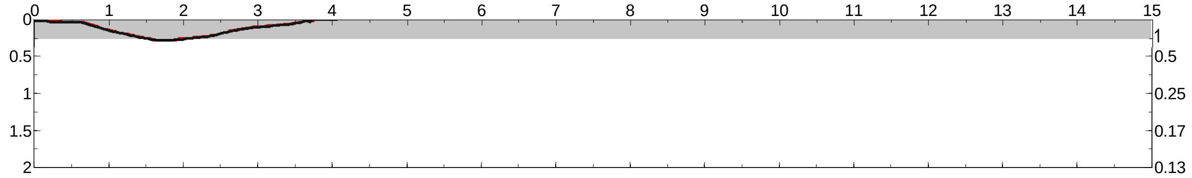

6g

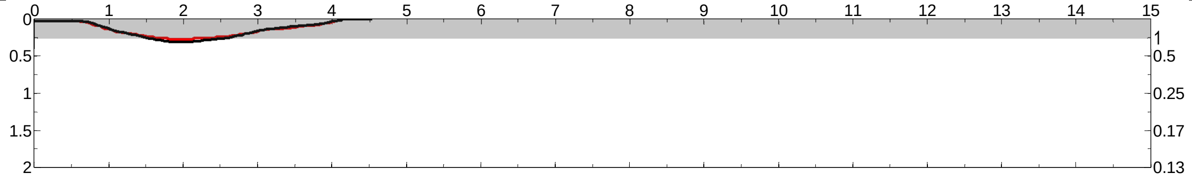

7

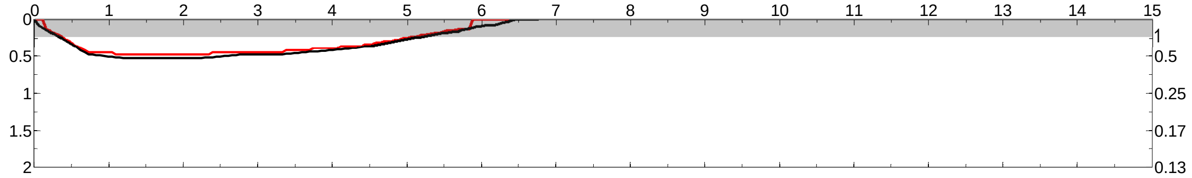

Fig. 2.2. The sediment-basement geometries of the nominal models. Left vertical axis in seconds: the reciprocal of four times fundamental resonant frequency, right vertical axis in Hertz: fundamental resonant frequency. Horizontal axis in seconds: the ratio of the width and $\overline{V_S}$. Black line: $h/\overline{V_S}$. Red line: estimate of the fundamental resonant frequency from the 1D transfer function. (Note: Mechanical parameters of Site 4 are defined point to point. Therefore no theoretical calculation of the fundamental resonant frequency was done.)

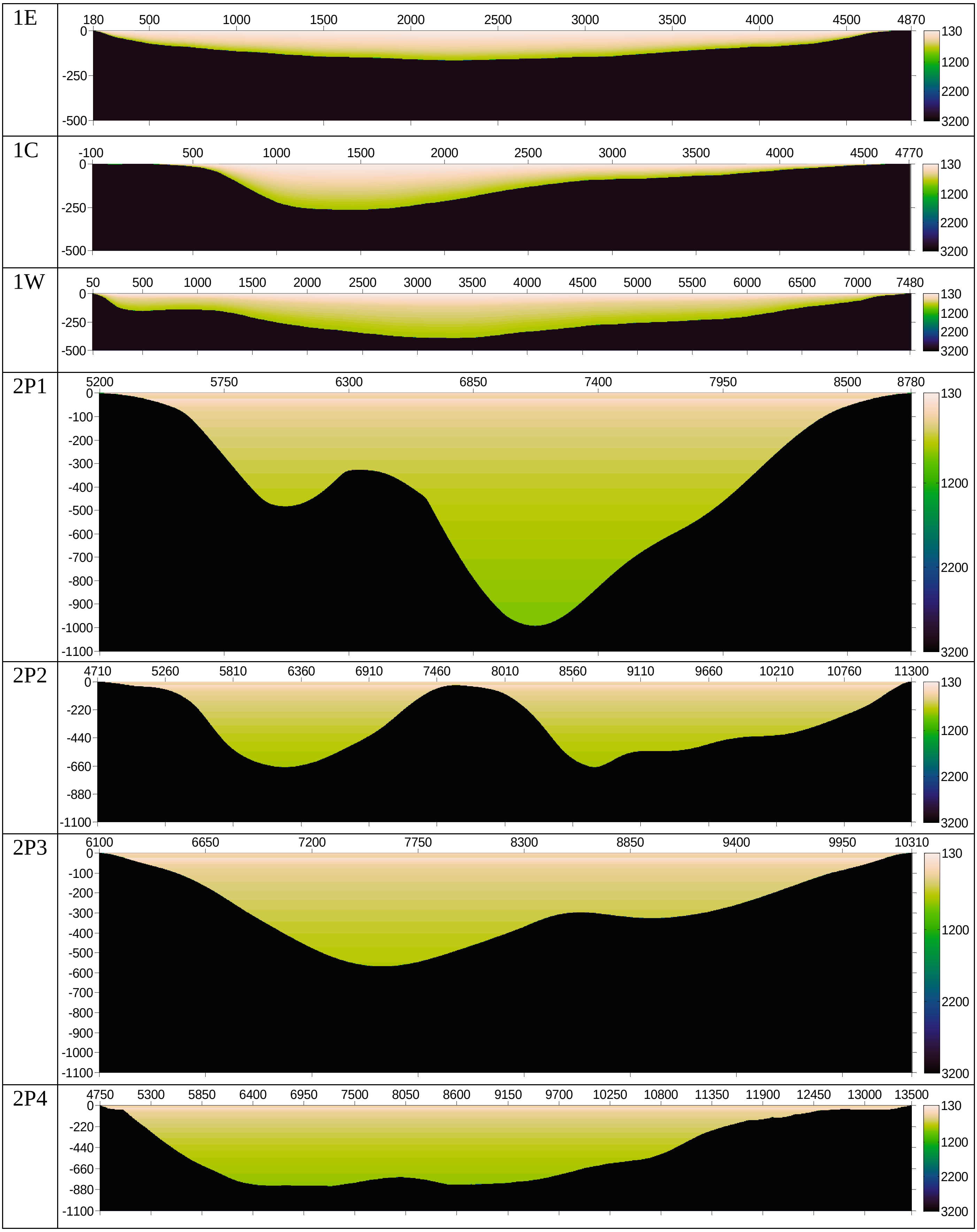

1E
180 500 1000 1500 2000 2500 3000 3500 4000 4500 4870
0 -250 -500
130 1200 2200 3200
1C
-100 500 1000 1500 2000 2500 3000 3500 4000 4500 4770
0 -250 -500
130 1200 2200 3200
1W
50 500 1000 1500 2000 2500 3000 3500 4000 4500 5000 5500 6000 6500 7000 7480
0 -250 -500
130 1200 2200 3200
2P1
5200 5750 6300 6850 7400 7950 8500 8780
0 -100 -200 -300 -400 -500 -600 -700 -800 -900 -1000 -1100
130 1200 2200 3200
2P2
4710 5260 5810 6360 6910 7460 8010 8560 9110 9660 10210 10760 11300
0 -220 -440 -660 -880 -1100
130 1200 2200 3200
2P3
6100 6650 7200 7750 8300 8850 9400 9950 10310
0 -100 -200 -300 -400 -500 -600 -700 -800 -900 -1000 -1100
130 1200 2200 3200
2P4
4750 5300 5850 6400 6950 7500 8050 8600 9150 9700 10250 10800 11350 11900 12450 13000 13500
0 -220 -440 -660 -880 -1100
130 1200 2200 3200

4

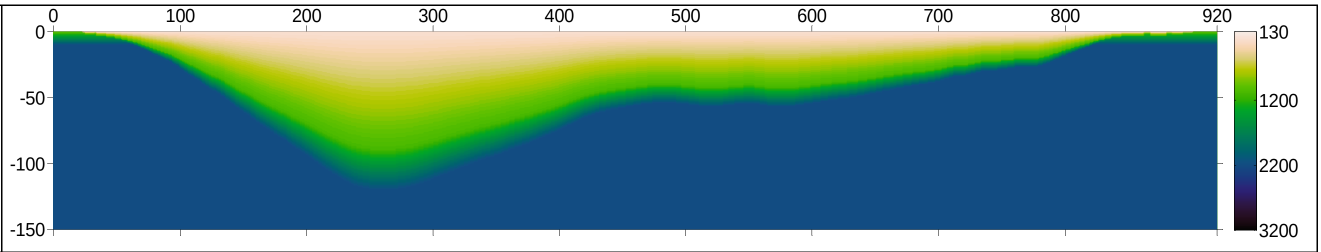

5

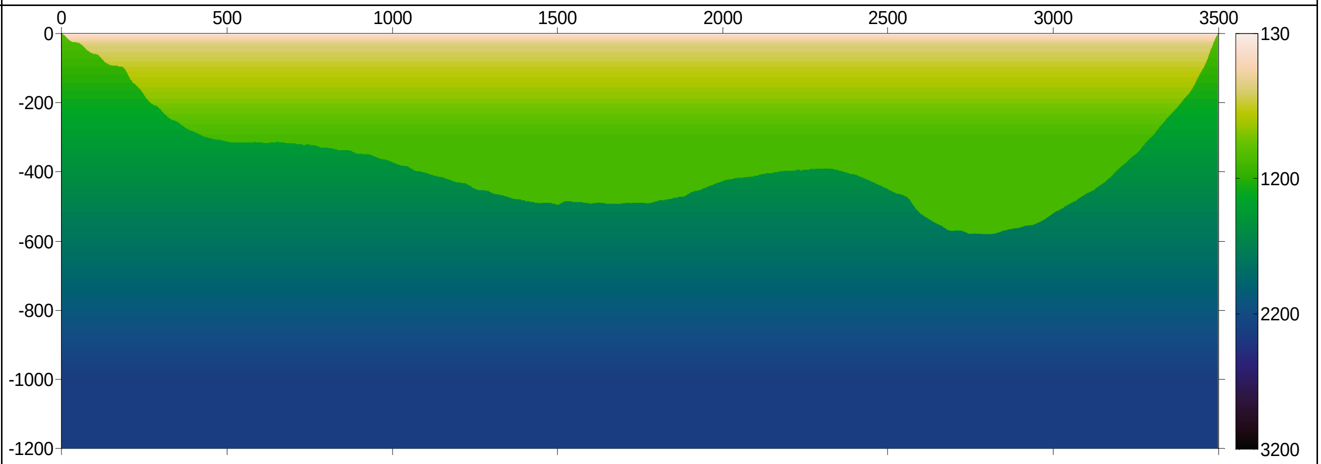

6h

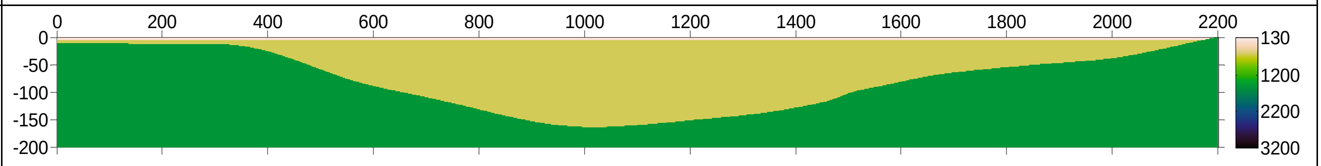

6g

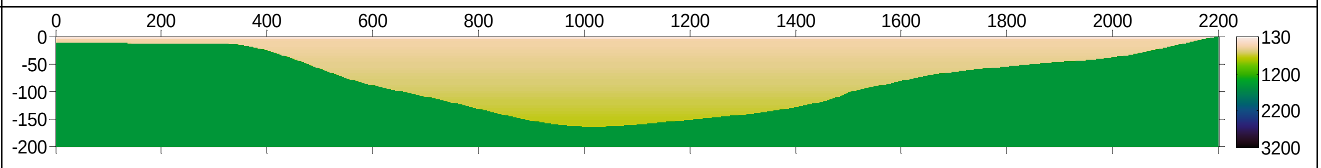

7

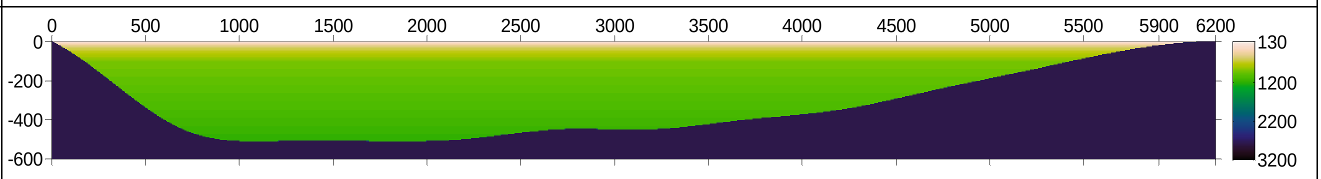

Fig. 2.3. S-wave speed along the model profiles.

- symbols in the left column denote profiles of the investigated nominal models
- S-wave speed is shown using the perceptually improved linear lightness rainbow colour scale
- the S-wave speed distributions in all models are absolutely scaled in the range of [130, 3200] m/s
- the horizontal-to-vertical scale is 1:1
- the horizontal dimension of each model is locally scaled to the table-column width
- all dimensions are shown in metres

Tab. 2.3. An overview of performed numerical simulations.

Site	profile		Nominal model						Modification of the nominal model																																			
									Velocity in sediments						Attenuation in sediments									Border slope (BS)								Velocity in bedrock								Locally fixed fundamental frequency (modified velocity and thickness of sediments)				3D meander extension
									w/oHVL						NLQ			Elastic		VS/20		VS/40		BS/2_a		BS×2_a		BS/2_b		BS×2_b		1200		2000		3000		grad		- 40%		+ 40%		
		Dim	3				2	1	3				2	1	3	2	1	2	1	2	1	2	1	2	1	2	1	2	1	2	1	2	1	2	1	2	1	2	1	2	1	2	1	3
		Exc	DC			P	P	P	DC			P	P	P	P	P	P	P	P	P	P	P	P	P	P	P	P	P	P	P	P	P	P	P	P	P	P	P	P	P	P	P	P	P
			A	B	C				A	B	C																																	
S1	pE					*	*	*																																				
	pC					*	*	*																																				
	pW					*	*	*																																				
S2	p1		*	*	*	*	*	*	*	*	*	*	*	*	*	*	*							*	*	*	*																	
	p2		*	*	*	*	*	*	*	*	*	*	*	*	*	*	*																											
	p3		*	*	*	*	*	*	*	*	*	*	*	*	*	*	*																											
	p4		*	*	*	*	*	*	*	*	*	*	*	*	*	*	*																											
S4							*	*																																				
S5							*	*												*	*	*	*	*	*	*	*					*	*	*	*	*	*	*	*					
S6h							*	*										*	*	*	*	*	*	*	*	*	*	*	*	*	*	*	*	*	*	*	*	*	*	*	*	*	*	*
S6g							*	*										*	*	*	*	*	*	*	*	*	*	*	*	*	*	*	*	*	*	*	*	*	*					*
S7							*	*										*	*	*	*	*	*									*	*	*	*	*	*	*	*					

Legend:

Dim – dimension: **3** = 3D, **2** = 2D, **1** = 1D; **Exc –** excitation: **DC** = point double-couple source, **P** = plane wave

HVL = high-velocity layer; **NLQ** = Q derived from nonlinear simulation

3 SITES, COMPUTATIONAL MODELS AND NUMERICAL SIMULATIONS – DESCRIPTION

3.1 Site 1 – Mygdonian basin

3.1.1 The meaning of the site and model

The Mygdonian basin, an elongated tectonic graben located approximately 30 km ENE of the city of Thessaloniki (Fig. 3.2), is one of the major threats for the city, as witnessed by the June 20, 1978 Stivos M6.4 earthquake which occurred on one of the fault branches shaping the graben (e.g., Soufleris et al. 1982; Theodulidis et al. 2006).

Kyriazis Pitilakis and Pierre-Yves Bard led the initiative to establish a test site in the Mygdonian basin for experimental and theoretical investigations of site effects. Their efforts were finally successful and, starting from 1994, the Mygdonian basin has become the object of focused research in many international and Greek projects (e.g., EUROSEIS-TEST, EUROSEIS-MOD, EUROSEIS-RISK, ISMOD, ITSAK-GR; among many other, see http://euroseisdb.civil.auth.gr). The Mygdonian basin also became a target site of E2VP.

A realistic 3D seismic model of the Mygdonian sedimentary basin has been developed with more than one decade of focused seismological, geophysical and geotechnical investigations by Greek seismologists and their international collaborators (e.g., Raptakis et al. 1998,2000,2005; Pitilakis et al. 1999,2011,2013; Chávez-García et al. 2000; Makra et al. 2001,2005; Manakou 2007; Manakou et al. 2007,2010).

The Mygdonian basin is a shallow sedimentary basin. The available model can be characterized by

- complicated geometry of the sediment–bedrock interface,
- relatively low VS in Layer 1,
- large VS contrast between sediments and bedrock ranging from 3 to 18,
- large VP /VS (more than 10 at the surface).

3.1.2 Table of material parameters

Tab. 3.1 Mechanical parameters – Mygdonian basin (Site1).

Unit	Thickness [m]	V_P1 [m/s]	V_P2 [m/s]	V_S1 [m/s]	V_S2 [m/s]	$\rho1$ $[\mathrm{kg/m^3}]$	$\rho2$ $[\mathrm{kg/m^3}]$	Q_S	Q_P
Layer 1	variable	1500	2100	130	475	2075	2130	$V_S/10$	max $(V_P/20, V_S/5)$
Layer 2	variable	2100	2700	475	800	2130	2250		
Bedrock	∞		4270		2400		2500		

$$V_S(z) = V_S1 + (V_S2 - V_S1)(z - z_1)/(z_2 - z_1)$$
$$V_P(z) = V_P1 + (V_P2 - V_P1)(z - z_1)/(z_2 - z_1)$$
$$V_S1, V_P1, \rho1, \mathrm{z}_1 \quad - \text{at the top of the layer}$$
$$V_S2, V_P2, \rho2, \mathrm{z}_2 - \text{at the bottom of the layer}$$

3.1.3 Graphs of material parameters

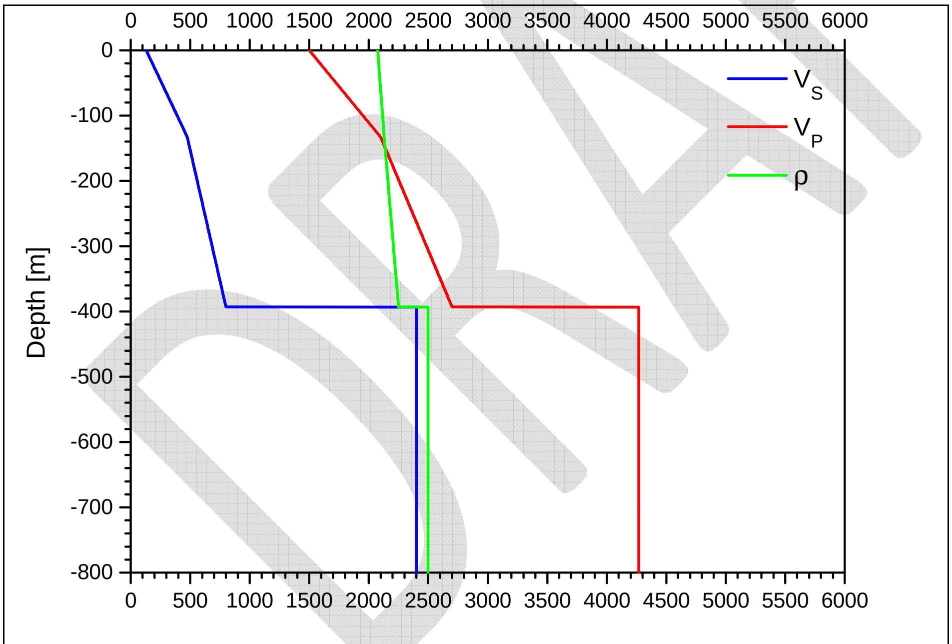

Fig. 3.1. S-wave speed V_S [m/s], P-wave speed V_P [m/s] and density ρ $[\mathrm{kg/m^3}]$ as functions of depth – Mygdonian basin (Site 1).

3.1.4 Geometry of the model

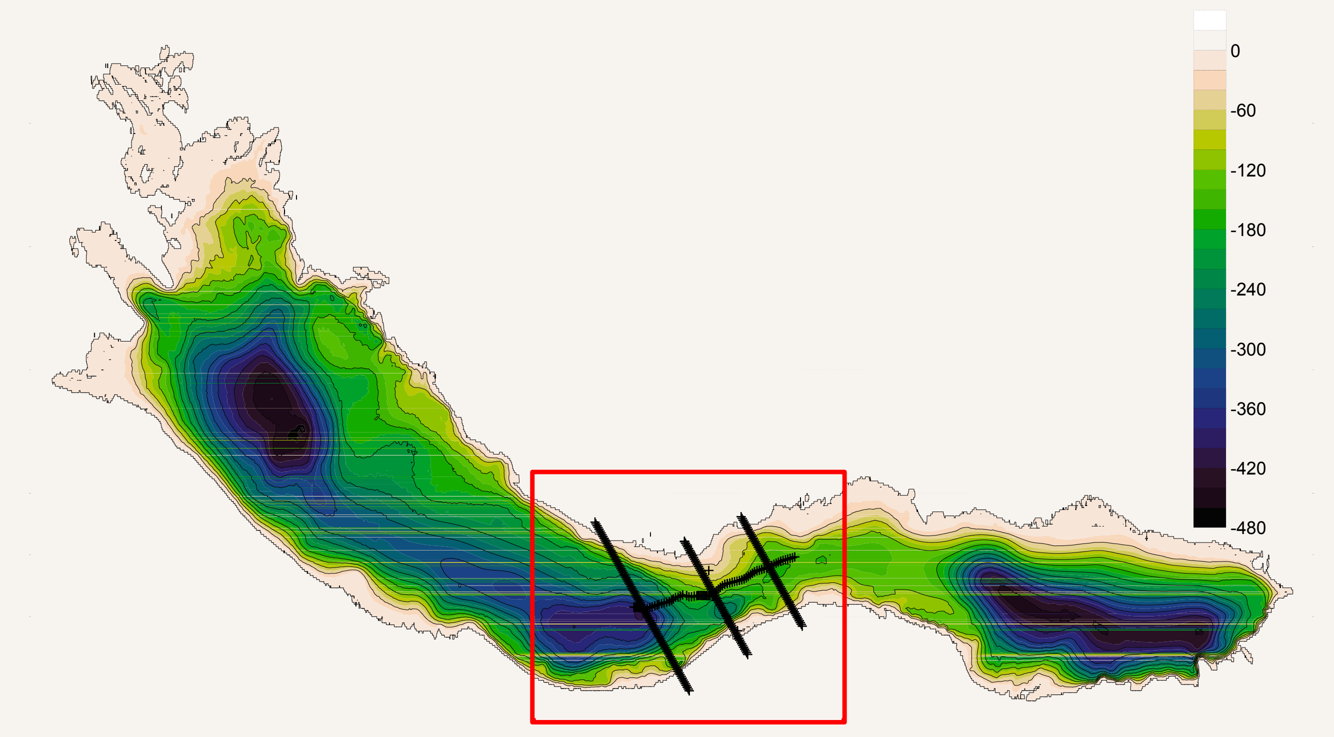

Fig. 3.2. Depth of the sediment-basement interface in the Mygdonian basin model (Site 1).The red frame shows the area of the computational model used for simulations. Black lines indicate receivers' positions. The colour bar shows depth in metres. Size of the whole depicted area is 64 990 m x 47 990 m. In this figure and throughout the entire report we used the perceptually improved linear lightness rainbow colour scale developed by Niccoli (2014).

3.1.5 Direct numerical simulations

3.1.5.1 3D simulations

The computational parameters of the FD numerical simulations for the Mygdonian basin (Site 1) model are summarized in Tab. 3.2.

Tab. 3.2 Computational parameters for the Mygdonian basin (Site 1) model, 3D simulations.

grid spacing	7.5 m
time step	8.10^{-4} s
frequency range	0.04 - 4 Hz
reference frequency for S-wave and P-wave speeds	1 Hz
number of relaxation frequencies	4
number of time levels	625 000
time window	50 s

thickness of PML	50 grid points
total number of grid cells including PML	1701 x 2101 x 185
simulation of the free surface	stress-imaging method
depth of excitation of the plane-wave vertical incidence	502.5 m
average CPU time on 192 cores	1600 min

Specification of theoretical receivers

Theoretical receivers positions are indicated by the black '+' symbols in Fig. 3.2. (Due to their number and the size of the figure, the symbols effectively make thick black lines in the figure.)

Specification of wavefield excitation

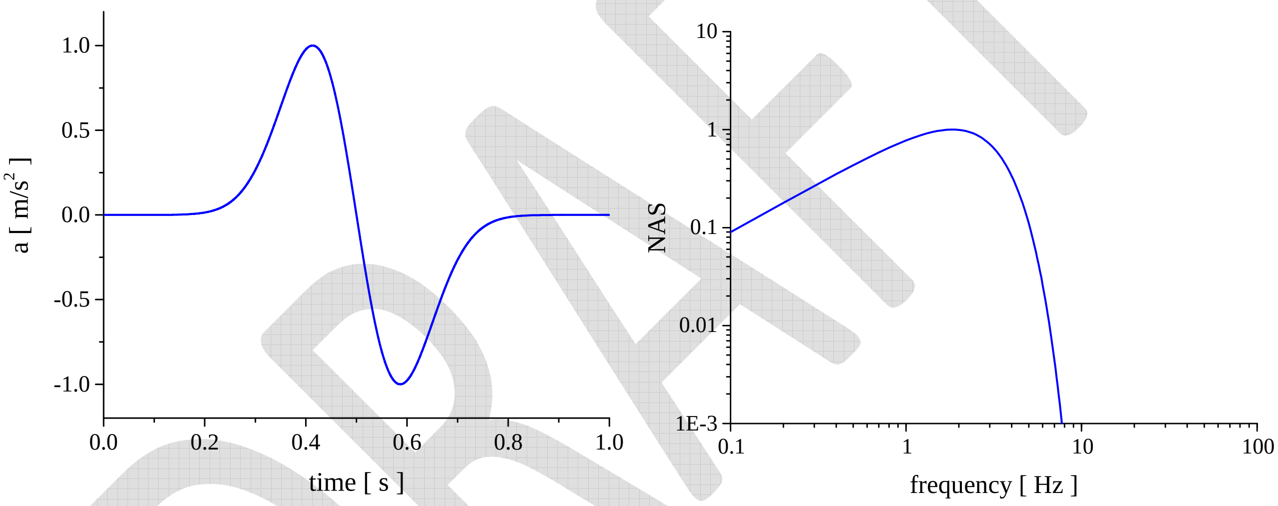

Fig. 3.3. The source time function of the incident wave. Left panel: acceleration, right panel: normalized amplitude Fourier spectrum.

Three excitations were applied: vertically incident plane P wave, SV wave and SH wave. The source time function (Fig. 3.3) was Gabor signal defined in subsection 10.3.1 by Eq. (10.27).

Specification of results

Three-component time history of acceleration at each theoretical receiver.

3.1.5.2 2D simulations

The computational parameters of the FD numerical simulations for the Mygdonian basin (Site 1) model are summarized in Tab. 3.3.

Tab. 3.3 Computational parameters for the Mygdonian basin (Site 1) model, 2D simulations.

grid spacing	1 m
time step	2.10^{-4} s
frequency range	0.2 - 17 Hz
reference frequency for S-wave and P-wave speeds	1 Hz
number of relaxation frequencies	3
number of time levels	500 000
time window	60 s
thickness of PML	200 grid points
total number of grid cells including PML	6601 x 1201
simulation of the free surface	AFDA method
depth of excitation of the plane-wave vertical incidence	500 m
average CPU time on 28 cores	700 min

Specification of 2D profiles

Three parallel 2D profiles (cross-sections) were selected in order to partially represent laterally varying basin. The profiles are indicated by the surface lines in Fig. 3.2. Theoretical receivers are distributed along the surface of the profiles. The selected three profiles are depicted in Fig. 3.4 - Fig. 3.6.

Geometry of the three profiles is shown in Fig. 3.7 - Fig. 3.9 in two horizontal-to-vertical scales: 1:1 and 1:4. The latter scale is used to better visualize geometrical details of the sediment-basement interfaces. It is obvious that the three selected profiles differ from each other considerably – indicating thus the 3D geometry of the basin.

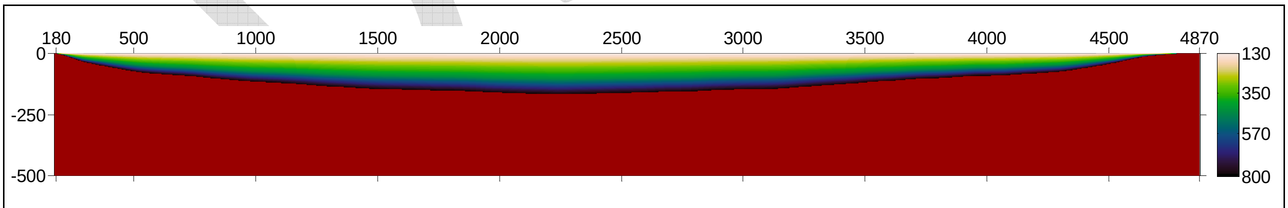

Fig. 3.4. S-wave speed V_S $[\mathrm{m/s}]$ along the 2D profile 1E – the eastern cross-section of the Mygdonian basin (Site 1, the rightmost receiver profile in Fig. 3.2). Both horizontal dimension and depth shown in metres. Red colour represents $V_S = 2400\ \mathrm{m/s}$ in the bedrock. (Technical note: layering inside sediments is an artefact of the graphical software, the true distribution is smooth.)

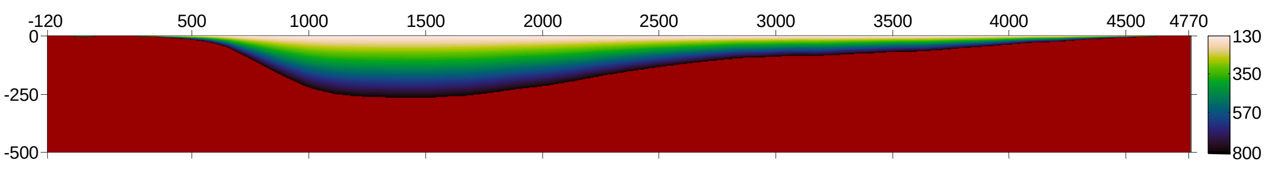

Fig. 3.5. S-wave speed V_S $[\mathrm{m/s}]$ along the 2D profile 1C – the central cross-section of the Mygdonian basin (Site 1, the profile between the leftmost and rightmost profiles in Fig. 3.2). Both horizontal dimension and depth shown in metres. Red colour represents $V_S = 2400\ \mathrm{m/s}$ in the bedrock. (Technical note: layering inside sediments is an artefact of the graphical software, the true distribution is smooth.)

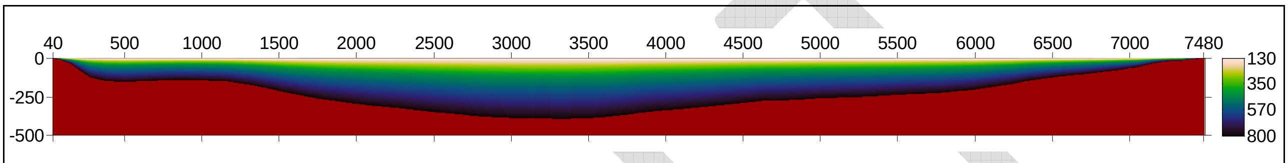

Fig. 3.6. S-wave speed V_S $[\mathrm{m/s}]$ along the 2D profile 1W – the western cross-section of the Mygdonian basin (Site 1, the leftmost receiver profile in Fig. 3.2). Both horizontal dimension and depth shown in metres. Red colour represents $V_S = 2400\ \mathrm{m/s}$ in the bedrock. (Technical note: layering inside sediments is an artefact of the graphical software, the true distribution is smooth.)

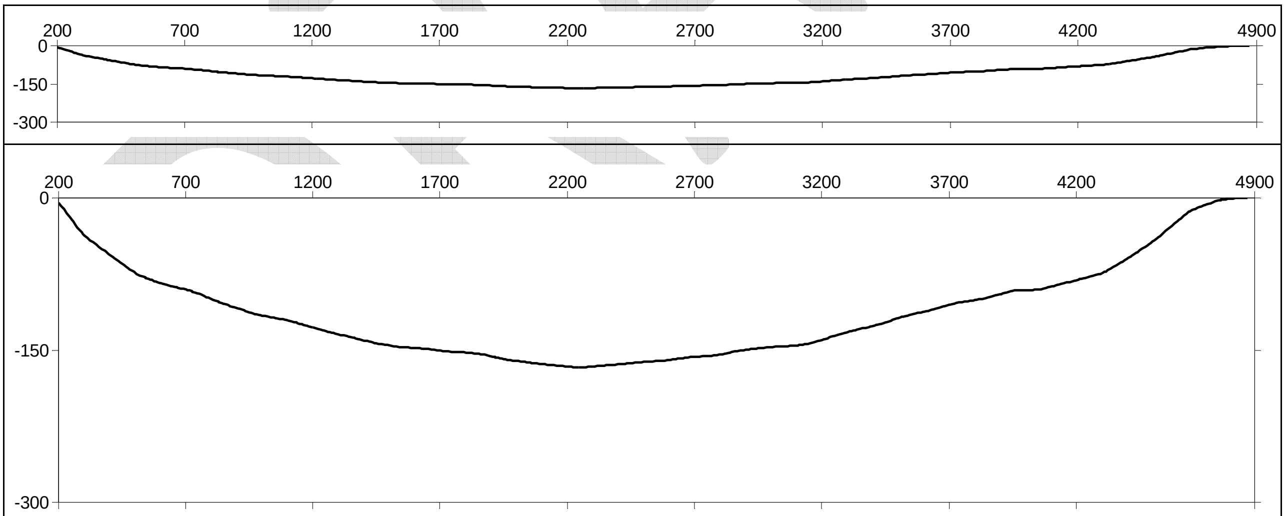

Fig. 3.7. Geometry of the sediment-basement interface along profile 1E – the eastern cross-section of the Mygdonian basin (Site 1). Both horizontal dimension and depth shown in metres. Upper panel: 1:1 horizontal-to-vertical scale. Bottom panel: 1:4 horizontal-to-vertical scale.

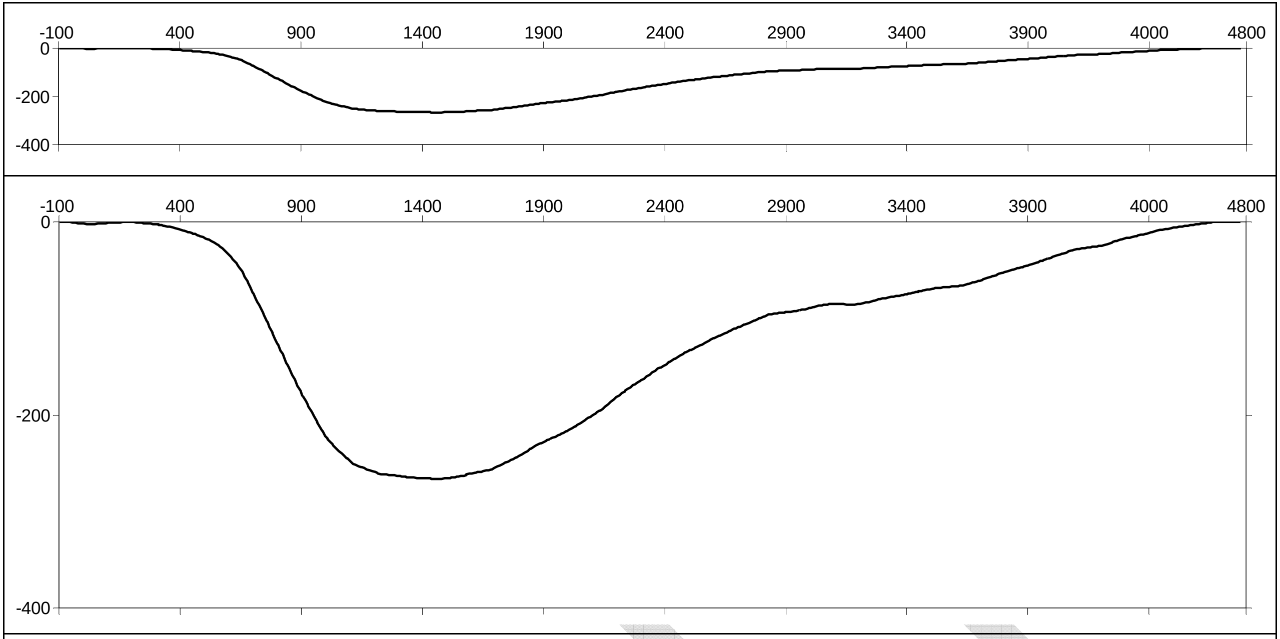

Fig. 3.8. Geometry of the sediment-basement interface along profile 1C – the central cross-section of the Mygdonian basin (Site 1). Both horizontal dimension and depth shown in metres. Upper panel: 1:1 horizontal-to-vertical scale. Bottom panel: 1:4 horizontal-to-vertical scale.

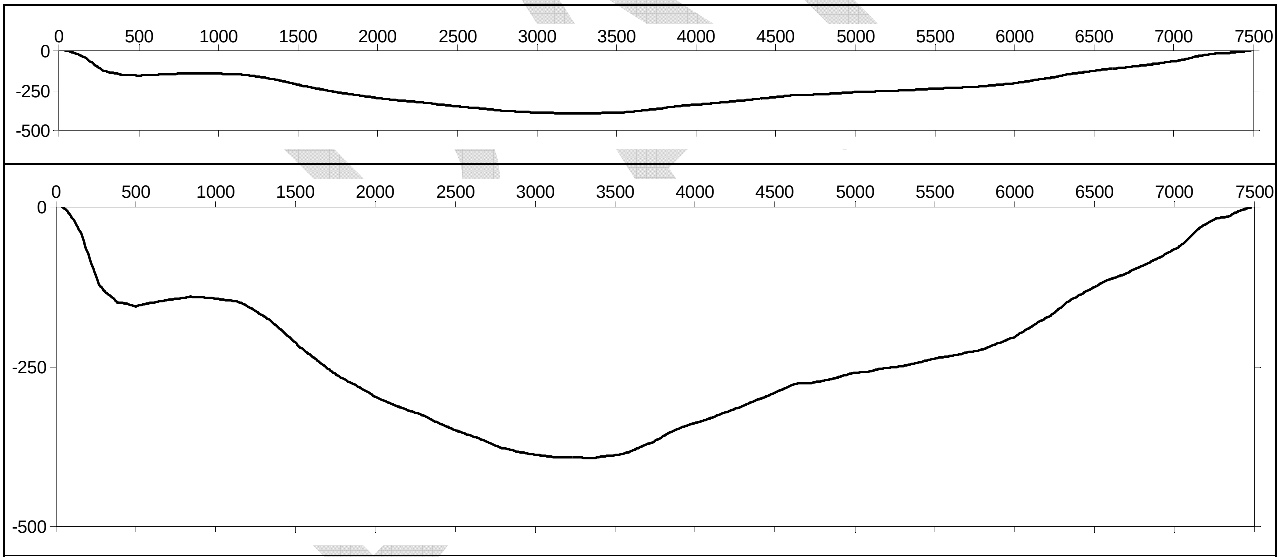

Fig. 3.9. Geometry of the sediment-basement interface along profile 1W – the western cross-section of the Mygdonian basin (Site 1). Both horizontal dimension and depth shown in metres. Upper panel: 1:1 horizontal-to-vertical scale. Bottom panel: 1:4 horizontal-to-vertical scale.

Specification of theoretical receivers

Receivers along profile 1E are equidistantly distributed at the free surface between points [-700 m, 0 m] and [5300 m, 0 m] with interdistance of 100 m in the horizontal direction. Points [180 m, 0 m] and [4880 m, 0 m] indicate edges of the sediment-filled basin.

Receivers along profile 1C are equidistantly distributed at the free surface between points [-1000 m, 0 m] and [5200 m, 0 m] with interdistance of 100 m in the horizontal direction. Points [-100 m, 0 m] and [4800 m, 0 m] indicate edges of the sediment-filled basin.

Receivers along profile 1W are equidistantly distributed at the free surface between points [-1000 m, 0 m] and [8300 m, 0 m] with interdistance of 100 m in the horizontal direction. Points [50 m, 0 m] and [7500 m, 0 m] indicate edges of the sediment-filled basin.

Specification of wavefield excitation

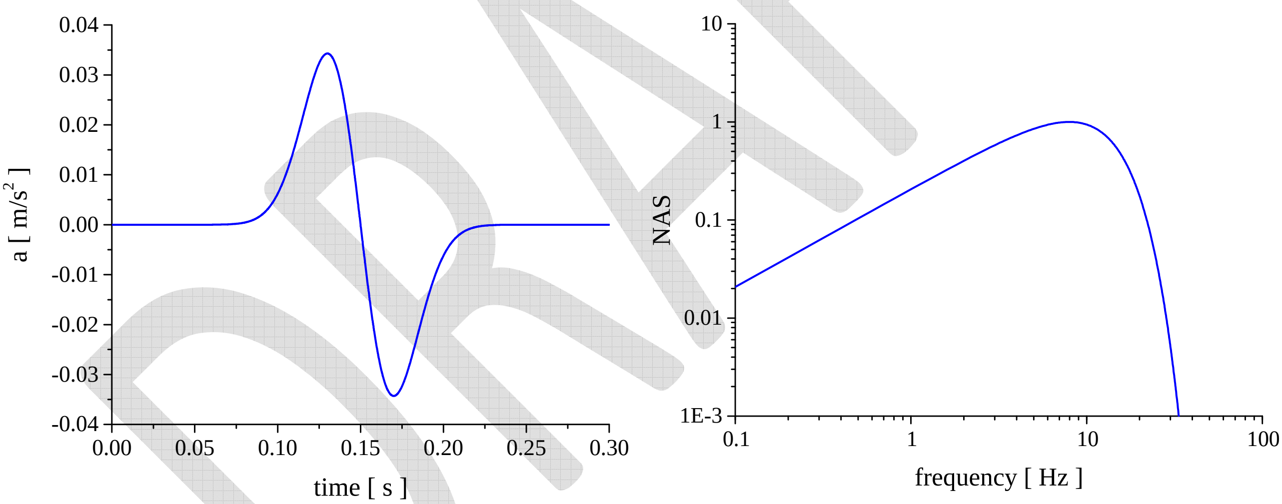

Fig. 3.10. The source time function of the incident wave. Left panel: acceleration, right panel: normalized amplitude Fourier spectrum.

Three excitations were applied: vertically incident plane P wave, SV wave and SH wave. The source time function (Fig. 3.10) was Gabor signal defined in subsection 10.3.1 by Eq. (10.27) with parameters $f_p = 0.45$, $\gamma_s = 0.08$, $\theta = \pi/2$ and $t_s = 0.15$.

Specification of results

Two-component (x - and z - components) time history of acceleration at each theoretical receiver in case of the P and SV incidence waves. One-component (y - component) time history of acceleration at each theoretical receiver in case of the SH incidence wave.

3.1.5.3 1D simulations

The computational parameters of the 1D simulations for the Mygdonian basin (Site 1) are the same as for 2D simulations (see Tab. 3.3).

Specification of theoretical receivers

The same as for the 2D simulations.

Specification of wavefield excitation

Two excitations were applied: vertically incident plane P wave and S wave. The source time function (Fig. 3.10) is the same as that for the 2D simulations.

Specification of results

One-component time history of acceleration at each theoretical receiver.

3.2 Site 2 – Grenoble valley

3.2.1 The meaning of the site and model

The Grenoble valley is a typical deep sediment-filled Alpine valley. The sediments are made of the Quaternary fluvial and post-glacial deposits. Two aspects make the site important: 1) Grenoble urban area with significant population, modern industry and research facilities. 2) Such "alpine valley" configuration is also met in different other areas within the European Alps, and in other mountainous areas with embanked valleys filled with young, post-glacial lacustrine sediments.

Grenoble valley is a junction of three large valleys with complex geometry of the sediment-basement interface. The junction mimics letter Y. The valley is surrounded by relatively high mountain ranges. The valley is shown in Fig. 3.11 and Fig. 3.13. The first one shows the free-surface topography, the second one geometry of the sediment-basement interface.

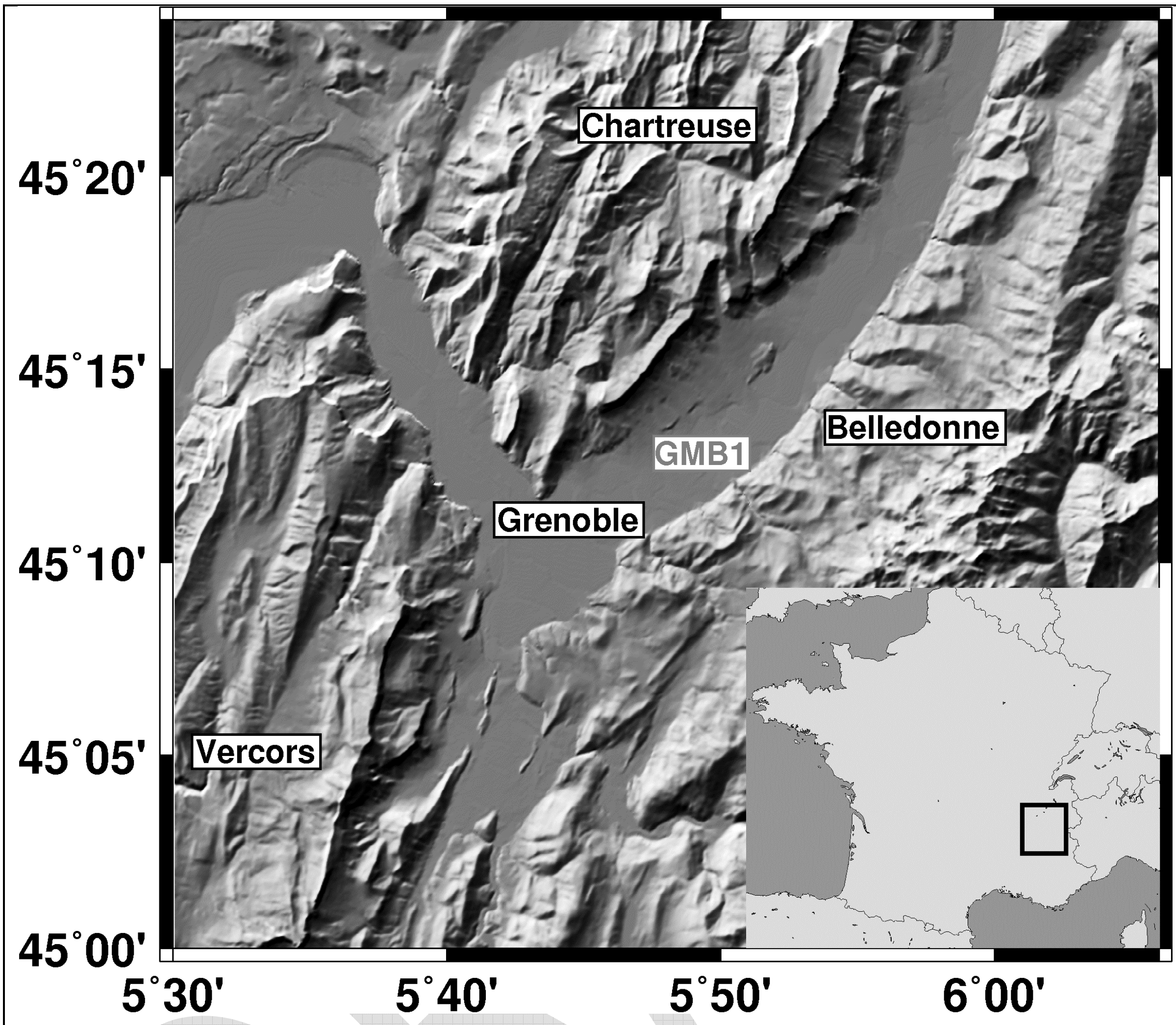

Fig. 3.11. The 'Y'-shaped Grenoble valley surrounded by the Belledonne chain (crystalline, max. elevation approx. 3000m), and Vercors and Chartreuse (limestone massifs, max. elevation approx. 2000m). GMB1 indicates the location of the Montbonnot borehole (according to Chaljub et al. 2010).

3.2.2 Table of material parameters

The concise characterization of the Grenoble valley and its investigations from the point of view of numerical modelling of seismic motion can be found in the article by Chaljub et al. (2010).

Tab. 3.4 Mechanical parameters – Grenoble valley (Site 2)

Unit	Position		V_P1	V_P2	V_S	$\rho1$	$\rho2$	Q_S	Q_P
	z_1	z_2	[m/s]		[m/s]	$[\mathrm{kg/m^3}]$			
	[m]								
Layer 1	0	24	$2200+1.2z$		$320+28\sqrt{z}$	$2140+0.125z$		$V_S/10$	$\max(V_P/20, 2Q_S)$
Layer 2	24	70	$1450+1.2z$		$54.6\sqrt{z}$				
Layer 3	variable				$300+19\sqrt{z}$				
Bedrock	∞		5600		3200	2720		∞	∞

3.2.3 Graphs of material parameters

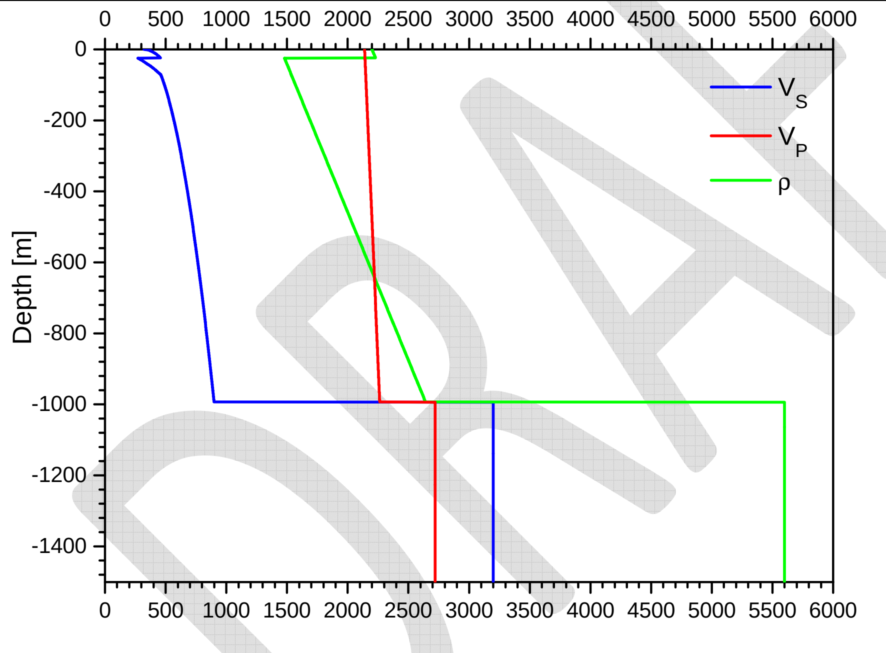

Fig. 3.12. S-wave speed V_S [m/s], P-wave speed V_P [m/s] and density $\rho\,[\mathrm{kg/m^3}]$ as functions of depth – Grenoble valley (Site 2).

3.2.4 Geometry of the model

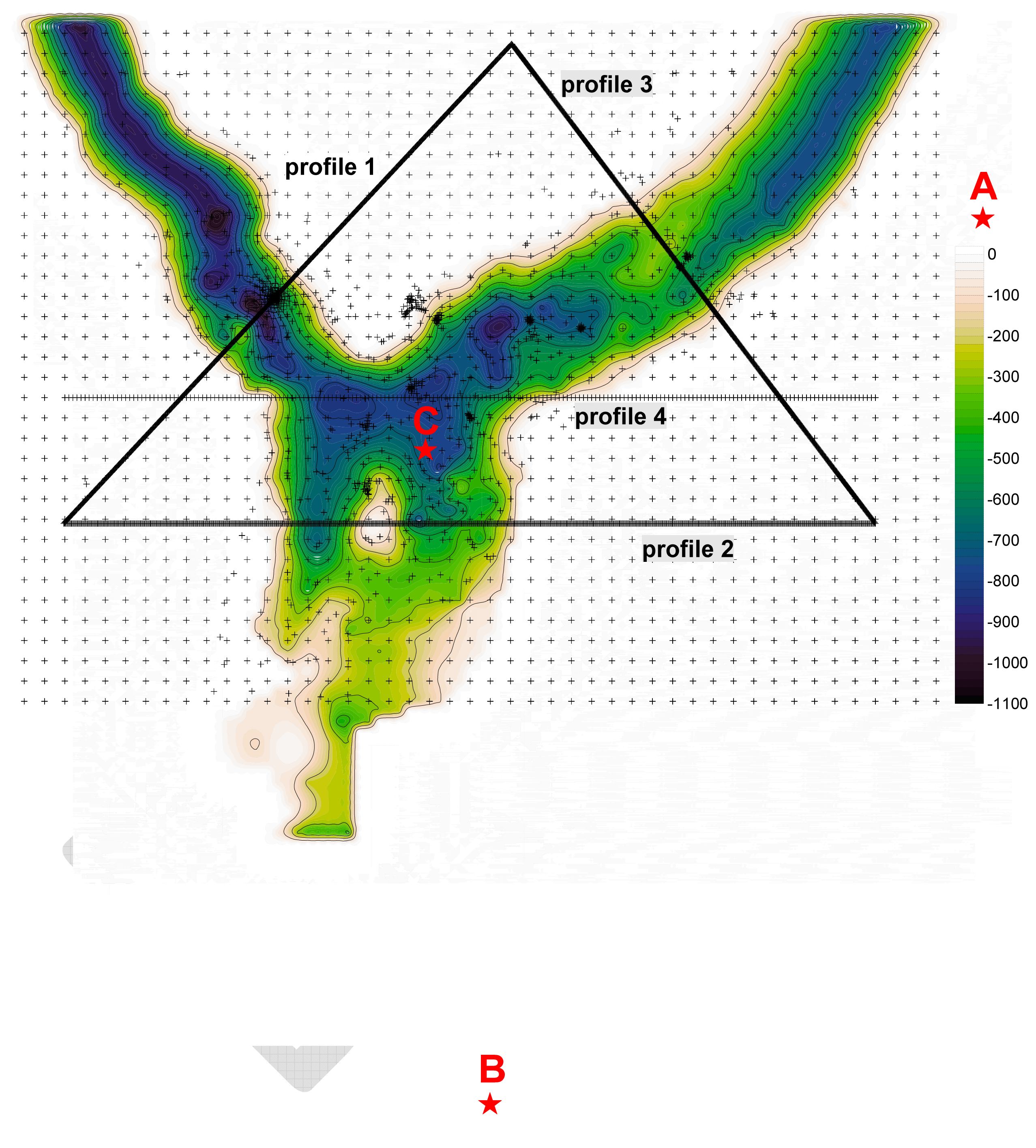

Fig. 3.13 Depth of the sediment-basement interface in the Grenoble valley model (Site 2). The red stars show positions of the point DC sources for 3D numerical simulations. (The + symbols, black lines and alphanumeric symbols relate to numerical simulations.). The colour bar shows depth in metres. Size of the whole depicted area is 26 550 m x 29 475 m.

3.2.5 Sensitivity study

In addition to the nominal model of Site 2, the Grenoble valley, a set of modified models was defined in order to investigate effects of the selected structural parameters on the ground motion characteristics.

The additional set of 3 models for 3D simulations is indicated in the logical tree. A modified model is indicated by a white box showing the modified model parameter. The grey-shaded boxes show parameters in the nominal model. A modified model differs from the nominal one only by a modified model parameter.

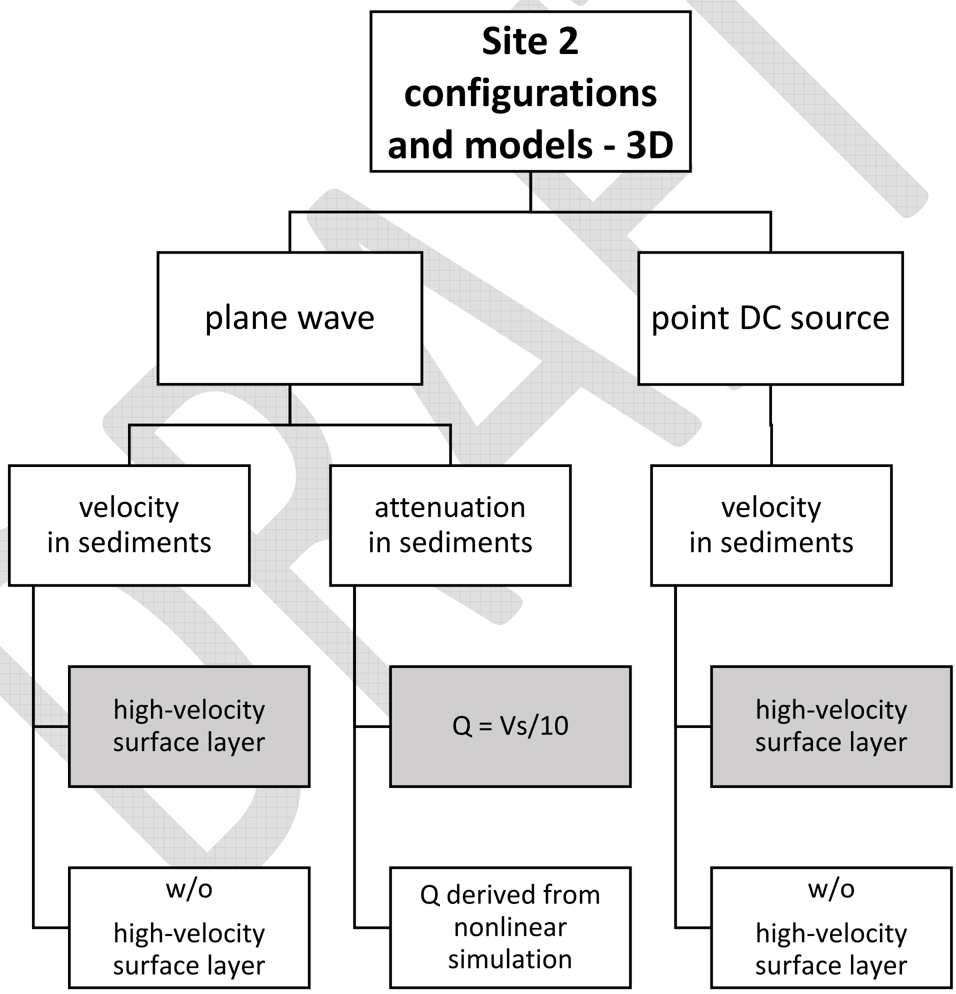

The additional set of 3 models for 3D simulations is indicated in the logical tree. A modified model is indicated by a white box showing the modified model parameter. The grey-shaded boxes show parameters in the nominal model. A modified model differs from the nominal one only by a modified model parameter.

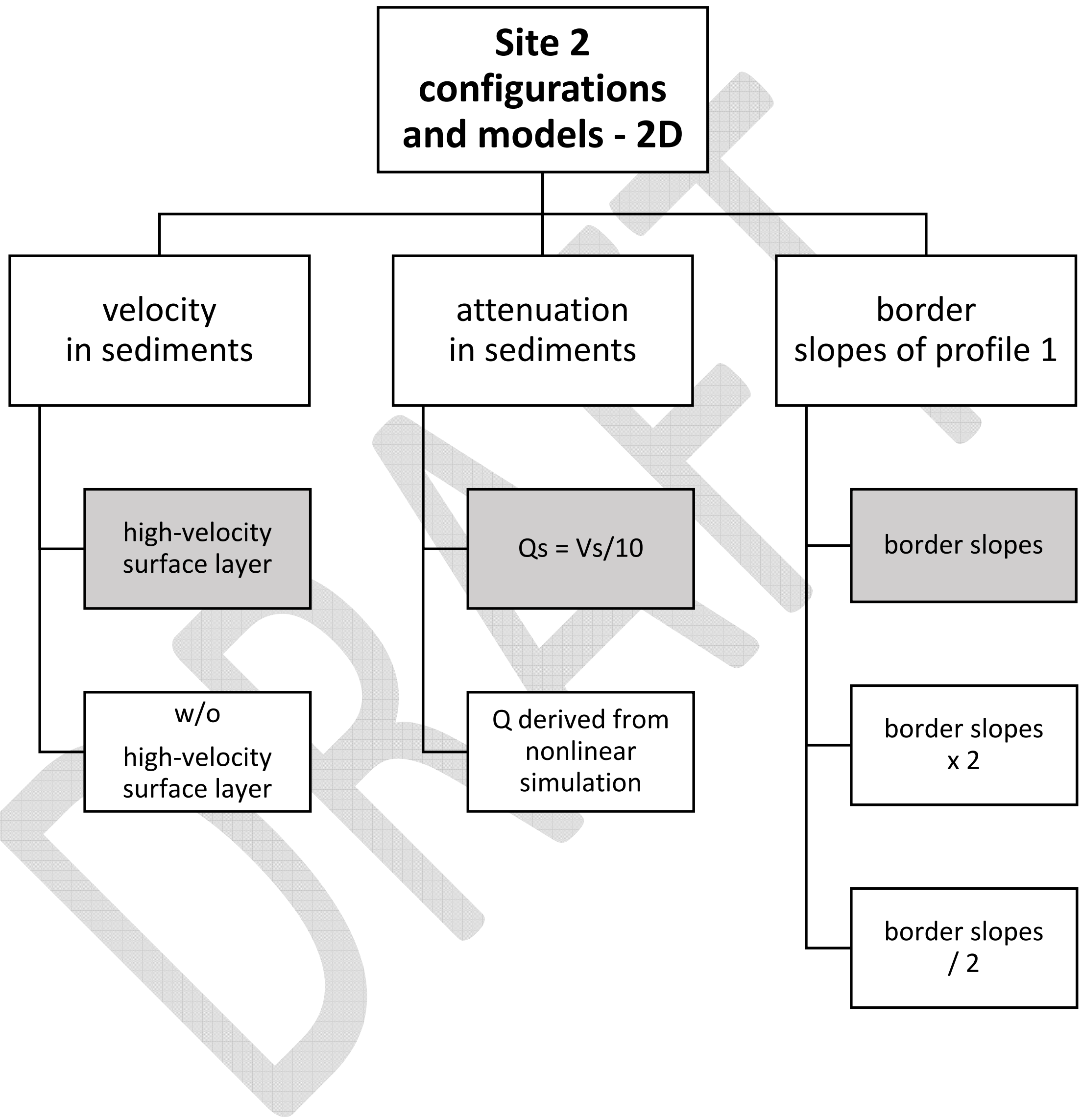

3.2.6 Direct numerical simulations

3.2.6.1 3D simulations

The computational parameters of the FD numerical simulations for the Grenoble valley (Site 2) models are summarized in Tab. 3.5.

Tab. 3.5. Computational parameters for the Grenoble valley (Site 2), 3D simulations.

coarser grid spacing	112.5 m
finer grid spacing	12.5 m
time step	1.10^{-3} s
frequency range	0.04 - 4 Hz
reference frequency for S-wave and P-wave speeds	1 Hz
number of relaxation frequencies	4
number of time levels	50 000
time window	50 s
thickness of PML in case of coarser grid	5 grid points
thickness of PML in case of finer grid	45 grid points
total number of grid cells including PML in case of coarser grid	273 x 247 x 152
total number of grid cells including PML in case of finer grid	2449 x 2215 x 105
simulation of the free surface	stress-imaging method
depth of excitation in case of the plane-wave vertical incidence	1150 m
depth of excitation in case of the point DC sources A and B	3000 m
depth of excitation in case of the point DC source C	4000 m
average CPU time on 128 cores	2000 min

Specification of theoretical receivers

Theoretical receivers positions are indicated by the black '+' symbols in Fig. 3.13. (Due to their number and the size of the figure, some of the symbols effectively make thick black lines in the figure.)

Specification of wavefield excitation

Two type of excitation were applied – a vertically incident plane wave and a point DC source. In the first type, three excitations were applied: vertically incident plane P wave, SV wave and SH wave. The source time function (Fig. 3.3) is the same as that for the 3D simulations for the Mygdonian basin (Site 1) model, described in paragraph 3.1.5.1. In the second type, three point DC sources were applied: A, B and C (see Fig. 3.13), each represented by six elementary dipoles.

Specification of results

Three-component time history of acceleration at each theoretical receiver.

3.2.6.2 2D simulations

The computational parameters of the FD numerical simulations for the Grenoble valley (Site 2) models are summarized in Tab. 3.6.

Tab. 3.6. Computational parameters for the Grenoble valley (Site 2), 2D simulations.

grid spacing	3 m
time step	2.10^{-4} s
frequency range	0.2 - 17 Hz
reference frequency for S-wave and P-wave speeds	1 Hz
number of relaxation frequencies	3
number of time levels	200 000
time window	50 s
thickness of PML	200 grid points
total number of grid cells including PML	5901 x 1868
simulation of the free surface	AFDA method
depth of excitation of the plane-wave vertical incidence	1150 m
average CPU time on 16 cores	1300 min

Specification of 2D profiles

Four 2D profiles (cross-sections) were selected in order to partially represent three branches and the central part of the ‘Y’-shaped Grenoble valley. The profiles are indicated by the surface lines in Fig. 3.13. Theoretical receivers are distributed along the surface of the profiles. The selected four profiles are depicted in Fig. 3.14 - Fig. 3.17. Geometry of the three profiles is shown in Fig. 3.18 - Fig. 3.22.

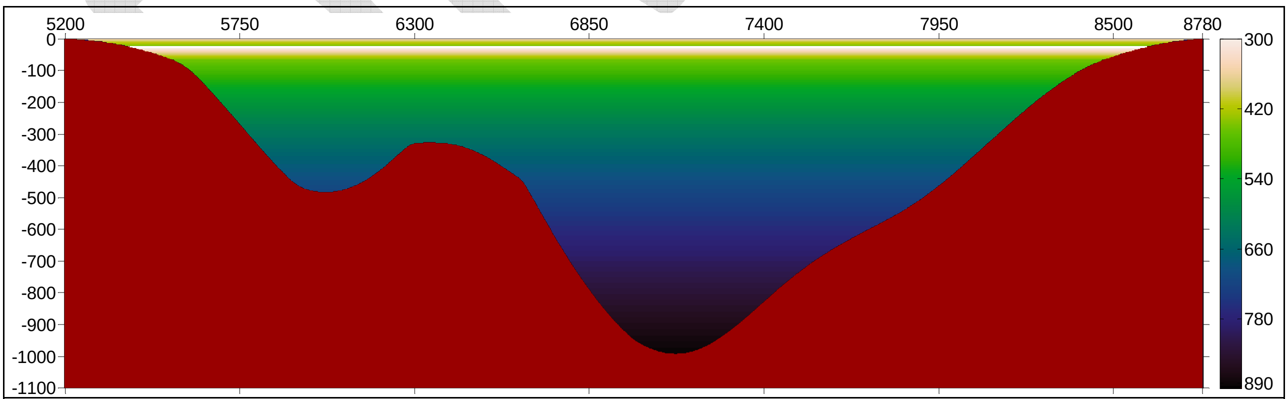

Fig. 3.14. S-wave speed V_S $[\mathrm{m/s}]$ along the 2D profile 2P1 – the profile 1 of the Grenoble valley (Site 2). Both horizontal dimension and depth shown in metres. Red colour represents $V_S = 3200\ \mathrm{m/s}$ in the bedrock. (Technical note: layering inside sediments is an artefact of the graphical software, the true distribution is smooth.)

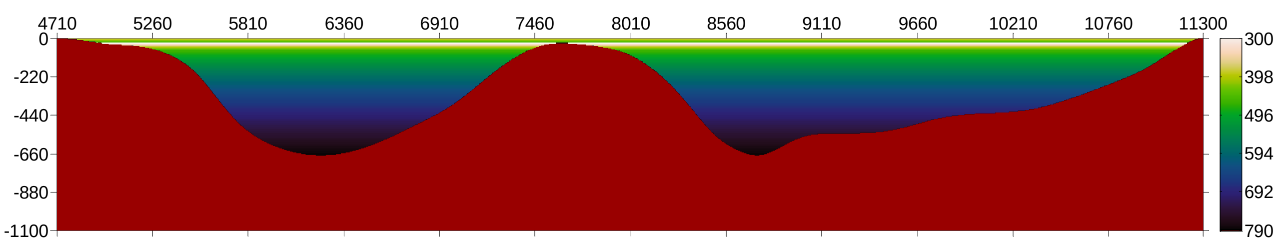

Fig. 3.15. S-wave speed V_S $[\mathrm{m/s}]$ along the 2D profile 2P2 – the profile 2 of the Grenoble valley (Site 2). Both horizontal dimension and depth shown in metres. Red colour represents $V_S = 3200\,\mathrm{m/s}$ in the bedrock. (Technical note: layering inside sediments is an artefact of the graphical software, the true distribution is smooth.)

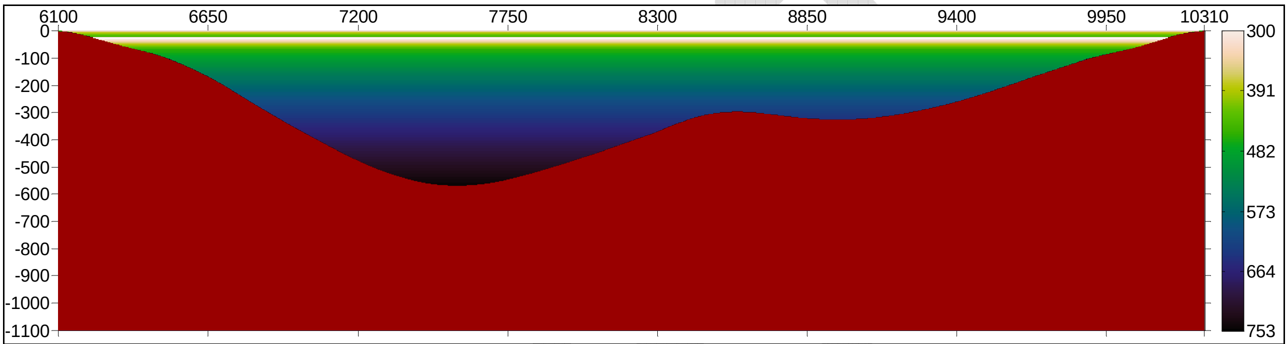

Fig. 3.16. S-wave speed V_S $[\mathrm{m/s}]$ along the 2D profile 2P3 – the profile 3 of the Grenoble valley (Site 2). Both horizontal dimension and depth shown in metres. Red colour represents $V_S = 3200\,\mathrm{m/s}$ in the bedrock. (Technical note: layering inside sediments is an artefact of the graphical software, the true distribution is smooth.)

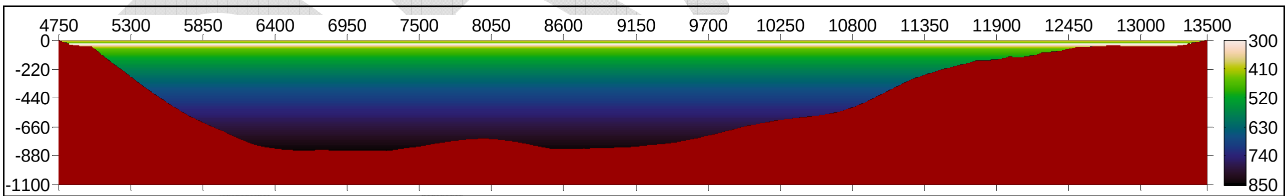

Fig. 3.17. S-wave speed V_S $[\mathrm{m/s}]$ along the 2D profile 2P4 – the profile 4 of the Grenoble valley (Site 2). Both horizontal dimension and depth shown in metres. Red colour represents $V_S = 3200\,\mathrm{m/s}$ in the bedrock. (Technical note: layering inside sediments is an artefact of the graphical software, the true distribution is smooth.)

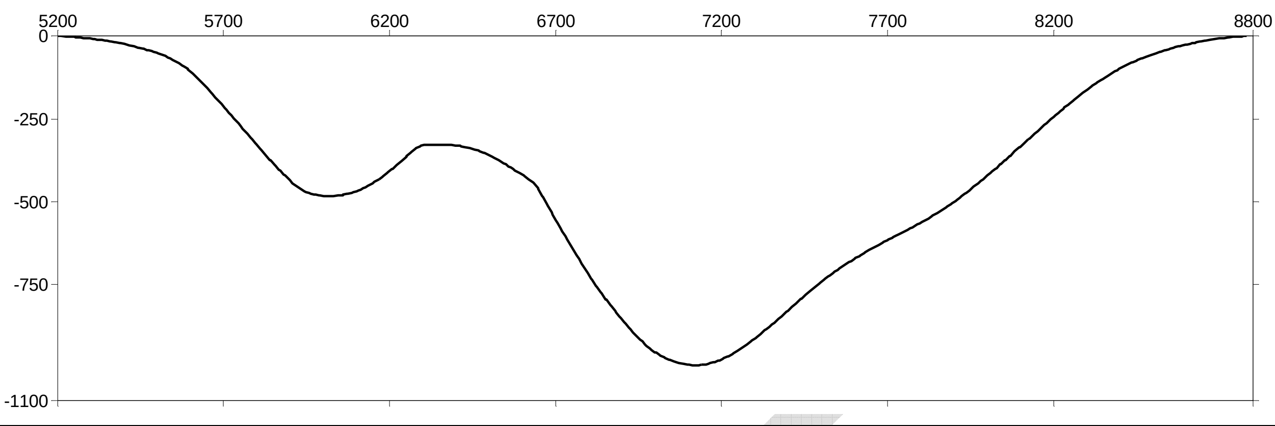

Fig. 3.18. Geometry of the sediment-basement interface along profile 2P1 – the profile 1 of the Grenoble valley (Site 2). Both horizontal dimension and depth shown in metres.

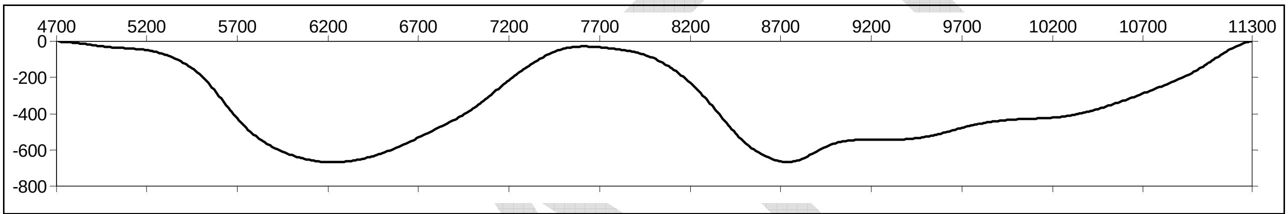

Fig. 3.19. Geometry of the sediment-basement interface along profile 2P2 – the profile 2 of the Grenoble valley (Site 2). Both horizontal dimension and depth shown in metres.

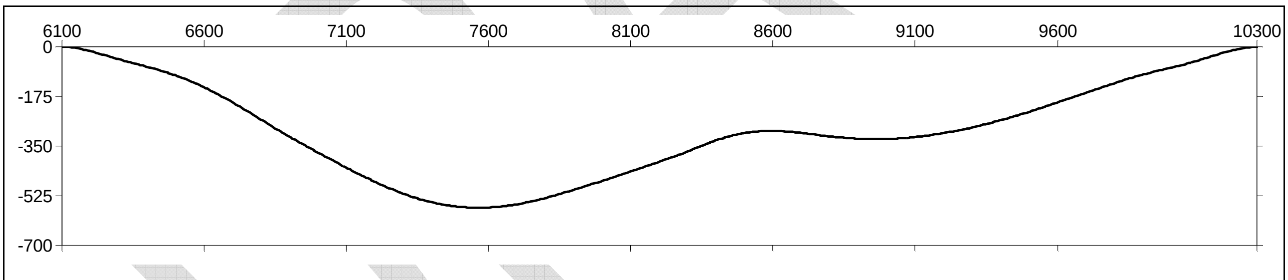

Fig. 3.20. Geometry of the sediment-basement interface along profile 2P3 – the profile 3 of the Grenoble valley (Site 2). Both horizontal dimension and depth shown in metres.

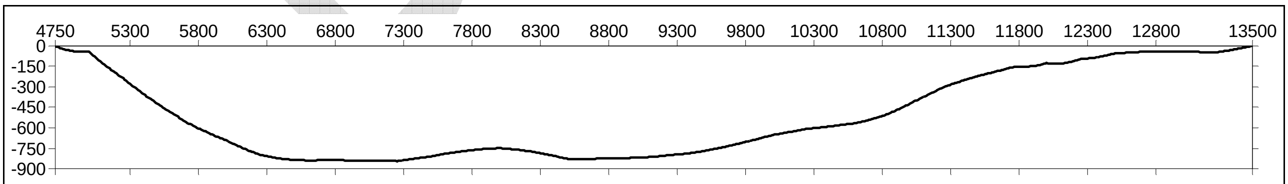

Fig. 3.21. Geometry of the sediment-basement interface along profile 2P4 – the profile 4 of the Grenoble valley (Site 2). Both horizontal dimension and depth shown in metres.

Specification of theoretical receivers

Receivers along profile 1 are equidistantly distributed at the free surface between points [0 m, 0 m] and [16200 m, 0 m] with interdistance of 25 m in the horizontal direction. Points [5200 m, 0 m] and [8780 m, 0 m] indicate edges of the sediment-filled valley.

Receivers along profile 2 are equidistantly distributed at the free surface between points [0 m, 0 m] and [19975 m, 0 m] with interdistance of 25 m in the horizontal direction. Points [4710 m, 0 m] and [11300 m, 0 m] indicate edges of the sediment-filled valley.

Receivers along profile 3 are equidistantly distributed at the free surface between points [0 m, 0 m] and [14850 m, 0 m] with interdistance of 25 m in the horizontal direction. Points [6100 m, 0 m] and [10310 m, 0 m] indicate edges of the sediment-filled valley.

Receivers along profile 4 are equidistantly distributed at the free surface between points [0 m, 0 m] and [19975 m, 0 m] with interdistance of 25 m in the horizontal direction. Points [4750 m, 0 m] and [13500 m, 0 m] indicate edges of the sediment-filled valley.

Specification of wavefield excitation

Three excitations were applied: vertically incident plane P wave, SV wave and SH wave. The source time function (Fig. 3.10) is the same as that for the 2D simulations for the Mygdonian basin (Site 1) model, described in paragraph 3.1.5.2.

Specification of results

Two-component (x - and z - components) time history of acceleration at each theoretical receiver in case of P and SV incidence waves. One-component (y - component) time history of acceleration at each theoretical receiver in case of SH incidence wave.

3.2.6.3 1D simulations

The computational parameters of the 1D simulations for the Grenoble valley (Site 2) are the same as for 2D simulations (see Tab. 3.6).

Specification of theoretical receivers

The same as for the 2D simulations.

Specification of wavefield excitation

Two excitations were applied: vertically incident plane P wave and S wave. The source time function (Fig. 3.10) is the same as that for the 2D simulations.

Specification of results

One-component time history of acceleration at each theoretical receiver.

3.3 Site 4

3.3.1 The meaning of the site and model

Site 4 is the smallest of the investigated sedimentary structures – the shallow sediment-filled valley with local fundamental resonant frequencies above 2 Hz. The spatial distribution of material parameters is solely specified point-to-point without explicitly specified sediment-bedrock interface.

3.3.2 Model

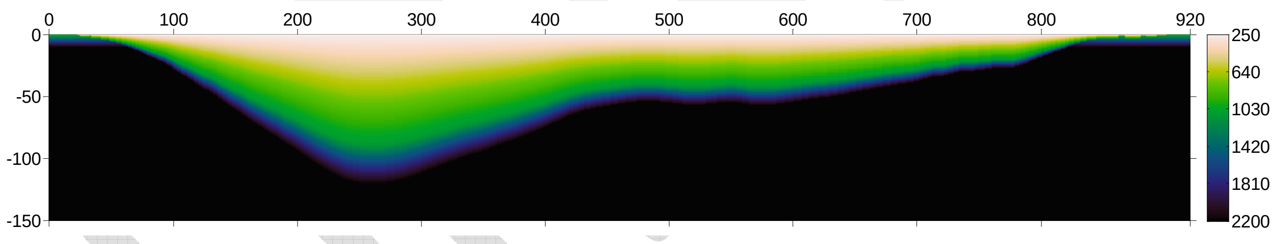

Fig. 3.22. S-wave speed $V_S\,[\mathrm{m/s}]$, P-wave speed $V_P\,[\mathrm{m/s}]$ and density $\rho\left[\mathrm{kg/m^3}\right]$ as functions of depth – Site 4. Both horizontal dimension and depth shown in metres. (Technical note: layering inside sediments is an artefact of the graphical software, the true distribution is smooth.)

3.3.3 Direct numerical simulations

3.3.3.1 2D simulations

The computational parameters of the FD numerical simulations for Site 4 model are summarized in Tab. 3.7.

Tab. 3.7. Computational parameters for the Site 4, 2D simulations.

grid spacing	1.75 m
time step	2.10^{-4} s
frequency range	0.2 - 25 Hz
reference frequency for S-wave and P-wave speeds	1 Hz
number of relaxation frequencies	3
number of time levels	55 000
time window	11 s
thickness of PML	n.a.
total number of grid cells including PML	7801 x 6501
simulation of the free surface	AFDA method
depth of excitation of the plane-wave vertical incidence	262.5 m
average CPU time on 1 core	3000 min

Specification of theoretical receivers

Receivers along profile are equidistantly distributed at the free surface between points [0 m, 0 m] and [920.5 m, 0 m] with interdistance of 1.75 m in the horizontal direction.

Specification of wavefield excitation

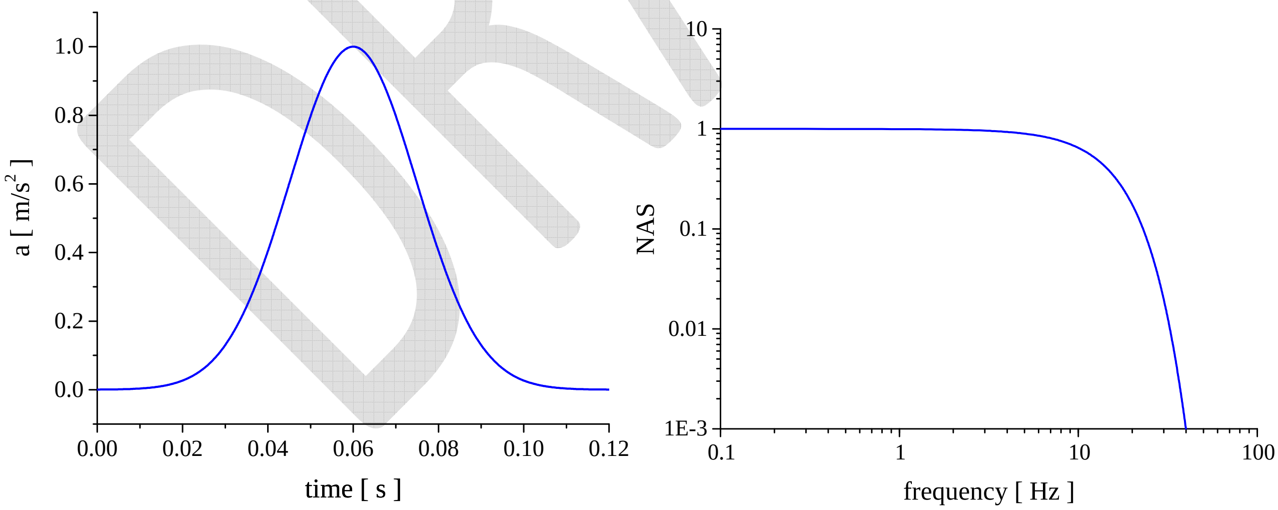

Fig. 3.23. The source time function of the incident wave. Left panel: acceleration, right panel: normalized amplitude Fourier spectrum.

Three excitations were applied: vertically incident plane P wave, SV wave and SH wave. The source time function (Fig. 3.10) was Gabor signal defined in subsection 10.3.1 by Eq. (10.27) with parameters $f_p = 0.2$, $\gamma_s = 1.5$, $\theta = 0$ and $t_s = 0.06$.

Specification of results

Two-component (x - and z - components) time history of acceleration at each theoretical receiver in case of P and SV incidence waves. One-component (y - component) time history of acceleration at each theoretical receiver in case of SH incidence wave.

3.3.3.2 1D simulations

The computational parameters of the 1D simulations for Site 4 are the same as for 2D simulations (see

Tab. 3.7).

Specification of theoretical receivers

The same as for the 2D simulations.

Specification of wavefield excitation

Two excitations were applied: vertically incident plane P wave and S wave. The source time function of the input (Fig. 3.23) is the same as that for the 2D simulations.

Specification of results

One-component time history of acceleration at each theoretical receiver.

3.4 Site 5

3.4.1 The meaning of the site and model

Site 5 is the mid-size sediment-filled valley with local fundamental resonant frequencies below 1 Hz, the minimum being around 0.5 Hz. There is a relatively strong gradient in sediments and relatively large velocity contrast at the sediment-bedrock interface.

3.4.2 Table of material parameters

Tab. 3.8. Mechanical parameters – Site 5.

Unit	Position z_1 [m]	Position z_2 [m]	$V_P 1$ [m/s]	$V_P 2$ [m/s]	$V_S 1$ [m/s]	$V_S 2$ [m/s]	$\rho\ 1$ [kg/m³]	$\rho\ 2$ [kg/m³]	Q_S	Q_P
Layer 1	0	30	800	2000	275	550	2000		$V_S/10$	max $(V_P/20, V_S/5)$
Layer 2	30	300	2000	2400	550	1100	2000	2200		
Layer 3	variable		2400		1100		2200			
Layered regional bedrock	0	1000	2300	4425	1050	2362.5	2400	2650	∞	∞
Layered regional bedrock	∞		4425		2362.5		2650			

$V_S(z) = V_S 1 + (V_S 2 - V_S 1)(z - z_1)/(z_2 - z_1)$ $\quad V_P(z) = V_P 1 + (V_P 2 - V_P 1)(z - z_1)/(z_2 - z_1)$

$V_S 1, V_P 1, z_1$ – at the top of the layer $\quad V_S 2, V_P 2, z_2$ – at the bottom of the layer

3.4.3 Graphs of material parameters

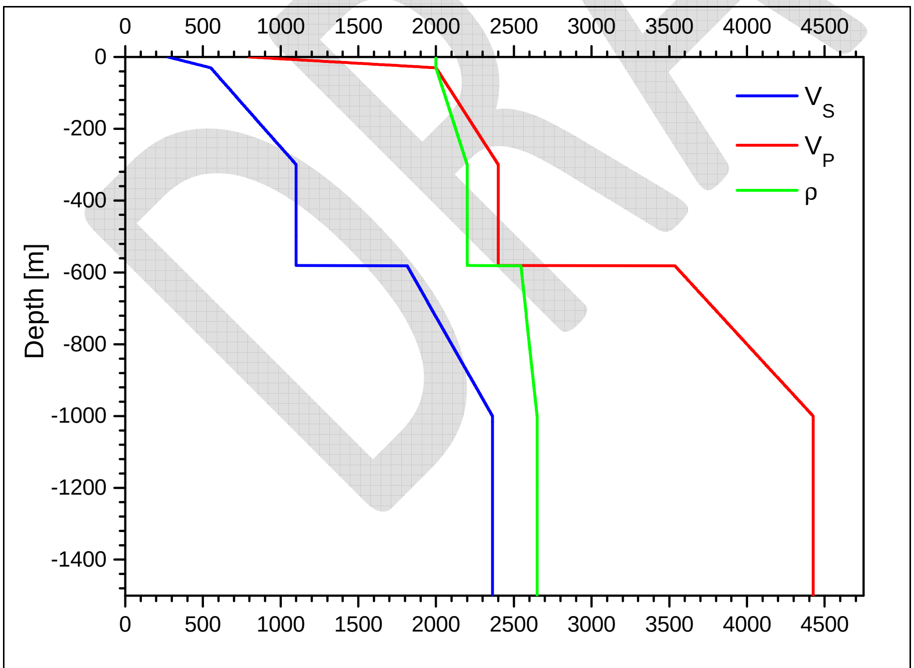

Fig. 3.24. S-wave speed V_S [m/s], P-wave speed V_P [m/s] and density ρ [kg/m³] as functions of depth – Site 5.

3.4.4 Geometry of the model

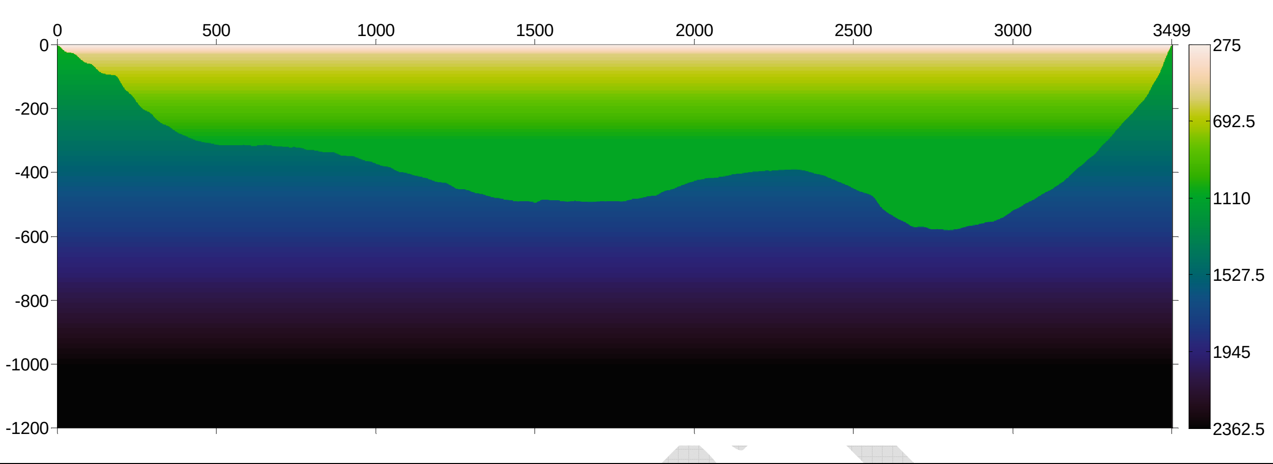

Fig. 3.25. S-wave speed V_S [m/s] along the 2D profile – Site 5. Both horizontal dimension and depth shown in metres. (Technical note: layering inside sediments is an artefact of the graphical software, the true distribution is smooth.)

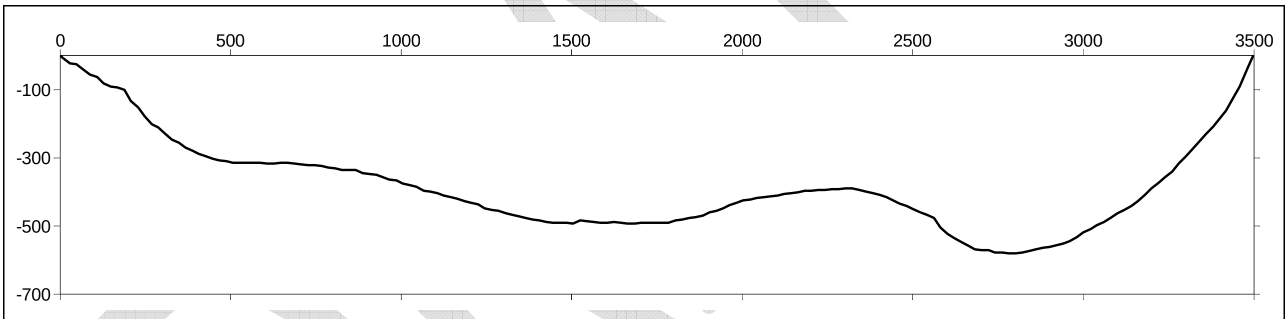

Fig. 3.26. Geometry of the sediment-basement interface along profile – Site 5. Both horizontal dimension and depth shown in metres.

3.4.5 Sensitivity study

In addition to the nominal model of Site 5, a set of modified models was defined in order to investigate effects of the selected structural parameters on the ground motion characteristics. A logical tree indicates 8 modified models. A modified model is indicated by a white box showing the modified model parameter. The grey-shaded boxes show parameters in the nominal model. A modified model differs from the nominal one only by a modified model parameter.

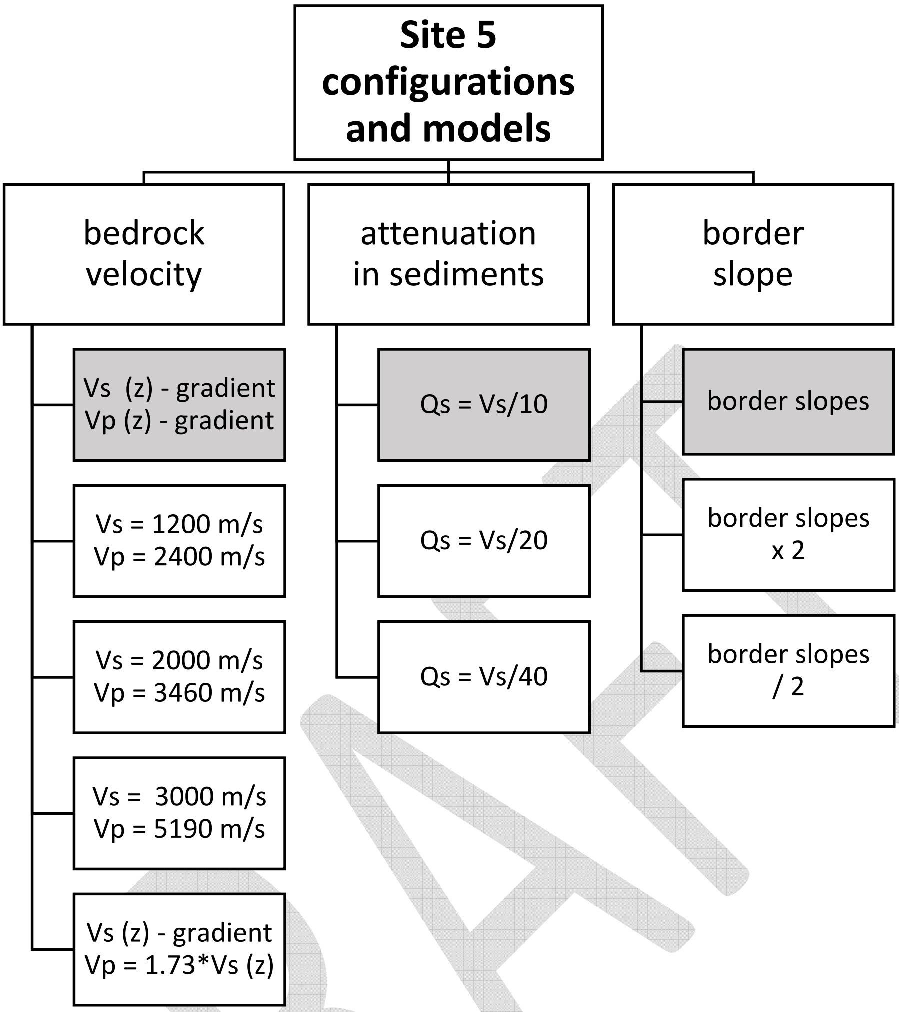

3.4.6 Direct numerical simulations

3.4.6.1 2D simulations

The computational parameters of the FD numerical simulations for the Site 5 model are summarized in Tab. 3.9.

Tab. 3.9. Computational parameters for the Site 5, 2D simulations.

grid spacing	1 m
time step	2.10^{-4} s
frequency range	0.2 - 20 Hz
reference frequency for S-wave and P-wave speeds	1 Hz
number of relaxation frequencies	3
number of time levels	250 000
time window	30 s
thickness of PML	200 grid points

total number of grid cells including PML	4501 x 1701
simulation of the free surface	AFDA method
depth of excitation of the plane-wave vertical incidence	1200 m
average CPU time on 18 cores	550 min

Specification of theoretical receivers

Receivers along profile are equidistantly distributed at the free surface between points [-300 m, 0 m] and [3790 m, 0 m], in depth 5 m between points [-300 m, -5 m] and [3790 m, -5 m] and in depth 10 m between points [-300 m, -10 m] and [3790 m, -10 m] with interdistance of 10 m in the horizontal direction. Points [0 m, 0 m] and [3500 m, 0 m] indicate edges of the sediment-filled valley.

Specification of wavefield excitation

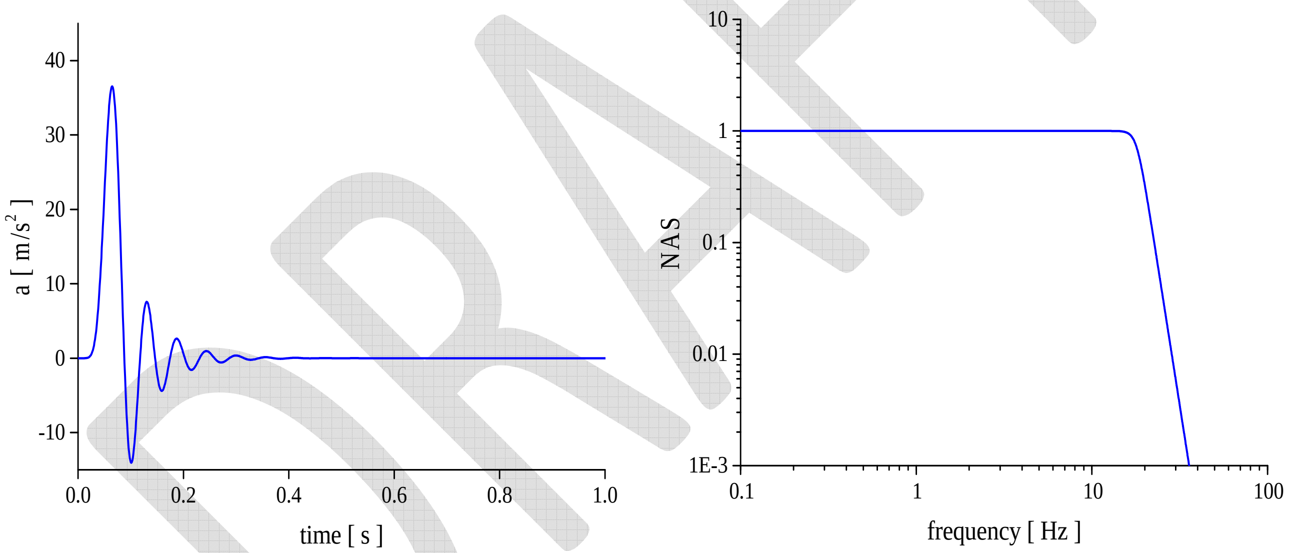

Fig. 3.27. The source time function of the incident wave. Left panel: acceleration, right panel: normalized amplitude Fourier spectrum.

Three excitations were applied: vertically incident plane P wave, SV wave and SH wave. The source time function (Fig. 3.27) was obtained by low-pass filtering a discrete Dirac pulse with a 10-pole (sharp) 1-pass (casual) Butterworth filter with corner frequency f_c = 18 Hz. The input signal has flat amplitude spectrum up to 15 Hz and no energy above 22.5 Hz (Chaljub et al. 2012).

Specification of results

Two-component (x - and z - components) time history of acceleration at each theoretical receiver in case of P and SV incidence waves. One-component (y - component) time history of acceleration at each theoretical receiver in case of SH incidence wave.

3.4.6.2 1D simulations

The computational parameters of the 1D simulations for Site 5 are the same as for 2D simulations (see Tab. 3.9).

Specification of theoretical receivers

The same as for the 2D simulations.

Specification of wavefield excitation

Two excitations were applied: vertically incident plane P wave and S wave. The source time function (Fig. 3.27) is the same as that for the 2D simulations.

Specification of results

One-component time history of acceleration at each theoretical receiver.

3.5 Site 6

3.5.1 The meaning of the site and model

Site 6 is the relatively small shallow sediment-filled valley with local fundamental resonant frequencies above 1 Hz. Relatively large velocity contrast at the sediment-bedrock interface. Two alternative models are specified – one with homogeneous sediments, one with gradient of the P- and S-wave speeds in Layer 2.

3.5.2 Table of material parameters

Tab. 3.10 and Tab. 3.11 show values of the P-wave and S-wave speeds, and density. The parameters are functions of depth. Inside sediments they do not change in the horizontal direction. Two basic models with respect to the S-wave and P-wave speeds in layer 2 will be considered: the model with constant speeds and model with gradients. The P-wave and S-wave speeds, and density in the two models are illustrated in Fig. 3.28.

Tab. 3.10. Mechanical parameters – Site 6h – homogeneous layers.

Unit	Position		V_P	V_S	ρ	Q_S	Q_κ
	z_1	z_2	[m/s]	[m/s]	[kg/m^3]		
	[m]						
Layer 1	0	5	960	230	2100	$V_S/10$	∞
Layer 2	5	160	2400	600	2200		
Bedrock	∞		4000	1500	2500	∞	

Tab. 3.11. Mechanical parameters – Site 6g – velocity gradient in Layer 2.

Unit	Position		V_P	V_S1	V_S2	ρ	Q_S	Q_κ
	z_1	z_2	[m/s]	[m/s]	[m/s]	[kg/m^3]		
	[m]							
Layer 1	0	5	960		230	2100	$V_S/10$	∞
Layer 2	5	160	$4V_S$	400	700	2200		
Bedrock	∞		4000		1500	2500	∞	

$$V_S(z) = V_S1 + (V_S2 - V_S1)(z - z_1)/(z_2 - z_1)$$

V_S1, z_1 – at the top of the layer

V_S2, z_2 – at the bottom of the layer

3.5.3 Graphs of material parameters

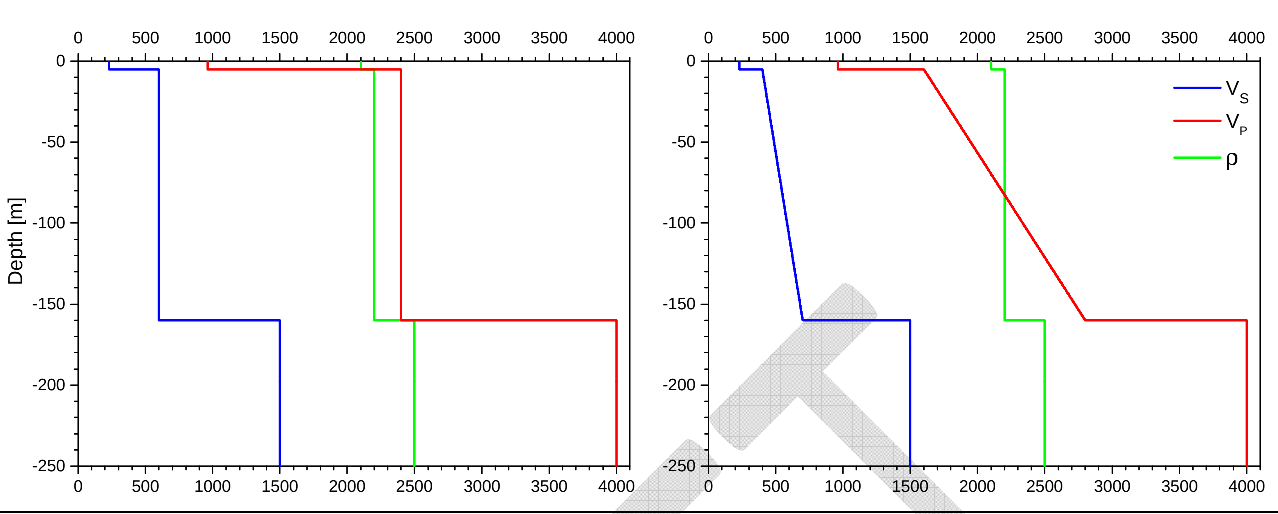

Fig. 3.28. S-wave speed $V_S\ [\mathrm{m/s}]$, P-wave speed $V_P\ [\mathrm{m/s}]$ and density $\rho\left[\mathrm{kg/m^3}\right]$ as functions of depth – Site 6. Left panel: Model with homogeneous layers. Right panel: Model with gradients in V_S and V_P in the second sedimentary layer.

3.5.4 Geometry of the model

For Site 6 there are two simplified models – 2D and 3D. Geometry of the 2D model is shown in Fig. 3.30. The model is a relatively small shallow weakly asymmetric sediment-filled valley. The left-hand valley margin is complicated by a thin (approximately 12 m thick) horizontal layer.

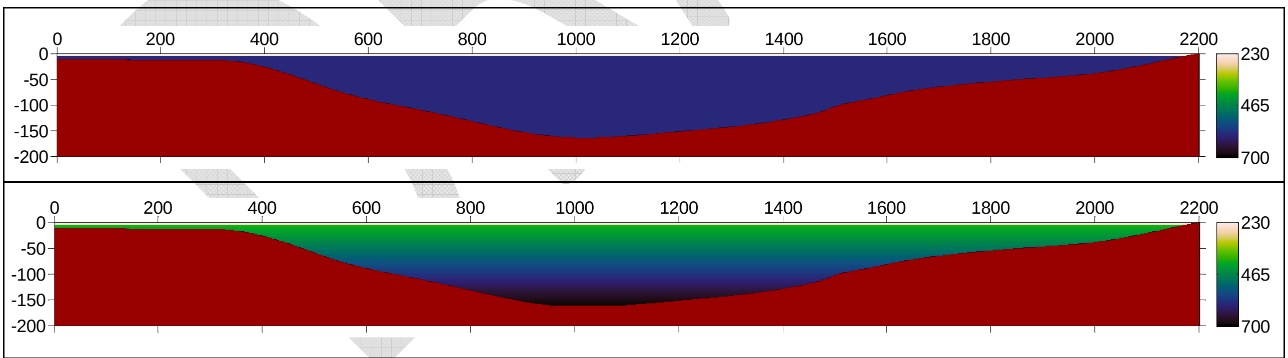

Fig. 3.29. S-wave speed $V_S\ [\mathrm{m/s}]$ along the 2D profile – Site 6. Both horizontal dimension and depth shown in metres. Red colour represents $V_S = 1500\ \mathrm{m/s}$ in the bedrock. Upper panel: Model with homogeneous layers. Bottom panel: Model with gradient in V_S in the second sedimentary layer. (Technical note: layering inside sediments is an artefact of the graphical software, the true distribution is smooth.)

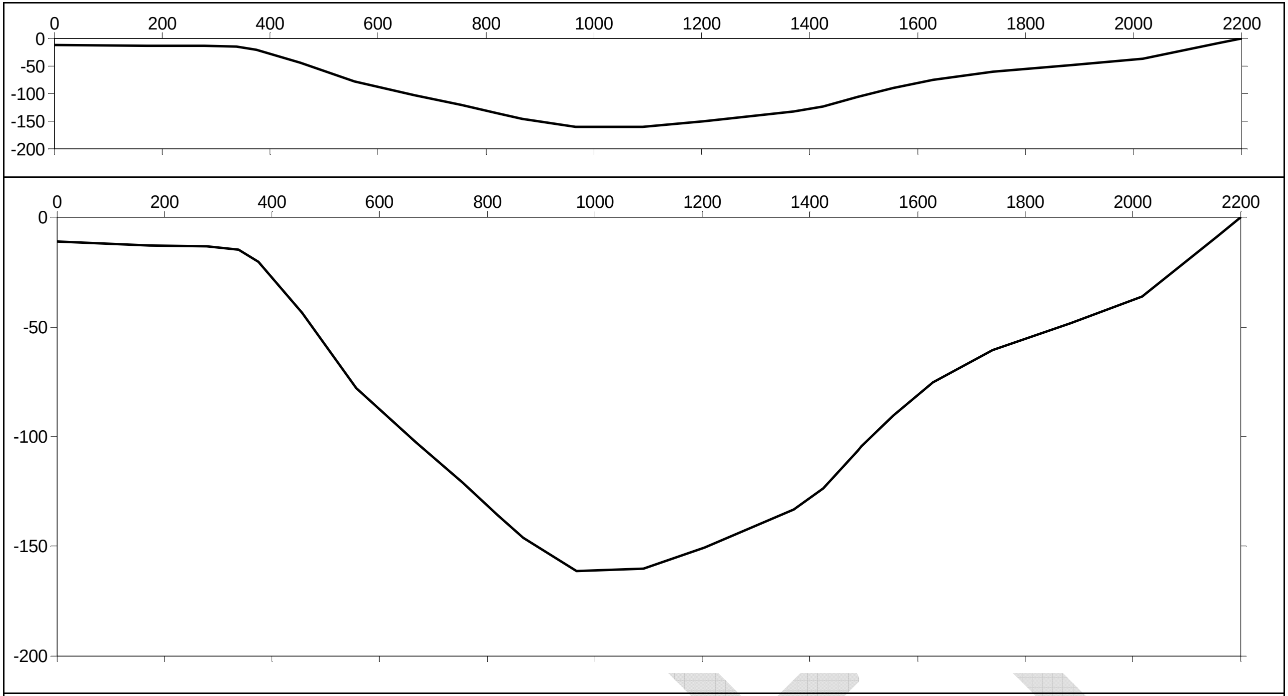

Fig. 3.30. Geometry of the sediment-basement interface along profile – Site 6. Both horizontal dimension and depth shown in metres. Upper panel: 1:1 horizontal-to-vertical scale. Bottom panel: 1:4 horizontal-to-vertical scale.

3.5.5 Sensitivity study

In addition to the nominal model of Site 6h, a set of modified models was defined in order to investigate effects of the selected structural parameters on the ground motion characteristics. A logical tree indicates 13 modified models. A modified model is indicated by a white box showing the modified model parameter. The grey-shaded boxes show parameters in the nominal model. A modified model differs from the nominal one only by a modified model parameter.

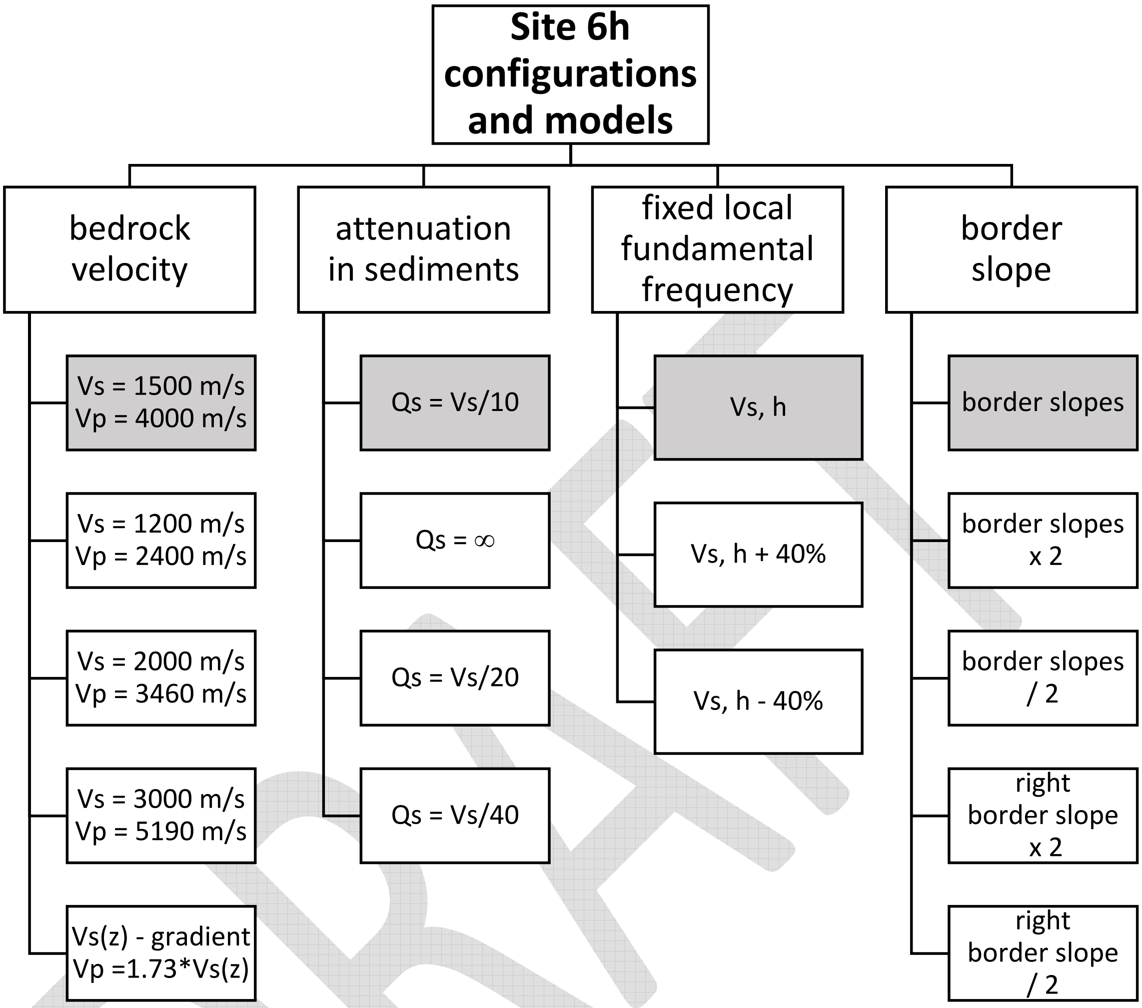

In addition to the nominal model of Site 6g, a set of modified models was defined in order to investigate effects of the selected structural parameters on the ground motion characteristics. A logical tree indicates 11 modified models. A modified model is indicated by a white box showing the modified model parameter. The grey-shaded boxes show parameters in the nominal model. A modified model differs from the nominal one only by a modified model parameter.

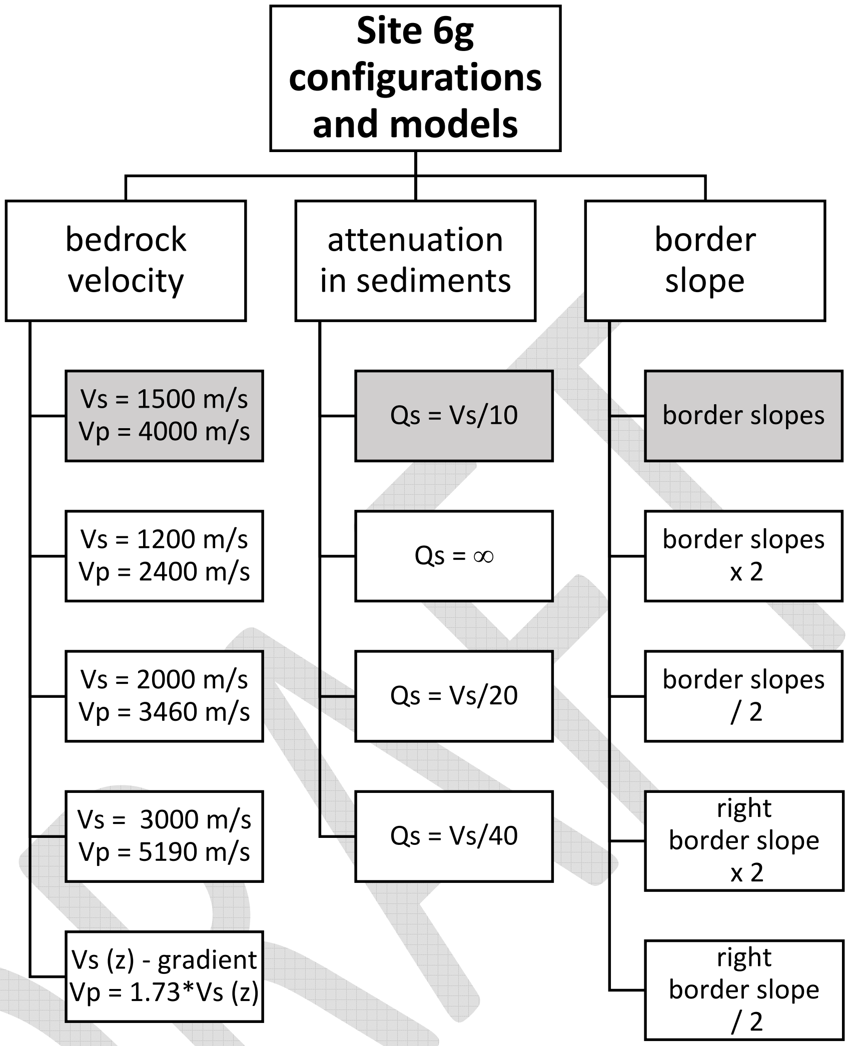

Specific modifications of the 2D models 6h and 6g are their 3D meander extensions. The geometry and 25 2D profiles are shown in Fig. 3.31.

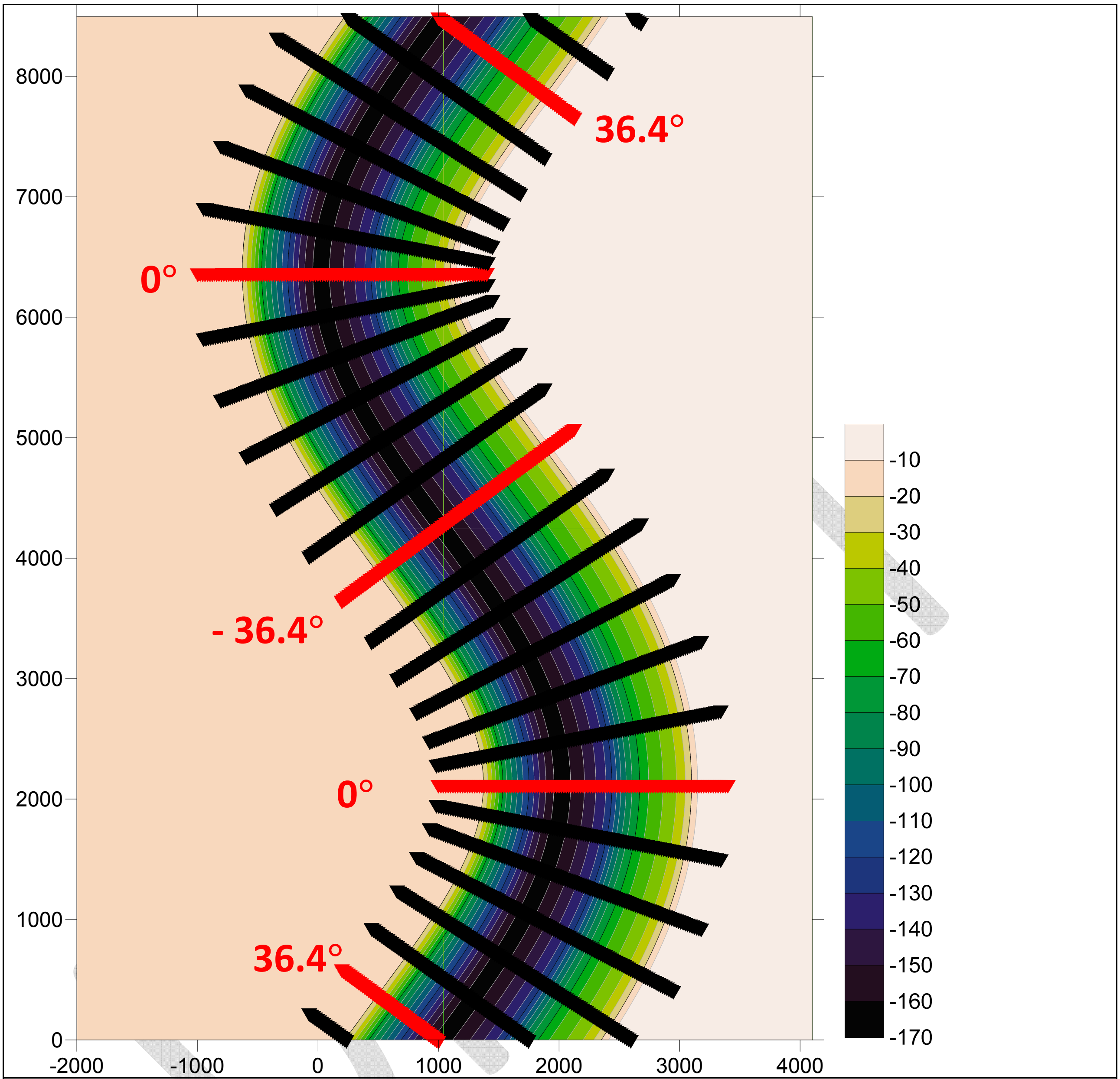

Fig. 3.31. Geometry of the sediment-basement interface of the 3D meander extensions of the 2D 6h and 6g models. Both the horizontal dimensions and depth are shown in metres. The red and black thick lines indicate 2D profiles of the surface receivers. Results for the red profiles are shown in the report, results for the black profiles are shown in the electronic supplement.

3.5.6 Direct numerical simulations

3.5.6.1 3D simulations

The computational parameters of the FD numerical simulations for the Site 6 – 3D meander-extension models are summarized in Tab. 3.12.

Tab. 3.12. Computational parameters for the Site 6 – meander extension, 3D simulations.

grid spacing	6 m
time step	7.10^{-4} s
frequency range	0.2 - 7 Hz
reference frequency for S-wave and P-wave speeds	1 Hz
number of relaxation frequencies	4
number of time levels	85 714
time window	60 s
thickness of PML	50 grid points
total number of grid cells including PML	951 x 1522 x 120
simulation of the free surface	stress-imaging method
depth of excitation of the plane-wave vertical incidence	200 m
average CPU time on 160 cores	1000 min

Specification of theoretical receivers

Theoretical receivers positions are indicated by the black and red '▼' symbols in Fig. 3.31. (Due to their number and the size of the figure, the symbols effectively make thick black and red lines.)

Specification of wavefield excitation

Three excitations were applied: vertically incident plane P wave, SV wave and SH wave. The source time function (Fig. 3.27) is the same as that for the 2D simulations for the Site 5, described in paragraph 3.4.6.1.

Specification of results

Three-component time history of acceleration at each theoretical receiver.

3.5.6.2 2D simulations

The computational parameters of the FD numerical simulations for the Site 6 models are summarized in Tab. 3.13.

Tab. 3.13. Computational parameters for Site 6, 2D simulations.

grid spacing	1.5 m
time step	2.10^{-4} s
frequency range	0.2 - 20 Hz
reference frequency for S-wave and P-wave speeds	1 Hz
number of relaxation frequencies	3
number of time levels	300 000

time window	60 s
thickness of PML	200 grid points
total number of grid cells including PML	2467 x 867
simulation of the free surface	AFDA method
depth of excitation of the plane-wave vertical incidence	200 m
average CPU time on 30 cores	180 min

Specification of theoretical receivers

Receivers along profile are equidistantly distributed at the free surface between points [0 m, 0 m] and [2400 m, 0 m] with interdistance of 20 m in the horizontal direction. Points [0 m, 0 m] and [2200 m, 0 m] indicate edges of the sediment-filled valley.

Specification of wavefield excitation

Three excitations were applied: vertically incident plane P wave, SV wave and SH wave. The source time function (Fig. 3.27) is the same as that for the 2D simulations for the Site 5, described in paragraph 3.4.6.1.

Specification of results

Two-component (x - and z - components) time history of acceleration at each theoretical receiver in case of P and SV incidence waves. One-component (y - component) time history of acceleration at each theoretical receiver in case of SH incidence wave.

3.5.6.3 1D simulations

The computational parameters of the 1D simulations for Site 6 are the same as for 2D simulations (see Tab. 3.13).

Specification of theoretical receivers

The same as for the 2D simulations.

Specification of wavefield excitation

Two excitations were applied: vertically incident plane P wave and S wave. The source time function (Fig. 3.27) is the same as that for the 2D simulations.

Specification of results

One-component time history of acceleration at each theoretical receiver.

3.6 Site 7

3.6.1 The meaning of the site and model

Site 7 is the relatively large shallow sediment-filled valley with fundamental resonant frequencies below 1 Hz, the minimum being approximately 0.5 Hz. There are strong gradients in Layer 1 and Layer 2, and large velocity contrast at the sediment-bedrock interface.

3.6.2 Table of material parameters

Tab. 3.14 shows values of the P-wave and S-wave speeds, and density. These parameters are illustrated in Fig. 3.32. The parameters are functions of depth. Inside sediments they do not change in the horizontal direction.

Tab. 3.14. Mechanical parameters – Site 7.

Unit	Position		$V_P 1$	$V_P 2$	$V_S 1$	$V_S 2$	ρ	Q_S	Q_κ
	z_1	z_2	[m/s]	[m/s]	[m/s]	[m/s]	[kg/m^3]		
	[m]								
Layer 1	0	30	1000	2200	200	600	2200	$V_S/10$	∞
Layer 2	30	100	2200	2700	600	900	2150		
Layer 3	100	510	2700	3600	900	1200			
Bedrock	∞		4850		2800		2500	∞	

$$V_S(z) = V_S 1 + (V_S 2 - V_S 1)(z - z_1)/(z_2 - z_1)$$

$V_S 1, z_1$ – at the top of the layer

$V_S 2, z_2$ – at the bottom of the layer

3.6.3 Graphs of material parameters

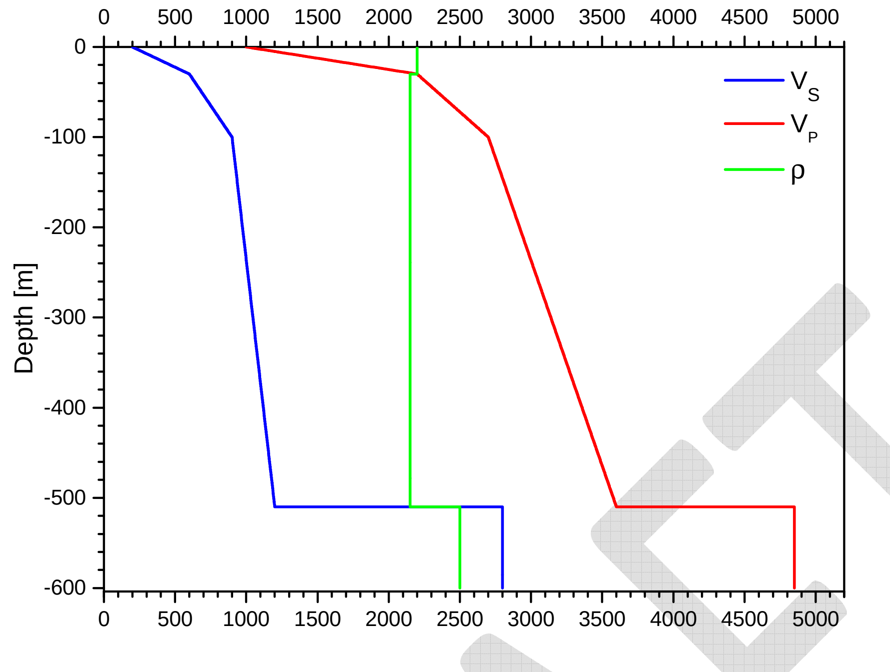

Fig. 3.32. S-wave speed $V_S\,[\mathrm{m/s}]$, P-wave speed $V_P\,[\mathrm{m/s}]$ and density $\rho\left[\mathrm{kg/m^3}\right]$ as functions of depth – Site 7.

3.6.4 Geometry of the model

For Site 7 there is one simplified 2D model. Its geometry is shown in Fig. 2.1. The model is a relatively large shallow strongly asymmetric sediment-filled valley.

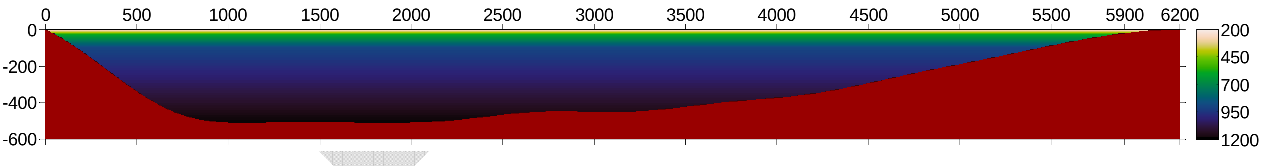

Fig. 3.33. S-wave speed $V_S\,[\mathrm{m/s}]$ along the 2D profile – Site 7. Red colour represents $V_S = 2800\,\mathrm{m/s}$ in the bedrock. Both horizontal dimension and depth shown in metres. (Technical note: layering inside sediments is an artefact of the graphical software, the true distribution is smooth.)

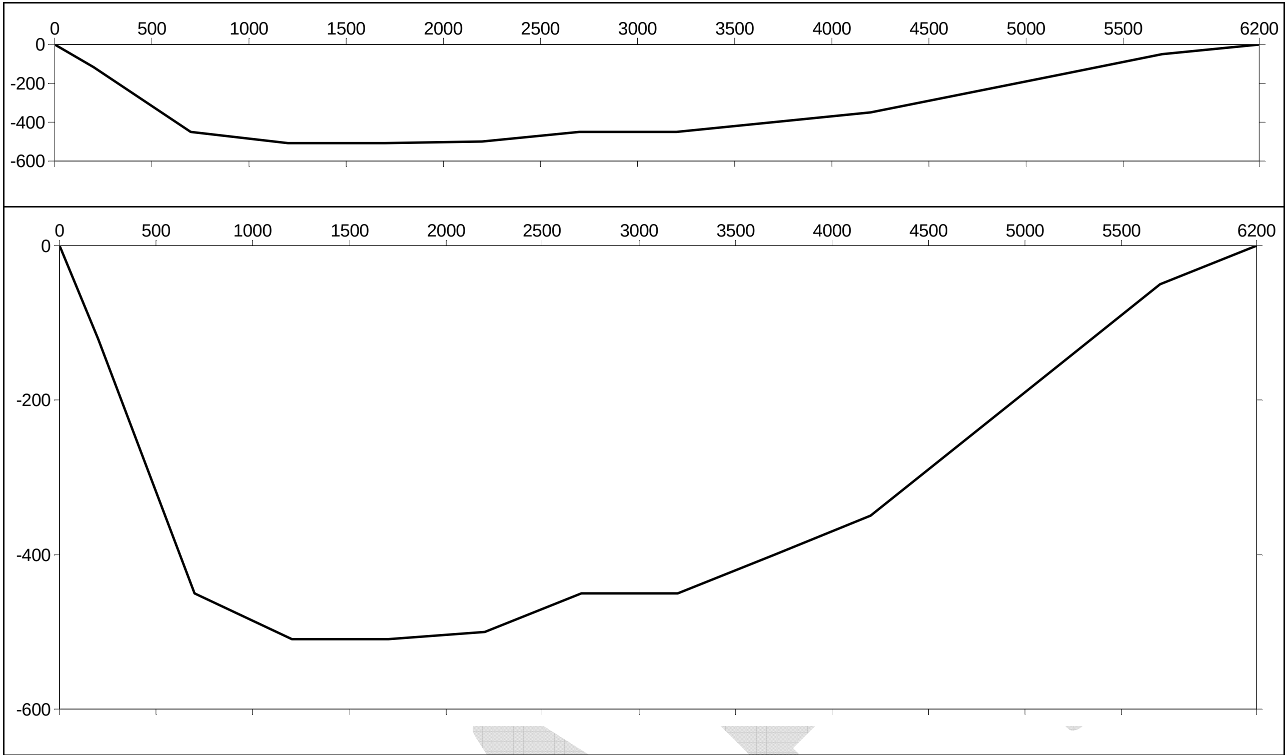

Fig. 3.34. Geometry of the sediment-basement interface along profile – Site 7. Both horizontal dimension and depth shown in metres. Upper panel: 1:1 horizontal-to-vertical scale. Bottom panel: 1:4 horizontal-to-vertical scale.

3.6.5 Sensitivity study

In addition to the nominal model of Site 7, a set of modified models was defined in order to investigate effects of the selected structural parameters on the ground motion characteristics. A logical tree indicates 7 modified models. A modified model is indicated by a white box showing the modified model parameter. The grey-shaded boxes show parameters in the nominal model. A modified model differs from the nominal one only by a modified model parameter.

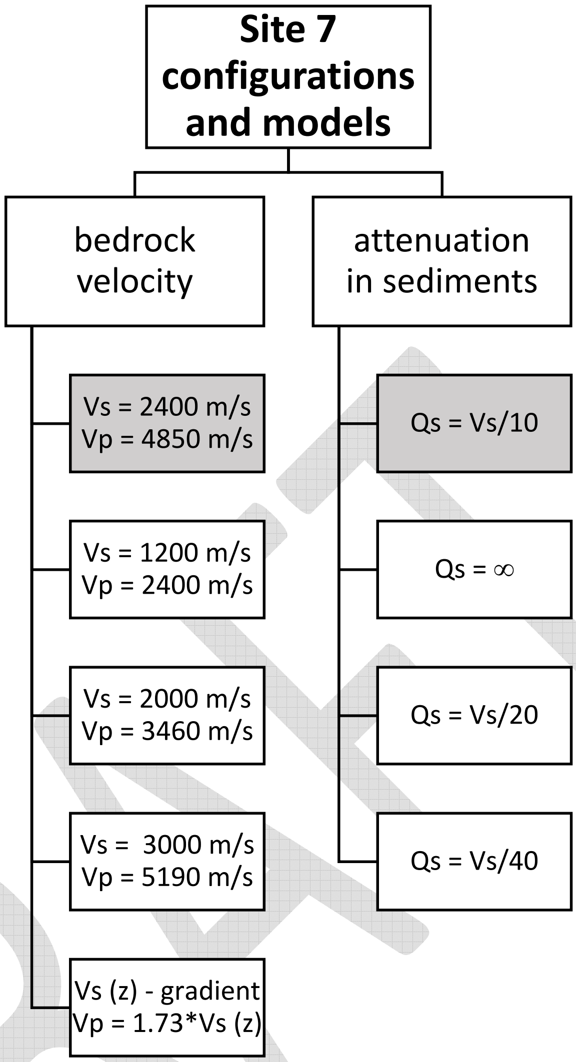

3.6.6 Direct numerical simulations

3.6.6.1 2D simulations

The computational parameters of the FD numerical simulations for the Site 7 model are summarized in Tab. 3.15.

Tab. 3.15. Computational parameters for Site 7, 2D simulations.

grid spacing	1.5 m
time step	1.6 .10^{-4} s
frequency range	0.2 - 20 Hz
reference frequency for S-wave and P-wave speeds	1 Hz
number of relaxation frequencies	3
number of time levels	375 000/875 000
time window	60 s/140 s

thickness of PML	200 grid points
total number of grid cells including PML	5734 x 1534
simulation of the free surface	AFDA method
depth of excitation of the plane-wave vertical incidence	600 m
average CPU time on 30/64 cores	1000 min

Specification of theoretical receivers

Receivers along profile are equidistantly distributed at the free surface between points [-100 m, 0 m] and [6500 m, 0 m] with interdistance of 50 m in the horizontal direction. Points [0 m, 0 m] and [6200 m, 0 m] indicate edges of the sediment-filled valley.

Specification of wavefield excitation

Three excitations were applied: vertically incident plane P wave, SV wave and SH wave. The source time function (Fig. 3.27) is the same as that for the 2D simulations for the Site 5, described in paragraph 3.4.6.1.

Specification of results

Two-component (x - and z - components) time history of acceleration at each theoretical receiver in case of P and SV incidence waves. One-component (y - component) time history of acceleration at each theoretical receiver in case of SH incidence wave.

3.6.6.2 1D simulations

The computational parameters of the 1D simulations for Site 7 are the same as for 2D simulations (see Tab. 3.15).

Specification of theoretical receivers

The same as for the 2D simulations.

Specification of wavefield excitation

Two excitations were applied: vertically incident plane P wave and S wave. The source time function (Fig. 3.27) is the same as that for the 2D simulations.

Specification of results

One-component time history of acceleration at each theoretical receiver.

4 INPUT AND OUTPUT

4.1 Selected accelerograms

The aggravation factors are looked for on several ground motion parameters (peak values, response spectra, duration, etc., see below) that are not related linearly with their value for the input motion (unlike for a Fourier spectral ratio). It is thus needed to consider several realistic input accelerograms, in order to get robust estimates on the corresponding average aggravation factors (and their signal-to-signal variability). As it has been shown in previous studies (Pegasos and PRP, for instance) that the amplification factors of response spectral ordinates is sensitive to the frequency contents of the input motion, it has been decided to select the input accelerograms on the basis of their frequency contents. The selection was performed in several steps as described below:

- Searching in the RESORCE (2012) data base of accelerograms recorded on rock or stiff soil sites, in the near source area (distance smaller than 40 km).
- Keeping only those with a very good signal-to-noise ratio over a wide frequency band, i.e., with very low high-pass frequency (< 0.25 Hz). In the end mainly digitally recorded accelerograms passed this step.
- Selecting a subset of 11 accelerograms exhibiting a wide distribution of peak frequencies (i.e., the frequency F_{peak} of the peak acceleration response spectrum), from around 1 Hz to beyond 16 Hz.

The corresponding normalized spectra (PSA/pga) are illustrated in Fig. 4.1, and the list of accelerograms is given in Tab. 4.1.

Tab. 4.1. Parameters of 11 selected accelerograms.

RESORCE waveform ID and station name	Site class (EC8)	Earthquake (Name, date, Magnitude)	Distance (Epicentral E our RJB R)	Compo-nent	Pga (cm/s²)	F_{peak} (Hz)	Source
00188 - Naso (NAS)	A	Baso-Tireno, Italy, 15/04/1978 23:33, Mw=6.1	E18, R16	H1	150	4.2	ITACA
				H2	129	6.7	
				V	80		
	A		E20, R15	H1	315	2.5	ESMD
				H2	339	10.0	

6756 - Flagbjarnarholt		South-Iceland, 17/06/2000 15:40, Mw=6.5		V	271		
6802 - Thjorsartun	A	Sud Islande 21/06/2000 00:51, Mw=6.4	E3, R3	H1	669	10.0	ESMD
				H2	544	2.0	
				V	331		
15205 - Hveragerdi-Church	A	Mt. Hengill Iceland 24/08/1997 03:04 Mw=4.9	E6	H1	168	7.7	ESMD
				H2	67	4.2	
				V	42		
15537 - Thjorarbru	A	South Iceland 17/06/2000 15:42 mb = 5.7	E10	H1	209	3.3	ESMD
				H2	231	3.3	
				V	47		
15560 - Thjorarbru	A	South Iceland 17/06/2000 17:40: Mw = 5.0	E10, R5	H1	176	5.9	ESMD
				H2	281	3.6	
				V	124		
14683 Borgo Cerreto - Torre	A	Umbria-Marche 14/10/1997 15:23, Mw=5.6	E9, R5	H1	333	4.6	ITACA
				H2	329	3.3	
				V	157		
16352 Selfoss - City Hall	A	Olfus (Iceland) 29/05/2008 15:45, Mw=6.1	E5, R3	H1	523	1.1	ESMD
				H2	324	1.3	
				V	246		
15905 - Zarrat	A	Firuzabad, 20/06/1994 09:09, Mw=5.9	E16, R11	H1	301	4.2	ESMD
				H2	253	4.6	
				V	102		
				H2	418	4.6	
				V	259		
16996 - L'Aquila - V. Aterno - Il Moro - AQM	A	L'Aquila Aftershock 07/04/2009 21:34, AMw=4.6	E2, R2	H1	247	8.3	ITACA
				H2	130	50	
				V	82		
17116 - Montereale - MTR	A	L'Aquila Aftershock 09/04/2009 19:38, Mw=5.3	E10	H1	108	10	ITACA
				H2	90	20	
				V	67		

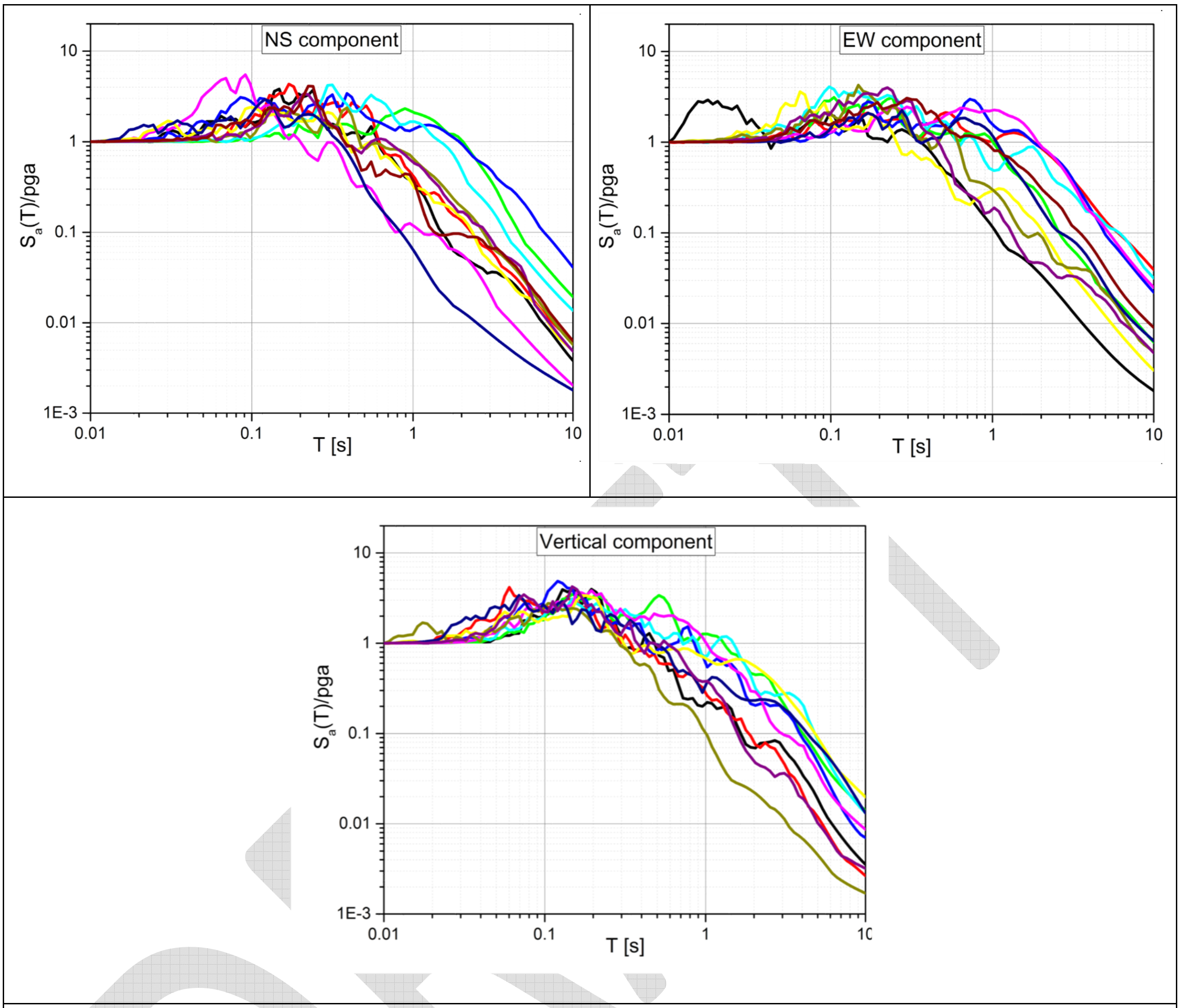

Fig. 4.1. Normalized response spectra for three components (NS, EW and vertical) of 11 selected accelerograms.

4.2 Output ground-motion characteristics

The main ground motion intensity parameter (GMIP) considered in all analysis (ISTerre/CUB and AUTH) was the acceleration spectra at a suite of periods / frequencies. Some additional GMIP were systematically computed by ISTerre / CUB:

- Peak time-domain values (pga , pgv)
- Short-period [F_A , around 0.1 s : average in the range 0.05 – 0.2 s] and long-period [F_V around 1 s: average in the range 0.5 – 2 s] amplification factors

- Spectrum intensity SI , Cumulative Absolute Velocity (CAV), Arias Intensity I_A , root mean square acceleration a_{rms} , and Trifunac-Brady duration D_{TB} .

The earthquake ground motion characteristics, calculated based on the direct FD numerical simulations and accelerogram database are listed in Tab. 4.2 and defined in Section 10.2.

Tab. 4.2. An overview of the calculated earthquake ground motion (EGM) characteristics.

<table>
<tr><th colspan="2">Absolute EGM characteristic χ</th><th>Relative EGM characteristics</th><th>Average relative EGM characteristics</th><th>Averages</th><th>2D/1D, 3D/2D, 3D/1D aggravation factors</th></tr>
<tr><td>S_D</td><td rowspan="3">Calculated for all receiver positions for each pair $[s_{\xi,i}(\mathrm{t}), a_{\xi,i}(\mathrm{t})]$ $i=1,...,n$ $\xi \in \{x,y,z\}$</td><td rowspan="2">Amplification factor $AF_{\xi,i}(\chi)$</td><td rowspan="2">Average (i) amplification factor $\overline{AF}_{\xi}(\chi)$</td><td>short-period
long-period
f_0-centred
f_{00}-centred</td><td rowspan="3">Calculated for all receiver positions for the anti-plane, in-plane and vertical components</td></tr>
<tr><td>pga
pgv
CAV
I_A
a_{rms}
SI</td><td rowspan="2"></td></tr>
<tr><td>D_{TB}^{95}
D_{TB}^{75}</td><td>Prolongation factor $PF_{\xi,i}(\chi)$</td><td>Average (i) prolongation factor $\overline{PF}_{\xi}(\chi)$</td></tr>
<tr><td colspan="6">S_D - relative displacement response spectrum, pga - peak ground acceleration
pgv - peak ground velocity, CAV - cumulative absolute velocity, I_A - Arias intensity
a_{rms} - root-mean-square acceleration, SI - spectrum intensity
D_{TB}^{95} and D_{TB}^{75} - durations of strong ground motion</td></tr>
</table>

5 CHARACTERISTICS OF GROUND MOTION FOR NOMINAL MODELS

5.1 All Sites

Figures of all determined characteristics as functions of receiver position for all nominal-model profiles are in the electronic supplement. Because we could not a priori exclude correlations between some characteristics, we first performed a descriptive statistical analysis and used scatter matrices for evaluation of correlations. Based on the found correlations we selected a subset of independent earthquake ground motion (EGM) characteristics.

5.1.1 Aggravation factors

5.1.1.1 2D/1D

Overall statistical analysis. Fig. 5.1 shows the 2D/1D aggravation factors for 10 EGM characteristics of the separately for each component. Each colour dot in the figure represents a value calculated for one receiver. The figure includes all receivers atop sediments in the all 12 investigated profiles. Excluded are receiver positions in case of the local fundamental frequency larger than 20 Hz.

Scatter matrices. Fig. 5.2 - Fig. 5.4 show the 2D/1D aggravation factors plotted against each other and the values of the correlation coefficients. The correlation here means a large value of the Pearson correlation coefficient. We compare aggravation factors for 10 EGM characteristics.

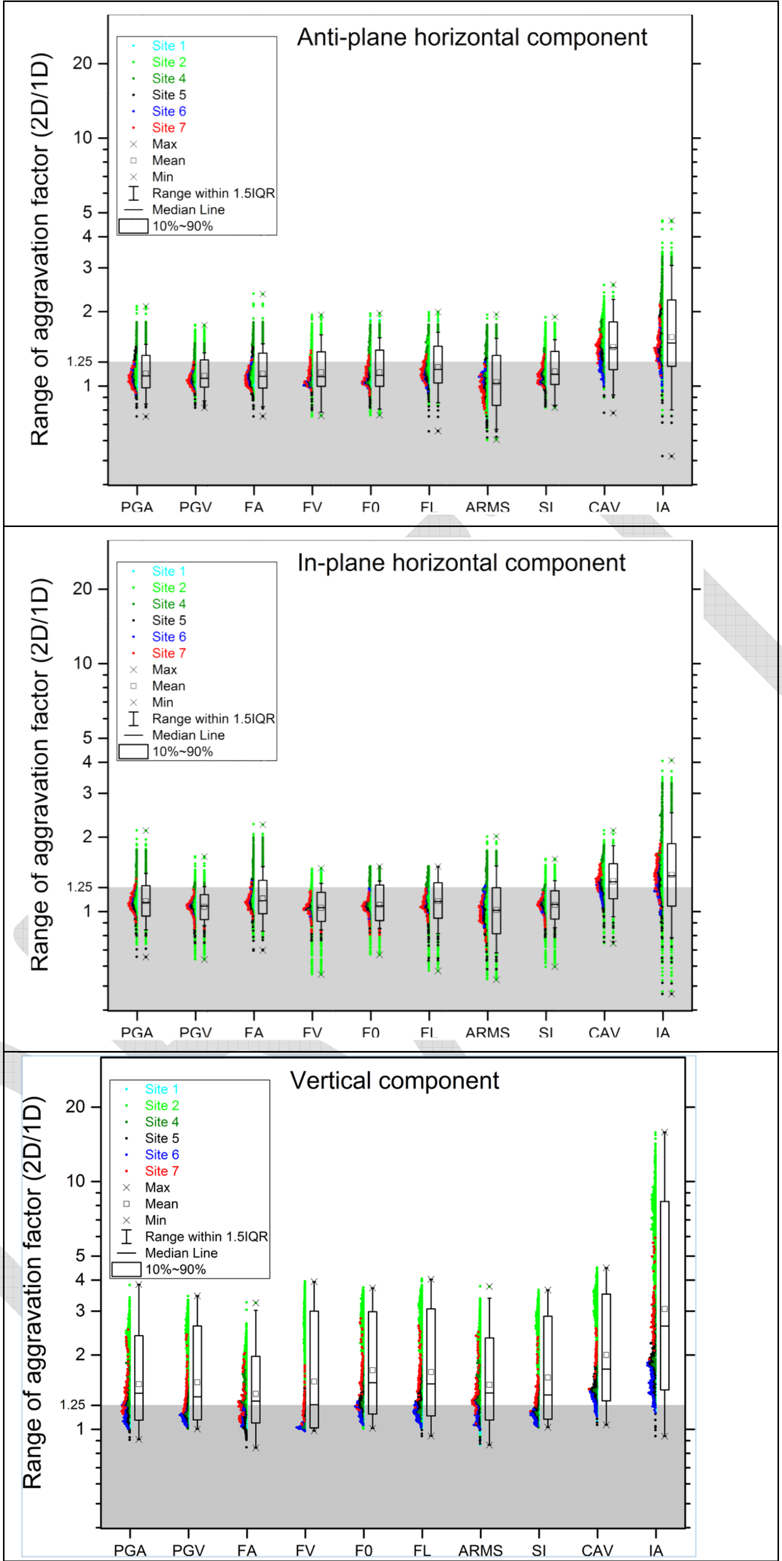

Fig. 5.1. Range of the 2D/1D aggravation factor for 10 characteristics of the earthquake ground motion.

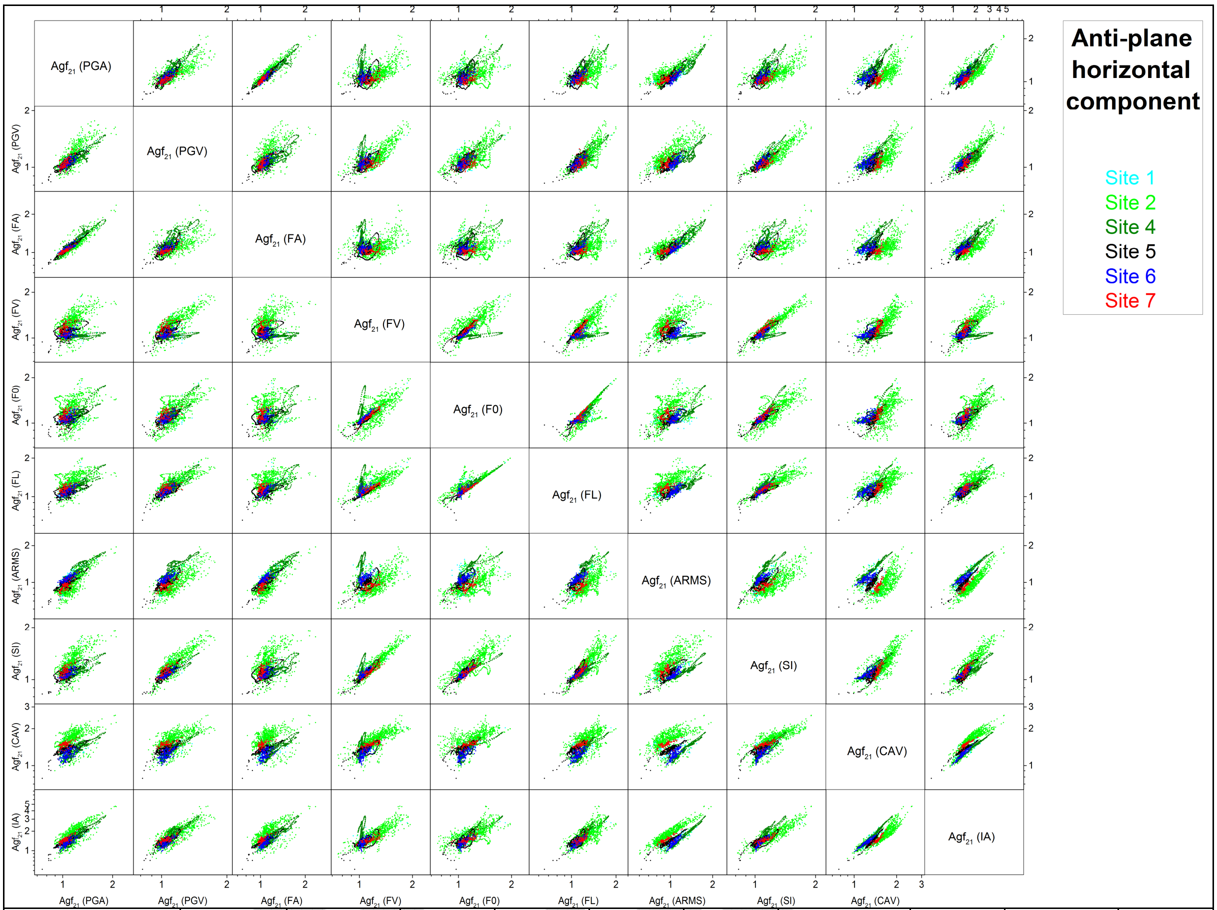

Pearson correlations	Agf_{21} (PGA)	Agf_{21} (PGV)	Agf_{21} (FA)	Agf_{21} (FV)	Agf_{21} (F0)	Agf_{21} (FL)	Agf_{21} (ARMS)	Agf_{21} (SI)	Agf_{21} (CAV)	Agf_{21} (IA)
Agf_{21}(PGA)		0.81	**0.94**	0.33	0.47	0.63	0.79	0.60	0.46	0.79
Agf_{21}(PGV)	0.81		0.66	0.68	0.72	0.81	0.65	**0.87**	0.64	0.84
Agf_{21}(FA)	**0.94**	0.66		0.13	0.34	0.51	**0.81**	0.42	0.29	0.68
Agf_{21}(FV)	0.33	0.68	0.13		0.72	0.69	0.20	**0.91**	0.78	0.68
Agf_{21}(F0)	0.47	0.72	0.34	0.72		**0.86**	0.48	0.84	0.67	0.75
Agf_{21}(FL)	0.63	0.81	0.51	0.69	**0.86**		0.53	0.86	0.68	0.79
Agf_{21}(ARMS)	0.79	0.65	**0.81**	0.20	0.48	0.53		0.47	0.20	0.68
Agf_{21}(SI)	0.60	**0.87**	0.42	**0.91**	0.84	0.86	0.47		0.82	**0.86**
Agf_{21}(CAV)	0.46	0.64	0.29	0.78	0.67	0.68	0.20	0.82		**0.85**
Agf_{21}(IA)	0.79	0.84	0.68	0.68	0.75	0.79	0.68	**0.86**	**0.85**	

Fig. 5.2. Scatter matrix and correlation coefficients for 10 characteristics of earthquake ground motion. The maximum correlation coefficients are in bold.

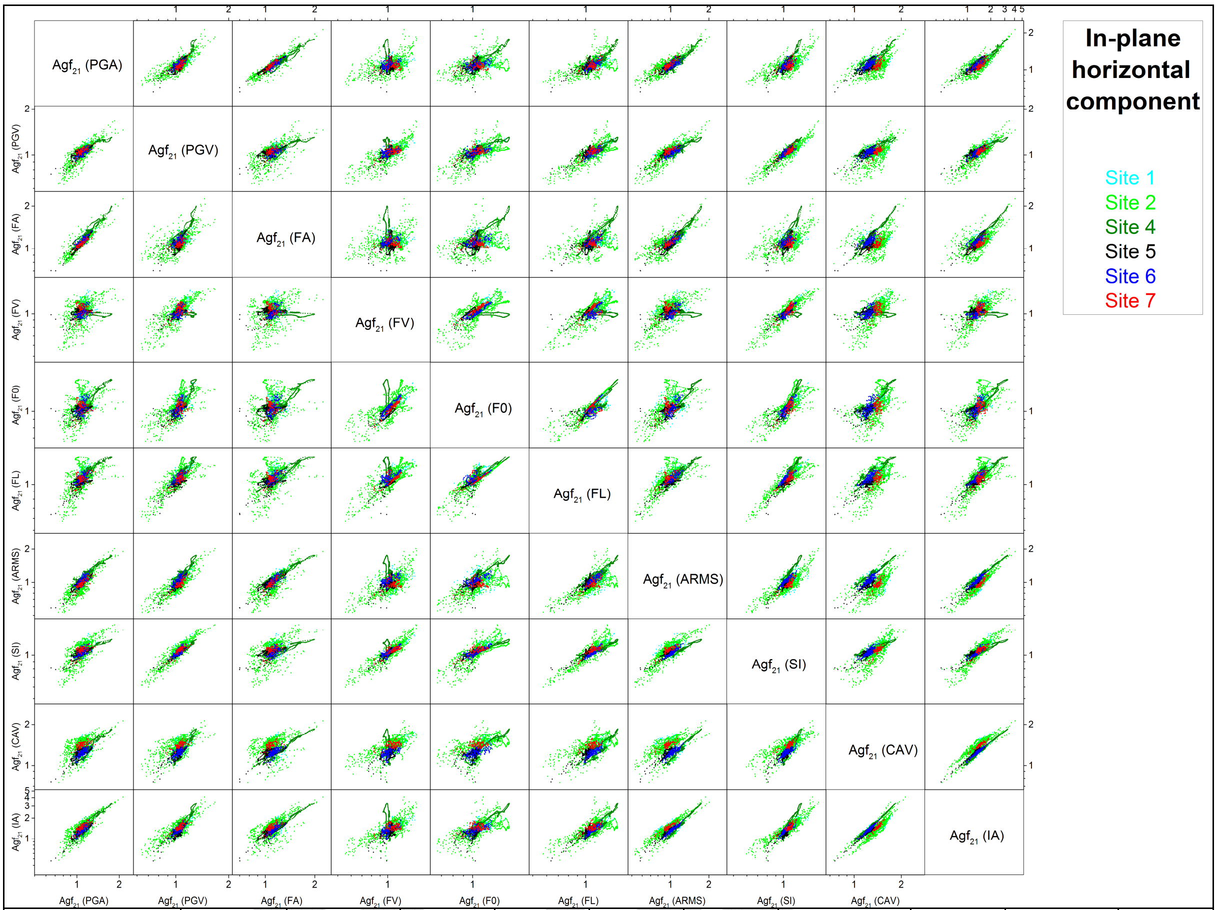

Pearson correlations	Agf_{21} (PGA)	Agf_{21} (PGV)	Agf_{21} (FA)	Agf_{21} (FV)	Agf_{21} (F0)	Agf_{21} (FL)	Agf_{21} (ARMS)	Agf_{21} (SI)	Agf_{21} (CAV)	Agf_{21} (IA)
Agf_{21}(PGA)		0.82	**0.94**	0.34	0.54	0.67	0.87	0.70	0.60	0.85
Agf_{21}(PGV)	0.82		0.68	0.68	0.69	0.81	0.84	**0.91**	0.62	0.84
Agf_{21}(FA)	**0.94**	0.68		0.17	0.46	0.58	0.82	0.54	0.49	0.76
Agf_{21}(FV)	0.34	0.68	0.17		0.62	0.66	0.49	**0.85**	0.54	0.57
Agf_{21}(F0)	0.54	0.69	0.46	0.62		**0.86**	0.66	0.78	0.60	0.71
Agf_{21}(FL)	0.67	0.81	0.58	0.66	**0.86**		0.77	0.85	0.63	0.79
Agf_{21}(ARMS)	0.87	0.84	0.82	0.49	0.66	0.77		0.79	0.55	**0.88**
Agf_{21}(SI)	0.70	**0.91**	0.54	**0.85**	0.78	0.85	0.79		0.73	0.86
Agf_{21}(CAV)	0.60	0.62	0.49	0.54	0.60	0.63	0.55	0.73		**0.87**
Agf_{21}(IA)	0.85	0.84	0.76	0.57	0.71	0.79	**0.88**	0.86	**0.87**	

Fig. 5.3. Scatter matrix and correlation coefficients for 10 characteristics of earthquake ground motion.

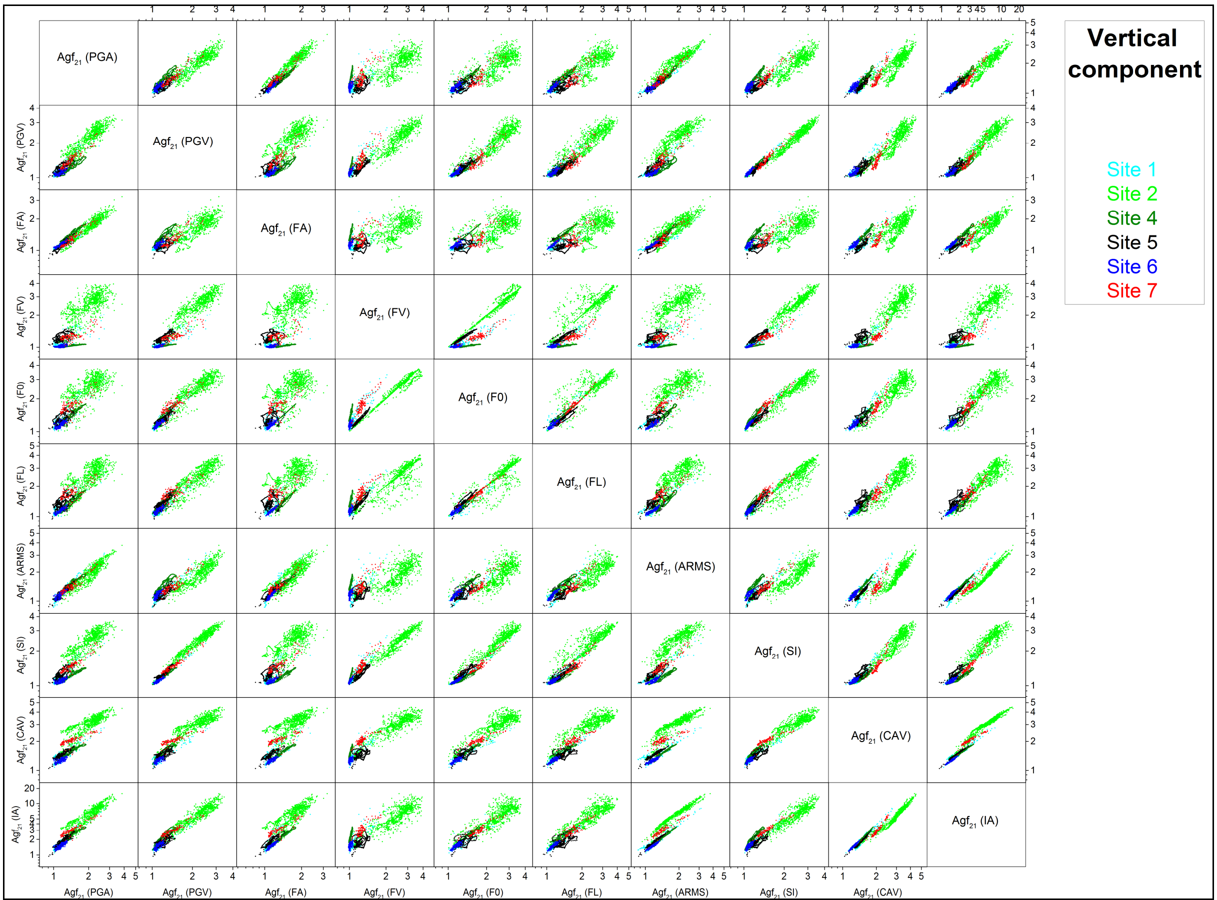

Pearson correlations	Agf21 (PGA)	Agf21 (PGV)	Agf21 (FA)	Agf21 (FV)	Agf21 (F0)	Agf21 (FL)	Agf21 (ARMS)	Agf21 (SI)	Agf21 (CAV)	Agf21 (IA)
Agf21(PGA)		0.947	**0.962**	0.842	0.897	0.901	**0.961**	0.919	0.915	**0.963**
Agf21(PGV)	0.947		0.855	0.951	0.967	0.957	0.906	**0.989**	0.963	0.972
Agf21(FA)	**0.962**	0.855		0.726	0.798	0.790	0.935	0.817	0.828	0.897
Agf21(FV)	0.842	0.951	0.726		0.954	0.923	0.782	**0.979**	0.947	0.915
Agf21(F0)	0.897	0.967	0.798	0.954		0.955	0.867	**0.978**	0.961	0.955
Agf21(FL)	0.901	0.957	0.790	0.923	0.955		0.885	**0.959**	0.950	0.954
Agf21(ARMS)	**0.961**	0.906	0.935	0.782	0.867	0.885		0.874	0.880	0.948
Agf21(SI)	0.919	**0.989**	0.817	**0.979**	**0.978**	**0.959**	0.874		0.975	0.968
Agf21(CAV)	0.915	0.963	0.828	0.947	0.961	0.950	0.880	0.975		**0.985**
Agf21(IA)	0.963	0.972	0.897	0.915	0.955	0.954	0.948	0.968	**0.985**	

Fig. 5.4. Scatter matrix and correlation coefficients for 10 characteristics of earthquake ground motion.

5.1.1.2 3D/2D

Overall statistical analysis. Fig. 5.5 shows the 3D/2D aggravation factors for 10 EGM characteristics separately for each component. Each colour dot in the figure represents a value calculated for one receiver. The figure includes all receivers atop sediments in the all 12 investigated profiles. Excluded are receiver positions in case of the local fundamental frequency larger than 20 Hz.

Scatter matrices. Fig. 5.6 - Fig. 5.8 show the 3D/2D aggravation factors plotted against each other and the values of the correlation coefficients. The correlation here means a large value of the Pearson correlation coefficient. We compare aggravation factors for 10 EGM characteristics.

The scatter matrices and values of the correlation coefficients make it possible to estimate the level of correlation of all pairs of the aggravation factors.

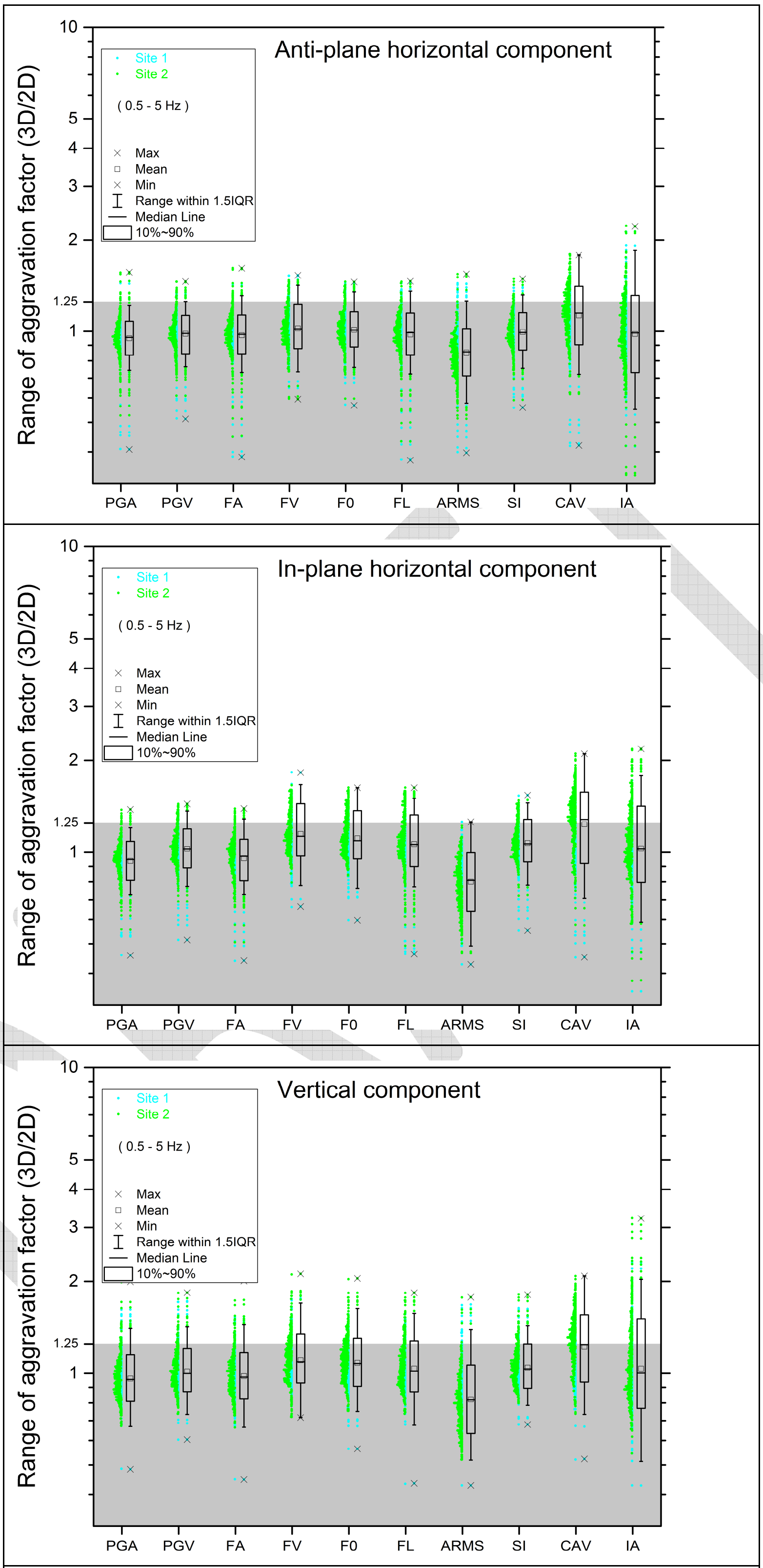

Fig. 5.5. Range of the 3D/2D aggravation factor for 10 characteristics of the earthquake ground motion.

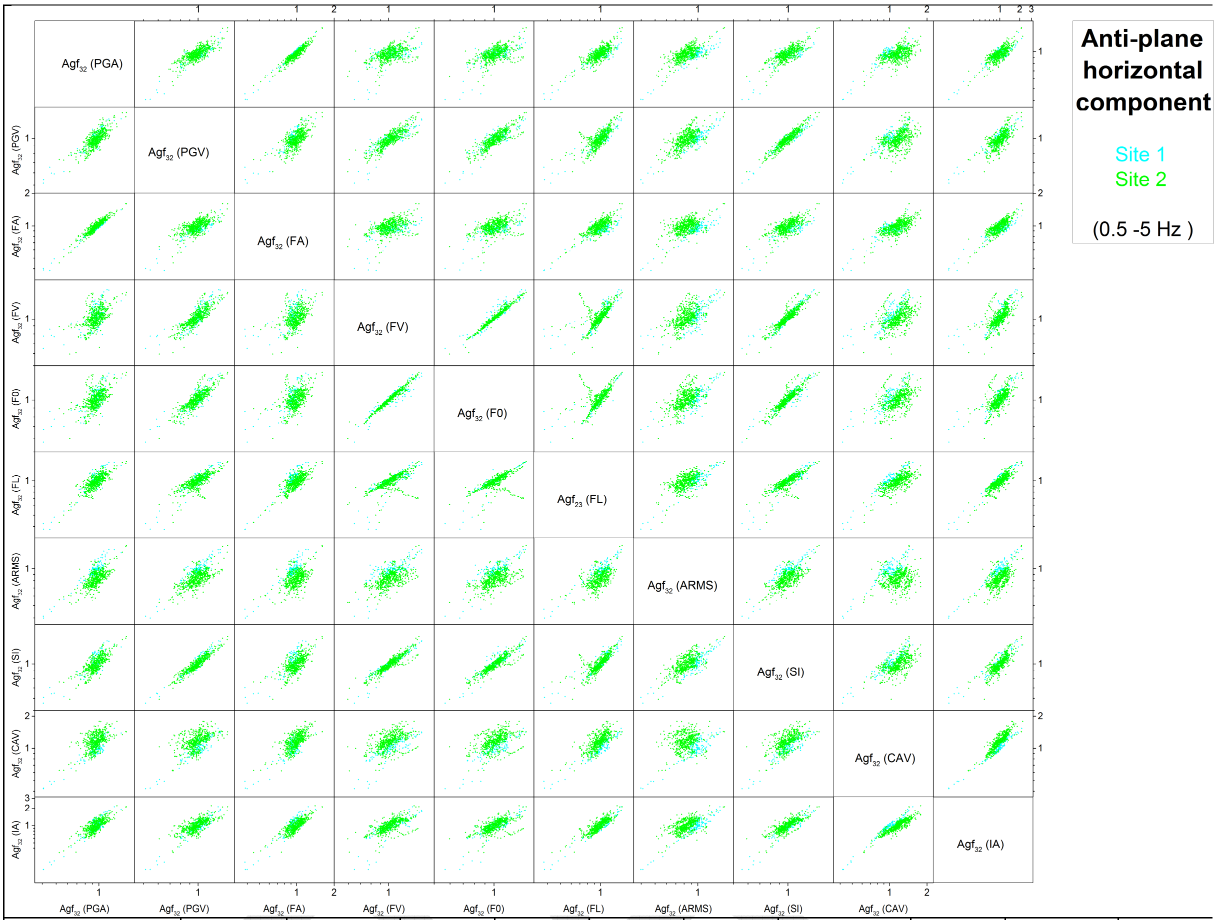

Pearson correlations	Agf_{32} (PGA)	Agf_{32} (PGV)	Agf_{32} (FA)	Agf_{32} (FV)	Agf_{32} (F0)	Agf_{32} (FL)	Agf_{32} (ARMS)	Agf_{32} (SI)	Agf_{32} (CAV)	Agf_{32} (IA)
Agf_{32}(PGA)		0.81	**0.95**	0.56	0.62	0.83	0.69	0.77	0.62	0.84
Agf_{32} (PGV)	0.81		0.72	0.85	0.86	0.80	0.70	**0.95**	0.57	0.78
Agf_{32} (FA)	**0.95**	0.72		0.48	0.53	0.80	0.52	0.68	0.74	0.85
Agf_{32} (FV)	0.56	0.85	0.48		**0.97**	0.68	0.60	0.93	0.53	0.69
Agf_{32} (F0)	0.62	0.86	0.53	**0.97**		0.70	0.62	0.92	0.53	0.70
Agf_{32} (FL)	0.83	0.80	0.80	0.68	0.70		0.66	0.83	0.74	**0.90**
Agf_{32} (ARMS)	0.69	0.70	0.52	0.60	0.62	0.66		**0.71**	0.24	0.64
Agf_{32} (SI)	0.77	**0.95**	0.68	0.93	0.92	0.83	**0.71**		0.64	0.84
Agf_{32} (CAV)	0.62	0.57	0.74	0.53	0.53	0.74	0.24	0.64		**0.89**
Agf_{32} (IA)	0.84	0.78	0.85	0.69	0.70	0.90	0.64	0.84	**0.89**	

Fig. 5.6. Scatter matrix and correlation coefficients for 10 characteristics of earthquake ground motion.

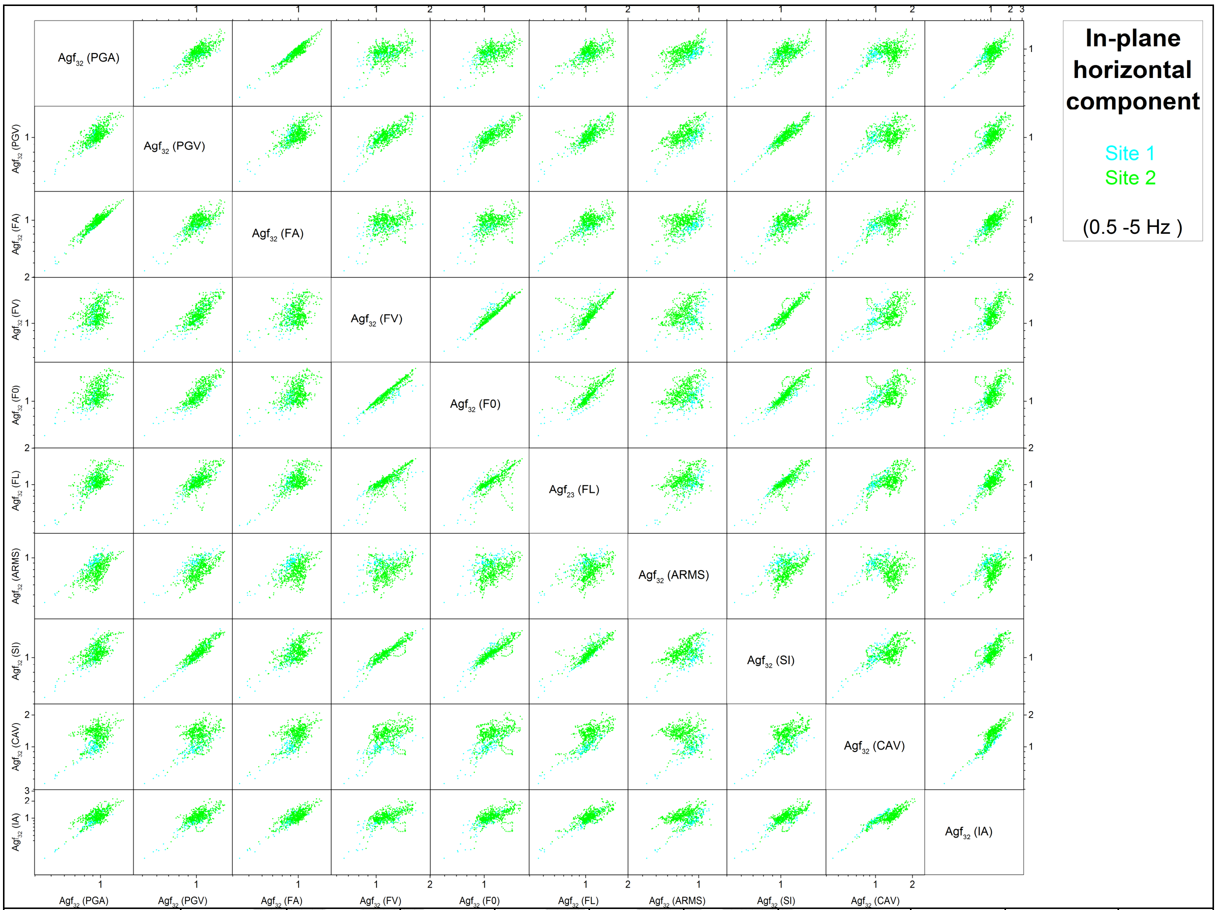

Pearson correlations	Agf_{32} (PGA)	Agf_{32} (PGV)	Agf_{32} (FA)	Agf_{32} (FV)	Agf_{32} (F0)	Agf_{32} (FL)	Agf_{32} (ARMS)	Agf_{32} (SI)	Agf_{32} (CAV)	Agf_{32} (IA)
Agf_{32}(PGA)		0.78	**0.94**	0.44	0.52	0.68	0.62	0.67	0.44	0.75
Agf_{32} (PGV)	0.78		0.70	0.81	0.83	0.78	0.60	**0.92**	0.46	0.72
Agf_{32} (FA)	**0.94**	0.70		0.39	0.46	0.67	0.44	0.63	0.62	0.82
Agf_{32} (FV)	0.44	0.81	0.39		**0.95**	0.75	0.38	**0.94**	0.52	0.63
Agf_{32} (F0)	0.52	0.83	0.46	**0.95**		0.74	0.41	0.91	0.51	0.64
Agf_{32} (FL)	0.68	0.78	0.67	0.75	0.74		0.44	**0.86**	0.68	0.83
Agf_{32} (ARMS)	0.62	0.60	0.44	0.38	0.41	0.44		0.51	-0.07	0.42
Agf_{32} (SI)	0.67	**0.92**	0.63	**0.94**	0.91	**0.86**	0.51		0.62	0.80
Agf_{32} (CAV)	0.44	0.46	0.62	0.52	0.51	0.68	-0.07	0.62		**0.86**
Agf_{32} (IA)	0.75	0.72	0.82	0.63	0.64	0.83	0.42	0.80	**0.86**	

Fig. 5.7. Scatter matrix and correlation coefficients for 10 characteristics of earthquake ground motion.

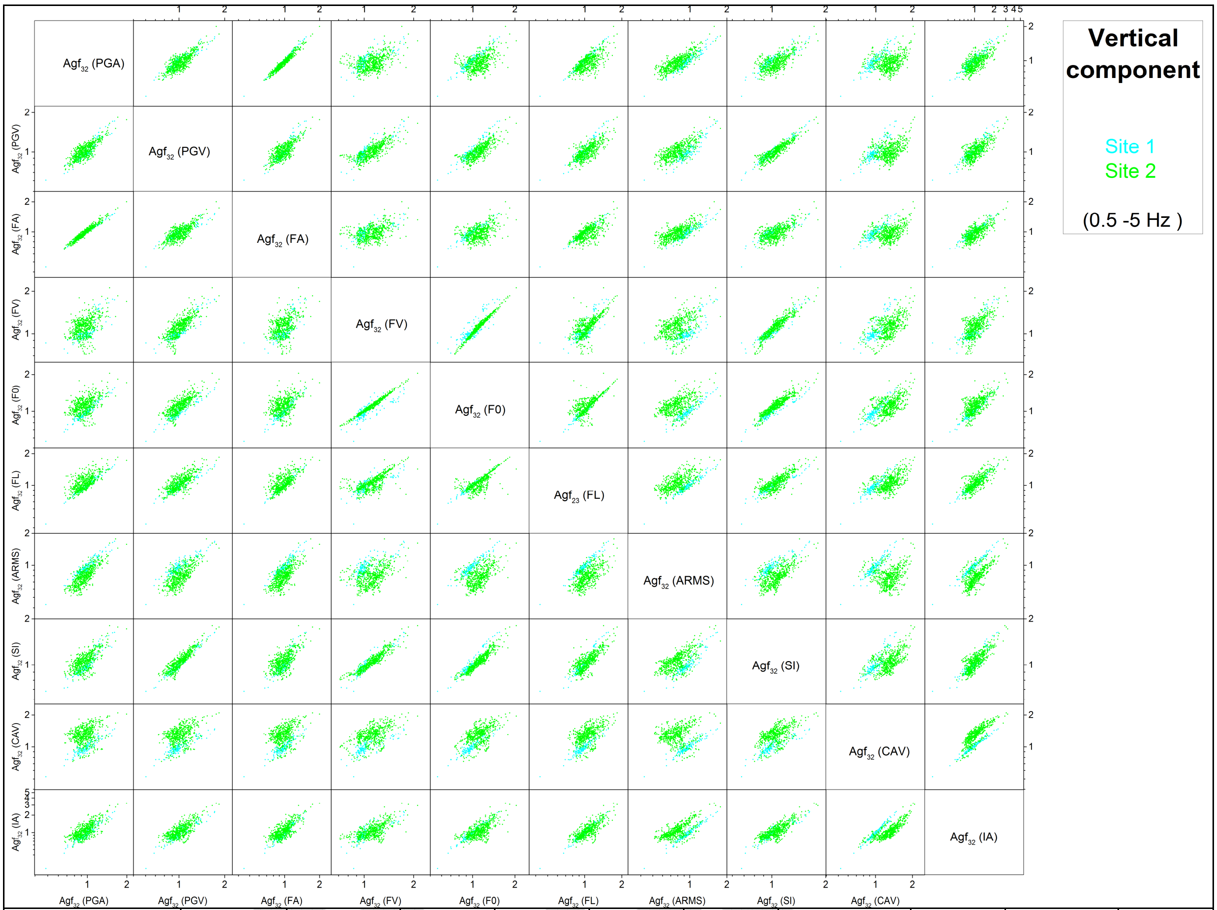

Pearson correlations	Agf_{32} (PGA)	Agf_{32} (PGV)	Agf_{32} (FA)	Agf_{32} (FV)	Agf_{32} (F0)	Agf_{32} (FL)	Agf_{32} (ARMS)	Agf_{32} (SI)	Agf_{32} (CAV)	Agf_{32} (IA)
Agf_{32}(PGA)		0.827	**0.972**	0.500	0.537	0.731	**0.801**	0.716	0.308	0.755
Agf_{32} (PGV)	0.827		0.787	0.800	0.786	0.777	0.690	**0.920**	0.438	0.774
Agf_{32} (FA)	**0.972**	0.787		0.474	0.528	0.729	0.716	0.689	0.398	0.775
Agf_{32} (FV)	0.500	0.800	0.474		**0.941**	0.714	0.416	**0.939**	0.576	0.696
Agf_{32} (F0)	0.537	0.786	0.528	**0.941**		0.773	0.405	0.924	0.653	0.746
Agf_{32} (FL)	0.731	0.777	0.729	0.714	0.773		0.581	0.810	0.594	**0.822**
Agf_{32} (ARMS)	**0.801**	0.690	0.716	0.416	0.405	0.581		0.598	0.020	0.625
Agf_{32} (SI)	0.716	0.920	0.689	**0.939**	0.924	0.810	0.598		0.604	0.837
Agf_{32} (CAV)	0.308	0.438	0.398	0.576	0.653	0.594	0.020	0.604		**0.786**
Agf_{32} (IA)	0.755	0.774	0.775	0.696	0.746	0.822	0.625	0.837	**0.786**	

Fig. 5.8. Scatter matrix and correlation coefficients for 10 characteristics of earthquake ground motion.

5.1.2 Amplification factors

5.1.2.1 1D

Overall statistical analysis. Fig. 5.9 shows the amplification factors calculated from results of the 1D simulations. The figure shows the amplification factors for 10 EGM characteristics separately for each component. Each colour dot in the figure represents a value calculated for one receiver. The figure includes all receivers atop sediments in the all 12 investigated profiles. Excluded are receiver positions in case of the local fundamental frequency larger than 20 Hz.

Scatter matrices. Fig. 5.10 - Fig. 5.12 show the amplification factors plotted against each other and the values of the correlation coefficients. The correlation here means a large value of the Pearson correlation coefficient. We compare the amplification factors for 10 EGM characteristics.

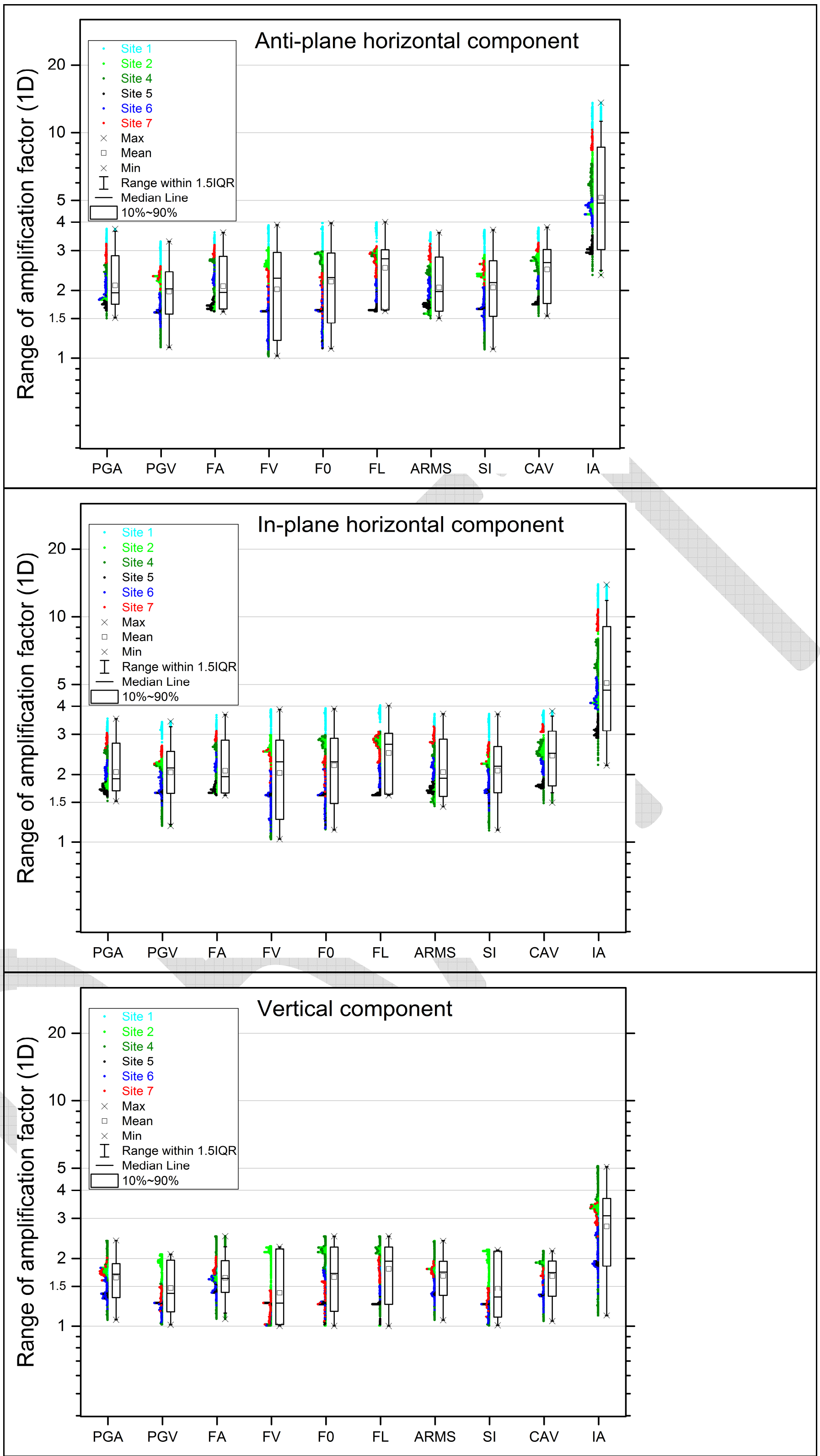

Fig. 5.9. Range of the amplification factor from the 1D simulations for 10 characteristics of the earthquake ground motion.

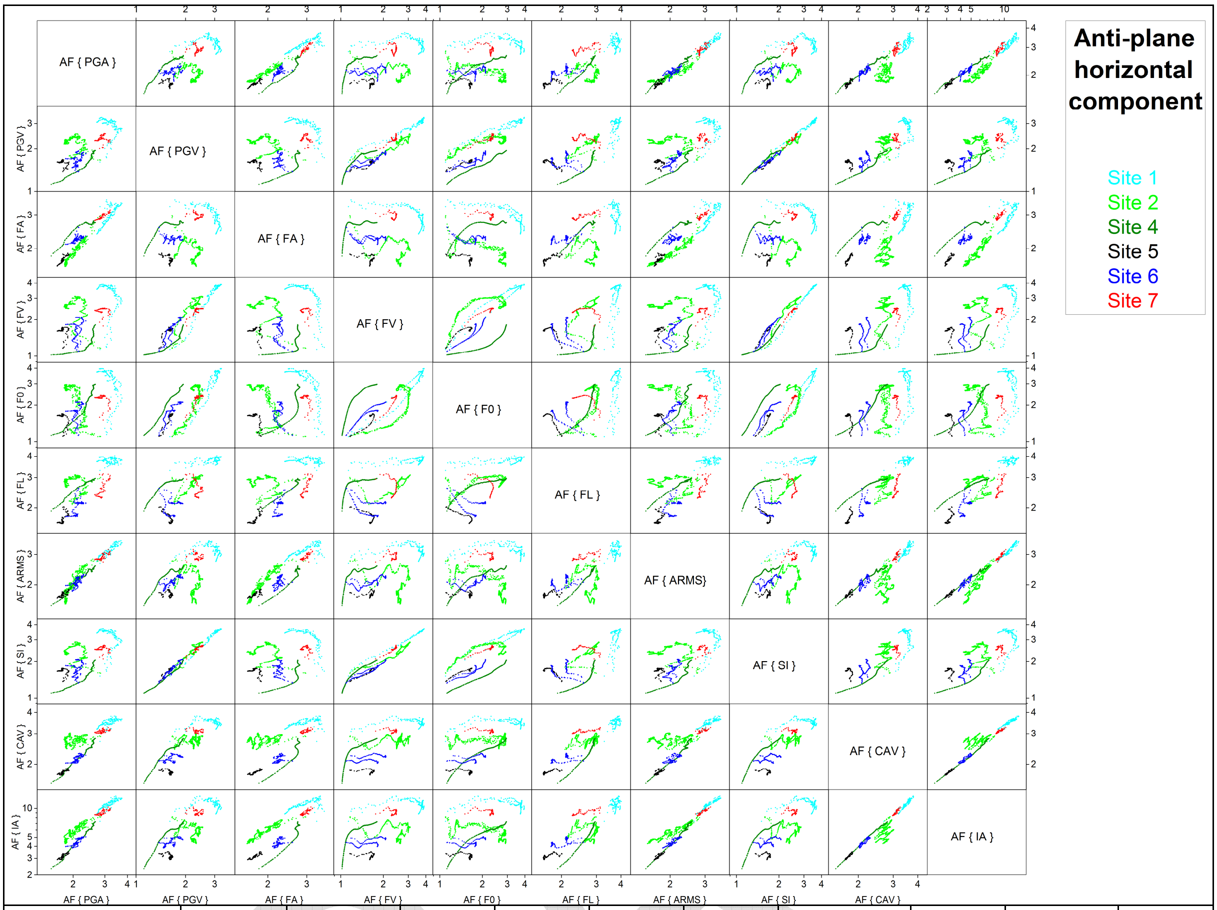

Pearson correlations	AF_{1D} (PGA)	AF_{1D} (PGV)	AF_{1D} (FA)	AF_{1D} (FV)	AF_{1D} (F0)	AF_{1D} (FL)	AF_{1D} (ARMS)	AF_{1D} (SI)	AF_{1D} (CAV)	AF_{1D} (IA)
AF_{1D}(PGA)		0.81	**0.94**	0.33	0.47	0.63	0.79	0.60	0.46	0.79
AF_{1D} (PGV)	0.81		0.66	0.68	0.72	0.81	0.65	**0.87**	0.64	0.84
AF_{1D} (FA)	**0.94**	0.66		0.13	0.34	0.51	**0.81**	0.42	0.29	0.68
AF_{1D} (FV)	0.33	0.68	0.13		0.72	0.69	0.20	**0.91**	0.78	0.68
AF_{1D} (F0)	0.47	0.72	0.34	0.72		**0.86**	0.48	0.84	0.67	0.75
AF_{1D} (FL)	0.63	0.81	0.51	0.69	**0.86**		0.53	**0.86**	0.68	0.79
AF_{1D} (ARMS)	0.79	0.65	**0.81**	0.20	0.48	0.53		0.47	0.20	0.68
AF_{1D} (SI)	0.60	0.87	0.42	**0.91**	0.84	**0.86**	0.47		0.82	**0.86**
AF_{1D} (CAV)	0.46	0.64	0.29	0.78	0.67	0.68	0.20	0.82		**0.85**
AF_{1D} (IA)	0.79	0.84	0.68	0.68	0.75	0.79	0.68	**0.86**	**0.85**	

Fig. 5.10. Scatter matrix and correlation coefficients for 10 characteristics of earthquake ground motion.

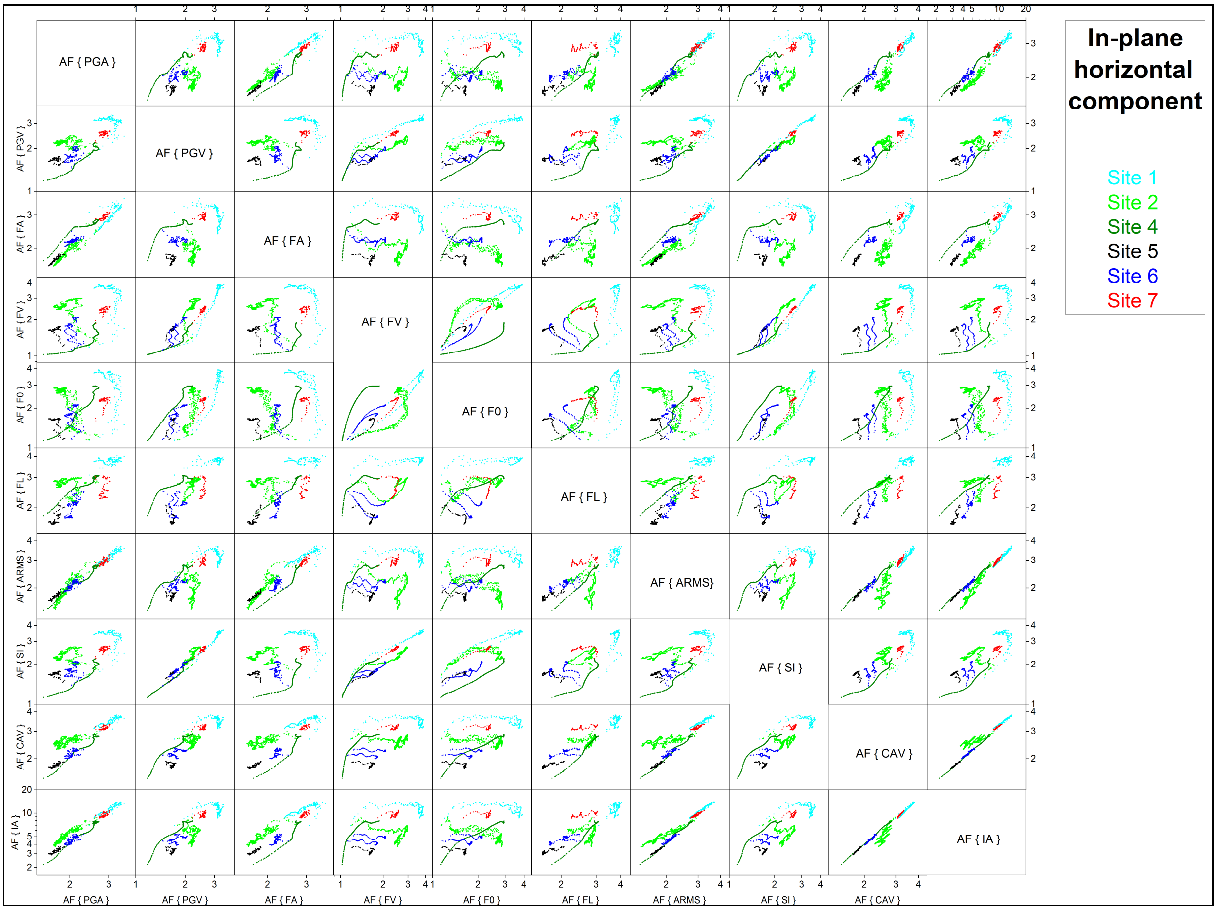

Pearson correlations	AF_{1D} (PGA)	AF_{1D} (PGV)	AF_{1D} (FA)	AF_{1D} (FV)	AF_{1D} (F0)	AF_{1D} (FL)	AF_{1D} (ARMS)	AF_{1D} (SI)	AF_{1D} (CAV)	AF_{1D} (IA)
AF_{1D}(PGA)		0.82	**0.94**	0.34	0.54	0.67	0.87	0.70	0.60	0.85
AF_{1D} (PGV)	0.82		0.68	0.68	0.69	0.81	0.84	**0.91**	0.62	0.84
AF_{1D} (FA)	**0.94**	0.68		0.17	0.46	0.58	0.82	0.54	0.49	0.76
AF_{1D} (FV)	0.34	0.68	0.17		0.62	0.66	0.49	**0.85**	0.54	0.57
AF_{1D} (F0)	0.54	0.69	0.46	0.62		**0.86**	0.66	0.78	0.60	0.71
AF_{1D} (FL)	0.67	0.81	0.58	0.66	**0.86**		0.77	0.85	0.63	0.79
AF_{1D} (ARMS)	0.87	0.84	0.82	0.49	0.66	0.77		0.79	0.55	**0.88**
AF_{1D} (SI)	0.70	**0.91**	0.54	**0.85**	0.78	0.85	0.79		0.73	0.86
AF_{1D} (CAV)	0.60	0.62	0.49	0.54	0.60	0.63	0.55	0.73		**0.87**
AF_{1D} (IA)	0.85	0.84	0.76	0.57	0.71	0.79	**0.88**	0.86	**0.87**	

Fig. 5.11. Scatter matrix and correlation coefficients for 10 characteristics of earthquake ground motion.

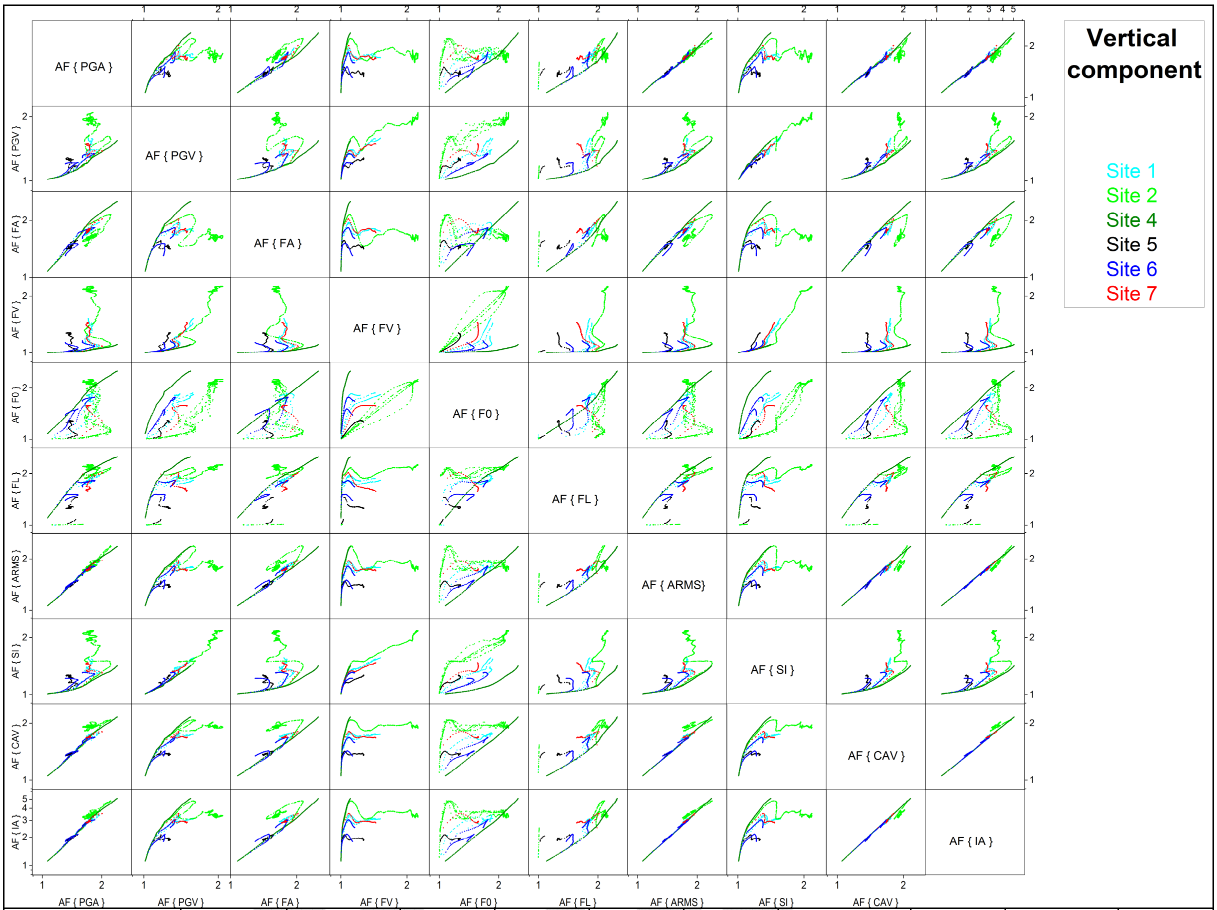

Pearson correlations	AF$_{1D}$ (PGA)	AF$_{1D}$ (PGV)	AF$_{1D}$ (FA)	AF$_{1D}$ (FV)	AF$_{1D}$ (F0)	AF$_{1D}$ (FL)	AF$_{1D}$ (ARMS)	AF$_{1D}$ (SI)	AF$_{1D}$ (CAV)	AF$_{1D}$ (IA)
AF$_{1D}$(PGA)		0.603	**0.891**	0.304	0.609	0.854	**0.990**	0.502	0.926	0.975
AF$_{1D}$ (PGV)	0.603		0.244	0.936	0.731	0.711	0.602	**0.988**	0.832	0.724
AF$_{1D}$ (FA)	**0.891**	0.244		-0.066	0.437	0.685	0.887	0.123	0.699	0.811
AF$_{1D}$ (FV)	0.304	**0.936**	-0.066		0.653	0.500	0.302	**0.969**	0.604	0.455
AF$_{1D}$ (F0)	0.609	0.731	0.437	0.653		0.788	0.590	0.709	0.722	0.668
AF$_{1D}$ (FL)	0.854	0.711	0.685	0.500	0.788		0.862	0.645	**0.906**	0.898
AF$_{1D}$ (ARMS)	**0.990**	0.602	0.887	0.302	0.590	0.862		0.498	0.936	0.984
AF$_{1D}$ (SI)	0.502	**0.988**	0.123	**0.969**	0.709	0.645	0.498		0.762	0.636
AF$_{1D}$ (CAV)	0.926	0.832	0.699	0.604	0.722	**0.906**	0.936	0.762		**0.983**
AF$_{1D}$ (IA)	0.975	0.724	0.811	0.455	0.668	0.898	0.984	0.636	**0.983**	

Fig. 5.12. Scatter matrix and correlation coefficients for 10 characteristics of earthquake ground motion.

5.1.2.2 2D

Overall statistical analysis. Fig. 5.13 shows the amplification factors calculated from results of the 2D simulations. The figure shows the amplification factors for 10 EGM characteristics separately for each component. Each colour dot in the figure represents a value calculated for one receiver. The figure includes all receivers atop sediments in the all 12 investigated profiles. Excluded are receiver positions in case of the local fundamental frequency larger than 20 Hz.

Scatter matrices. Fig. 5.14 - Fig. 5.16 show the amplification factors plotted against each other and the values of the correlation coefficients. The correlation here means a large value of the Pearson correlation coefficient. We compare the amplification factors for 10 EGM characteristics.

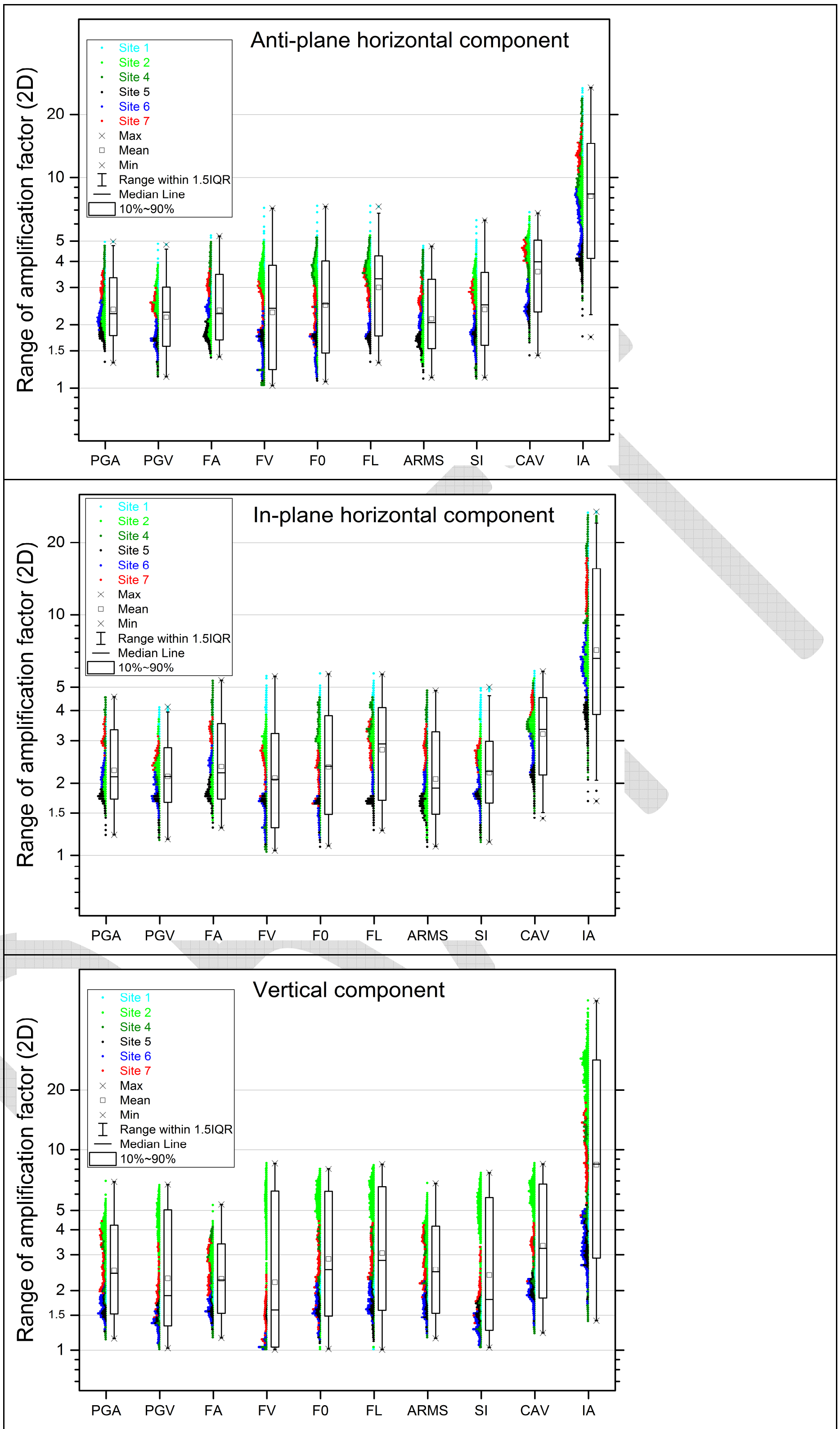

Fig. 5.13. Range of the amplification factor from the 2D simulations for 10 characteristics of the earthquake ground motion.

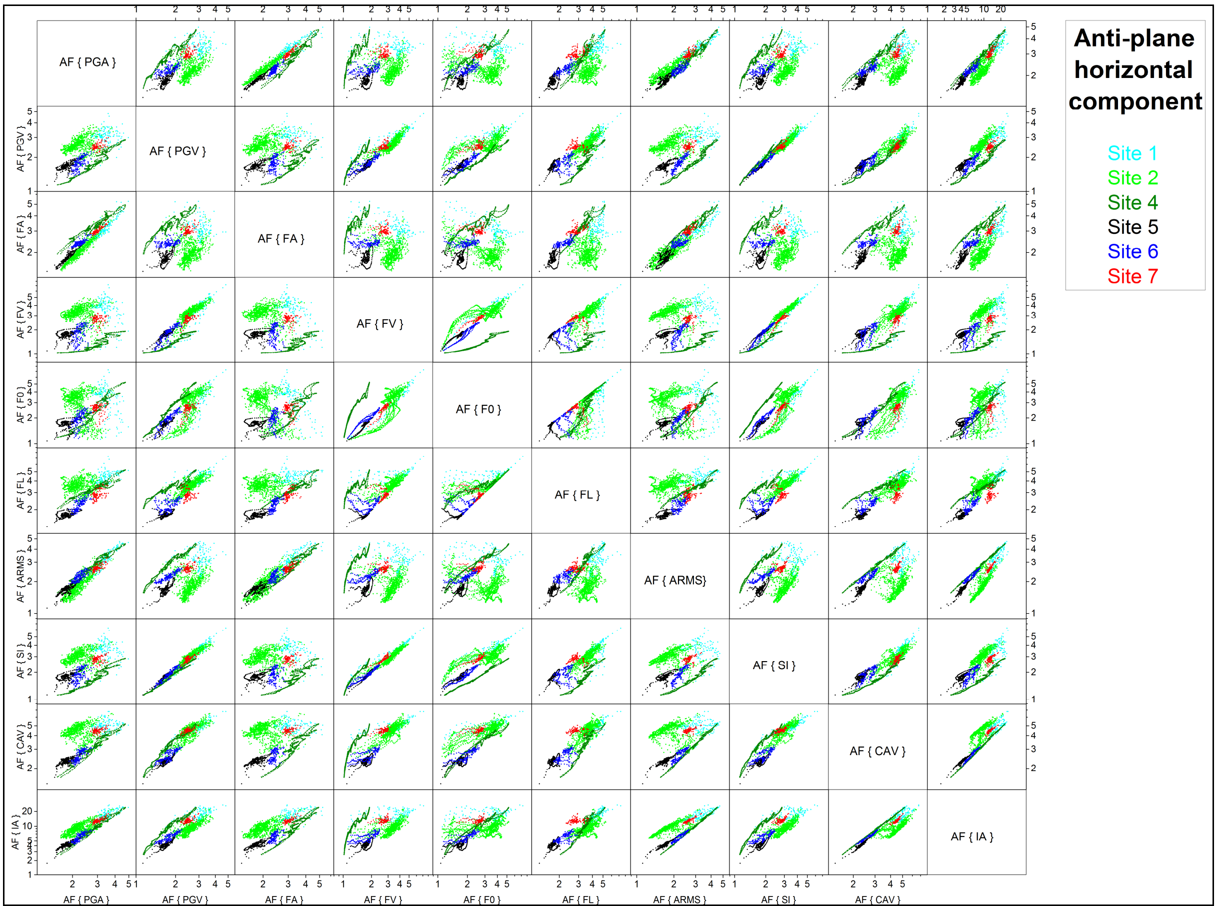

Pearson correlations	AF_{2D} (PGA)	AF_{2D} (PGV)	AF_{2D} (FA)	AF_{2D} (FV)	AF_{2D} (F0)	AF_{2D} (FL)	AF_{2D} (ARMS)	AF_{2D} (SI)	AF_{2D} (CAV)	AF_{2D} (IA)
AF_{2D}(PGA)		0.42	**0.93**	0.04	0.28	0.59	**0.93**	0.29	0.47	0.85
AF_{2D} (PGV)	0.42		0.09	0.90	0.79	0.76	0.20	**0.98**	**0.93**	0.79
AF_{2D} (FA)	**0.93**	0.09		-0.29	0.04	0.39	**0.94**	-0.04	0.18	0.64
AF_{2D} (FV)	0.04	0.90	-0.29		0.69	0.54	-0.16	**0.96**	0.80	0.50
AF_{2D} (F0)	0.28	0.79	0.04	0.69		0.74	0.11	0.77	**0.83**	0.66
AF_{2D} (FL)	0.59	0.76	0.39	0.54	0.74		0.41	0.69	**0.86**	0.84
AF_{2D} (ARMS)	**0.93**	0.20	**0.94**	-0.16	0.11	0.41		0.08	0.24	0.70
AF_{2D} (SI)	0.29	**0.98**	-0.04	**0.96**	0.77	0.69	0.08		0.91	0.70
AF_{2D} (CAV)	0.47	**0.93**	0.18	0.80	**0.83**	**0.86**	0.24	0.91		**0.86**
AF_{2D} (IA)	0.85	0.79	0.64	0.50	0.66	0.84	0.70	0.70	**0.86**	

Fig. 5.14. Scatter matrix and correlation coefficients for 10 characteristics of earthquake ground motion.

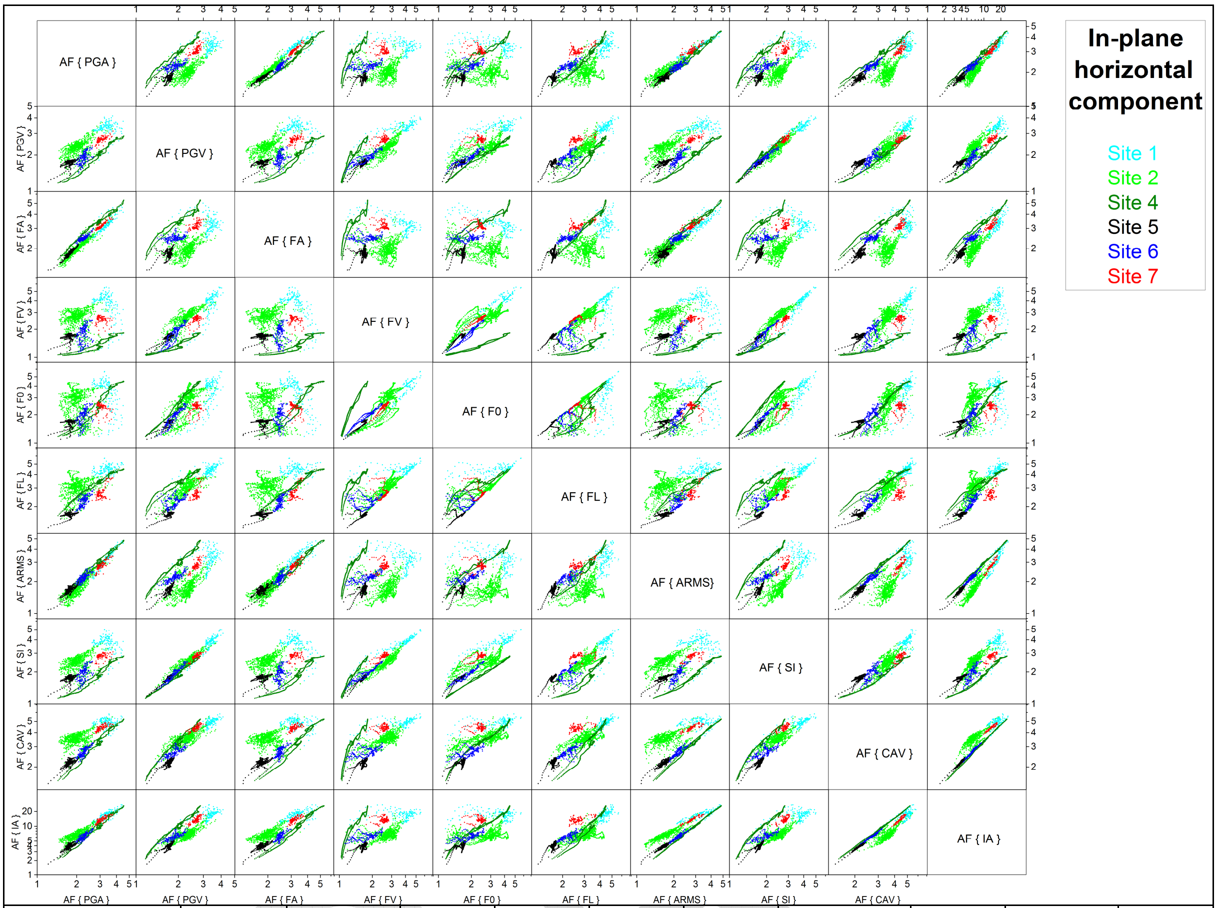

Pearson correlations	AF$_{2D}$ (PGA)	AF$_{2D}$ (PGV)	AF$_{2D}$ (FA)	AF$_{2D}$ (FV)	AF$_{2D}$ (F0)	AF$_{2D}$ (FL)	AF$_{2D}$ (ARMS)	AF$_{2D}$ (SI)	AF$_{2D}$ (CAV)	AF$_{2D}$ (IA)
AF$_{2D}$(PGA)		0.61	**0.97**	0.06	0.38	0.65	**0.96**	0.46	0.66	**0.92**
AF$_{2D}$ (PGV)	0.61		0.42	0.80	0.80	0.77	0.51	**0.97**	**0.91**	0.82
AF$_{2D}$ (FA)	**0.97**	0.42		-0.16	0.23	0.55	0.95	0.25	0.51	0.83
AF$_{2D}$ (FV)	0.06	0.80	-0.16		0.67	0.47	-0.05	**0.90**	0.67	0.36
AF$_{2D}$ (F0)	0.38	**0.80**	0.23	0.67		0.79	0.30	0.79	**0.80**	0.63
AF$_{2D}$ (FL)	0.65	0.77	0.55	0.47	0.79		0.57	0.70	**0.85**	0.80
AF$_{2D}$ (ARMS)	**0.96**	0.51	0.95	-0.05	0.30	0.57		0.36	0.54	0.87
AF$_{2D}$ (SI)	0.46	**0.97**	0.25	**0.90**	0.79	0.70	0.36		0.88	0.71
AF$_{2D}$ (CAV)	0.66	**0.91**	0.51	0.67	**0.80**	**0.85**	0.54	0.88		0.88
AF$_{2D}$ (IA)	**0.92**	0.82	0.83	0.36	0.63	0.80	0.87	0.71	0.88	

Fig. 5.15. Scatter matrix and correlation coefficients for 10 characteristics of earthquake ground motion.

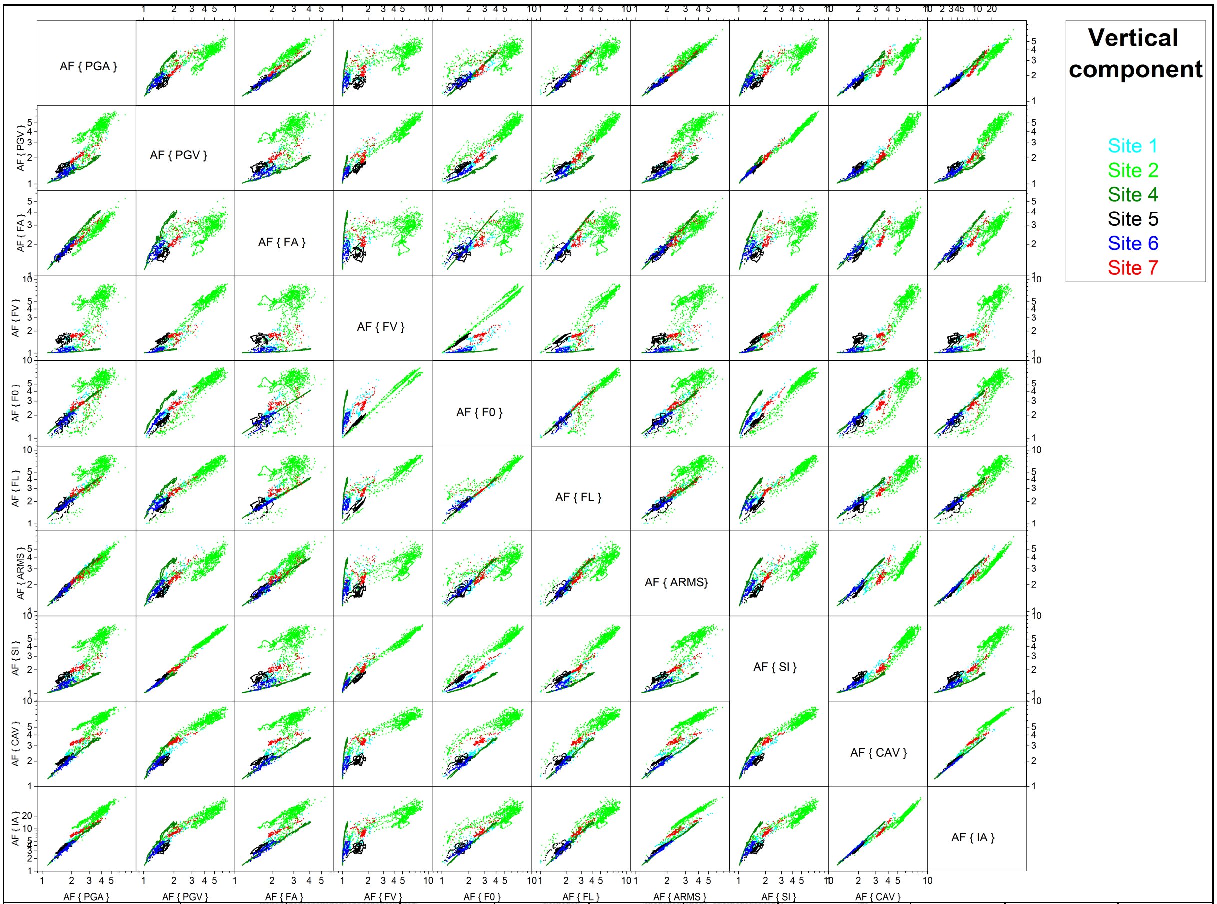

Pearson correlations	**AF_{2D} (PGA)**	**AF_{2D} (PGV)**	**AF_{2D} (FA)**	**AF_{2D} (FV)**	**AF_{2D} (F0)**	**AF_{2D} (FL)**	**AF_{2D} (ARMS)**	**AF_{2D} (SI)**	**AF_{2D} (CAV)**	**AF_{2D} (IA)**
AF_{2D}(PGA)		0.893	**0.936**	0.760	0.883	0.931	**0.980**	0.854	0.935	0.975
AF_{2D} (PGV)	0.893		0.693	**0.965**	0.933	0.951	0.859	**0.995**	0.971	0.949
AF_{2D} (FA)	**0.936**	0.693		0.510	0.736	0.795	**0.938**	0.634	0.784	0.864
AF_{2D} (FV)	0.760	**0.965**	0.510		0.872	0.876	0.717	**0.984**	0.911	0.855
AF_{2D} (F0)	0.883	0.933	0.736	0.872		**0.966**	0.880	0.918	0.929	0.930
AF_{2D} (FL)	0.931	0.951	0.795	0.876	**0.966**		0.922	0.932	0.962	0.967
AF_{2D} (ARMS)	**0.980**	0.859	0.938	0.717	0.880	0.922		0.818	0.910	0.964
AF_{2D} (SI)	0.854	**0.995**	0.634	**0.984**	0.918	0.932	0.818		0.961	0.927
AF_{2D} (CAV)	0.935	0.971	0.784	0.911	0.929	0.962	0.910	0.961		**0.987**
AF_{2D} (IA)	0.975	0.949	0.864	0.855	0.930	0.967	0.964	0.927	**0.987**	

Fig. 5.16. Scatter matrix and correlation coefficients for 10 characteristics of earthquake ground motion.

5.1.2.3 3D

Overall statistical analysis. Fig. 5.17 shows the amplification factors calculated from results of the 3D simulations. The figure shows the amplification factors for 10 EGM characteristics separately for each component. Each colour dot in the figure represents a value calculated for one receiver. The figure includes all receivers atop sediments in the all 12 investigated profiles. Excluded are receiver positions in case of the local fundamental frequency larger than 20 Hz.

Scatter matrices. Fig. 5.18 - Fig. 5.20 show the amplification factors plotted against each other and the values of the correlation coefficients. The correlation here means a large value of the Pearson correlation coefficient. We compare the amplification factors for 10 EGM characteristics.

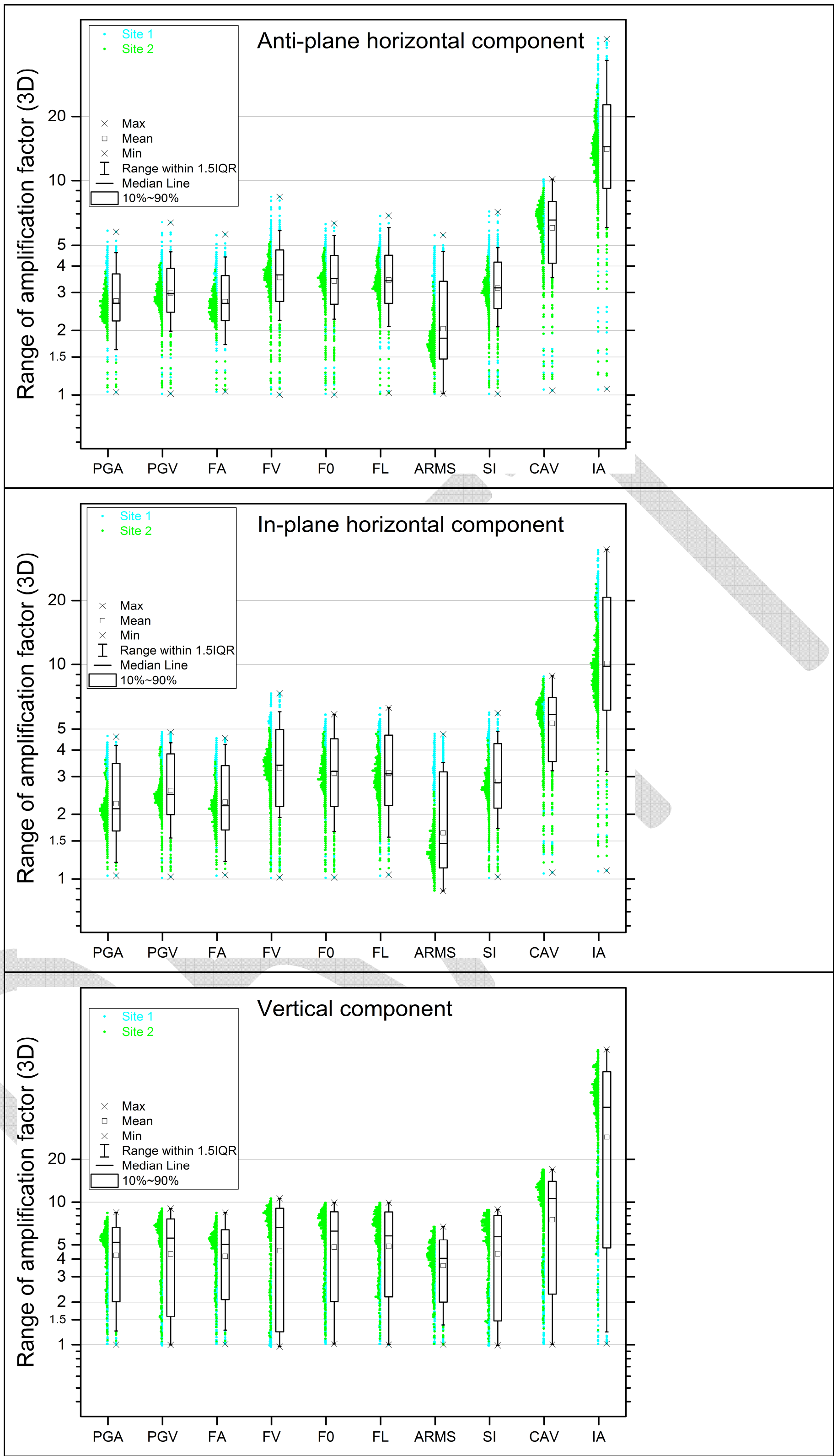

Fig. 5.17. Range of the amplification factor from the 3D simulations for 10 characteristics of the earthquake ground motion.

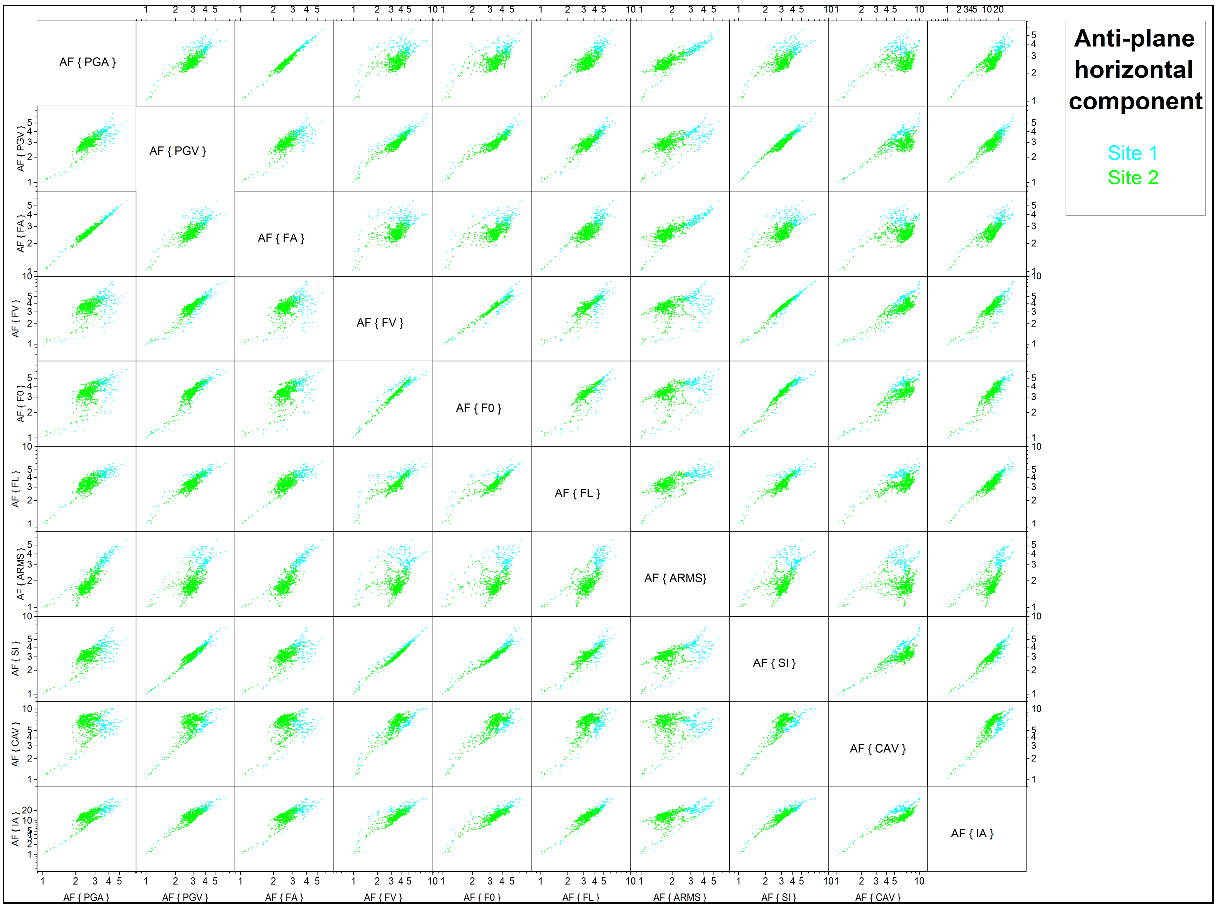

Pearson correlations	AF_{3D} (PGA)	AF_{3D} (PGV)	AF_{3D} (FA)	AF_{3D} (FV)	AF_{3D} (F0)	AF_{3D} (FL)	AF_{3D} (ARMS)	AF_{3D} (SI)	AF_{3D} (CAV)	AF_{3D} (IA)
AF_{3D}(PGA)		0.82	**0.98**	0.56	0.65	0.84	**0.89**	0.71	0.35	0.79
AF_{3D} (PGV)	0.82		0.80	0.90	0.92	0.89	0.64	**0.96**	0.68	0.90
AF_{3D} (FA)	**0.98**	0.80		0.53	0.63	0.83	0.85	0.68	0.38	0.80
AF_{3D} (FV)	0.56	0.90	0.53		**0.97**	0.81	0.38	**0.97**	**0.85**	0.87
AF_{3D} (F0)	0.65	0.92	0.63	**0.97**		0.86	0.46	0.96	0.83	0.90
AF_{3D} (FL)	0.84	0.89	0.83	0.81	0.86		0.71	0.89	0.66	**0.93**
AF_{3D} (ARMS)	**0.89**	0.64	0.85	0.38	0.46	0.71		0.54	0.08	0.64
AF_{3D} (SI)	0.71	**0.96**	0.68	**0.97**	0.96	0.89	0.54		0.80	**0.93**
AF_{3D} (CAV)	0.35	0.68	0.38	**0.85**	0.83	0.66	0.08	0.80		0.82
AF_{3D} (IA)	0.79	0.90	0.80	0.87	0.90	**0.93**	0.64	**0.93**	0.82	

Fig. 5.18. Scatter matrix and correlation coefficients for 10 characteristics of earthquake ground motion.

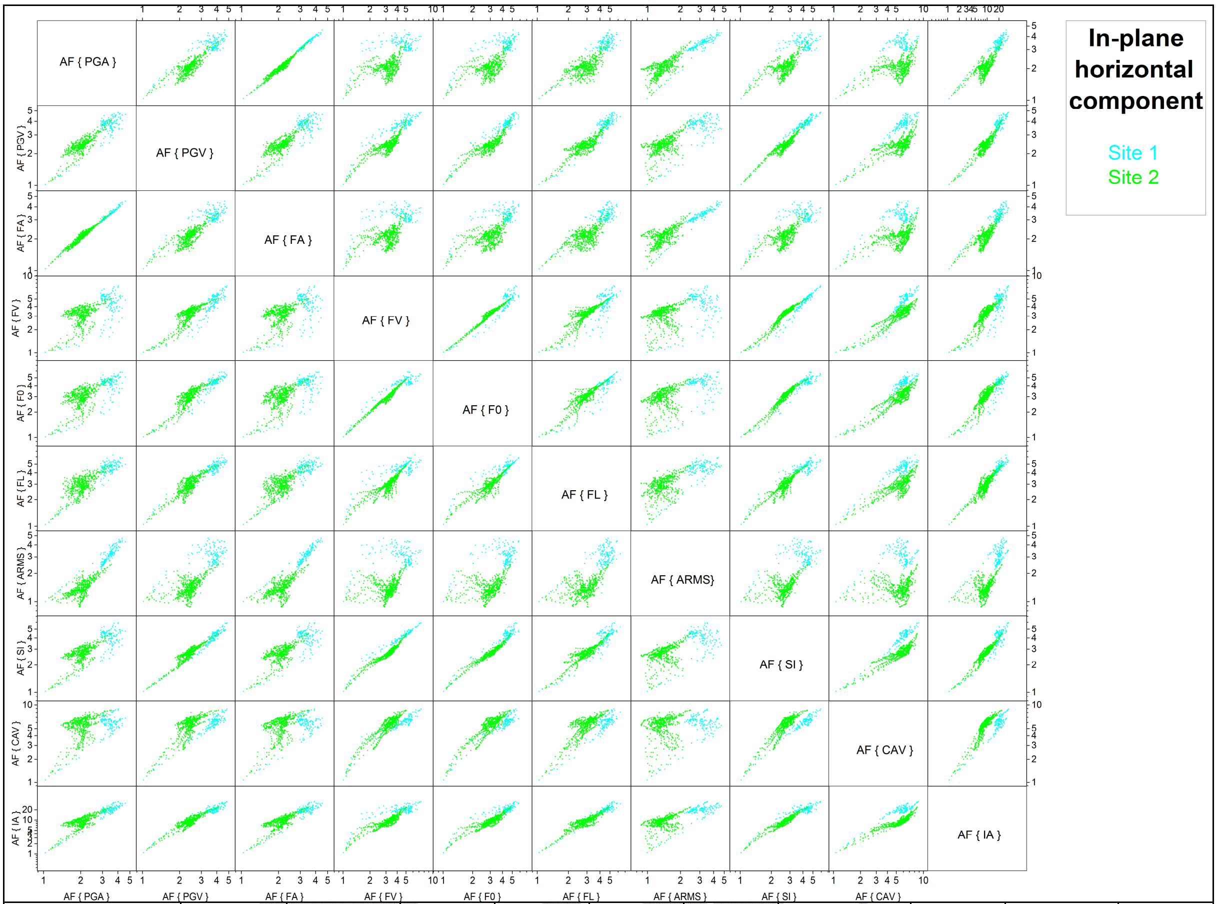

Pearson correlations	**AF_{3D} (PGA)**	**AF_{3D} (PGV)**	**AF_{3D} (FA)**	**AF_{3D} (FV)**	**AF_{3D} (F0)**	**AF_{3D} (FL)**	**AF_{3D} (ARMS)**	**AF_{3D} (SI)**	**AF_{3D} (CAV)**	**AF_{3D} (IA)**
AF_{3D}(PGA)		0.90	**0.99**	0.61	0.69	0.82	**0.90**	0.79	0.43	0.86
AF_{3D} (PGV)	0.90		0.88	0.87	0.91	0.92	0.76	**0.97**	0.69	0.95
AF_{3D} (FA)	**0.99**	0.88		0.60	0.69	0.81	0.87	0.78	0.46	0.86
AF_{3D} (FV)	0.61	0.87	0.60		**0.97**	0.86	0.45	0.96	**0.88**	0.88
AF_{3D} (F0)	0.69	0.91	0.69	**0.97**		0.91	0.53	**0.97**	0.86	0.92
AF_{3D} (FL)	0.82	0.92	0.81	0.86	0.91		0.71	0.93	0.74	**0.94**
AF_{3D} (ARMS)	**0.90**	0.76	0.87	0.45	0.53	0.71		0.65	0.18	0.73
AF_{3D} (SI)	0.79	**0.97**	0.78	0.96	**0.97**	0.93	0.65		0.81	**0.95**
AF_{3D} (CAV)	0.43	0.69	0.46	**0.88**	0.86	0.74	0.18	0.81		0.80
AF_{3D} (IA)	0.86	0.95	0.86	0.88	0.92	**0.94**	0.73	**0.95**	0.80	

Fig. 5.19. Scatter matrix and correlation coefficients for 10 characteristics of earthquake ground motion.

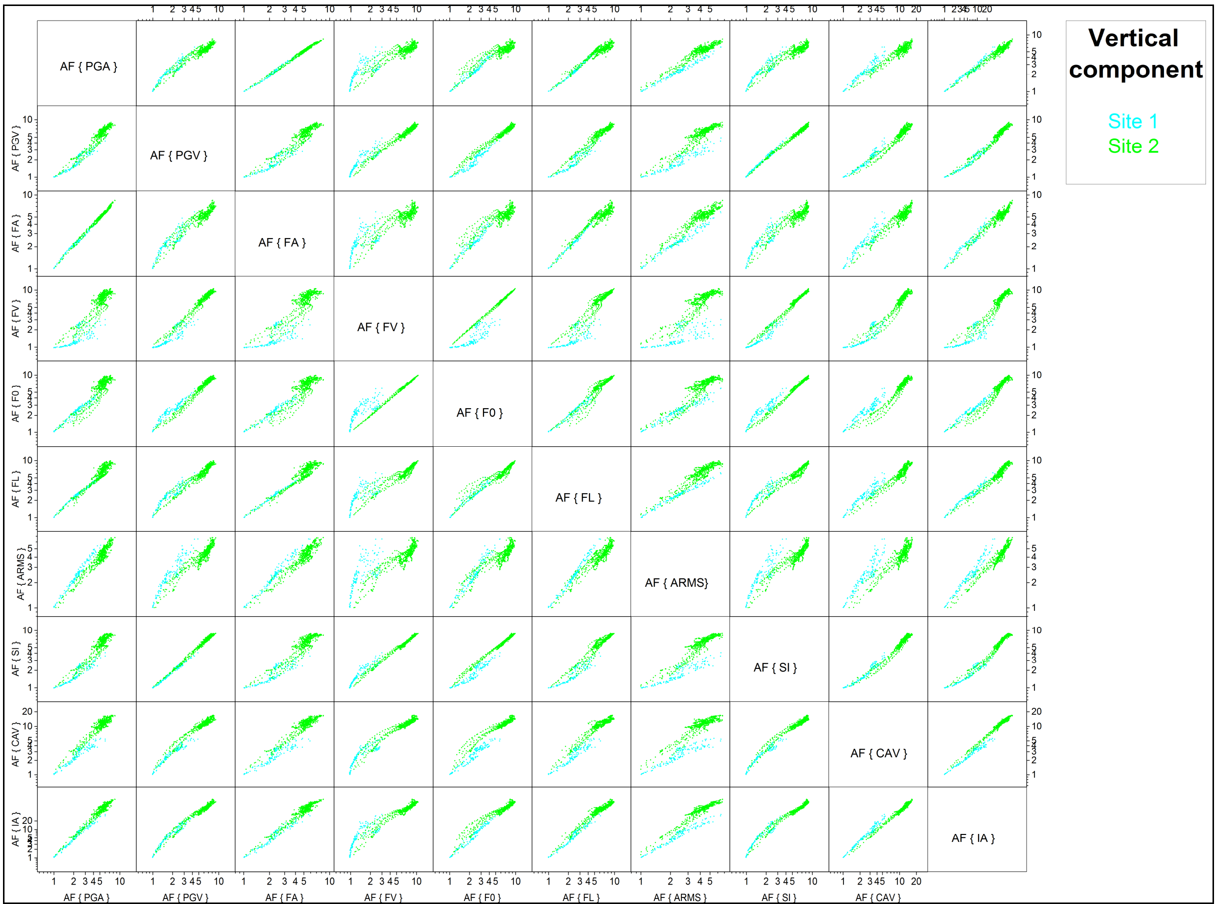

Pearson correlations	AF_{3D} (PGA)	AF_{3D} (PGV)	AF_{3D} (FA)	AF_{3D} (FV)	AF_{3D} (F0)	AF_{3D} (FL)	AF_{3D} (ARMS)	AF_{3D} (SI)	AF_{3D} (CAV)	AF_{3D} (IA)
AF_{3D}(PGA)		0.971	**0.997**	0.923	0.952	0.976	**0.955**	0.959	0.962	0.985
AF_{3D} (PGV)	0.971		0.963	0.983	0.983	0.978	0.918	**0.997**	0.984	0.988
AF_{3D} (FA)	**0.997**	0.963		0.914	0.944	0.973	0.949	0.951	0.960	0.982
AF_{3D} (FV)	0.923	0.983	0.914		0.964	0.942	0.850	**0.992**	0.978	0.962
AF_{3D} (F0)	0.952	0.983	0.944	0.964		**0.976**	0.926	0.982	0.960	0.973
AF_{3D} (FL)	0.976	0.978	0.973	0.942	**0.976**		0.945	0.971	0.964	0.982
AF_{3D} (ARMS)	**0.955**	0.918	0.949	0.850	0.926	0.945		0.903	0.888	0.942
AF_{3D} (SI)	0.959	**0.997**	0.951	**0.992**	0.982	0.971	0.903		0.987	0.985
AF_{3D} (CAV)	0.962	0.984	0.960	0.978	0.960	0.964	0.888	0.987		**0.990**
AF_{3D} (IA)	0.985	0.988	0.982	0.962	0.973	0.982	0.942	0.985	**0.990**	

Fig. 5.20. Scatter matrix and correlation coefficients for 10 characteristics of earthquake ground motion.

5.1.3 Analysis and partial conclusions

Aggravation factors

The scatter matrices and values of the correlation coefficients make it possible to estimate the level of correlation of all pairs of the aggravation factors. In the following statements and considerations we symbolically say, e.g., "PGA is correlated with FA" but mean, in fact, that the aggravation factor of PGA is correlated with the aggravation factor of FA. The scatter matrices and values of the correlation coefficients lead us to the following statements and partial conclusions:

-
    - PGA is correlated with FA.
    - PGA is correlated with other quantities more than FA is.
    - Consequently, PGA will be excluded.
-
    - SI is correlated with PGV and also with FV.
    - PGV and FV are more used characteristics.
    - Consequently, SI will be excluded.
-
    - IA is correlated with CAV.
    - IA is correlated with other quantities more than CAV is.
    - Consequently, IA will be excluded.
-
    - ARMS is correlated with FA mainly for values larger than 1.25.
    - FA is kept due to correlation with PGA.
    - Consequently, ARMS will be excluded.
-
    - F0 is correlated with FL.
    - F0 is more artificial (less founded) quantity.
    - Consequently, F0 will be excluded.
-
    - PGV is correlated with FV and FL.
    - FV and FL are less correlated.
    - Consequently, PGV will be excluded.

The considerations are valid consistently for AGF32 and AGF21.

Based on the above partial conclusions we decide to further investigate the aggravation factors of the four EGM characteristics: FA, FV, FL and CAV.

The conclusions are also true for the EGM characteristics calculated using accelerograms which are band-pass filtered in [0.5, 5] Hz; see the electronic supplement. This is important for comparing AGF32 with AGF21 because the 3D simulations are limited for [0.5, 5] Hz.

Amplification factors

The scatter matrices and values of the correlation coefficients for amplification factors are largely consistent with those obtained for aggravation factors. Therefore we can further investigate the amplification factors of the same four EGM characteristics as in the case of the aggravation factors: FA, FV, FL and CAV.

5.2 Site by site

5.2.1 Aggravation factors

Descriptive statistics of the FA and FV 2D/1D aggravation factors for all 12 nominal-model profiles is shown in Fig. 5.21. Fig. 5.22 similarly shows the statistics for the FL and CAV 2D/1D aggravation factors for the 12 profiles.

Fig. 5.23 shows the statistics for the FA and FV 3D/2D aggravation factors for 7 profiles in models of Site1 and Site 2. Similarly, Fig. 5.24 shows the statistics for the FL and CAV 3D/2D aggravation factors for the 7 profiles.

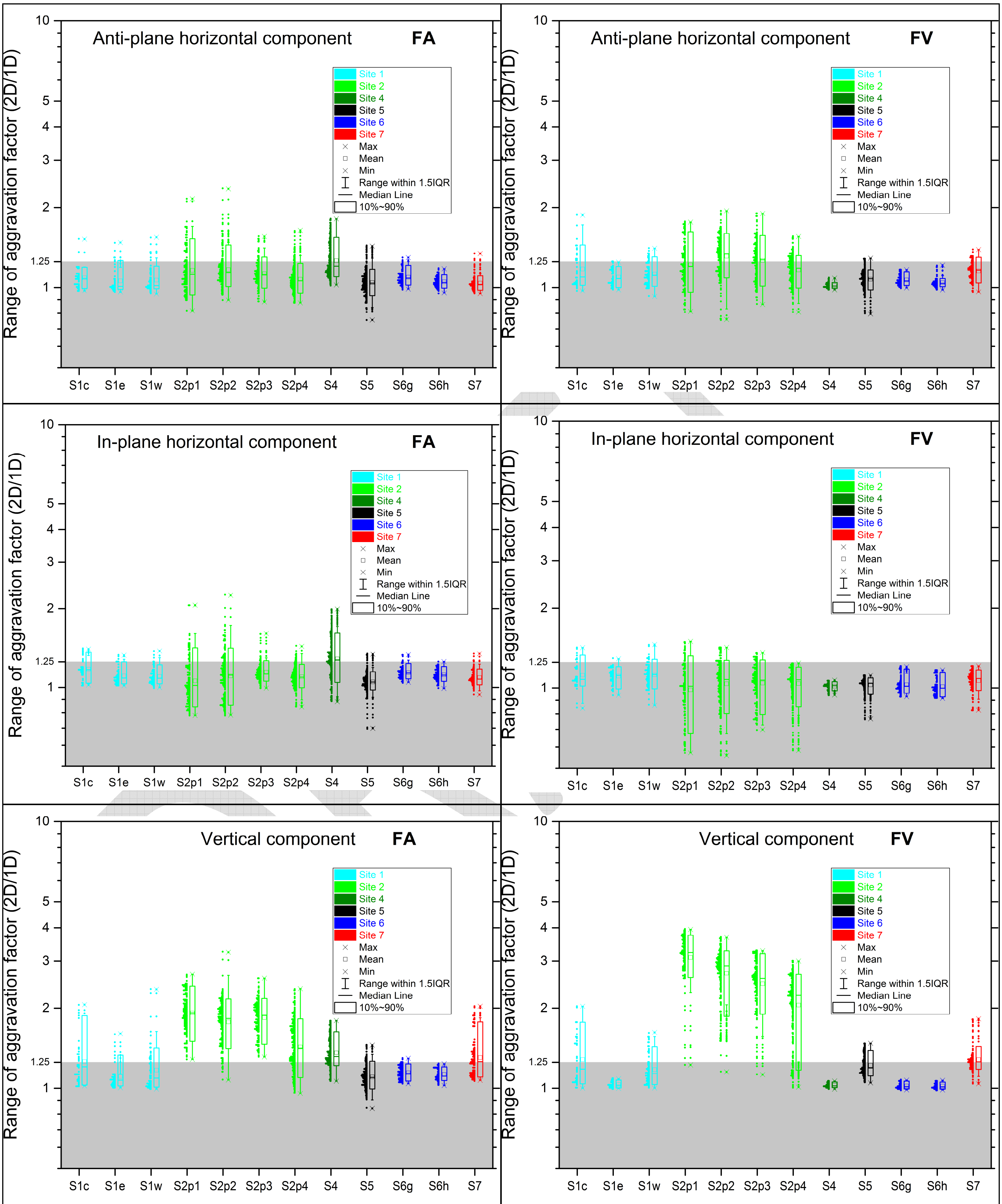

Fig. 5.21. FA and FV 2D/1D aggravation factors for all 12 nominal-model profiles.

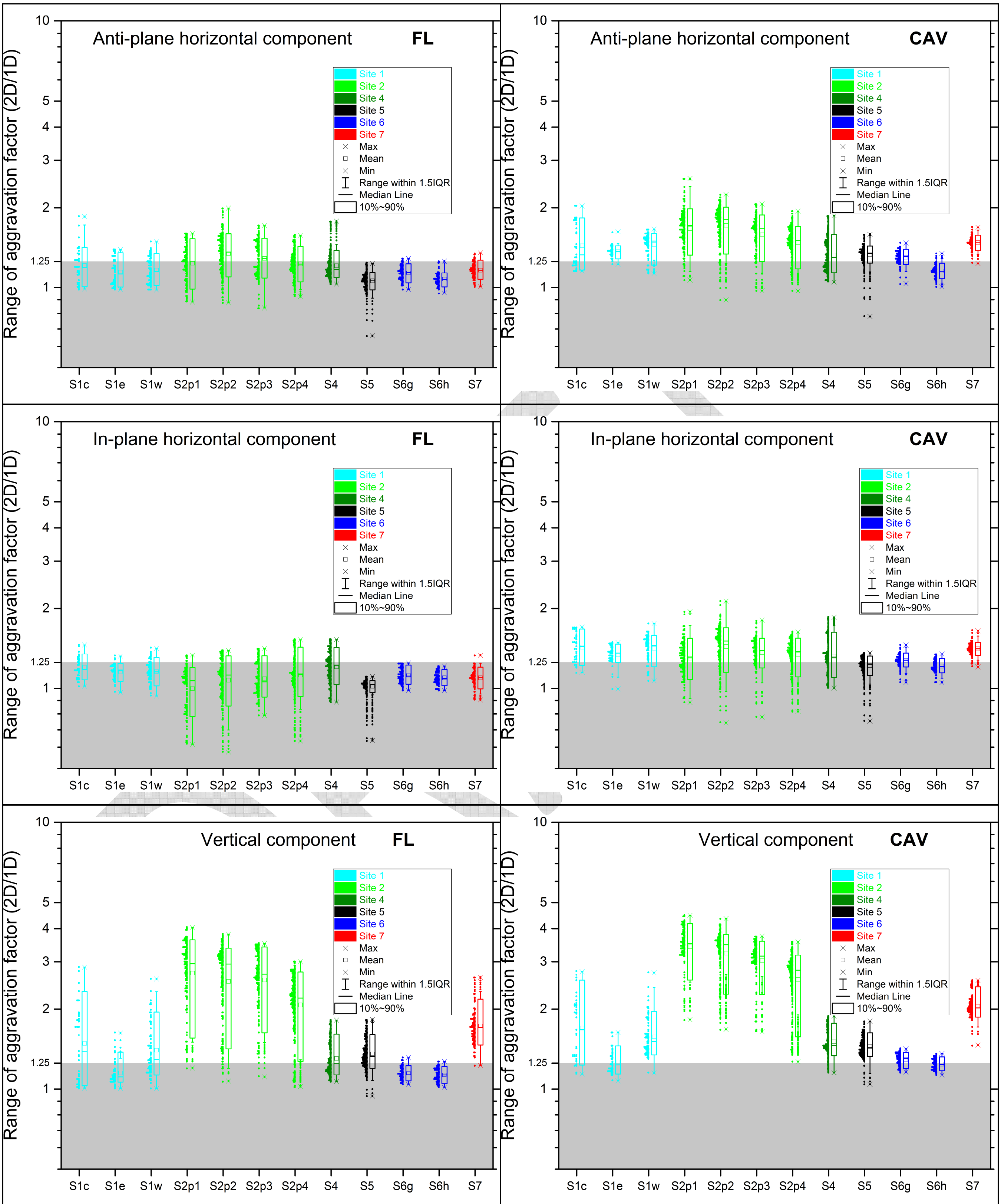

Fig. 5.22. FL and CAV 2D/1D aggravation factors for all 12 nominal-model profiles.

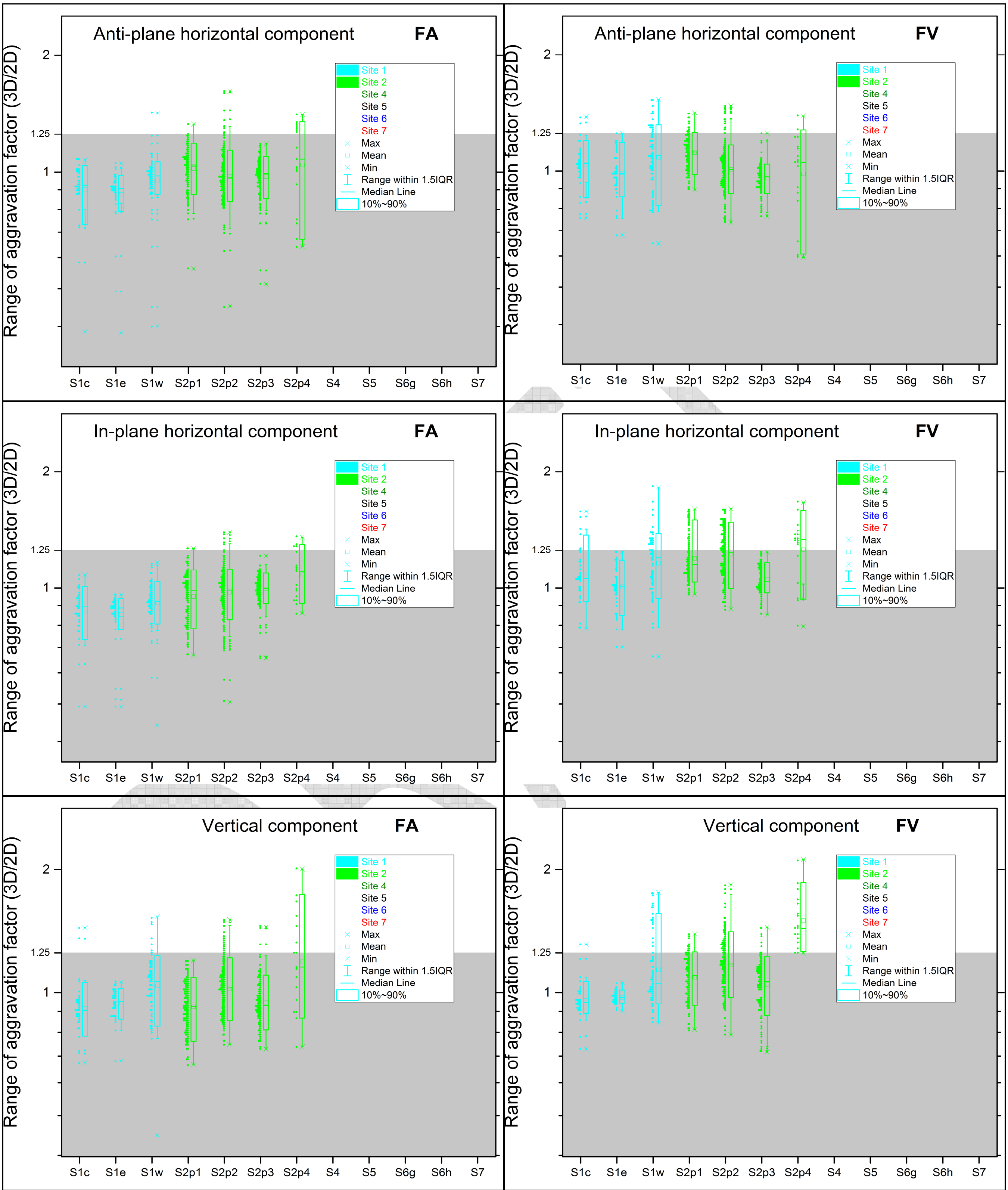

Fig. 5.23. FA and FV 3D/2D aggravation factors for 7 profiles at Site 1 and Site 2.

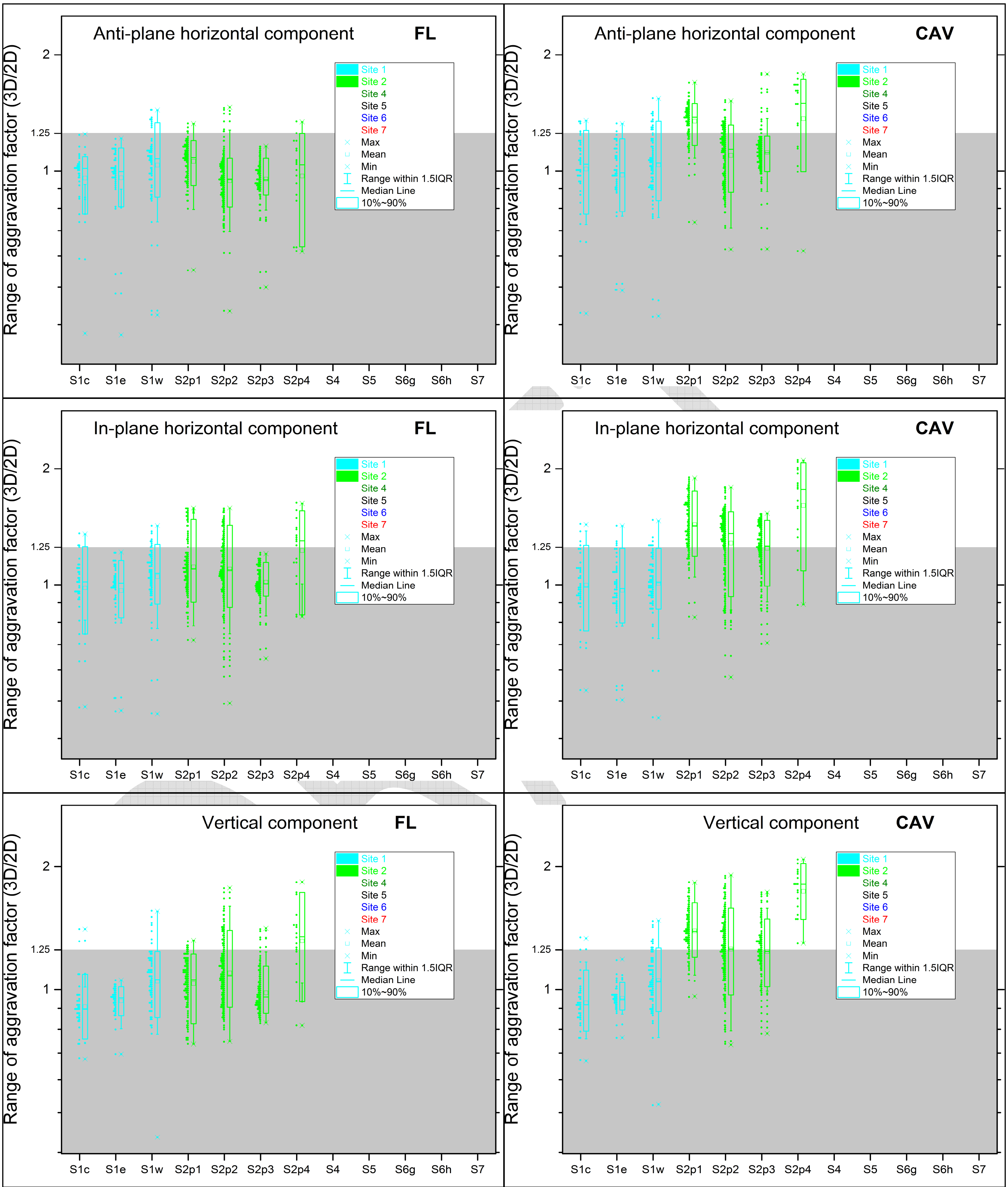

Fig. 5.24. FL and CAV 3D/2D aggravation factors for 7 profiles at Site 1 and Site 2.

5.2.2 Amplification factors

Descriptive statistics of the FA and FV amplification factors from 1D simulations for all 12 nominal-model profiles is shown in Fig. 5.25. Fig. 5.26 similarly shows the statistics for the FL and CAV amplification factors for the 12 profiles.

Descriptive statistics of the FA and FV amplification factors from 2D simulations for all 12 nominal-model profiles is shown in Fig. 5.27. Fig. 5.28 similarly shows the statistics for the FL and CAV amplification factors for the 12 profiles.

Fig. 5.29 shows the statistics for the FA and FV amplification factors from 3D simulations for 7 profiles in models of Site1 and Site 2. Similarly, Fig. 5.30 shows the statistics for the FL and CAV amplification factors for the 7 profiles.

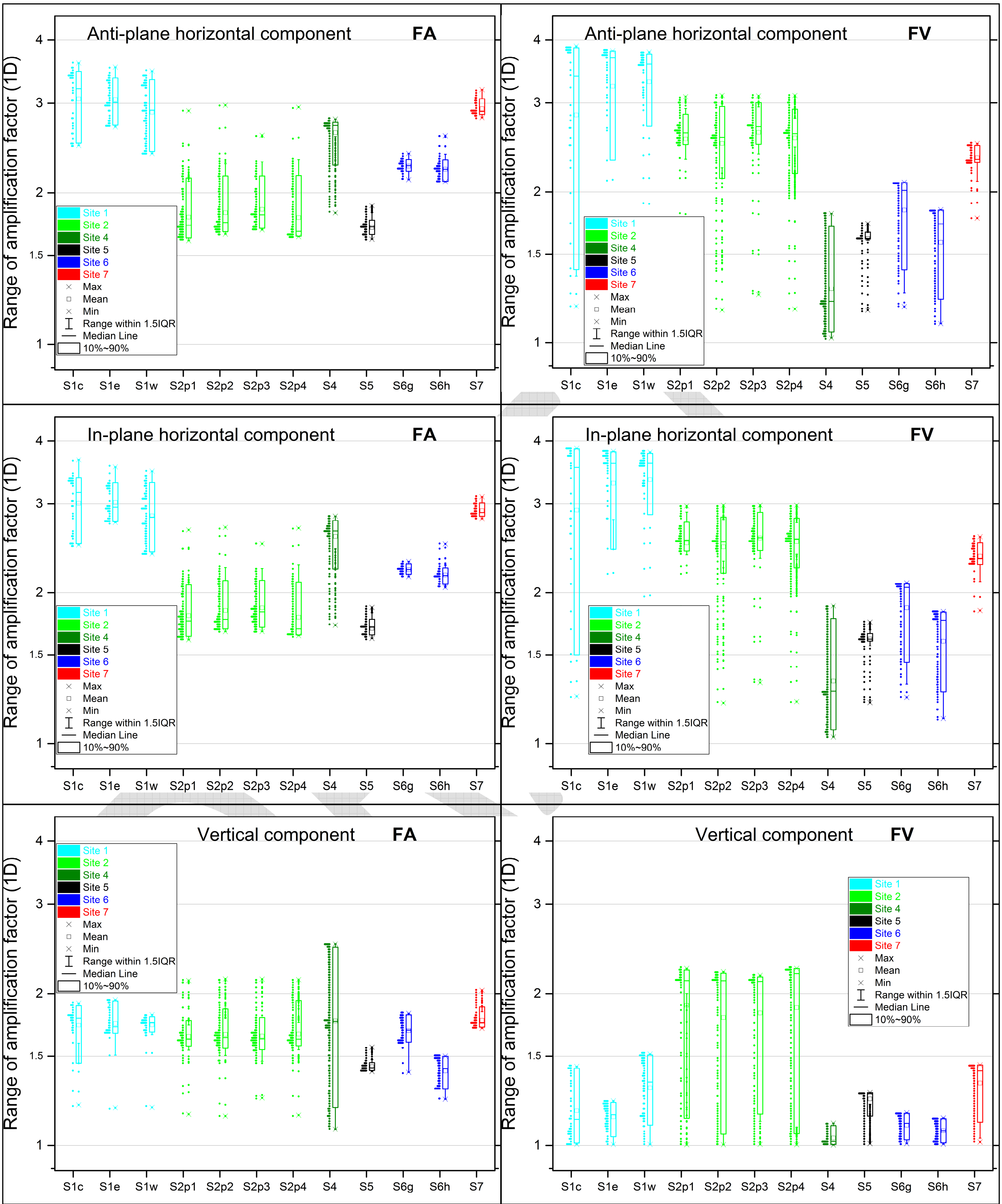

Fig. 5.25. FA and FV amplification factors from the 1D simulations for all 12 profiles.

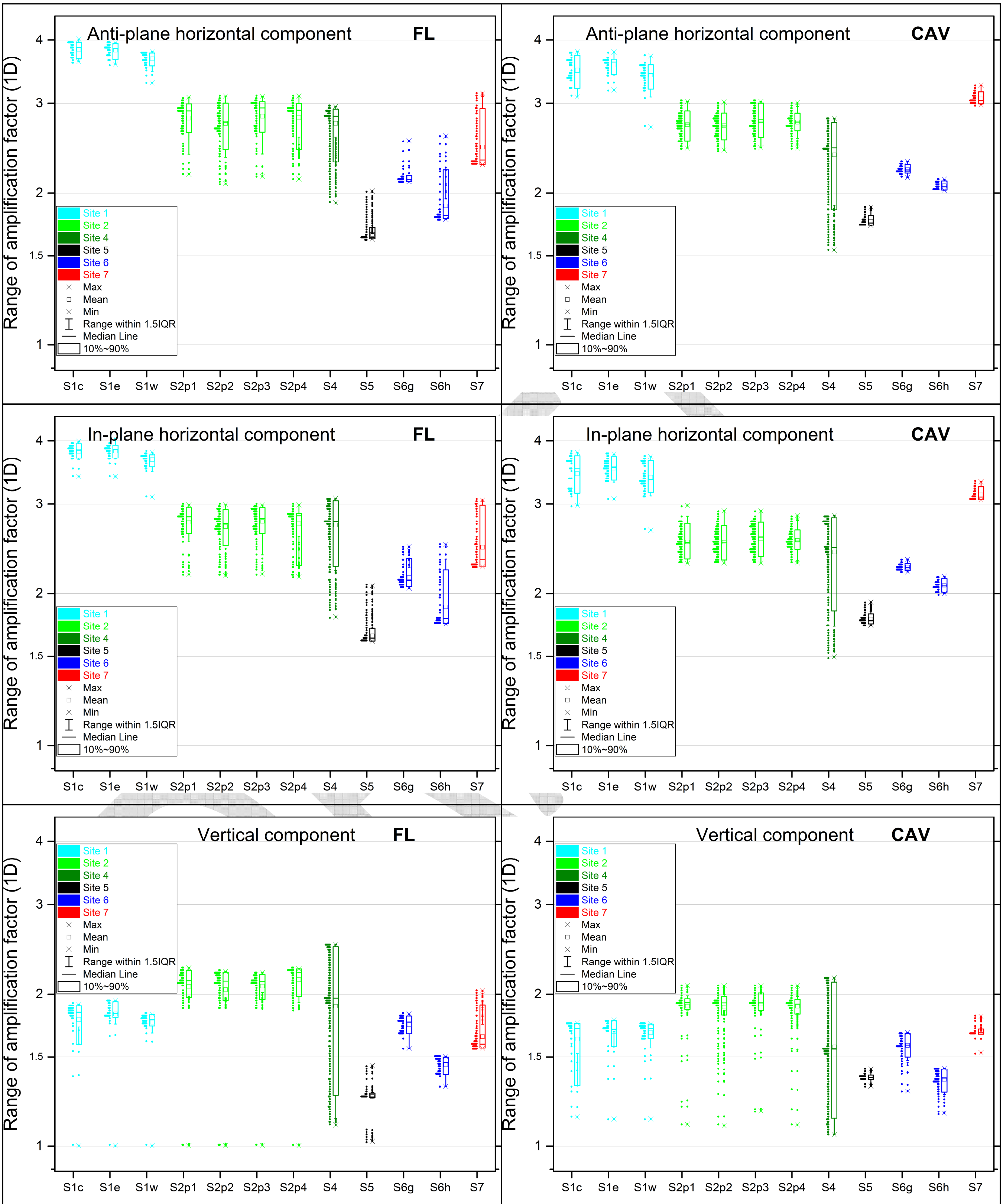

Fig. 5.26. FL and CAV amplification factors from the 1D simulations for all 12 profiles.

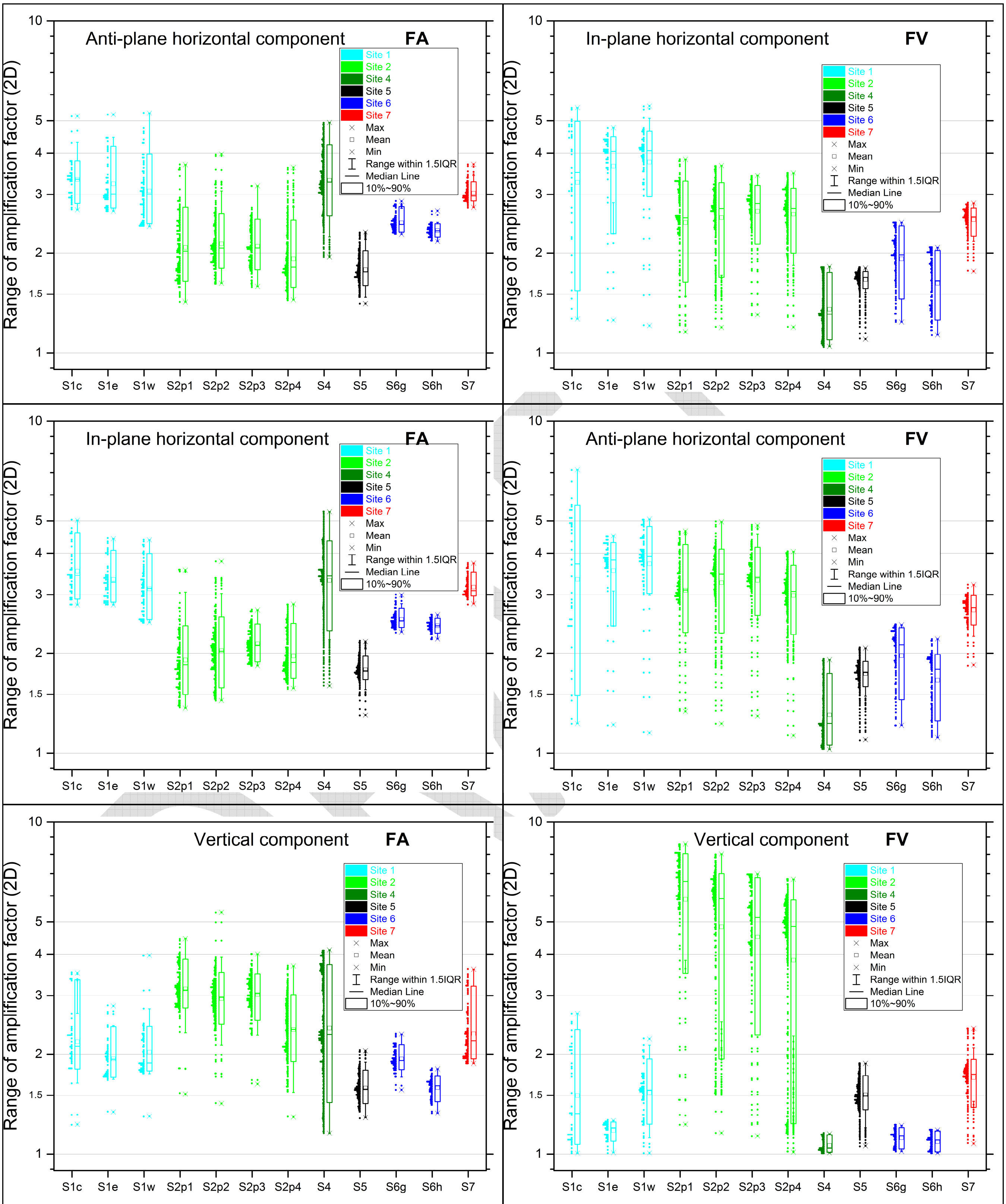

Fig. 5.27. FA and FV amplification factors from the 2D simulations for all 12 profiles.

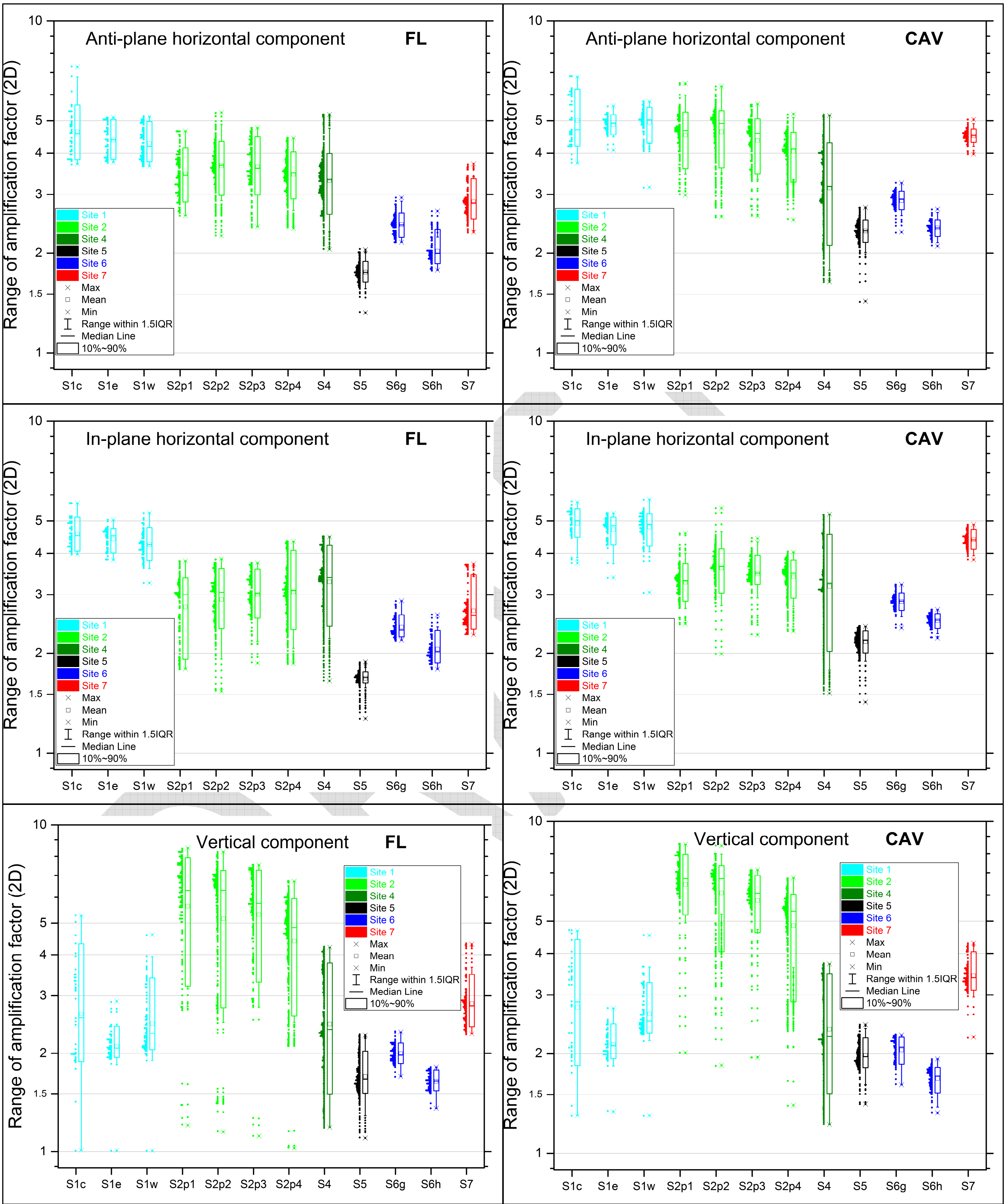

Fig. 5.28. FL and CAV amplification factors from the 2D simulations for all 12 profiles.

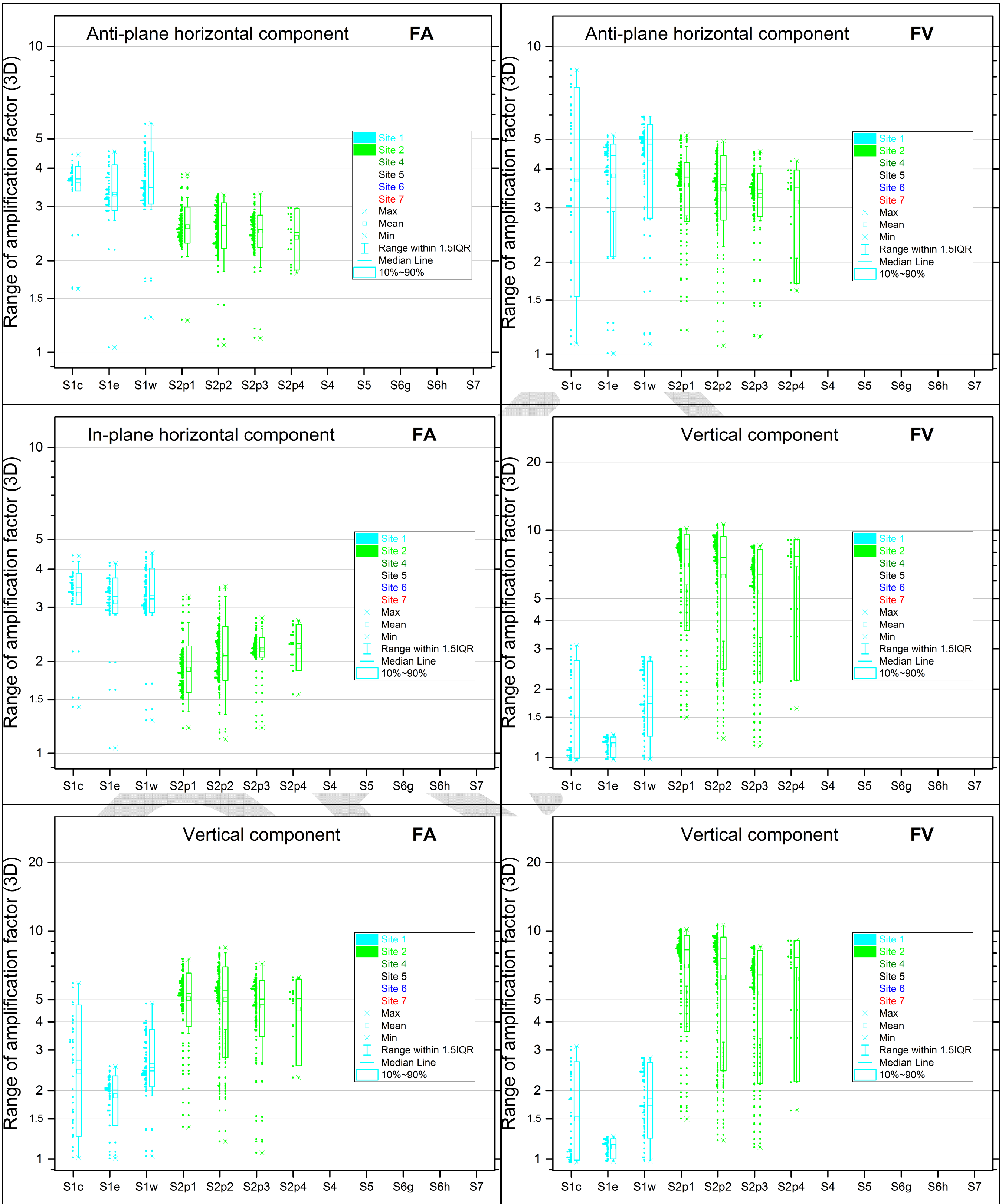

Fig. 5.29. FA and FV amplification factors from the 3D simulations for 7 profiles of Site 1 and Site 2.

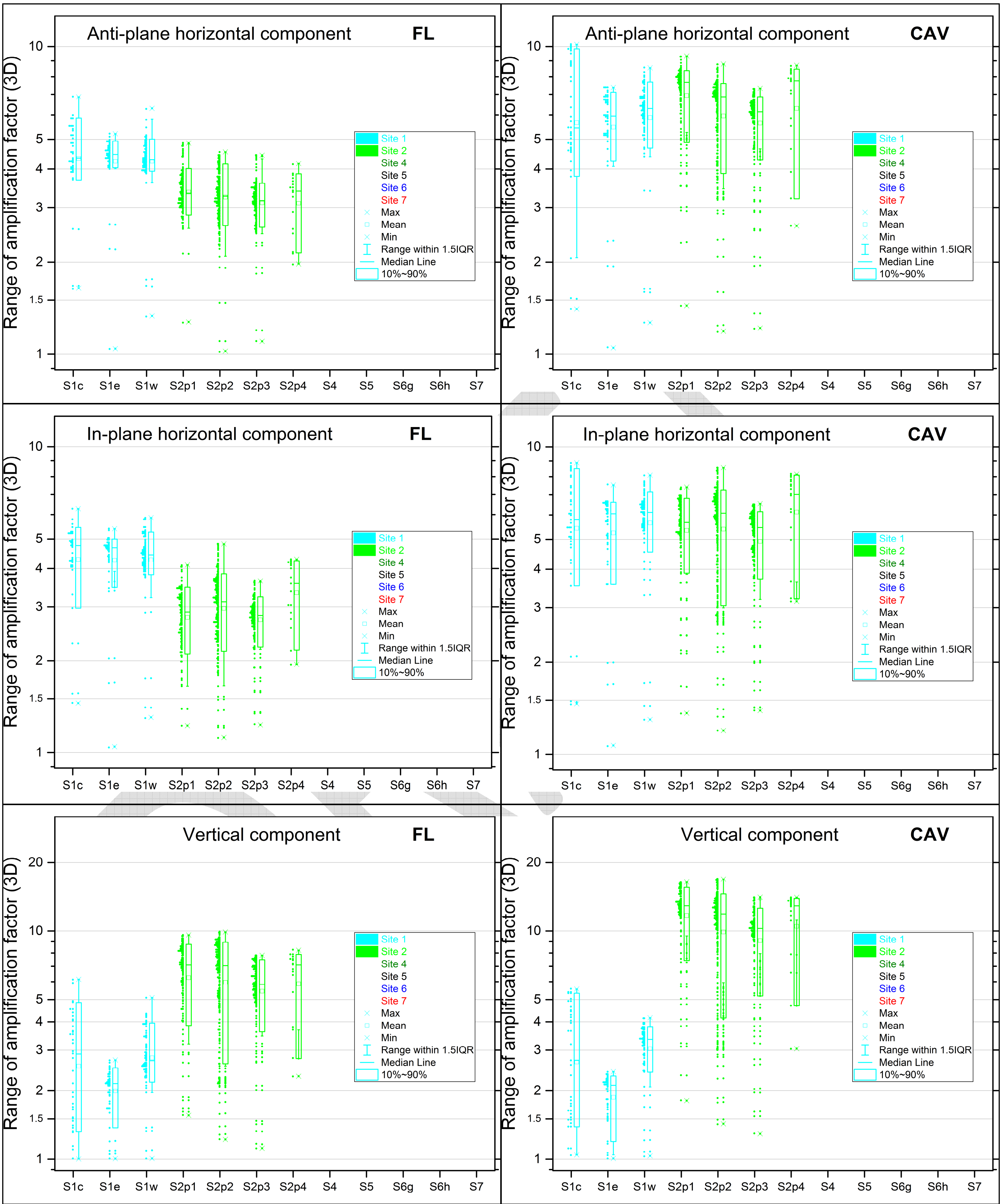

Fig. 5.30. FL and CAV amplification factors from the 3D simulations for 7 profiles of Site 1 and Site 2.

5.2.3 Analysis and partial conclusions

- For all sites there is at least one EGM characteristic with significant 2D/1D aggravation factor.
- All characteristics exhibit significant 2D/1D aggravation factor on the vertical component.
- The anti-plane and in-plane horizontal components exhibit different behaviour.
- The CAV 2D/1D aggravation factor is significant at all components and all sites.

1D simulations are not sufficient for any of the investigated sites.

3D effects are pronounced in the Grenoble valley (Site 2). They are most visible on the CAV 3D/2D aggravation factors (all components). The 3D effects are less visible in the Mygdonian basin (Site 1).

6 SENSITIVITY STUDY

Figures of all determined characteristics are in the electronic supplement.

6.1 Effect of uncertainty in bedrock velocity

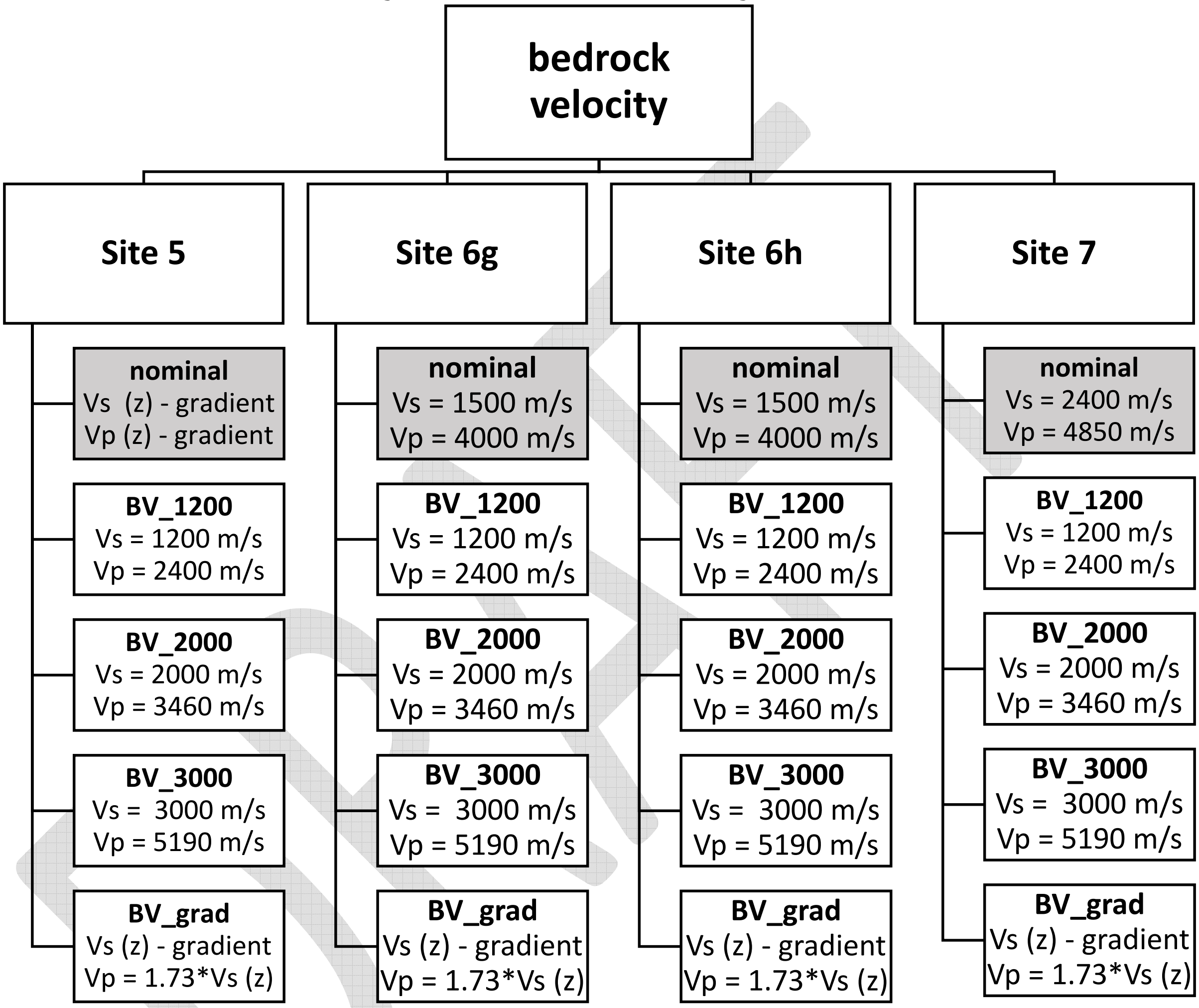

The amplification factors and aggravation factors (mainly for the vertical component) increase with the impedance contrast. This is mainly evident at frequencies close to the fundamental resonant frequency. These conclusions are valid for all models. Examples for Site 6h: CAV amplification factor in Fig. 6.1, CAV 2D/1D aggravation factor in Fig. 6.2.

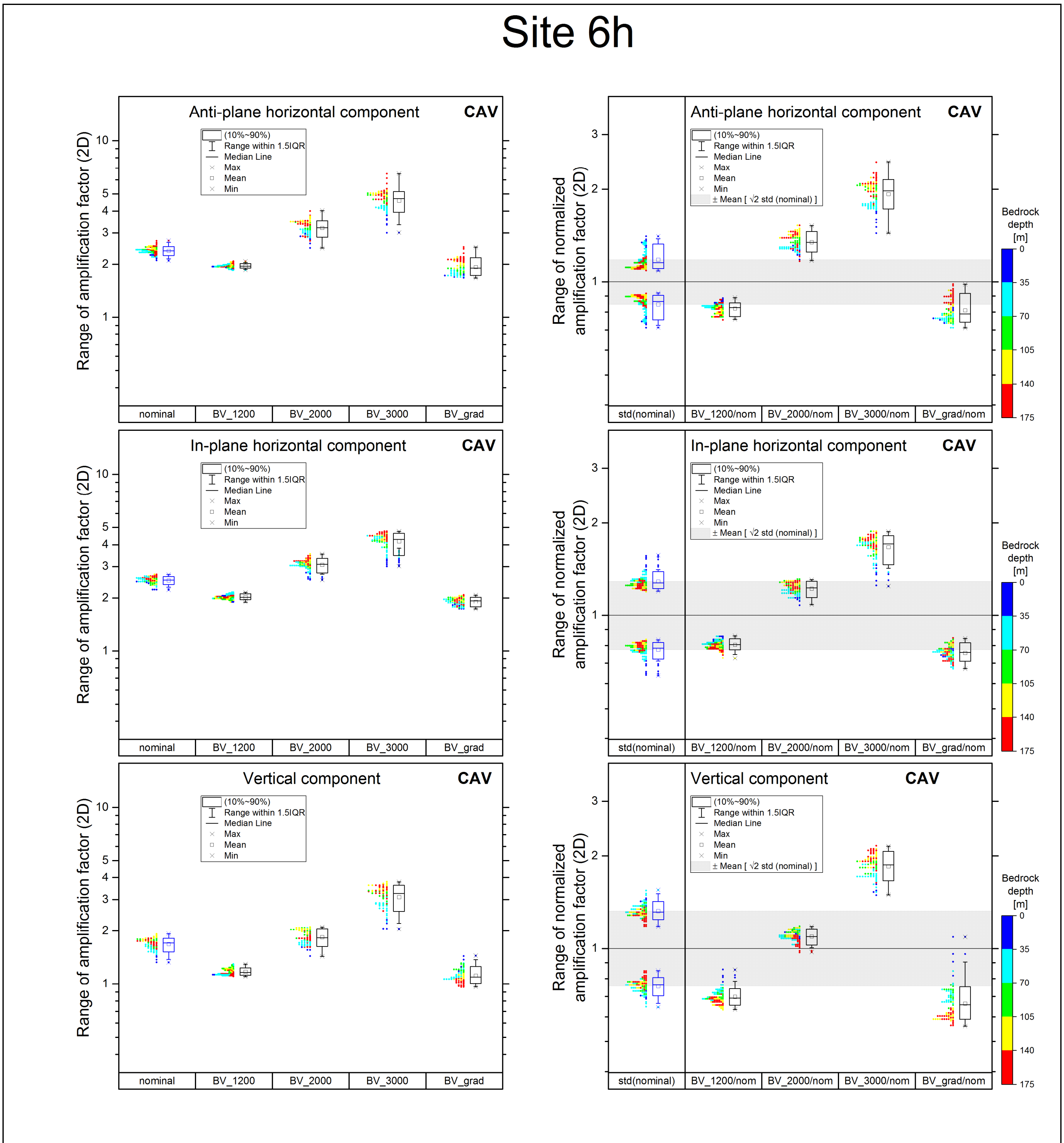

Fig. 6.1. CAV amplification factor from 2D simulations for Site 6h.

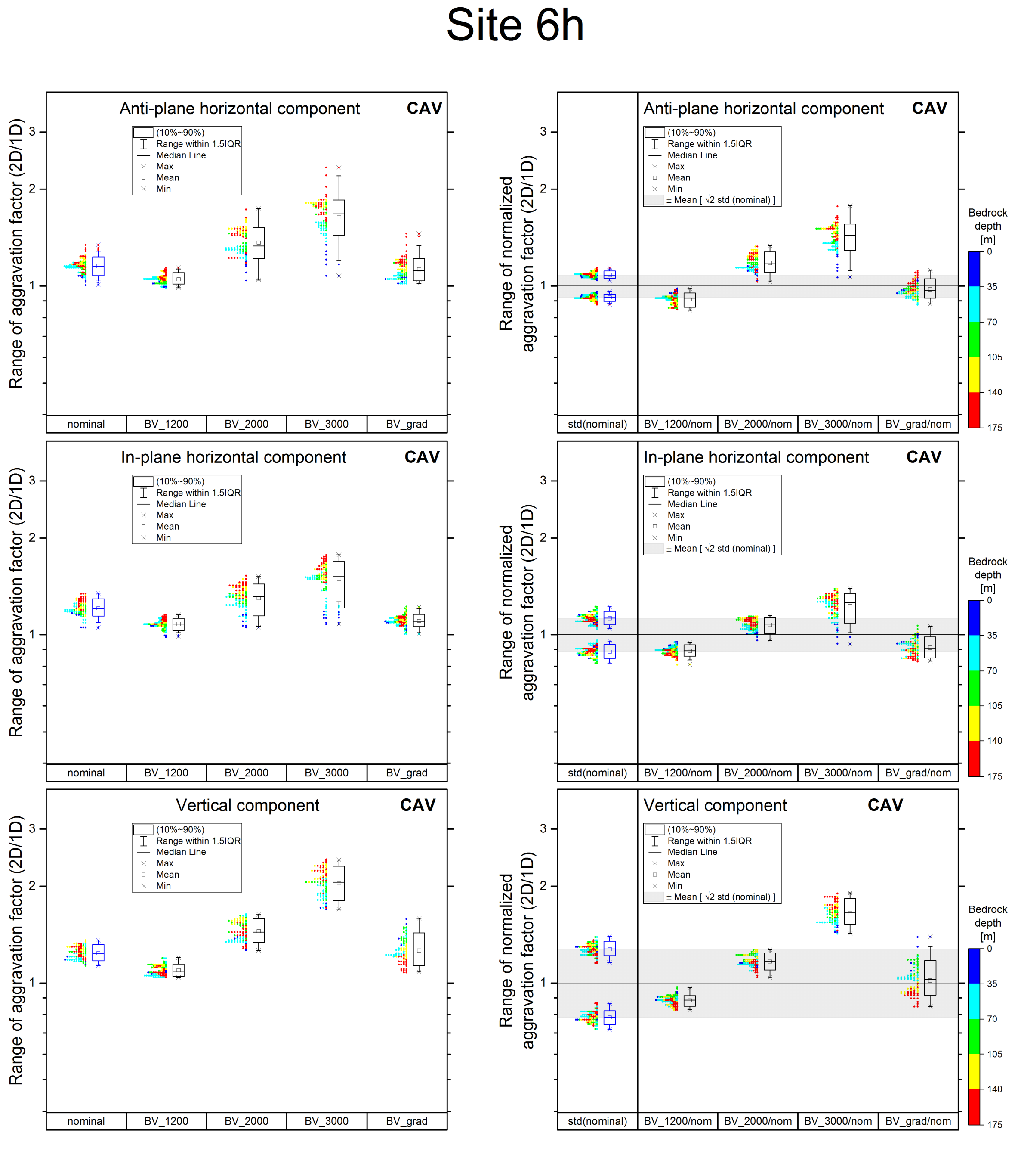

Fig. 6.2. CAV 2D/1D aggravation factor for Site 6h.

6.2 Effect of uncertainty in velocity in sediments

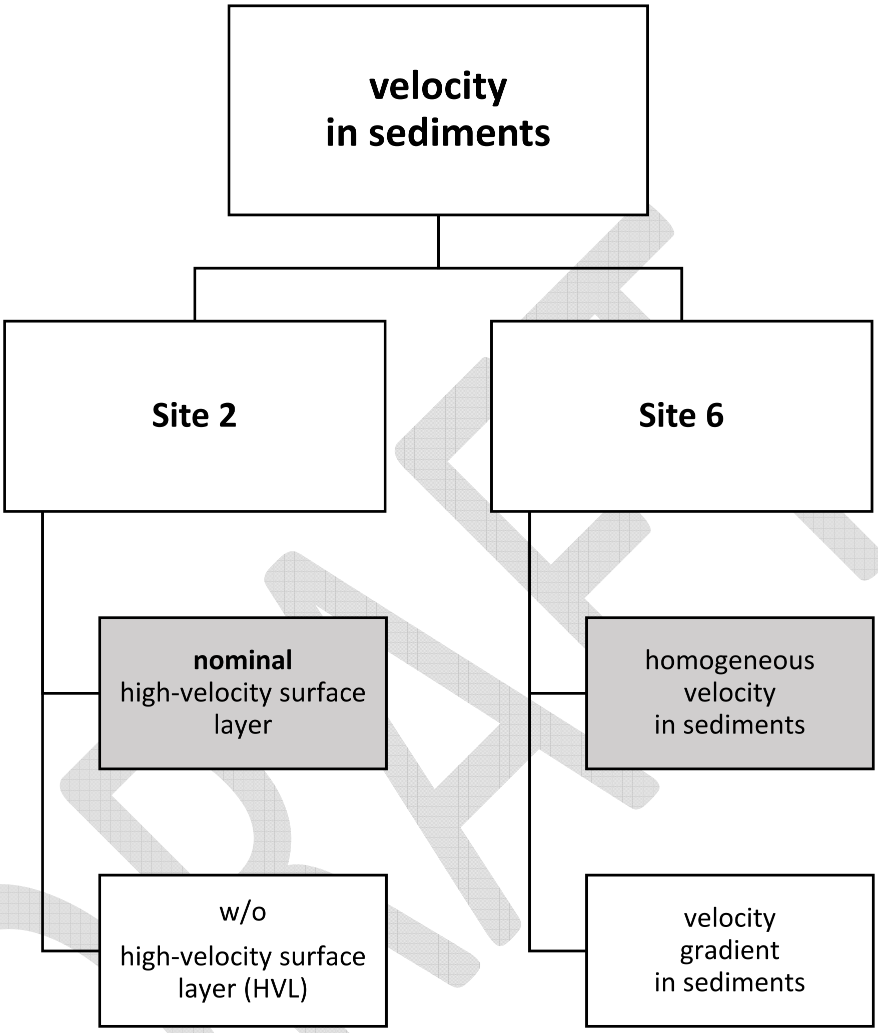

The effect of presence of the high-velocity surface layer in the Site-2 model is negligible consistently in 1D, 2D and 3D simulations. Fig. 6.3 show an example for the CAV amplification factor from 3D simulations.

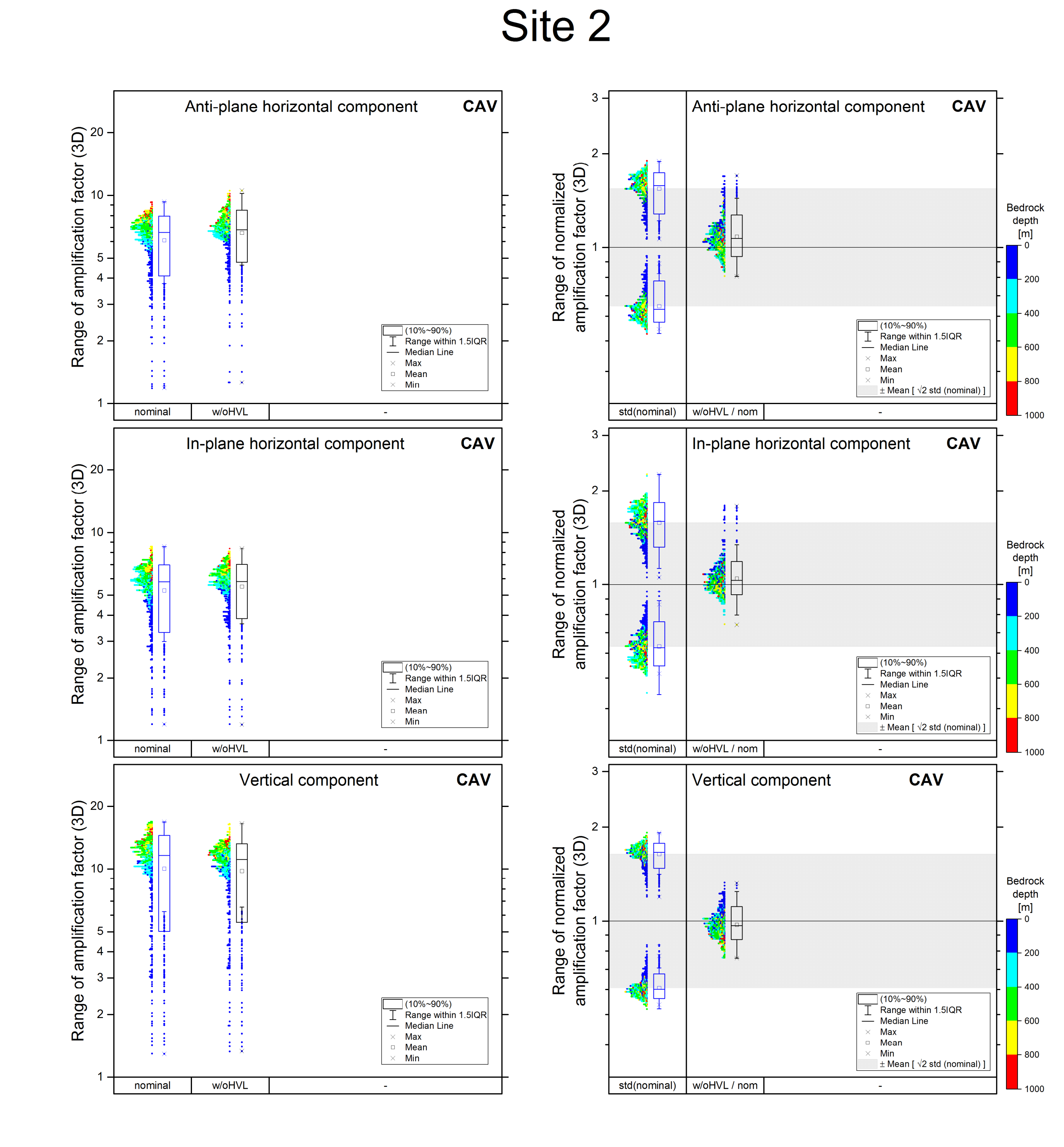

Fig. 6.3. CAV amplification factor from 3D simulations for Site 2.

The difference between the velocity distributions in sediments in 6h and 6g has no effect on the 2D/1D aggravation factor. The small difference in the amplification factors for 6h and 6g can be attributed to the different impedance contrast at the sediment-bedrock interface (due to different velocity distribution in sediments). Fig. 6.4 shows examples of the CAV amplification factor from 2D simulations and CAV 2D/1D aggravation factor for Site 6.

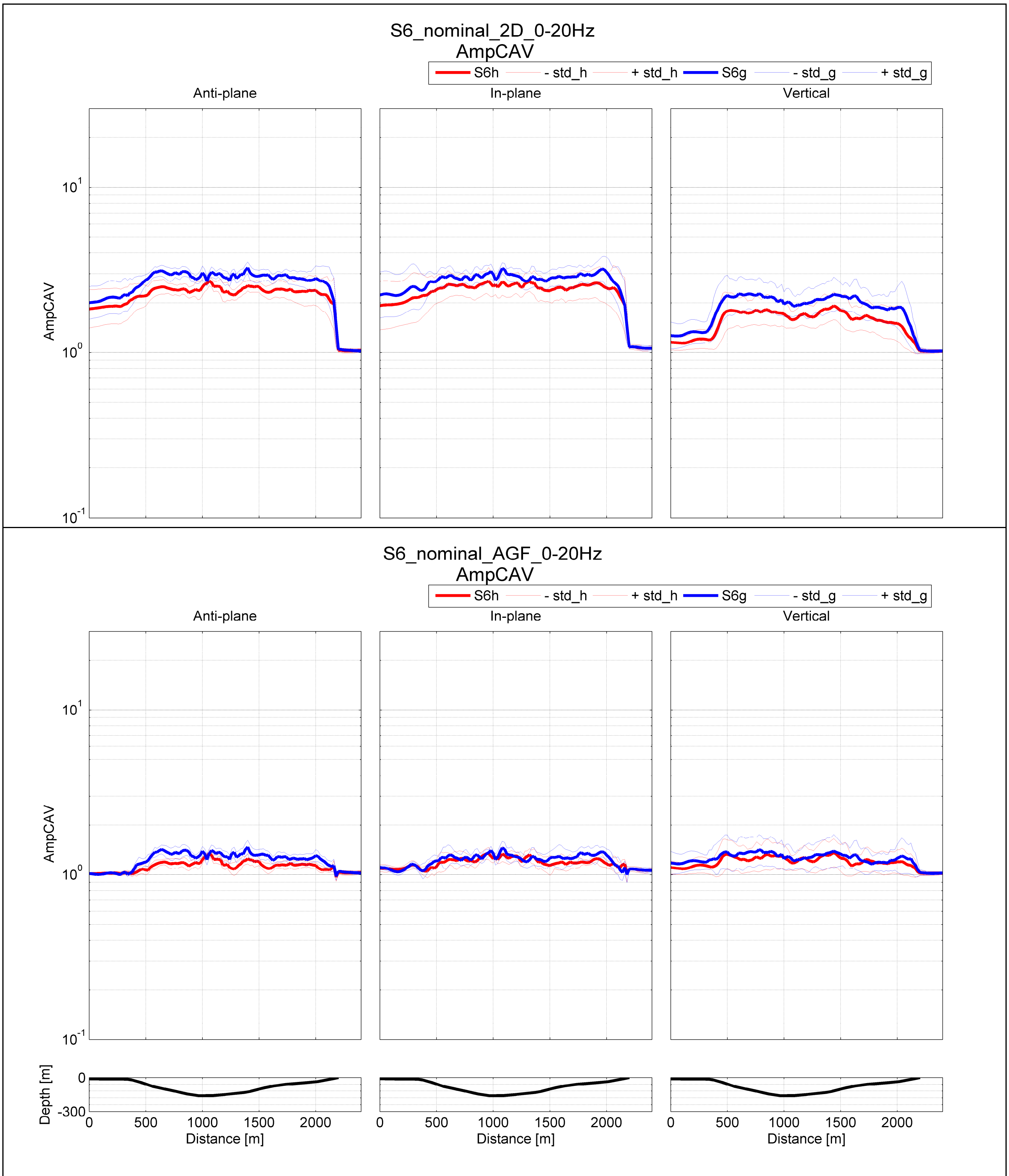

Fig. 6.4. Upper panel: CAV amplification factor from 2D simulations for Site 6. Bottom panel: CAV 2D/1D aggravation factor for Site 6.

6.3 Effect of uncertainty in attenuation

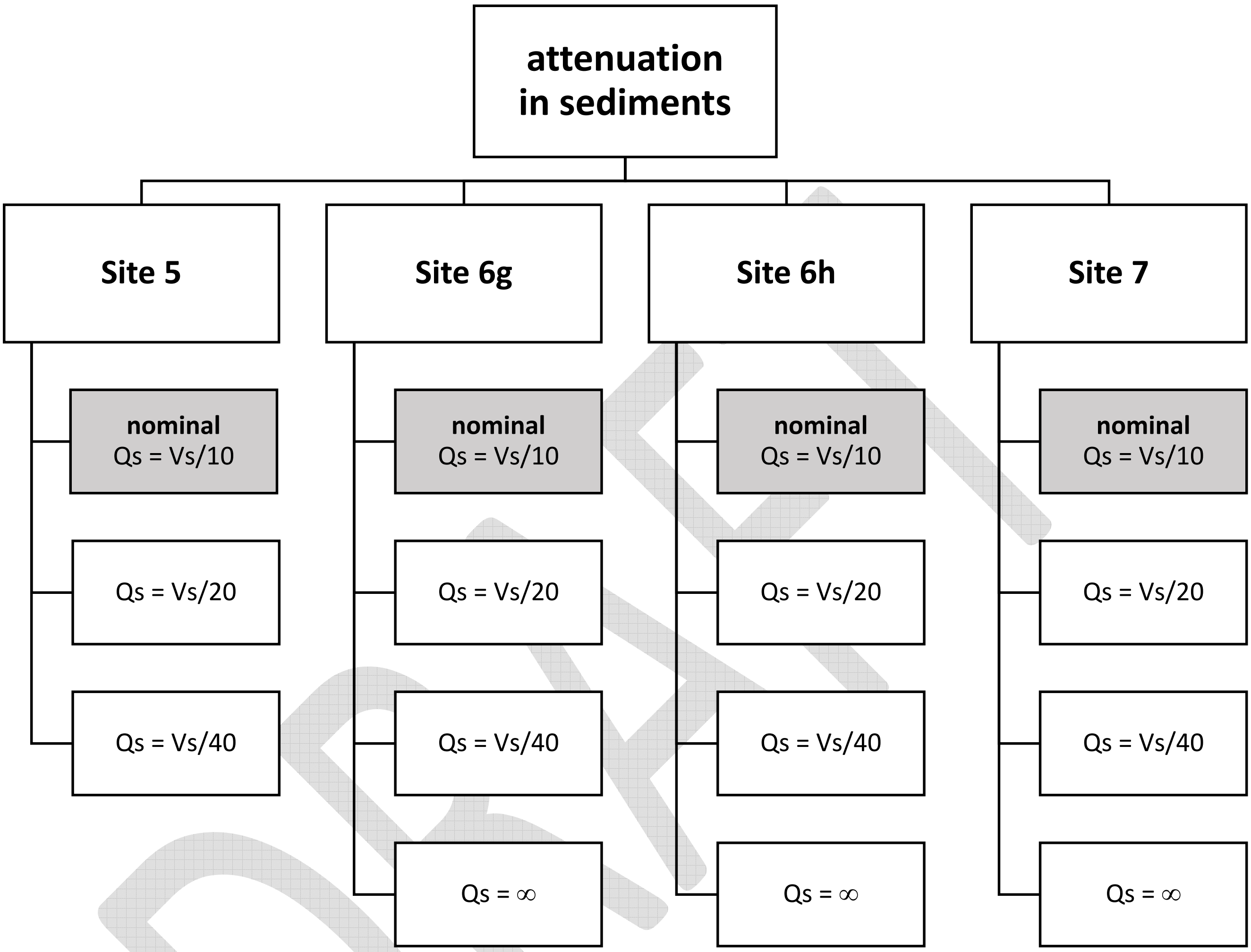

As expected, the effect of attenuation is more evident at higher frequencies. The amplification factor decreases with increasing attenuation. This effect is more pronounced with increasing local thickness of sediments. Values of EGM characteristics are unrealistically large if attenuation is neglected. The 2D/1D aggravation factor is rather insensitive to variations in the attenuation. Fig. 6.5 and Fig. 6.6 show examples for the CAV amplification and CAV 2D/1D aggravation factor, respectively.

The results suggest that the effect of attenuation on the amplification can be sufficiently estimated from 1D simulations.

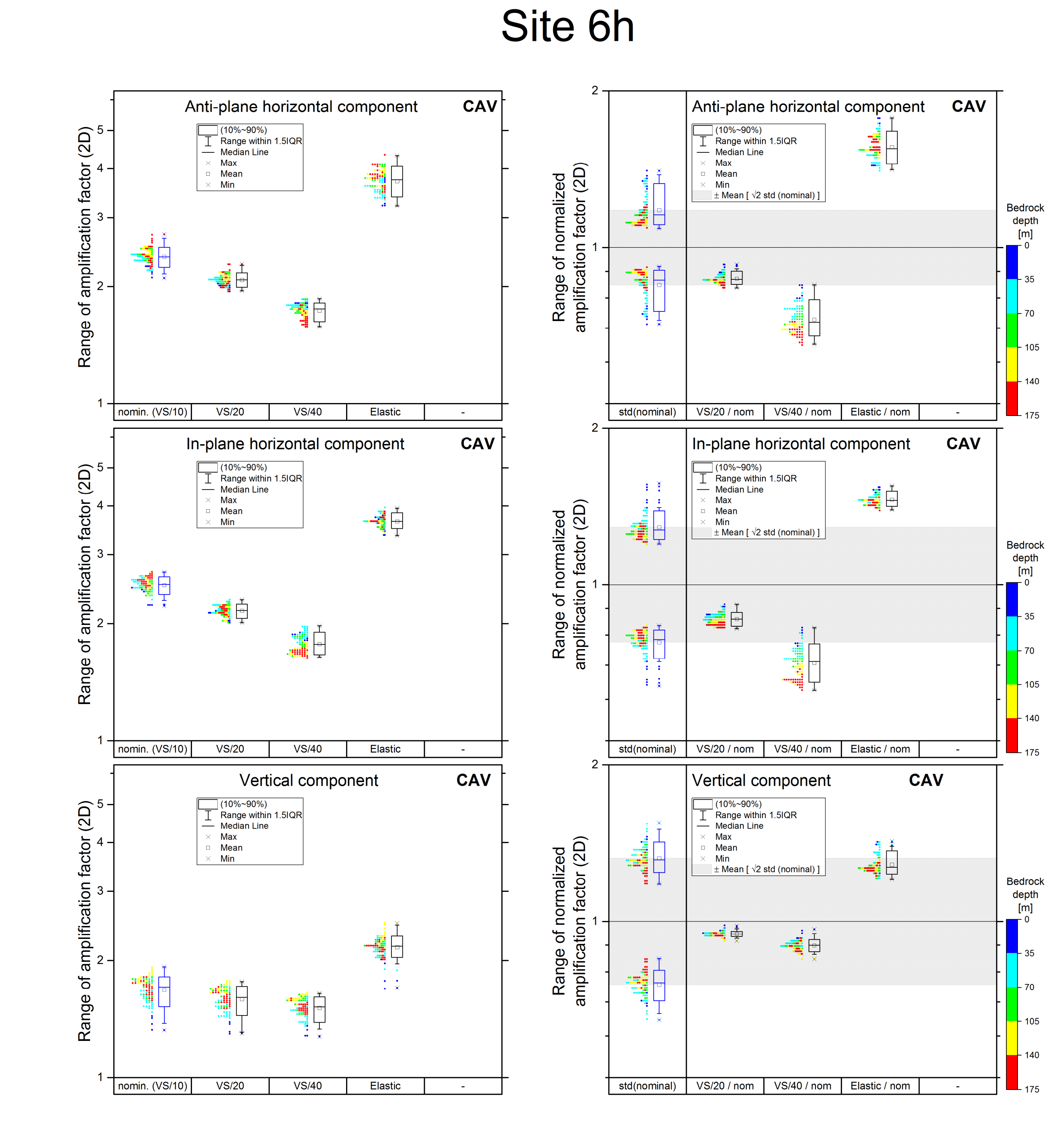

Fig. 6.5. CAV amplification factor from 2D simulations for Site 6h.

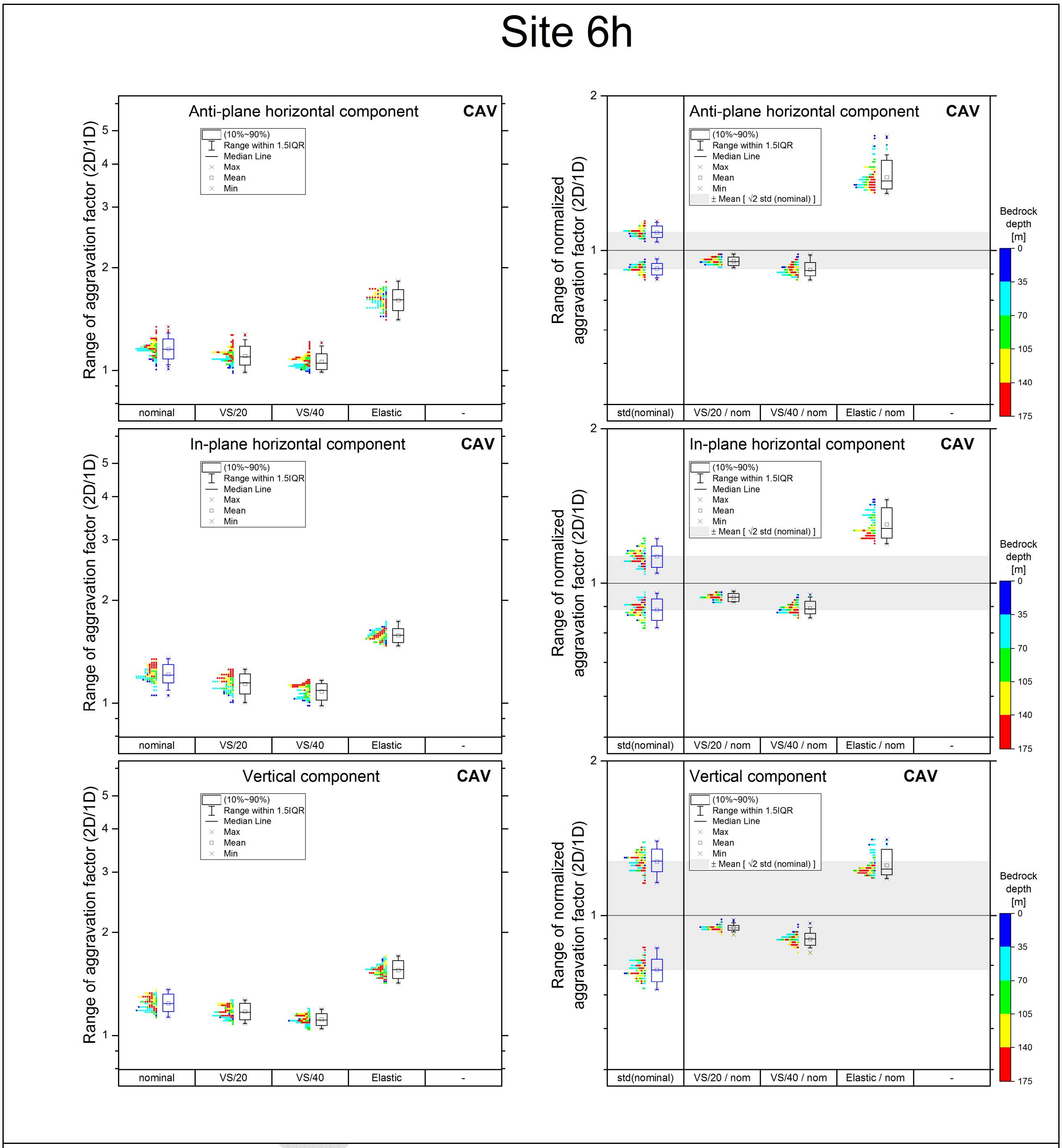

Fig. 6.6. CAV 2D/1D aggravation factor for Site 6h.

6.4 Effect of uncertainty in interface geometry

6.4.1 Effect of border slope

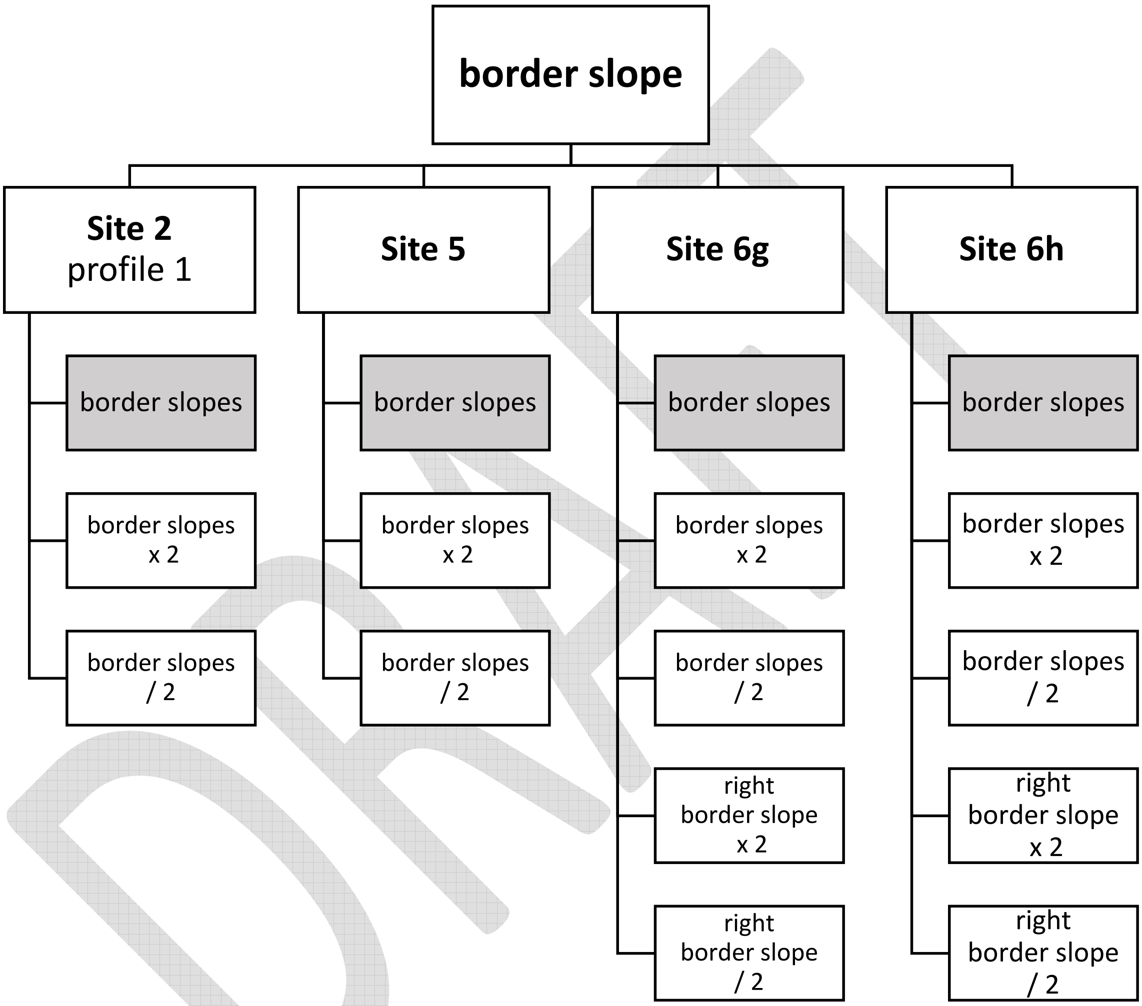

The effect of the border slope is not significant away from the border. Fig. 6.7 shows examples for the CAV amplification and 2D/1D aggravation factors for Site 6h. Note that this conclusion is consistent with that by Moczo (1989).

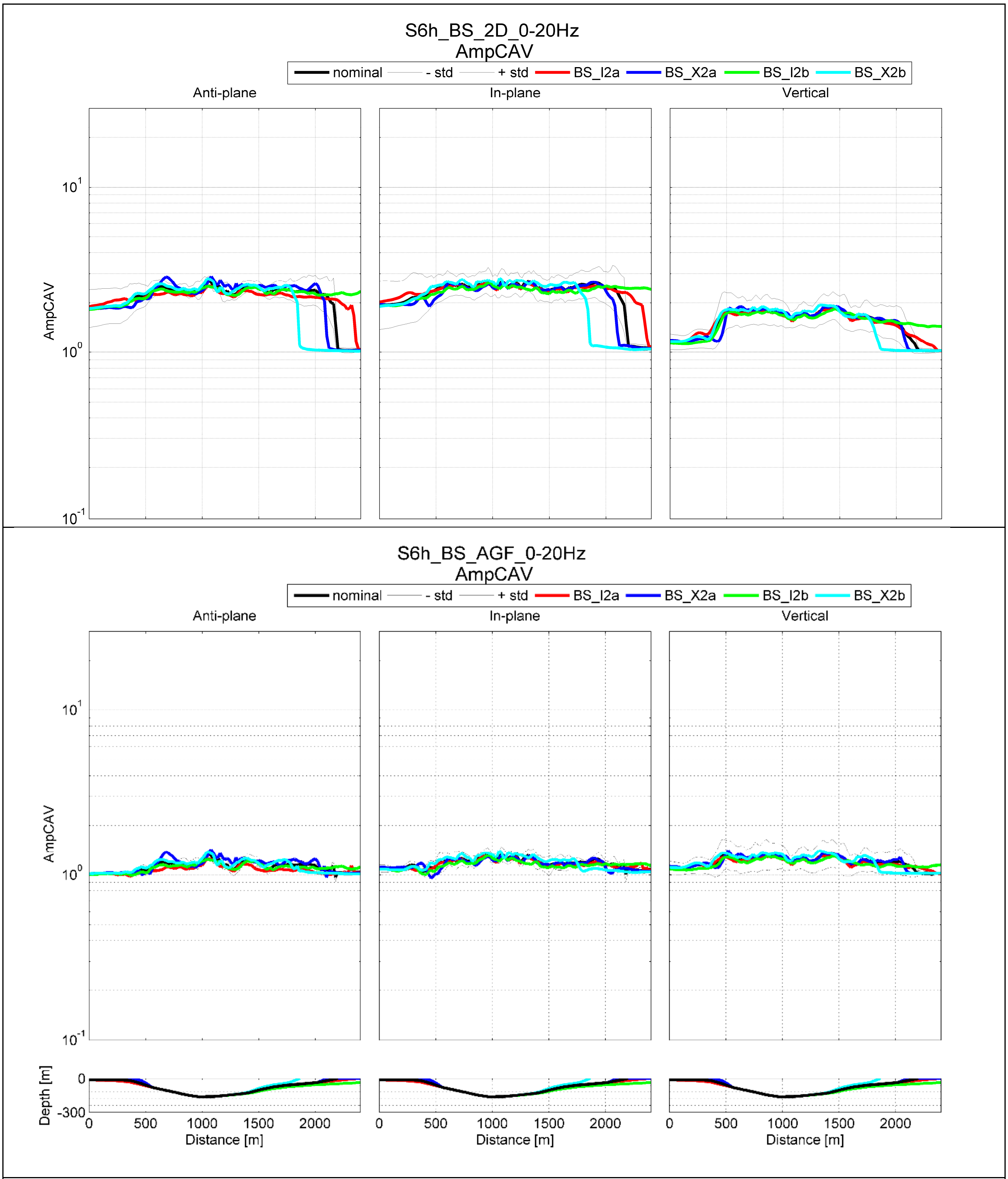

Fig. 6.7. Upper panel: CAV amplification factor from 2D simulations for Site 6h. Bottom panel: CAV 2D/1D aggravation factor for Site 6h.

6.4.2 Effect of meander

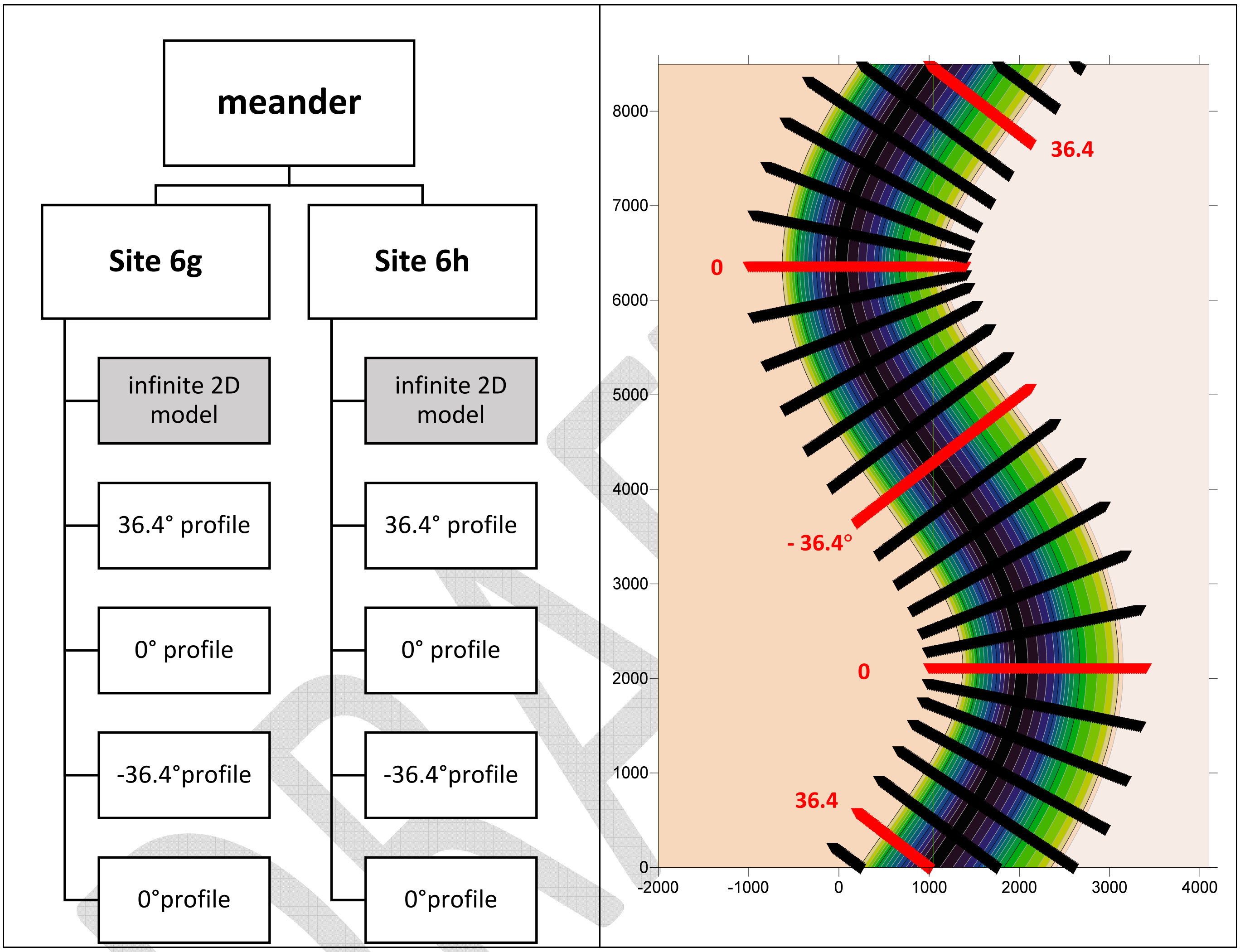

No visible effect on any EGM characteristic – for the chosen type of meander and the investigated frequency range of [0.5, 7] Hz. Fig. 6.8 and Fig. 6.9 show examples for the CAV amplification factor from 2D simulations and CAV 2D/1D aggravation factor for Site 6h, respectively.

Site 6h

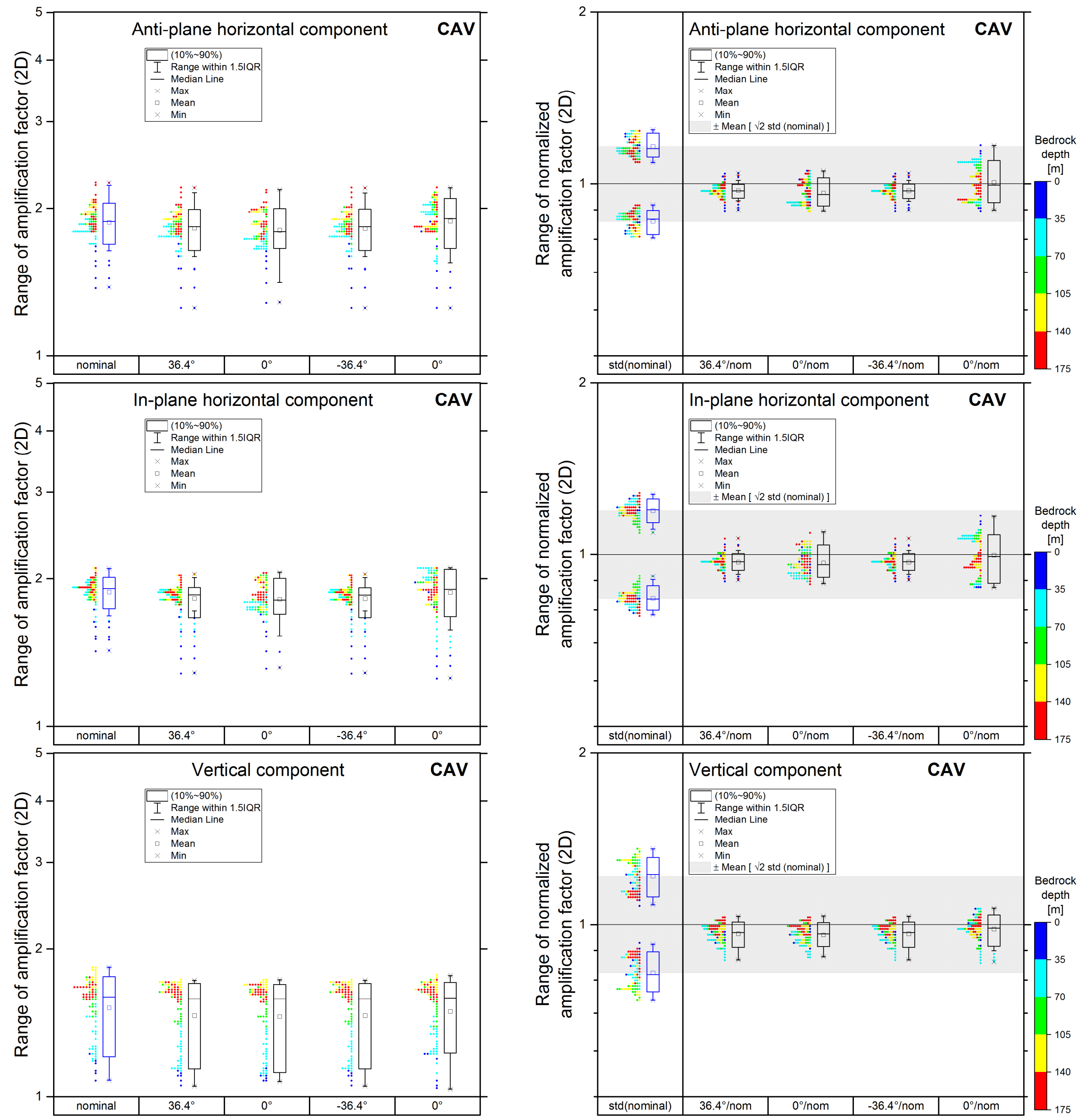

Fig. 6.8. CAV amplification factor from 2D simulations for Site 6h.

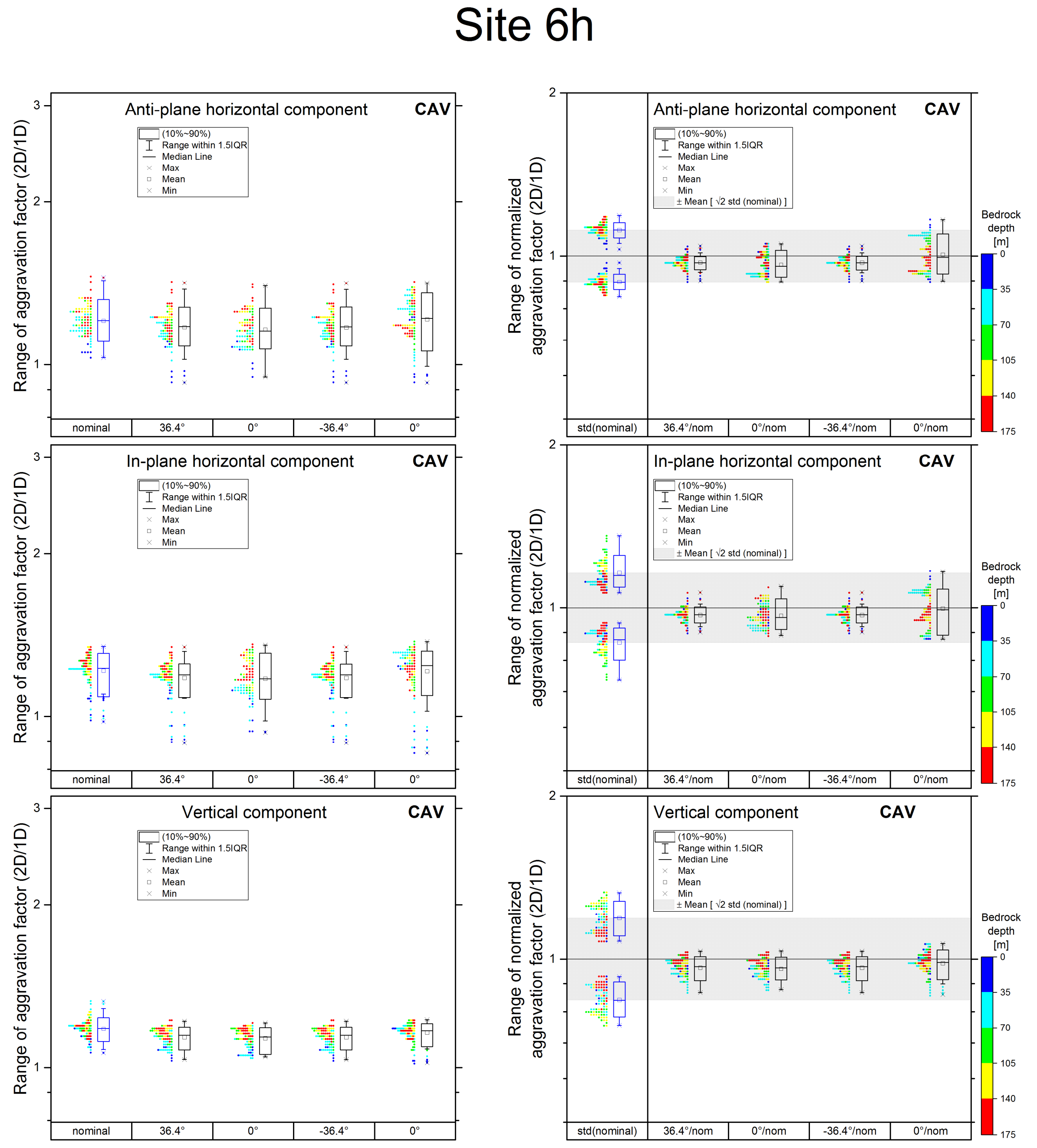

Fig. 6.9. CAV 2D/1D aggravation factor for Site 6h.

6.5 Effect of simultaneous variation in velocity and thickness of sediments

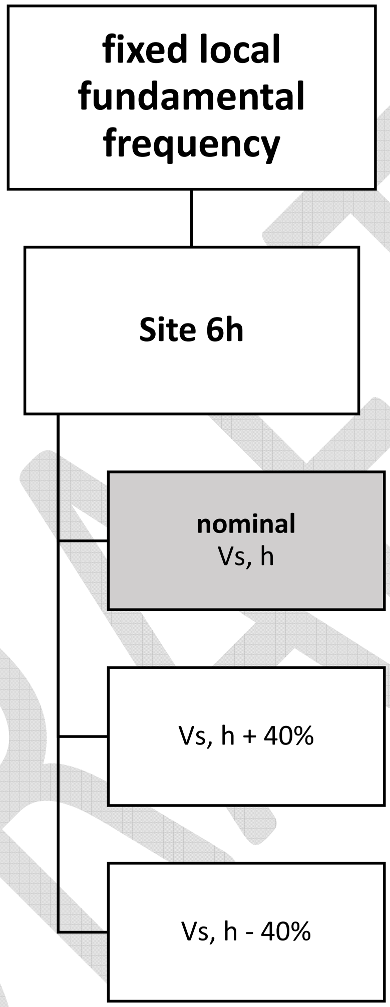

No visible effect on the vertical component due to the fact that V_P is not modified. As expected, the amplification factors, mainly FL, increase with the impedance contrast. Fig. 6.10 and Fig. 6.11 show examples of the FL amplification factor from 2D simulations and FL 2D/1D aggravation factor, respectively. The 2D/1D aggravation factors are less sensitive to modifications of V_S and h than the amplification factors. The least sensitivity is at receivers atop thin sediments.

Site 6h

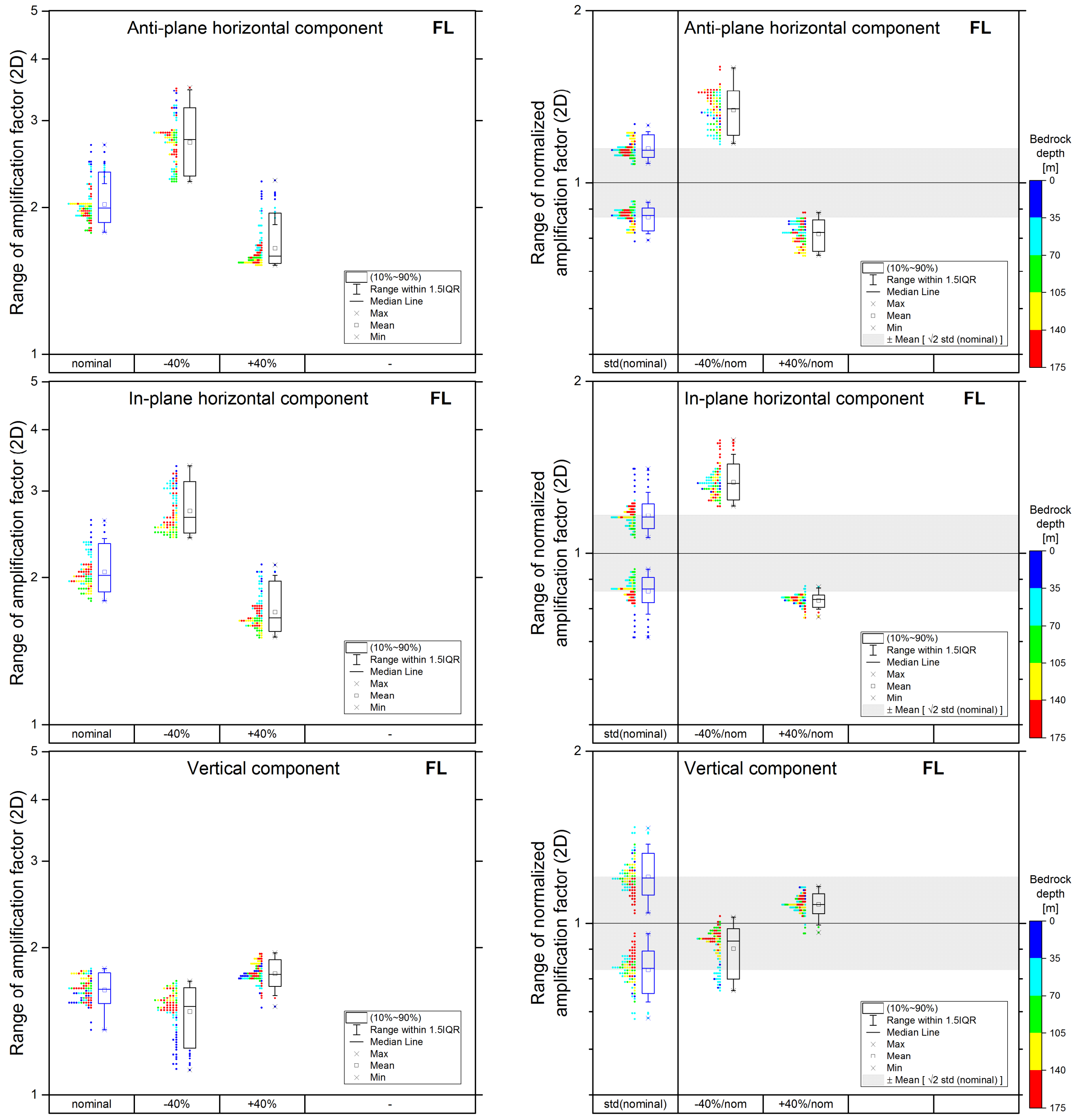

Fig. 6.10. FL amplification factor from 2D simulations for Site 6h

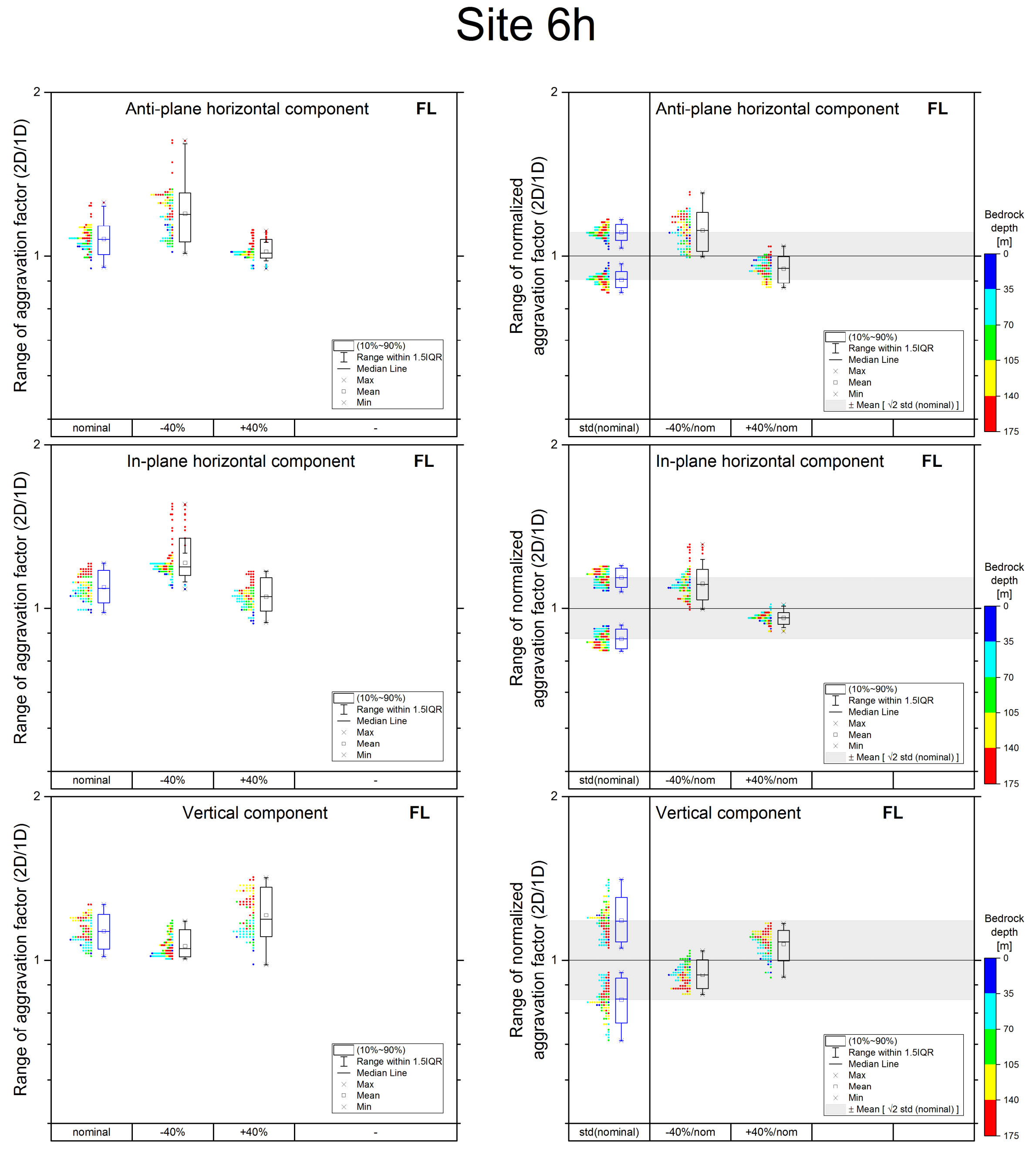

Fig. 6.11. FL 2D/1D aggravation factor for Site 6h.

6.6 Effect of excitation

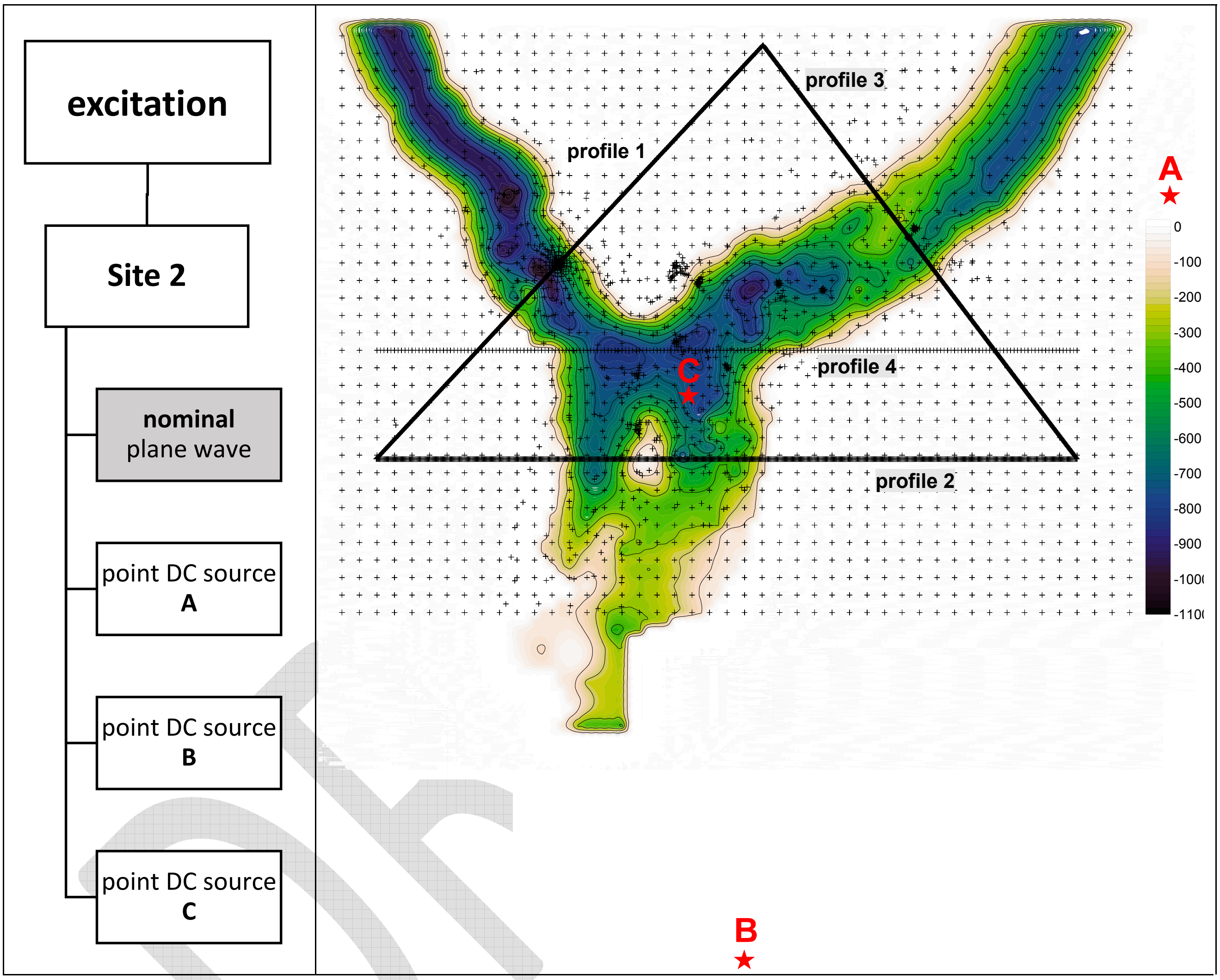

Results for the plane wave excitation may be considered a robust approximation of those for a particular point DC source. The plane-wave excitations should not, however, replace a point DC source if such a source better represents a possible excitation from a known source zone.

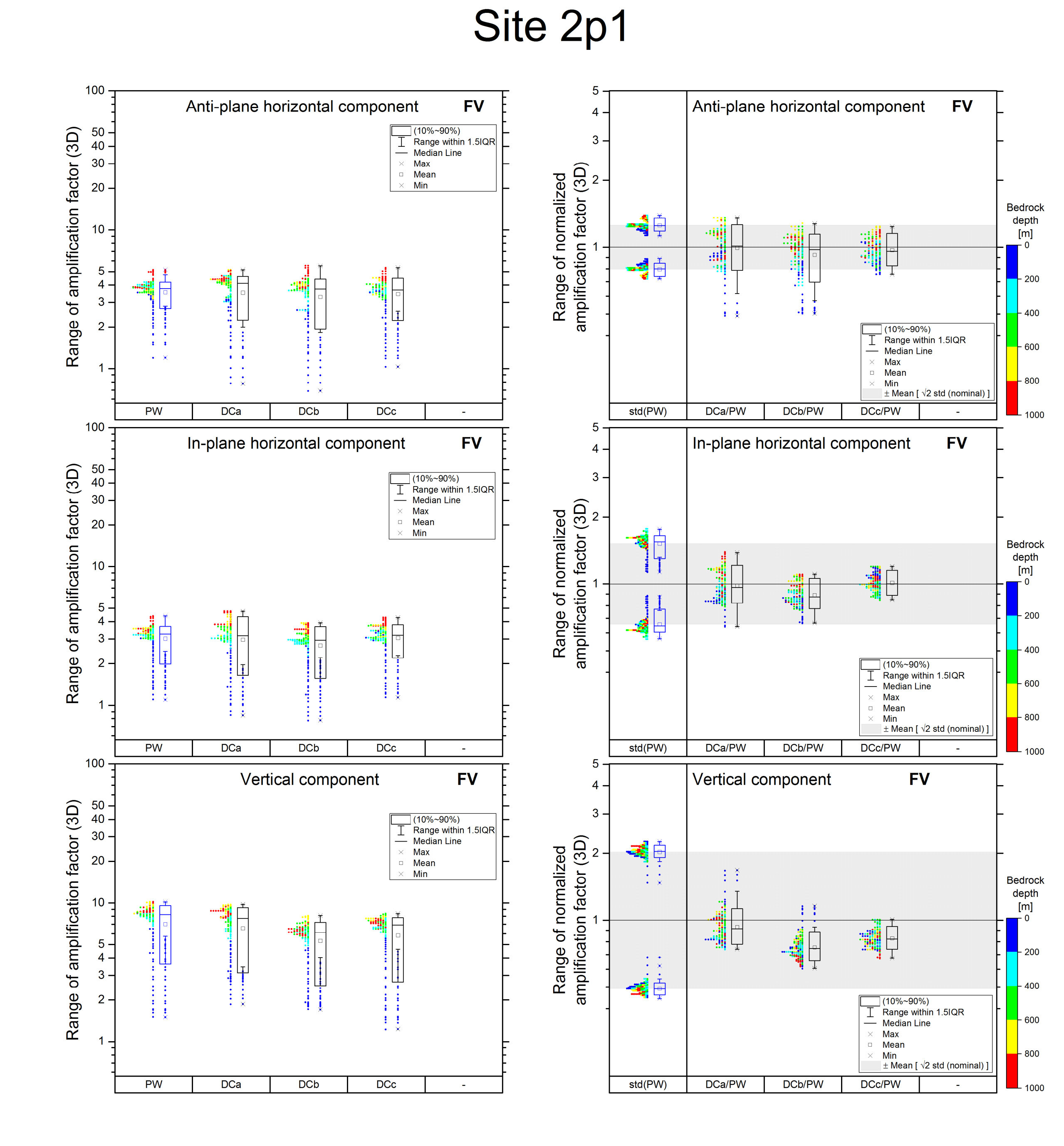

Fig. 6.12. FV amplification factor from 3D simulations for Site-2 profile 1.

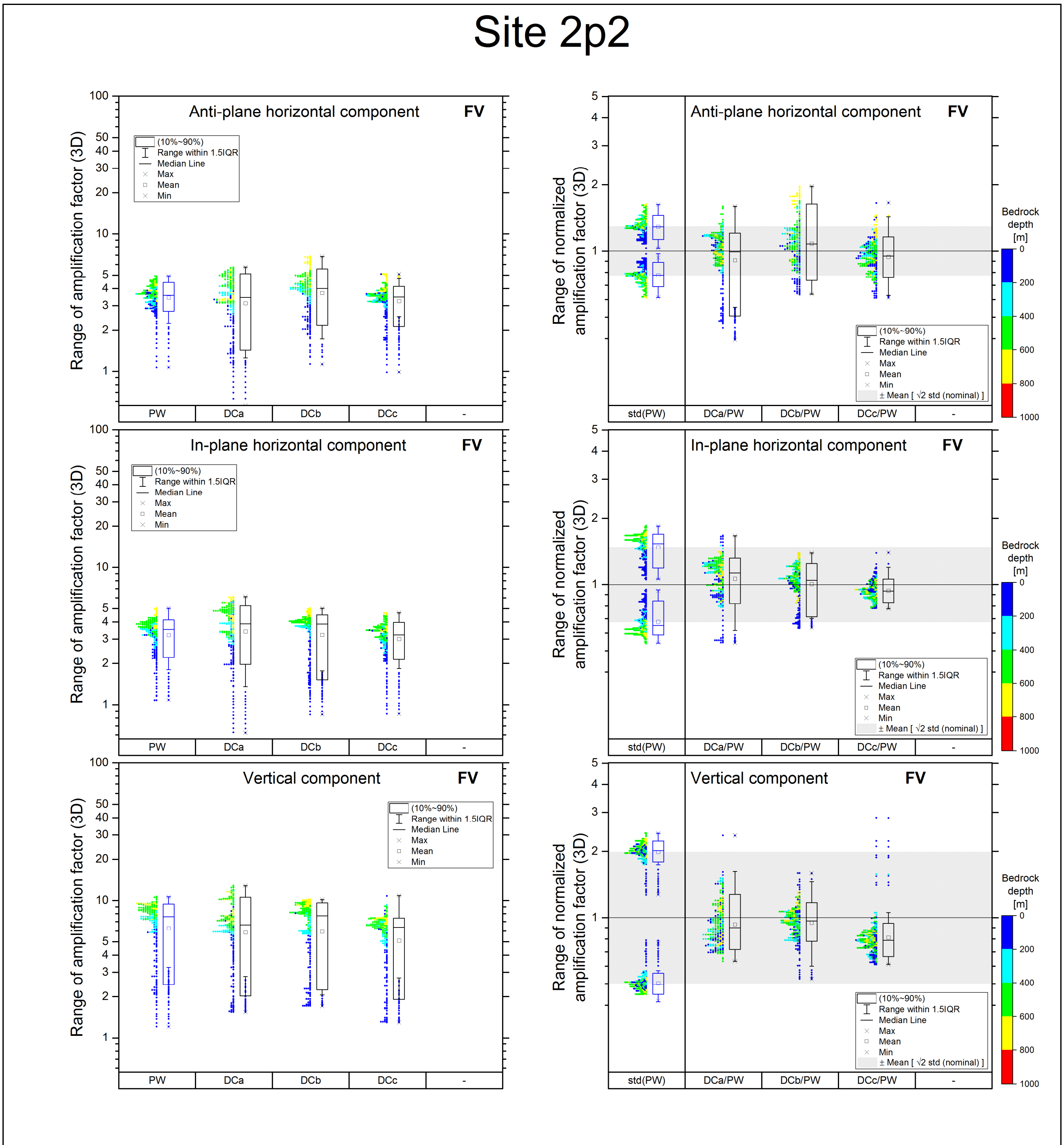

Fig. 6.13. FV amplification factor from 3D simulations for Site-2 profile 2.

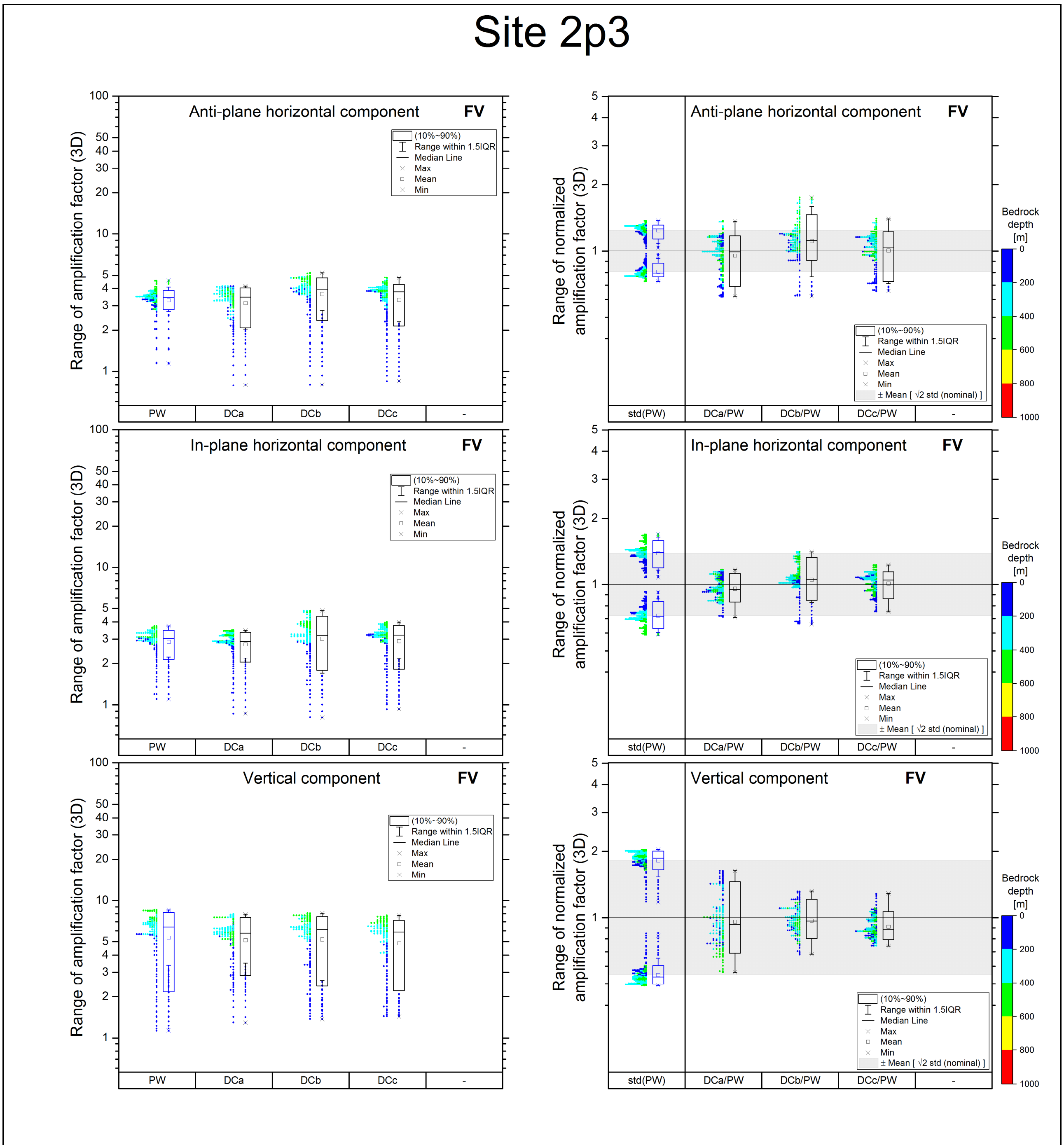

Fig. 6.14. FV amplification factor from 3D simulations for Site-2 profile 3.

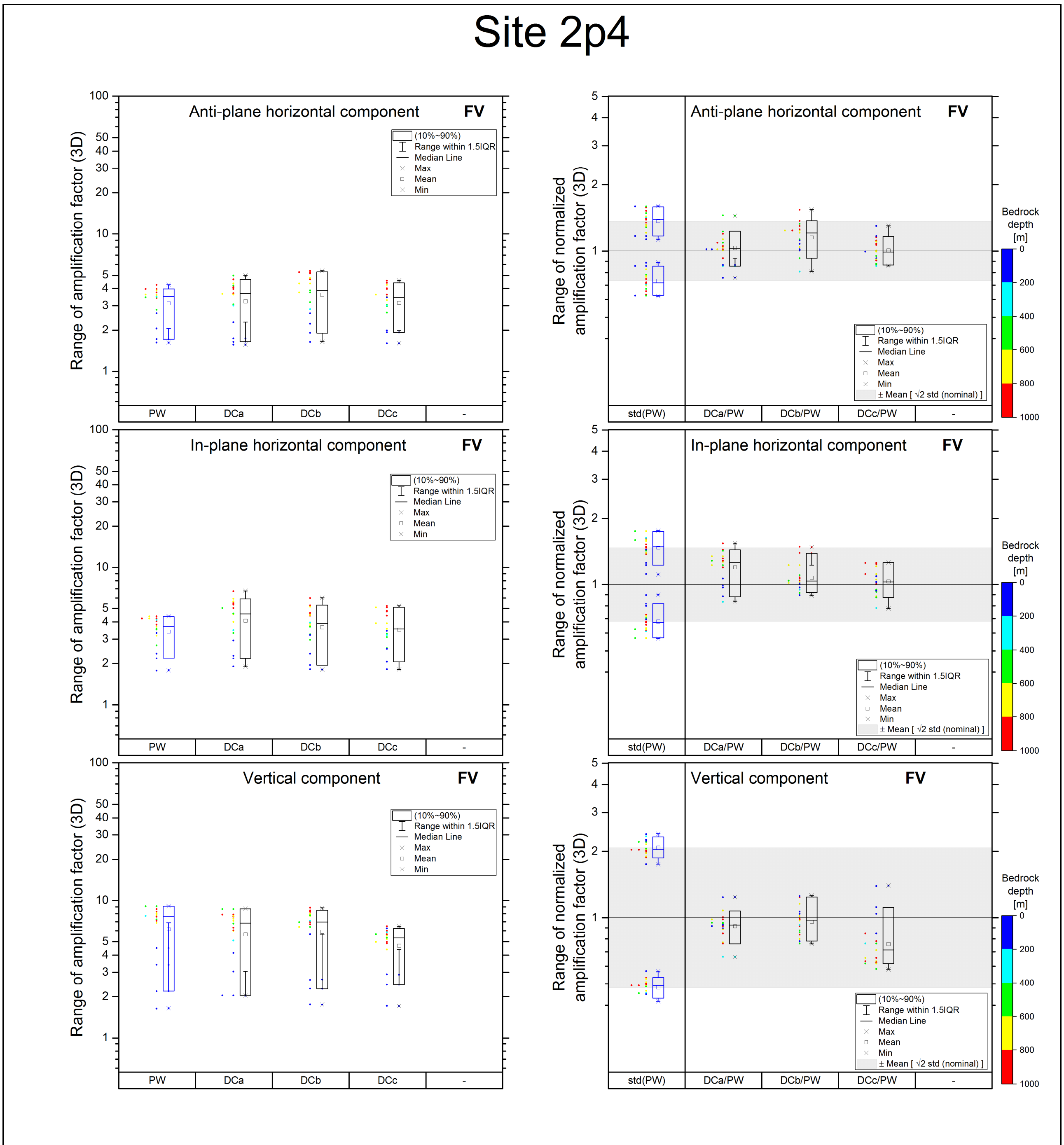

Fig. 6.15. FV amplification factor from 3D simulations for Site-2 profile 4.

7 KEY PARAMETERS FOR SITE AMPLIFICATION

Recall that we

- performed
  - 3D simulations for 3 3D structures,
  - 2D simulations for 12 2D structures (some of them being selected 2D profiles in the 3D structures),
  - 1D simulations for local 1D models in the 2D models,
- assumed a vertical plane-wave incidence for all structures,
- assumed point DC sources for one 3D structure,
- assumed a linear behaviour,
- used a set of selected reference accelerograms from the RESORCE database,
- investigated effects of uncertainty in the bedrock velocity, velocity in sediments, attenuation in sediments, interface geometry (border slope), simultaneous variations in velocity and thickness of sediments using 12 characteristics of earthquake ground motion.

The following identification of the key structural parameters is solely based on quantitative arguments (values of the aggravation and amplification factors) obtained for the considered set of structural models, assumptions and used characteristics of earthquake ground motion.

The investigation of the aggravation factors led to conclusion that 1D numerical simulations are not sufficient for estimating possible site effects (in the set of the investigated local surface sedimentary structures). This implies that the **geometry of the sediment-bedrock interface is a key parameter** of the local surface sedimentary structures. The aggravation factor can reach value even larger than 4.

For 5 of the 6 investigated sites 2D simulations seem sufficient for the robust estimation of possible site effects. However, sites similar to Site 2 (Grenoble valley), that is deep sediment-filled valleys with obvious 3D geometry of the sediment-bedrock interface and sufficiently strong impedance contrast, need 3D simulations.

More important is the overall geometry of the interface. A detailed geometry close to margins of the basin or valley affects mainly motions close to the margins.

The investigations of the effects of a) uncertainty in bedrock velocity, b) simultaneous variation in velocity and thickness of sediments, and c) uncertainty in velocity in sediments led to conclusion that both the amplification and aggravation factors (mainly for the vertical component) increase with the impedance contrast (mainly evident at frequencies close to the fundamental resonant frequency). This implies that the **impedance contrast at the sediment-bedrock interface is a key parameter** of the local surface sedimentary structures.

The investigations of the effect of uncertainty in attenuation led to conclusion that the level of attenuation considerably influences level of amplification. At the same time, the effect on amplification can be robustly estimated from 1D simulations. Omission of attenuation in sediments (that is assumption of perfect elasticity) leads to unrealistically large EGM characteristics. The effect of attenuation is more pronounced for thicker sediments. Consequently, **attenuation is a key parameter** of the local surface sedimentary structures. (It is worth noting that attenuation usually is a very poorly known parameter. It is presently most often purely guessed in a rule-of-thumb manner for numerical simulation.)

8 LINK WITH NERA: AN OUTLINE OF NERA COMPUTATIONS AND RESULTS

8.1 Summary

The NERA programme (EU Seventh Framework Programme, EC project # 262330) included a specific "Joint Research Activity" entitled "*Waveform modelling and site coefficients for basin response and topography*". Besides a component on effects associated with elevated topographies, and another one on seismic wavefield and spatial variability within alluvial valleys, it also included a huge amount of numerical simulations in order to derive "aggravation factors" quantifying the difference between 2D site response and the 1D response [the latter being supposed to be the "standard" accounted for in building codes or first level site-specific studies].

This has been achieved through the design of a comprehensive parametric study of the linear response of more than 1000 2D valleys (162 trapezoidal or triangular geometries combined with six velocity profiles involving realistic velocity gradients for both sediments and rock, plus 32 similar geometries combined with 3 different homogeneous velocity profiles). The valley width range from 500 m to 20 km, the sediment thickness from 30 m to 1 km, V_{S30} values from 125 m/s to 500 m/s, and velocity contrast at depth from 1.5 to 8. The 2D response has been computed for at least 100 surface receivers under vertical incidence of pulse-like SH and SV waves, and later convolved with 10 to 20 real input accelerograms. These computations were performed with the various modelling techniques and codes available with the consortium: Finite Difference, Finite Element, and Spectral Element, in the linear case and for some cases taking into account the soil non-linearities. It was thus necessary to start with a "verification" exercise to ensure that all codes provide the same results when applied to the same case.

The results are described first in terms of average "amplification factors AF" (average ratio of output response spectrum to input response spectrum for various realistic input signals), and ultimately in terms of 2D/1D "aggravation factors AGF" quantifying the additional effect of the 2D geometry by comparing the 2F AF to the 1D AF (taking into account only the local vertical soil column). These AGF are found in the range 1.3 – 2 in most cases, with a maximum generally near the valley edges and sometimes in the centre of embanked valleys, while they also often exhibit some deamplification (AGF values smaller than 1) on the very edges of valleys (over dipping sediment-basement interface). The largest aggravation factors correspond to large velocity contrasts, embanked valleys, and are located either in valley centres (mainly for embanked or small size valleys), or on the lateral edges of the central, constant thickness central part. Gently sloping edges have long distance effects, while steeply sloping edges have mainly local effects.

Contributors: *ISTerre: P.-Y. Bard, E. Chaljub, C. Durand*; *CUB: P. Moczo, J. Kristek, S. Stripajova*

Project: NERA, EC project number: 262330, WP11: *Waveform modelling and site coefficients for basin response and topography*

8.2 Introduction

Alluvial valleys or basins are characterized by lateral thickness variations which have been shown to generate peculiar wave propagation phenomena (diffraction of surface waves, possible focusing of body waves, vertical and lateral reverberations) leading to increased wave trapping and interferences, and significant differences (increased duration,; generally overamplification, sometimes deamplification) with respect to the case of horizontally stratified layers ("1D soil columns").

Such effects have been qualitatively predicted by theory for about 3-4 decades, and have been actually observed in real recordings or damage distribution (for instance in Kobe in 1995). However, they are only very rarely accounted for even in site-specific studies, because of a) the cost of the required geophysical surveys to constrain geo-mechanical characteristics of the underground structure not only underneath but also around the target site, b) the insufficient number of well-documented observations that prevents any statistical treatment for a purely empirical prediction, and c) the lack of comprehensive enough parameter study that would allow to identify the key controlling parameters and to quantify their effects.

This was explicitly the goal of this task to take advantage in the recent improvements in computing facilities, software accuracy and storage capacity, to perform a large number of computations for a wide variety of geometrical characteristics, velocity contrasts, and receiver locations within the valley, in order to derive statistically meaningful relationships describing the gross dependence of the amplification on the main site "meta-parameters".

The routine engineering practice to account for effects of subsurface conditions is either to consider the building code provisions based on site classification and the associated pre-defined spectral shapes (most often derived as a function of the "V_{S30}" parameter), or to perform 1D site response studies taking into account the local soil column. Both approaches have in common to be based only on the local soil structure, i.e. implicitly assuming a 1D site response. Therefore, in order to be consistent with the usual practice and to propose the simplest possible procedures to account for subsurface geometry effects, it was decided to quantify their effects only in terms of "aggravation factors" (Chávez-García and Faccioli 2000; Chávez-García 2007) describing the ratio between 2D (or 3D) and 1D amplifications for a variety of representative ground motion parameters.

This section will successively describe the overall work flow adopted in that aim (section 2), and the actual, complementary computations performed by the two partners which were simultaneously involved in this NERA JRA1 Task and the SIGMA WP3, i.e. ISTerre and CUB.

8.3 Work Organization

8.3.1 General flow-chart

The basic idea and goal is to quantify the changes in amplification (increase = overamplification, or decrease = deamplification) compared to the 1D case. In that aim, the work was divided in the successive steps listed below:

a) Selection of the models to be computed : geometry, mechanical characteristics, incident wavefield
b) Selection of a representative number of input accelerograms
c) Selection of the (surface) receivers where to compute the resulting motion
d) Selection of the ground motion parameters for which should be computed the 2D/1D aggravation factors
e) Selection and checks of the numerical simulation software
f) Computations for all the considered cases of the time-domain response for a simple, pulse-like, short-duration signals, in both 2D and 1D cases for each receiver
g) Linear convolution of the pulse response at each receiver l or each valley j with the selected input accelerograms i and derivation of the aggravation factor AGF for each considered ground motion parameter GMP_k: $AGF(R_{ljki}) = GMP_k\text{-}2D(R_{lji}) / GMP_k\text{-}1D(R_{lji})$
h) Averaging these aggravation factors over all the considered input accelerorgams to derive a mean aggravation factor $AGF_m(R_{ljk})$

i) Using statistical tools to correlate $AGF_m(R_{ljk})$ to valley geometrical (width, thickness, etc.) and mechanical (velocity profile) characteristics, and also receiver location at valley surface

This procedure is valid only for a linear response; however, non-linear computations were NOT considered by ISTerre and CUB; they actually were by some NERA partners (Aristotles University of Thessaloniki) for a limited number of geometries and material properties, who replaced steps (f) and (g) by a direct computation of the response to the selected input accelerogram scaled to a given pga level. Step (h) was indeed applied only to accelerograms with similar pgas, and the statistical tools of step i) should then include pga as an explanatory variable.

The subsections below describe in more detail the implementation of the preparatory steps (a) to (d) for the computations performed by ISTerre and CUB.

8.3.2 Model selection

8.3.2.1 Geometry

After discussion in the first year f the project, it was decided to consider a set of trapezoidal and triangular valleys with a broad range of thickness and widths, and various slope angles on each edge, as indicated in Fig. 8.1.

More specifically,

- 6 values are considered for valley width W from 500 m to 20 km
- 6 values are considered for valley maximum thickness H, from 30 m to 1 km
- 6 sets are considered for slope angles: 4 symmetrical cases with edge slope angles equal to 10°, 20°, 45° and 65°, and two non-symmetrical cases with one edge angle at 10°, and the other edge at 45° or 65°

In total, this resulted in 162 geometries, as only 27 (H, W) combinations were considered as indicated in Fig. 8.1. Out of them, 131 have a trapezoidal shape, and 31 a triangular shape with a maximum thickness lower than or equal to the H value.

The advantages of such a geometry and parameter set are that it is simple, while it allows to investigate the effect of the thickness/width "shape ratio" and of the sloping angles on each edge; in addition, a quick survey of the available cross-sections indicated that it is not uncommon to have triangular shapes with some dissymmetry.

Geometry of 2D valleys

- Trapezoidal or triangular shape
- Control parameters: H, W, α_1, α_2

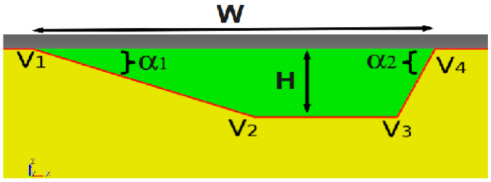

h(m) \ w (km)	0.5	1	2.5	5	10	20
30	0.06	0.03	0.012	-	-	-
60	0.12	0.06	0.024	0.012	-	-
120	0.24	0.12	0.048	0.024	0.012	-
250	0.5	0.25	0.1	0.05	0.025	0.0125
500	-	0.5	0.2	0.1	0.05	0.025
1000	-	-	0.4	0.2	0.1	0.05

27 (H,W) combinations * 6 (α_1, α_2) combinations = 162 geometries
31 with triangular shape, 131 with trapezoidal shape

Fig. 8.1. Geometry of the trapezoidal and triangular valleys considered.

8.3.2.2 Mechanical characteristics

Considering the large thickness values, velocity profiles with a velocity gradient were considered more realistic. Their functional form is provided in Fig. 8.2: it is controlled by the velocity at surface V_{S0} et at a 1 km depth V_{S1}, and the exponent describing the depth dependence: a value of 0.5 was consider reasonable. The values at surface and depth were then tuned to have V_{S30} values providing integer velocity contrast with the underlying bedrock, which was considered homogeneous with a constant S-wave velocity equal to 1 km/s. The bedrock / sediment surface velocity contrast thus ranges from 2 to 8 (2, 3, 4, 5, 6 and 8). The total number of considered geomechanical cases was thus 972.

The damping was tuned to the velocity with the "rule-of-thumb" relation $Q_S = V_S/10$ (i.e., the damping $\varsigma = 0.5/Q_S$ is decreasing with increasing depth.

The unit mass was taken as linearly related to the S-wave velocity through the relationship unit mass $\rho(z) = 1600 + 0.6\,(V_S(z) - 100)$ in the sediments, and $\rho_b = 2500$ kg/m^3.

The P-wave velocity was taken equal to 1.5 km/s in the sediments (considered as water saturated), and 2 km/s in the bedrock.

The quality factor for P-waves was taken according to the following formula:

$Q_P(z) = \mathrm{Min}\,(2{*}Q_S(z), V_P(z)/10)$

In addition, it was decided to perform some sensitivity tests to investigate more specifically the effects of damping, incidence angle, non-linear behaviour, and bedrock velocity.

8.3.3 Input wavefield and accelerograms

The seismic excitation has been basically defined as vertically incident plane S-waves, in order to provide a meaningful comparison with respect with the routine 1D analysis. The motion may be in-plane (incident "SV" waves) or out-of-plane (incident "SH" waves).

A sensitivity analysis was performed however in one case to investigate the changes in case on obliquely incident plane waves.

As the aggravation factors are looked for on several ground motion parameters (peak values, response spectra, duration, etc., see below) that are not related linearly with their analogue on input motion, it is needed to considered several realistic input accelerograms, in order to get robust estimates on the corresponding average aggravation factors. The option in AUTH has been to select 9 input accelrograms corresponding to events with magnitude ranging from 5.6 to 7.3, distance from 3 to 30 km, and various faulting mechanisms. The option in ISTerre was to select accelerograms on the basis of their frequency contents, as it has been shown in previous studies that the amplification factors of response spectral ordinates do vary as a function of the frequency contents: their spectra are illustrated in Fig. 8.3.

Mechanical properties

- $VS(z) = VS_0 + (VS_1 - VS_0)\,[(z - z_0)/(z_1 - z_0)]^{0.5}$, z_0=0 m, z_1=1000 m

	1	2	3	4	5	6
VS_0 (m/s)	80	100	120	160	247	434
VS_1 (m/s)	480	700	835	950	1000	1000
VS_{30} (m/s)	**125**	**167**	**200**	**250**	**333**	**500**

162 geometries * 6 velocity models = 972 valleys

Computation of P-SV and SH response to vertically incident plane wave = 1944 simulations in 2D

Fig. 8.2. Velocity profiles considered for the valley sediments.

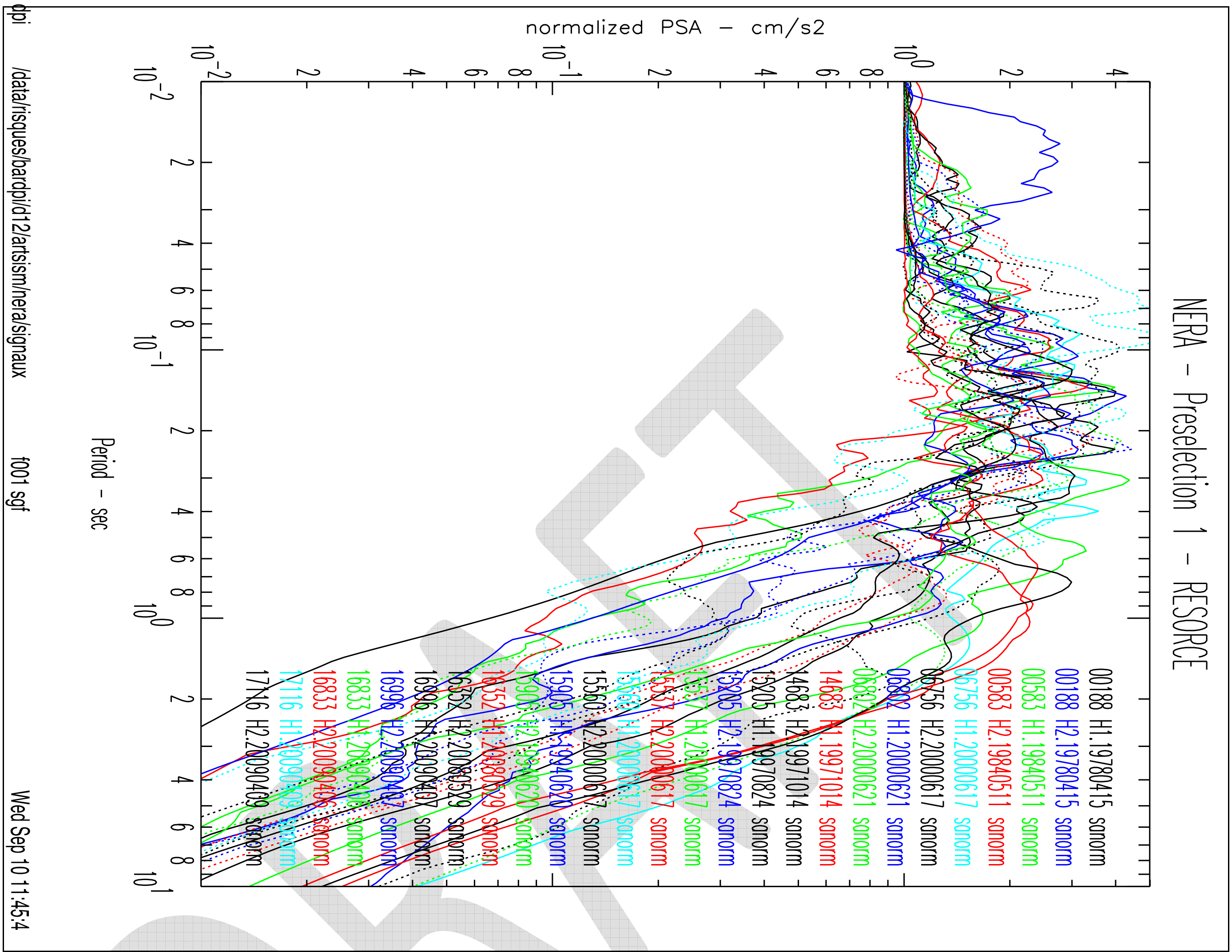

Fig. 8.3. Normalized response spectra of the input accelerograms considered by ISTErre/CUB.

8.3.4 Surface receivers

The ground motion has been computed at a minimum of 101 receivers within the valley, with a maximum spacing of 50 m : for valleys having a width smaller than 5km, the receiver spacing thus ranges from 5 m (w = 500 m) to 50 m (w= 5 km), and for valleys wider than 5 km (i.e., 10 or 20 km wide), the number of surface receivers was extended to 200 and 400, respectively.

10 additional receivers have been considered on each side, on the outcropping bedrock, with a spacing equal to w/20 (i.e., from 25 m to 1000 m, over distances from 125 m to 5 km), as displayed on Fig. 8.4.

Definition of surface receivers

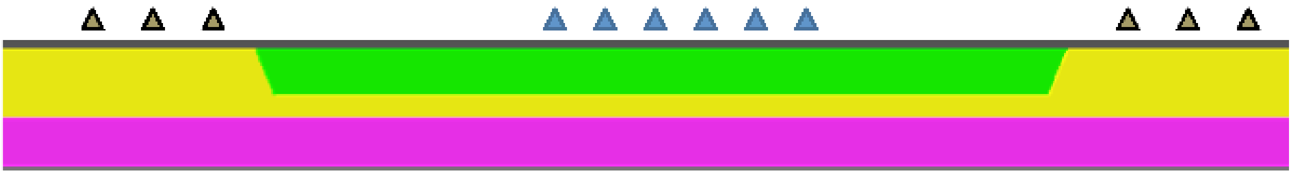

Within the Valley
Constant inter-receiver distance = **Δ<50 m**
Maximum # of receivers = **nrec**

W	Δ	nrec
250 m – 5000 m	W/100	101
10000 m	50 m (= W/200)	201
20000 m	50 m (= W/400)	401

Outside the Valley
Constant inter-receiver distance: **Δ =W/20**
Constant # of receivers = **10** (5 each side)

Total number of receivers (all simulations) = 154 692

Fig. 8.4. Location of the surface receivers for the investigated geometries.

8.3.5 Ground motion intensity parameters

The main ground motion intensity parameter (GMIP) considered in all analysis (ISTerre/CUB) was the acceleration spectra at a suite of periods / frequencies. Some additional, mainly scalar, GMIP were also systematically computed:

- Peak time domain values (pga, pgv)
- Short period [Fa, around 0.1 s : average in the range 0.05 – 0.2 s] and intermediate period [Fv, around 1 s: average in the range 0.5 – 2 s] amplification factors
- Spectral intensity SI [average in the range 0.10 – 2.5 s], Cumulative Absolute Velocity (CAV), Arias Intensity I_A, root mean square acceleration a_{rms}, and Trifunac-Brady duration D_{TB}. (5-95 % and 5-75 %)

8.3.6 Verification

Different codes were used for sharing the computational work:

- ISTerre : Spectral Element Method (SEM)
- CUB : Finite Difference Method

Given our previous experience in this field (Tsuno et al. 2009; Chaljub et al. 2010, 2015), they were thus verified (compared to each other) on a few of the considered geometries and velocity contrasts.

These specific verification cases were a small size, symmetrical valley (w = 500 m, h = 100 m, $\alpha_1 = \alpha_2 = 45°$), and an intermediate size, asymmetrical trapezoidal valley (w=2.5km, h = 500 m, α_1 = 20° ; α_2 = 65°; soft soil). Its response was to be computed for vertically incident SH and SV waves, with or without damping. Some results of such a comparison are displayed in Fig. 8.5, Fig. 8.6 and Fig. 8.7 for the comparison between Finite Difference (FDM) and Spectral Element (SEM) codes on the intermediate size valley case.

As mentioned in Chaljub et al. (2015), important issues are the proper implementation of damping – which is actually the case for the 2 codes used SEM and FDM -, and the proper meshing near the sharp discontinuities.

These verification steps proved to be useful in improving the implementation of damping in the SEM code, and refining the meshing so as to ensure an extremely good fit between SEM and FDM results.

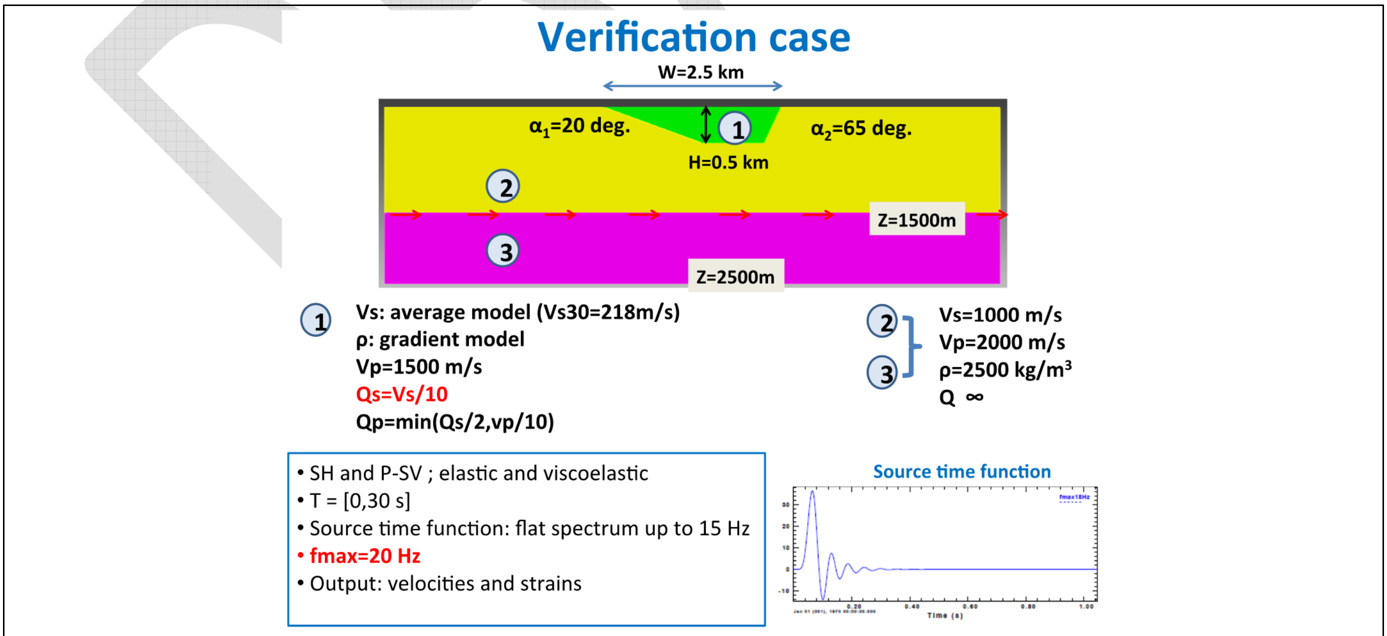

Fig. 8.5. Example of verification cases, intermediate size, asymmetrical trapezoidal valley.

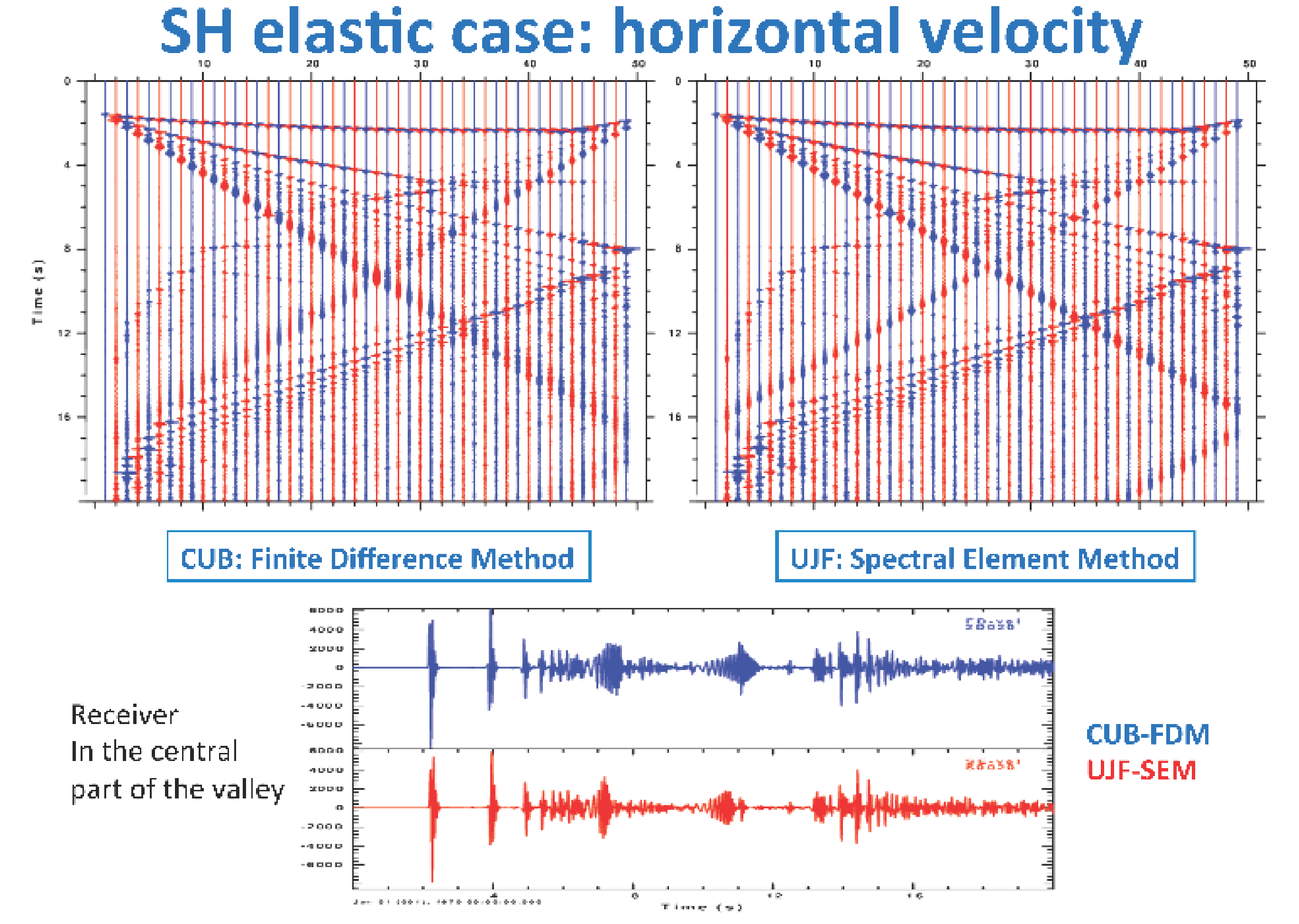

Fig. 8.6. Example comparison between FDM (blue) and SEM(red) for the intermediate size, asymmetrical trapezoidal valley in the elastic case (no damping) for vertically incident SH waves

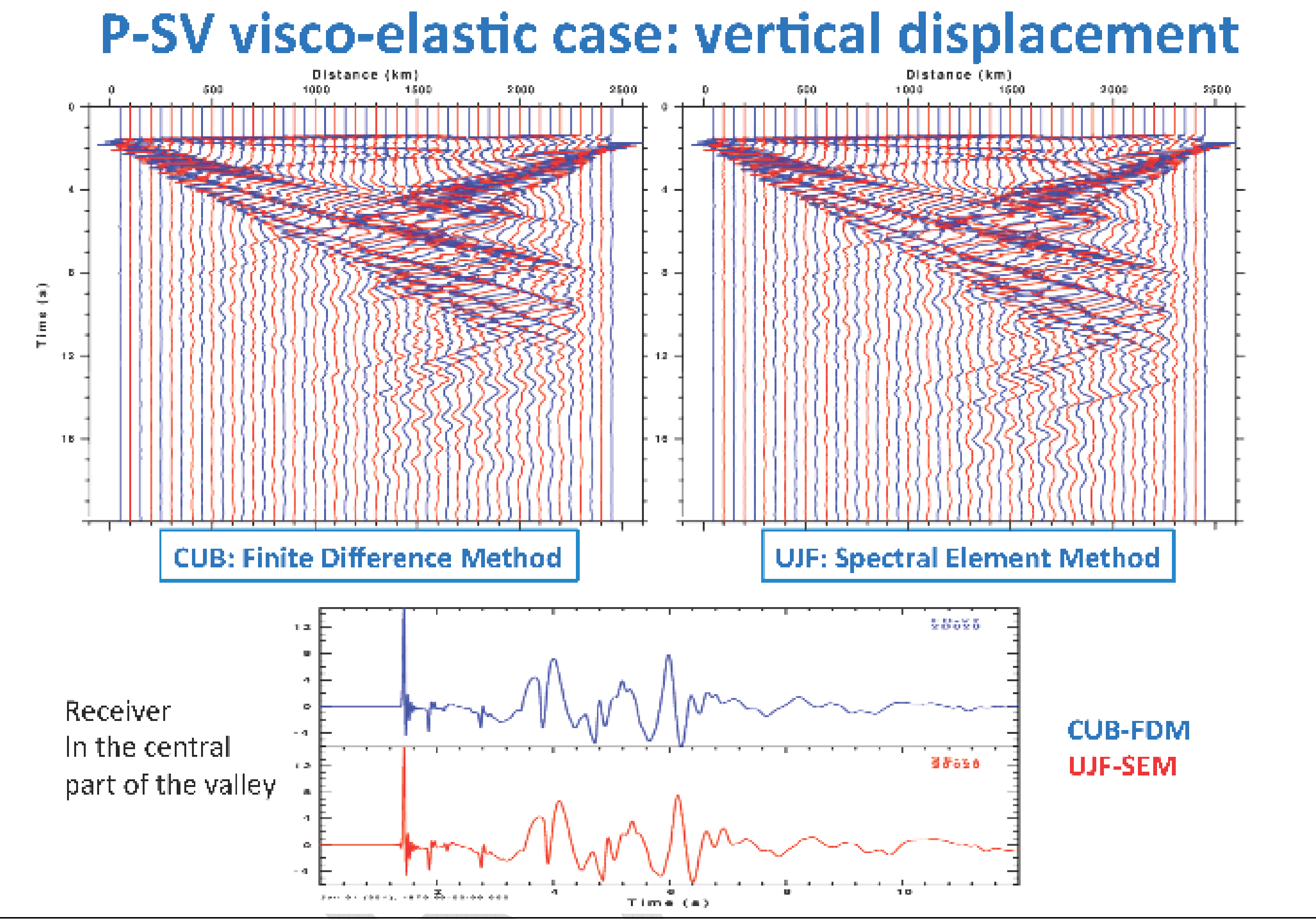

Fig. 8.7. Example comparison between FDM (blue) and SEM(red) for the intermediate size, asymmetrical trapezoidal valley in the viscoelastic case (with damping) for vertically incident SV waves

8.3.7 Indications on numerical issues

Only linear computations were performed, but on a total of 1956 cases. The work was shared between ISTerre and CUB: ISTerre performed the comprehensive simulations for 1944 cases listed on Fig. 8.1 and Fig. 8.2 on their grid computers, while CUB performed the sensitivity studies and the post-processing to derive aggravation factors for the various ground motion intensity parameters mentioned in section 8.3.5, including all the 1D response computations for all the receivers in view of deriving the 2D/1D aggravation factors (3600 different soil columns in total).

The computations were designed to be accurate up to a frequency of 15 Hz, so as to include the whole frequency range of interest in earthquake engineering.

23 one-component input accolerograms were considered to derive average aggravation factors for each receiver (i.e., a total of 154 692 surface receivers).

The next section provides some hints on the numerical difficulties of the considered cases, and the volume of computations

8.3.7.1 Meshing issues

The requirement is to have accurate computations up to a frequency of 15 Hz. The corresponding wavelengths are indicated in Fig. 8.8 which implies to have two different mesh size within the valleys depending on the velocity profile (soft or stiff).

The procedure for meshing using the CUBIT approach is summarized in the NERA deliverable D11.5. Specific numerical difficulties were faced in the case of very small edge slope angles (10° and 20°), which led to some specific mesh adjustment and adaptations (truncating the acute angle by a – very shallow: 4 m thick only – wall like edge) in order to avoid the high-frequency numerical instabilities.

Mesh design for the whole set of Valleys

- $VS(z) = VS_0 + (VS_1\text{-}VS_0)\,[(z - z_0)/(z_1\text{-}z_0)]^{0.5}$, z_0=0 m, z_1=1000 m

	1	2	3	4	5	6
VS_0 (m/s)	80	100	120	160	247	434
VS_1 (m/s)	480	700	835	950	1000	1000
VS_{30} (m/s)	125	167	200	250	333	500
λ Love 20 Hz (m)	5.3	6.8	8.2	10.7	15.5	31
λ Rayleigh 20 Hz (m)	5.1	6.6	8.0	10.4	14.9	29.4

5 m resolution in the valley (1–3)   10 m resolution in the valley (4–6)

2 spectral element meshes for each of the 162 geometries = **324 meshes**

Fig. 8.8. Basic information to be accounted for in the mesh design

8.3.7.2 Computational effort

Once performed the selection of the models and adopted the meshing strategy, the computations had to be launched. The a priori estimation of computational time was the following:

- For full P-SV (in plane motion, 972 models) calculations over a T= 30s duration, the requirement was 230 000 hours of cpu cores (i.e., ~3 months of 100 cpu cores). It was estimated that the mesh adaptation strategy on valley edges could possibility reduce this time by a factor 2 to 3.
- For full SH calculations (out-of-plane motion, 972 models), the estimated requirement was about 1/3 of full P-SV calculations (i.e., about 1 more month without optimization)

A few preliminary computations indicated that the a priori considered 30s duration was too small: it was thus extended to 60s.

The final computations were performed in Winter 2013-2014 on the "Froggy" machine, which is the very recently installed Grenoble High Performance Computing platform, with 3040 cpu cores and 66 TFlops. The full P-SV and SH calculations over a 60s duration actually required 280 000 hours of one cpu core (~4 years of 8 cores = ~1 month of 400 cores) on Froggy. This was possible thanks to the very deep involvement of E. Chaljub in the management of High-Performance Computing tools for the scientific community of the Grenoble area.

The "raw" results of this set of computations are the time-domain response to an pulse-like input signal at each of the 154692 receivers. 6 time series are available for each receiver, 3 translational velocity components and the corresponding 3 spatial derivatives with respect to the distance along the valley cross-section (in order to estimate ground strains)

- Out-of-plane velocity component for vertically incident, plane SH waves
- Spatial derivative of the out-of-plane velocity component (= torsional strain) for vertically incident, plane SH waves
- In-plane horizontal velocity component for vertically incident, plane SV waves
- In-plane vertical velocity component for vertically incident, plane SV waves
- Spatial derivative of the in-plane horizontal velocity component (= axial strain along the x direction) for vertically incident, plane SV waves
- Spatial derivative of the in-plane vertical velocity component (= rocking strain) for vertically incident, plane SV waves

These 928152 time series are sampled with a time step dt = 0.004 s and are 60 s long (15000 samples, 60 Kbytes). The size of the raw archive, distributed in the Grenoble area computing cloud, is thus 56 Gbytes: this affordable, but cannot be easily accessed from other locations. The post-processing work had thus to be performed on site.

The structure of the archive and post-processing is as follows:

- Storage of results in a local Data Grid infrastructure handled by **IRODS** system (cloud like)
- Metadata are defined for each time-series in order to ease the post-processing of the results: valley geometry, velocity model, position…
- Metadata are added directly to the **IRODS** metadata catalogue (no need to create specific database)
- Post-processing is done on the Grenoble HPC centre local computing grid (**CIGRI**) as much as possible
- Data query and transfer from **IRODS** to a local computer is possible for more interactive data mining

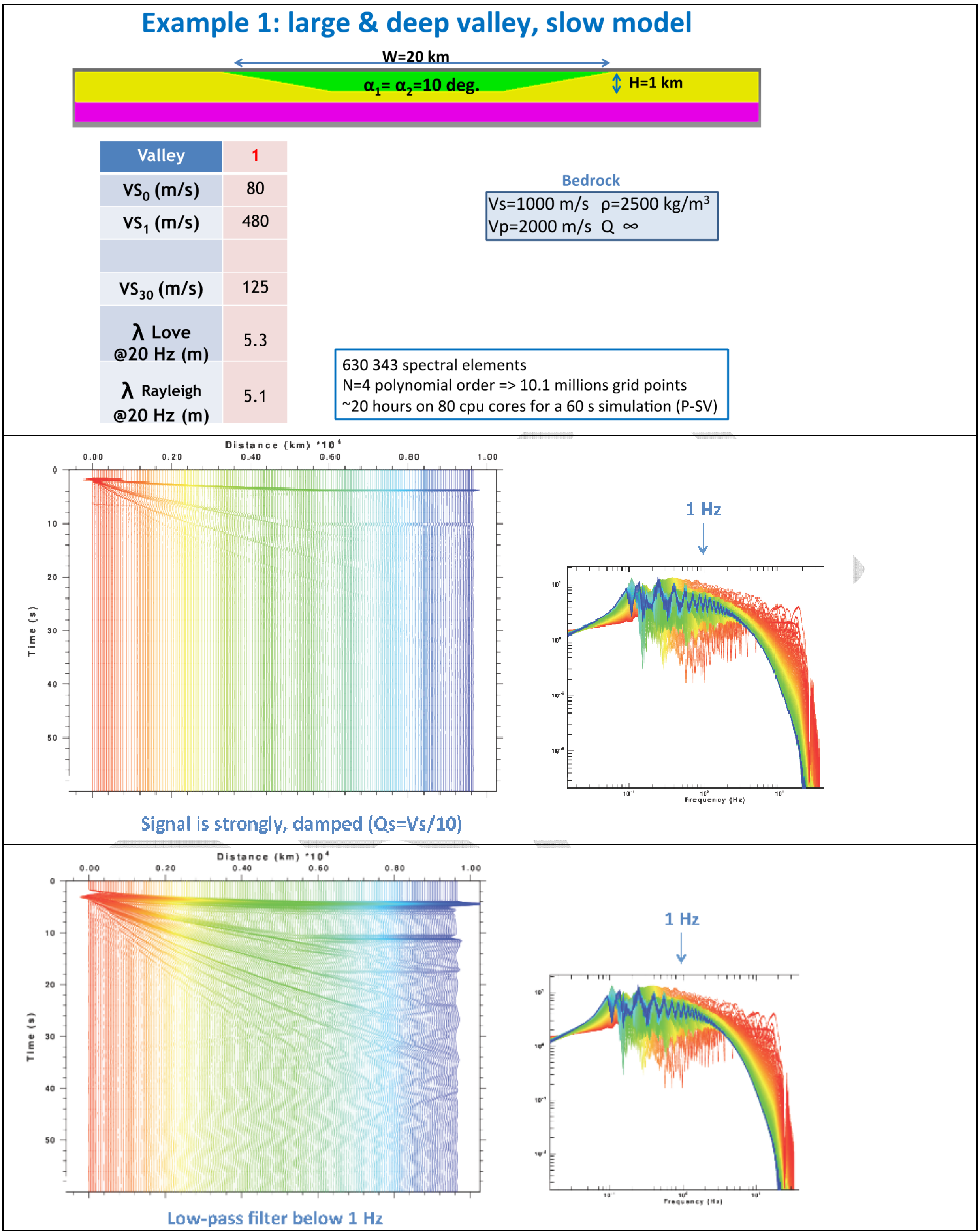

Fig. 8.9. Example results for the widest, thickest and softest valley with the smaller edge slope angles. The middle panel displays the raw time series for horizontal displacement along half the valley cross-section (left) and the corresponding Fourier spectra on the right, with a colour code depending on the receiver position (red = valley left edge, blue = valley centre). The bottom panel is similar, but for low-pass filtered horizontal displacement (below 1 Hz).

Example 1: large & deep valley, slow model

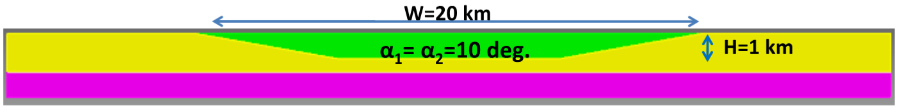

Valley	1
VS_0 (m/s)	80
VS_1 (m/s)	480
VS_{30} (m/s)	125
λ Love @20 Hz (m)	5.3
λ Rayleigh @20 Hz (m)	5.1

Bedrock

Vs=1000 m/s ρ=2500 kg/m³
Vp=2000 m/s Q ∞

630 343 spectral elements
N=4 polynomial order => 10.1 millions grid points
~20 hours on 80 cpu cores for a 60 s simulation (P-SV)

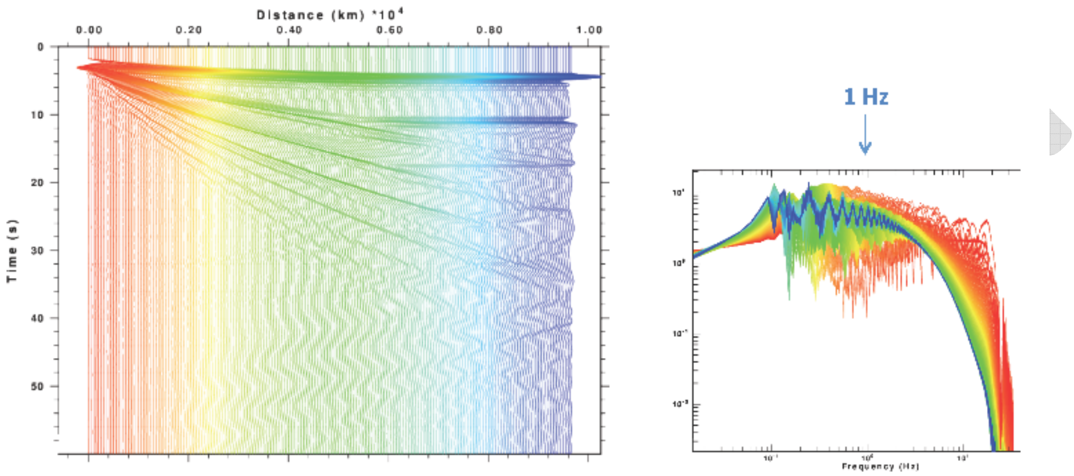

Low-pass filter below 1 Hz

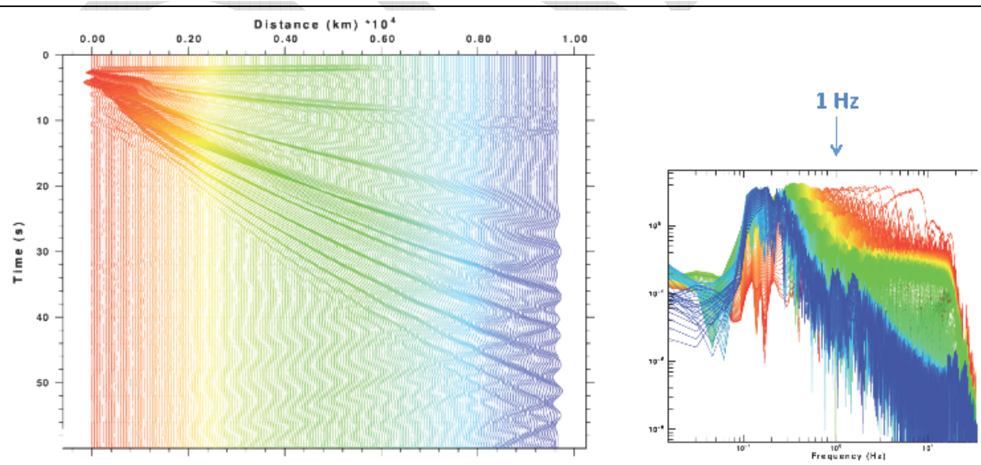

Low-pass filter below 1 Hz

Fig. 8.10. Example results for the same widest, thickest and softest valley with the smaller edge slope angles. Are shown here in the same way as in Fig. 8.9 the low-pass filtered displacement time series (below 1 Hz) for the horizontal (middle panel) and the vertical (bottom panel) components. Despite the high attenuation, a total duration of 60 s is needed.

Example 2: small triangular valley, slow model

Valley	1
VS_0 (m/s)	80
VS_1 (m/s)	480
VS_{30} (m/s)	125
λ Love @20 Hz (m)	5.3
λ Rayleigh @20 Hz (m)	5.1

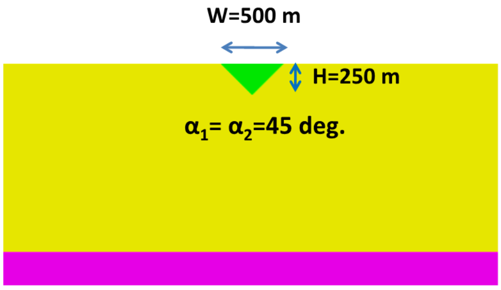

12 235 spectral elements
N=4 polynomial order => 0.2 millions grid points
~2,5 hours on 8 cpu cores for a 60 s simulation (P-SV)

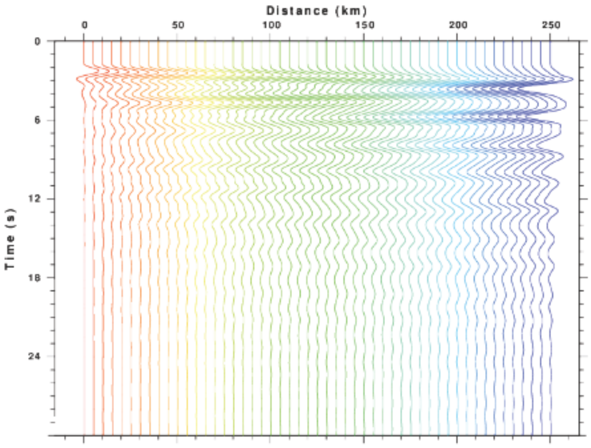

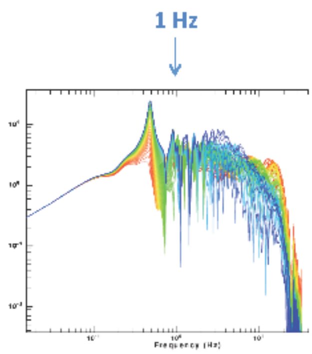

Low-pass filter below 1 Hz

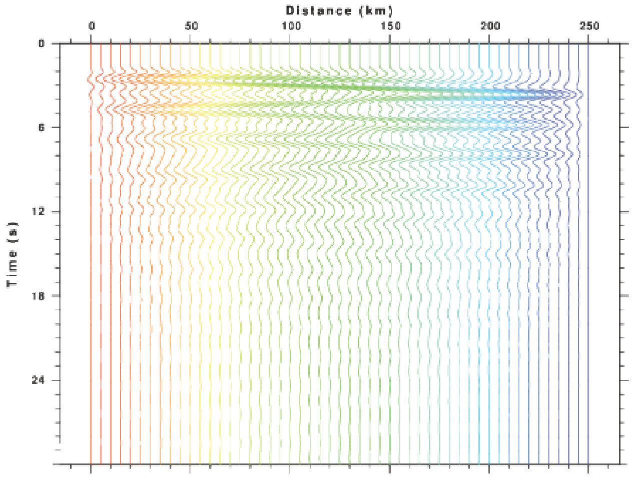

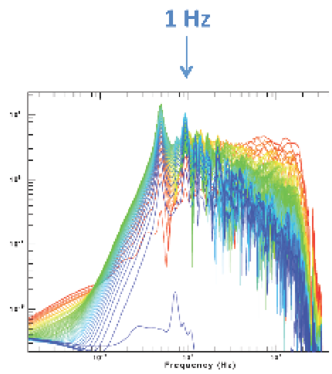

Low-pass filter below 1 Hz

Fig. 8.11. Example results for the narrowest, intermediate thickness and softest valley with steep slope angles. Are shown here in the same way as in Fig. 8.10 the low-pass filtered displacement time series (below 1 Hz) for the horizontal (middle panel) and the vertical (bottom panel) components.

Example 3: small triangular valley, fast model

Valley	6
VS_0 (m/s)	434
VS_1 (m/s)	1000
VS_{30} (m/s)	500
λ Love @20 Hz (m)	31
λ Rayleigh @20 Hz (m)	29.4

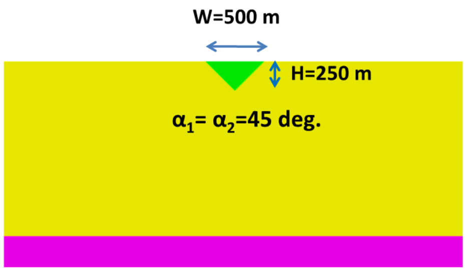

9 932 spectral elements
N=4 polynomial order => 0.16 millions grid points
~2 hours on 8 cpu cores for a 60 s simulation (P-SV)

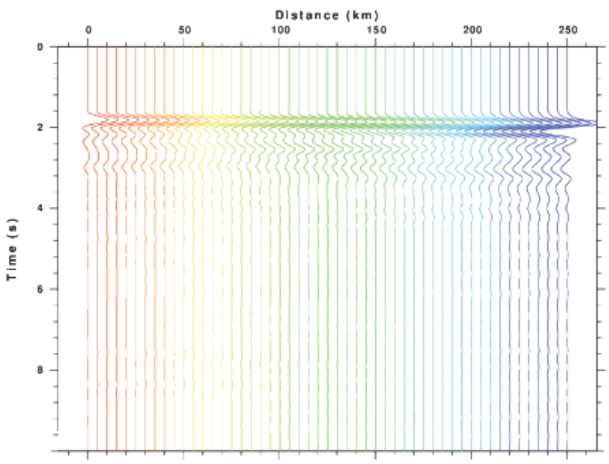

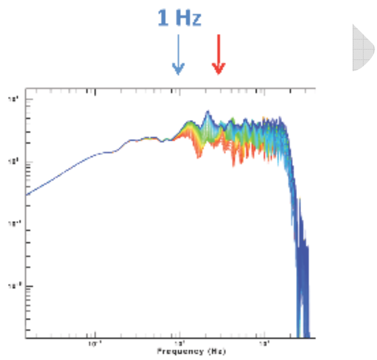

Low-pass filter below 3 Hz

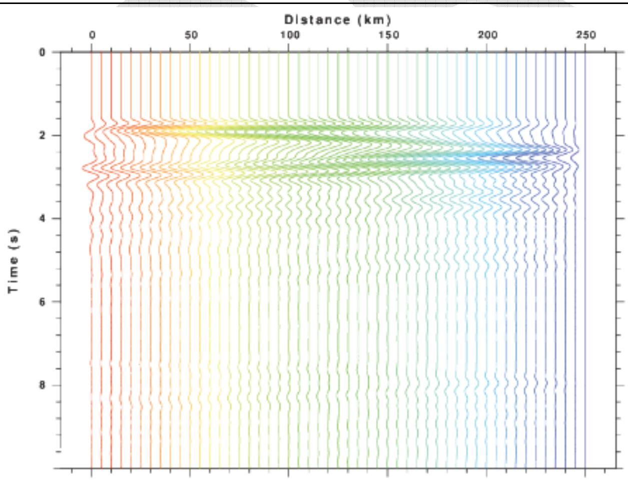

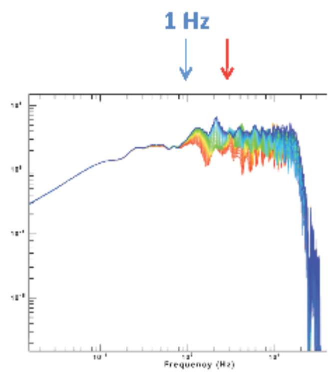

Low-pass filter below 3 Hz

Fig. 8.12. Example results for the narrowest, intermediate thickness and stiffest valley with steep slope angles (45°). Are shown here in the same way as in Fig. 8.10 the low-pass filtered displacement time series (below 3 Hz) for the horizontal (middle panel) and the vertical (bottom panel) components.

Given the amount of receivers, the whole set of results cannot be shown in a reasonable-size report. Only example results are displayed on Fig. 8.11 to Fig. 8.14 for some "extreme" cases : widest, thickest and softest valley with the most acute edge angles on Fig. 8.9 and Fig. 8.10, smallest, intermediate thickness and softest valley in Fig. 8.11, and smallest, intermediate thickness and softest valley in Fig. 8.12. These few examples illustrate

- The need to compute up to 60s long duration
- The effects on vertical component
- The important effects of damping at high-frequencies

8.4 Post-processing : computation of aggravation factors and dependence on geo-mechanical parameters

8.4.1 Considered GMI parameters

The Ground motion intensity parameters (GMIP) listed in Section 8.3.5 have been computed for each receiver and each input accelerogram, in both the 1D and 2D cases. The 2D over 1D aggravation factor (i.e., the ratio of the 2D value over the 1D value) has been computed for each input signal, and then averaged over the whole set of input signals. Both the average and the associated signal-to-signal variability (standard deviation) have been saved.

For each receiver, this aggravation factor has been computed as a ratio GMIP(2D)/GMIP(1D), and thus averaged geometrically over the whole set of input accelerograms for all GMIP BUT the Trifunac-Brady duration D_{TB}, for which the 2D-1D changes have been considered through the duration increase $D_{TB}(2D)$ - $D_{TB}(1D)$, which were then arithmetically averaged over the 23 input accelerograms. Examples of such averages for some valleys are displayed on Fig. 8.13 to Fig. 8.15, providing some hints on the following (still qualitative) results:

- The aggravation factor are parameter dependent :
    - o "energy-related" GMIP (Arias Intensity, Cumulative Absolute Velocity) generally exhibit larger values (up to 3-4), while high-frequency indicators (pga, 0.1s amplification factor Fa, arms), exhibit lower values..
- The geometry has a significant control on the aggravation factor

  - For embanked valleys, the highest aggravation factors occur in the centre because of constructive interferences
  - Steep edge slopes have large effects (with aggravation factors lower than 1, i.e., deamplification effects), but only very locally just over the valley edges
  - Gentle edge slopes have significant, long distance effects because of their energetic diffraction effect
- The mechanical characteristics within the valley do affect the aggravation factor
  - Increase in damping induce decrease of the aggravation factor, especially for high-frequency indicators
  - The aggravation factor for intermediate to long period GMIP tends to increase with decreasing soil stiffness, but this effect is variable from one geometry to another

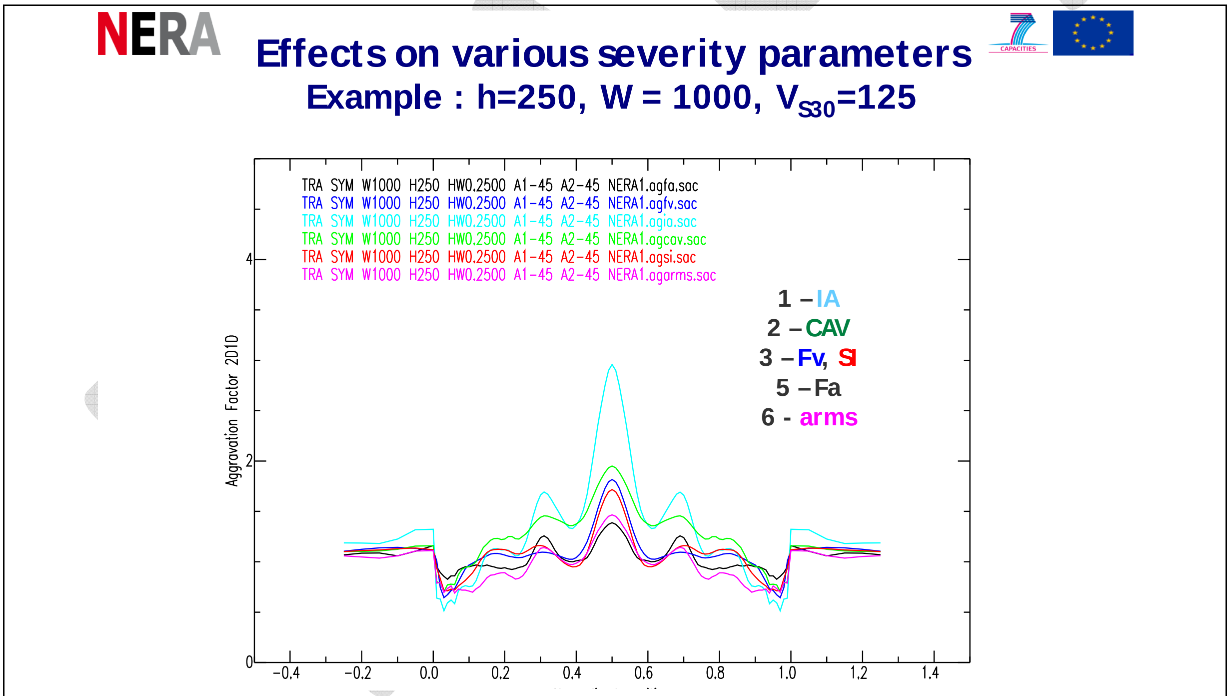

Fig. 8.13. Average aggravation factors for 6 different Ground Motion Intensity Parameters for a given valley (symmetrical, h=250m, W = 1 km, softest sediments, steep edge slope angles 45°). The x axis represents the normalized position along the valley cross-section (x=0.5 corresponds to valley centre, x=0 or 1 to valley edges).

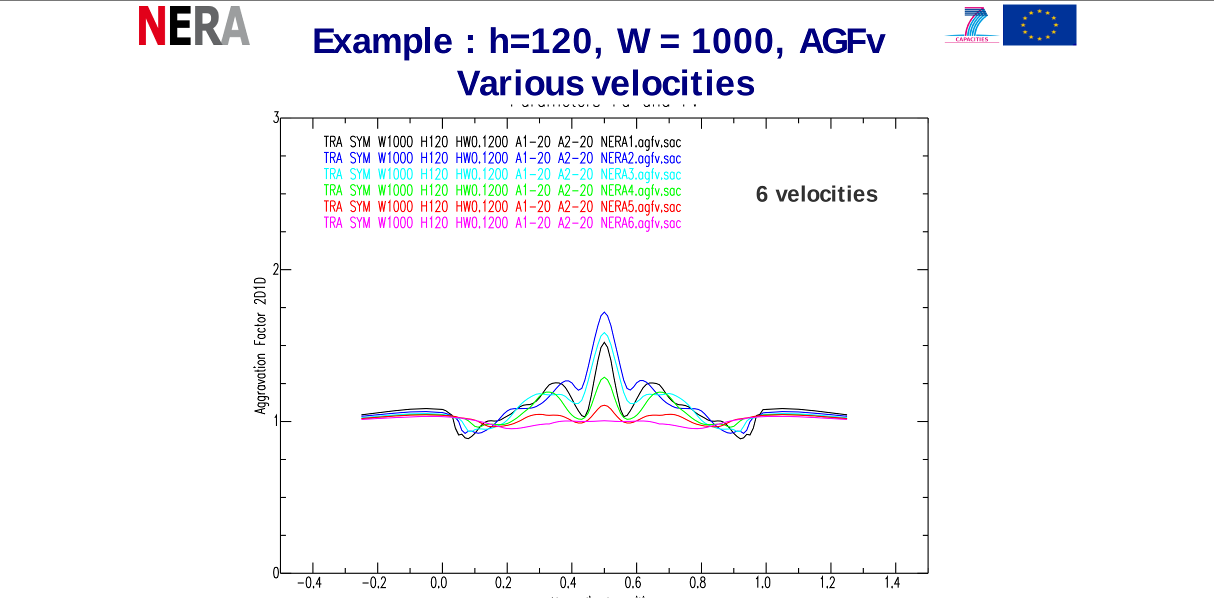

Fig. 8.14. Effect of the sediment stiffness on the average aggravation factors for the intermediate period (1 s) amplification Fv for a given valley (symmetrical, h=120m, W = 1 km, moderate edge slope angles 20°) – SH incidence. The x axis represents the normalized position along the valley cross-section (x=0.5 corresponds to valley centre, x=0 or 1 to valley edges).

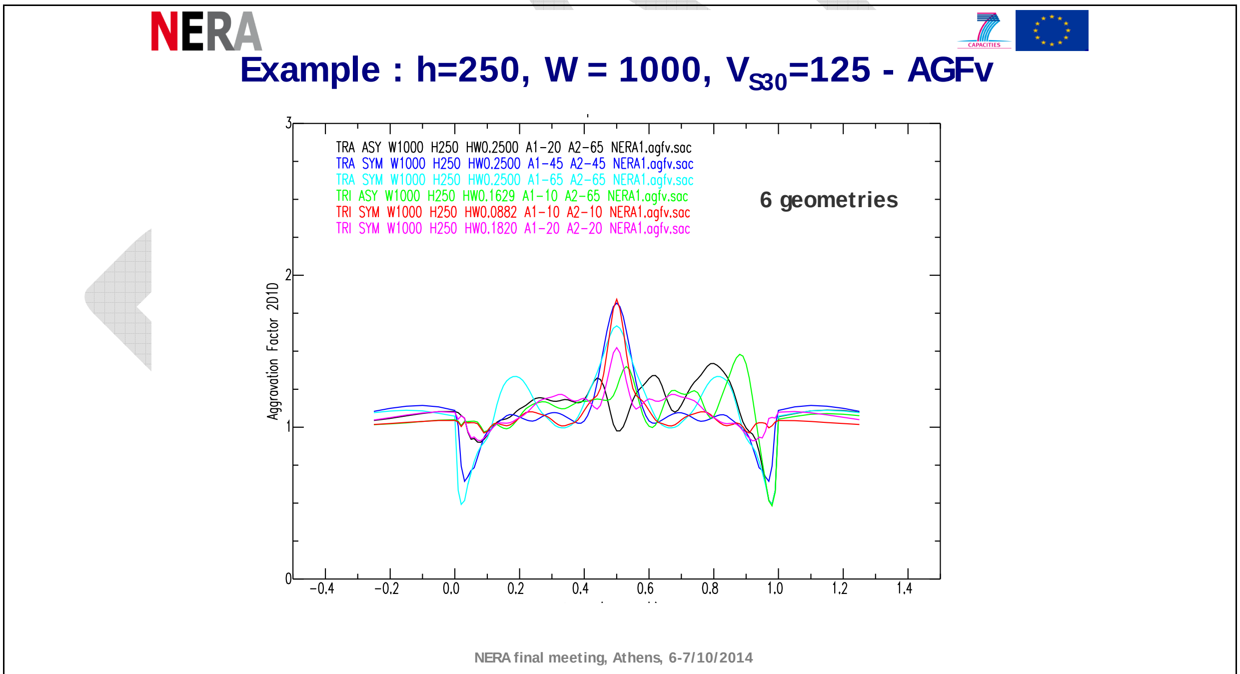

Fig. 8.15. Effect of the geometrical shape on the average aggravation factors for the intermediate period (1 s) amplification Fv for a given valley (h=120m, W = 1 km, soft sediments, all kinds of slope angles) – SH incidence. The x axis represents the normalized position along the valley cross-section (x=0.5 corresponds to valley centre, x=0 or 1 to valley edges).

8.4.2 Overview of aggravation factor results

8.4.2.1 Objectives or present analysis

We thus obtained a huge collection of average aggravation factors (154692 receivers, 10 severity index + frequency dependent aggravation factors at 100 frequencies). These aggravation factors have been archived in summary files with all the needed metadata.

In order to propose acceptable aggravation factor to the engineering community, it is needed to establish a simple correspondence between the gross geo-mechanical characteristics of the valley, the site position (near the edge or near the centre) and the value of this aggravation factor. This work has been undertaken with the help of the Tlemcen University (Algeria), who has built an expertise in the application of the neural network approach to engineering seismology (see Derras et al. 2012, 2014).

The investigations presently focus on two issues

- Identifying the criteria for large, significant or negligible effects within the valley as a function of the shape ratio h/w, the edge slopes, the velocity contrast or V_{S30}, fundamental frequency f_0)
- Establish simple, approximate relationships providing a satisfactory estimate as the aggravation factor for different zones in the valley (edge, central part) as a function of the geomechanical characteristics, with a special attention to the short and intermediate period amplification factors Fa and Fv, which are easy to use to modify the reference spectra

This work is under way and should be over, at least for a first phase, by the end of 2015.

We present here some statistical results in the same way as they were performed for the 7 SIGMA virtual sites, which provide the main trends as to the sensitivity of the aggravation factors on the main geometrical and mechanical parameters

8.4.2.2 Statistics for each zone

Eight different zones were chosen to provide a first gross indication the location within the valley, as displayed in Fig. 8.16. The total valley width W is first separated in three subwidths wwe, wfc and wee, which are the width of the western edge, of the central flat part, and of the eastern edge, respectively.

- wwe = H / tg(α_1)
- wee = H / tg(α_2)
- wfc = max [0, w – H/tg(α_1) – H/tg(α_2)]

The "central flat zone" may have a nul width for gentle slope angles and too large H/w shape ratios : in such cases, the valley is triangular instead of trapezoidal, and the "central zone" is reduced to one single point, with a local maximum depth Z_{max} and a position xwe with respect to the western edge given by :

- $Z_{max} = w / [1./tg(\alpha_1) + 1./tg(\alpha_2)]$
- $xwe = w / [1 + tg(\alpha_1) / tg(\alpha_2)]$

The 8 zones are then defined as follows:

- BR corresponds to the outcropping bedrock (10 receivers, 5 on each side)
- W2 and W1 are two equal-width zones located over the western (left) slope of the valley; their width is wwe/2 =Min {0.5 H/tg(α_1), 0.5 w/[1+tg(α_1)/ tg(α_2)]}
- Similarly, E2 and E1 are two equal-width zones located over the eastern (right) slope of the valley; their width is wee/2 =Min {0.5 H/tg(α_2), 0.5 w/[1+tg(α_2)/ tg(α_1)]}.
- FW, FC and FE are three equal-width zones located in the central, constant thickness part of the valley. For trapezoidal valleys, such zones may be reduced to one single point, with a local thickness Z_{max}.

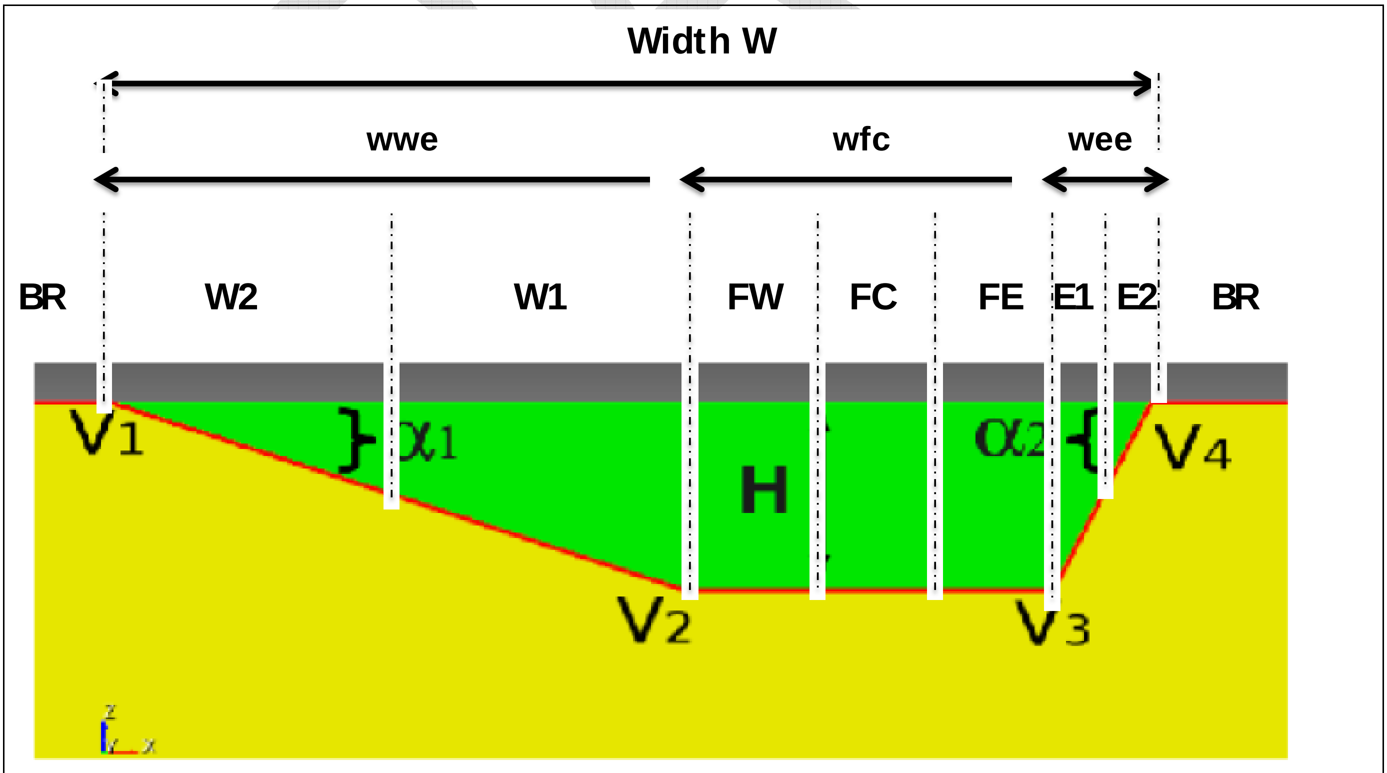

Fig. 8.16. Definition of valley zones. The total valley width W is separated in three

Then, in each zone, and for each GMIP and each considered valley (h, w, α_1, α_2 + velocity profile) and a given type of motion (in-plane/SV or out-of-plane/SH), the maximum, minimum and average aggravation factor were extracted from the archive of simulation results, leading to the following values

- AGAFMAX (zone) = maximum over the zone of the aggravation factor for the amplification factor (i.e. ratio of 2D acceleration response spectrum over 1D acceleration response spectrum). This agafmax may occur at different frequencies. It generally occurs around the site fundamental frequency
- AGPGAMAX (zone) = maximum over the zone of the aggravation factor for the peak ground acceleration
- AGPGVMAX (zone) = maximum over the zone of the aggravation factor for the peak ground velocity
- AGFAMAX (zone) = maximum over the zone of the aggravation factor for the short period range (around 0.1 s : 0.05 – 0.2 s) amplification factor
- AGFVMAX (zone) = maximum over the zone of the aggravation factor for the intermediate period range (around 1.0 s: : 0.5 – 2.0 s) amplification factor
- AGSIMAX (zone) = maximum over the zone of the aggravation factor for the (Housner definition) Spectrum Intensity
- AGCAVMAX (zone) = maximum over the zone of the aggravation factor for the Cumulative Absolute Velocity
- AGIAMAX (zone) = maximum over the zone of the aggravation factor for the Arias Intensity
- AGARMSMAX (zone) = maximum over the zone of the aggravation factor for the root mean square acceleration over the 5-95% duration
- AGDTB1MAX (zone) = maximum over the zone of the aggravation factor for the 5-95% Trifunac-Brady duration
- AGDTB2MAX (zone) = maximum over the zone of the aggravation factor for the 5-75% Trifunac-Brady duration

Minimum and average values of the same quantities were defined and derived in an analogue way. In the present report however, only the maximum values of each zone are investigated.

A maximum of 972 such values were thus derived for each considered valley (h, w, α_1, α_2 + velocity profile) and a given type of motion (in-plane/SV or out-of-plane/SH). The statistical distribution of these parameters were derived and are summarized in Appendix: NERA in Tables 1 - 11. (one Table for each GMIP), and displayed in Figures 1 to 8 (one Figure for each zone. The "extreme" horizontal bars display the values "F75 + 1,5 (F75-F25)" and "F25 - 1,5 (F75-F25)", which, for a normal distribution, would correspond to ±2.7 σ, and the red symbols to extreme values beyond these limits.

Some other summary plots displaying the variation of GMIP across the valley are displayed in Fig. 8.17 (amplitude parameters) and Fig. 8.18 (increase of duration), for the out-of-plane motion only. Several comments can be made on this basis:

- The "out-of-plane" aggravation factors are almost systematically larger than the in-plane one. This has been checked for all the amplitude parameters
- The largest AGF values correspond to the Arias intensity, the spectral amplification factor (reaching up to about 4), and the Cumulative Absolute Velocity slightly exceeding value of 2).
- As to the locations prone to higher aggravation factors, Fig. 8.17 indicates it concerns mainly the inner valley zones, (flat central part + zones W& and E1).
- A noticeable result from the mean values in Fig. 8.17c is the trend to decreased amplitude values on the very edges, especially when the underlying slopes are very steep.
- Finally the duration results (Fig. 8.18) indicates duration increase that may significantly exceed 10 s (for signals which are 10 to 30 s long), with a maximum occurring almost systematically in valley centre (FE), and a trend to duration decrease on the very edges (zones W2 and E2).
- One may notice also non-negligible effects even on the side rock sites: this corresponds to the waves partly reflected in the bedrock on the sloping interface. The mean values are very close to 1, basically from 1.04 to 1.12, but may exceed 1.2 in exceptional cases: such effects should also contribute to the aleatory variability on rock.

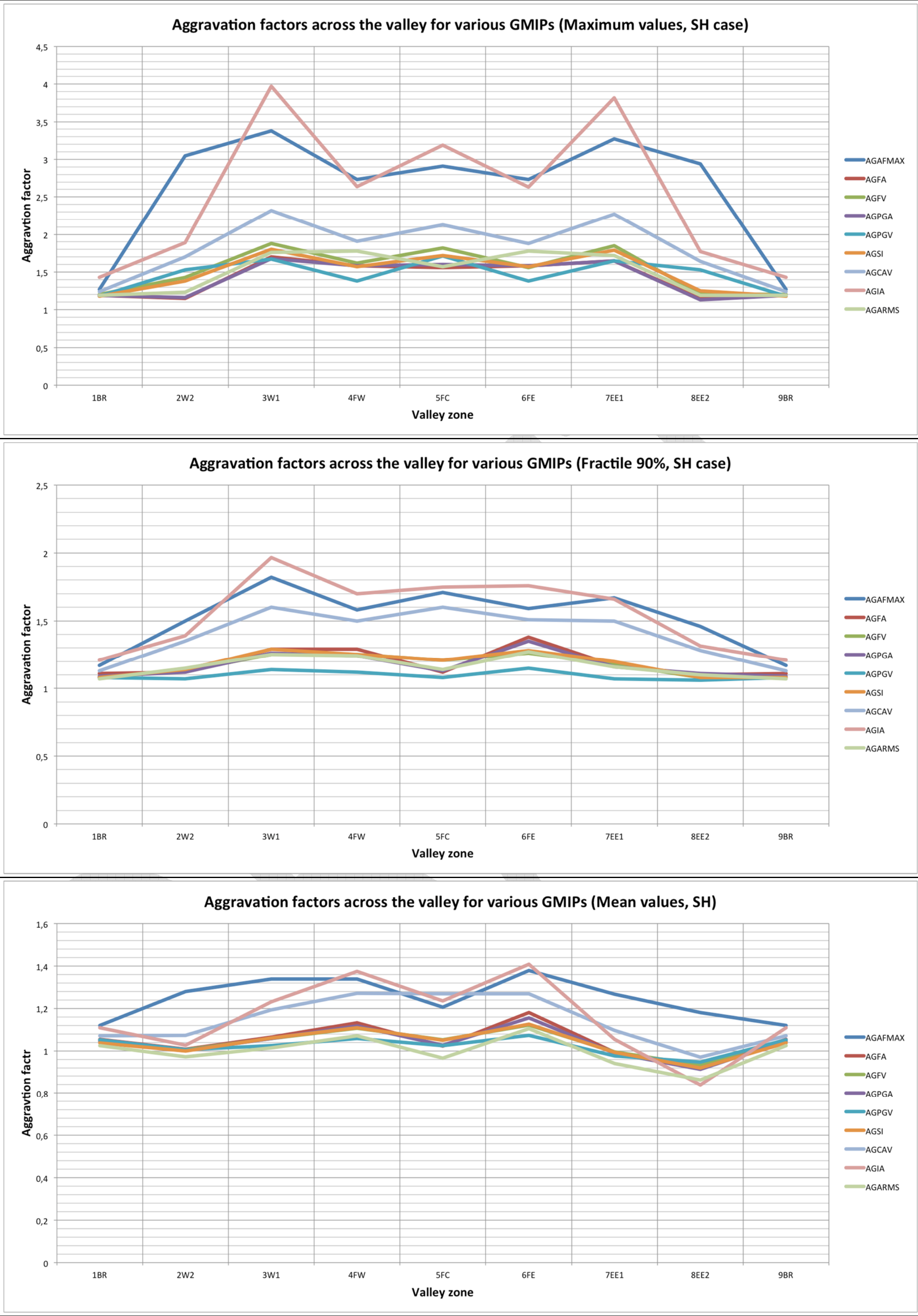

Fig. 8.17. Variability across the valley of a few statistical values for the various considered GMIP (aggravation factors on amplification factor, Fa, Fv, pga, pgv, SI, CAV, IA and arms), here only in the out-of-plane case. From top to bottom: maximum values (all cases considered); F90 values; mean values.

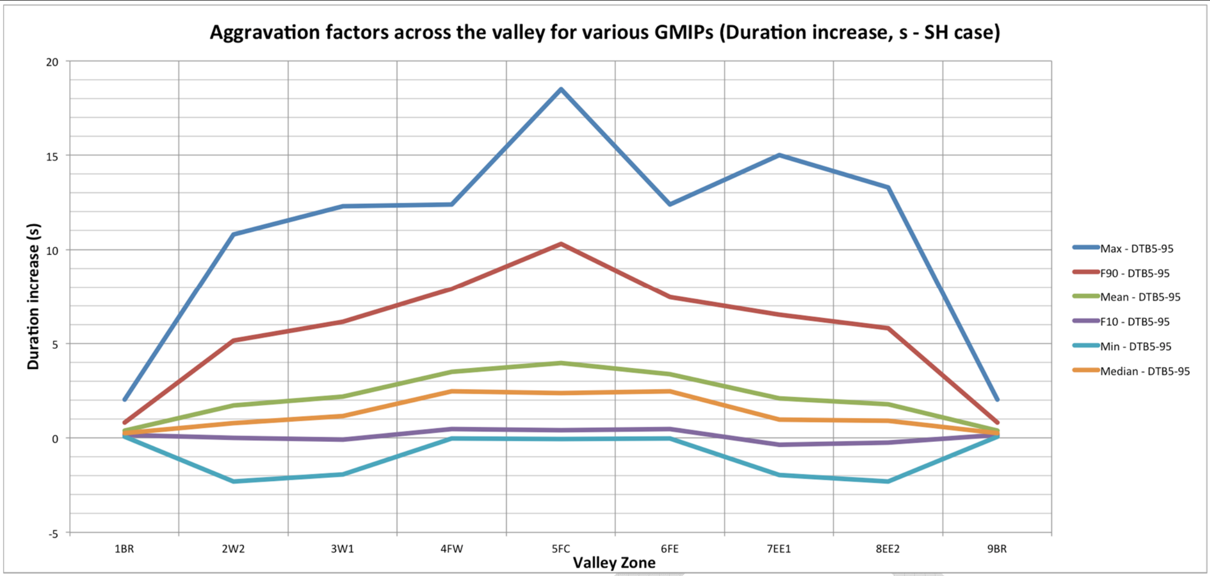

Fig. 8.18. Variability of the duration increase across the valley of a few statistical indicators (maximum, F90, mean, median, F10 and minimum values)

8.4.3 Dependence on geo-mechanical parameters

In order to detect which are the key parameters which control the large values of aggravation factors, we focus here on the last decile, i.e. all the cases corresponding, in a given zone and for a given GMIP, to the values between 90% and 100% of the cdf.

We more specifically investigate the effect of velocity contrast, depth to width ratio (shape ratio), edge slopes, and site location within the valley or even each zone.

8.4.3.1 Velocity profile / Impedance contrast

Fig. 8.19 and Fig. 8.20 display the respective contributions of the 6 velocity profile cases (see Fig. 8.2) to the last 90-100% decile in both SH and SV cases, respectively, for one of the most sensitive GMIP, i.e. AGAFMAX (peak AG for the spectral amplification factor), and for the two GMIP that may be used to control the shape of the response spectra, i.e., FA and FV, and for each of the 8 zones. Fig. 8.21 and Fig. 8.22 show the corresponding aggravation factor values for AGAFMAX, for each of the 8 zones, again for each kind of motion (SH and SV).

- On the edges W2, E1, E2) and on the side bedrock (BR), the occurrence of the largest AGF corresponds predominantly to large velocity contrast (exceeding 5 between surface V_{S30} and bedrock). Simultaneously, the largest AGF values are associated with large velocity contrast, and within each zone, the extreme values decrease with decreasing velocity contrast
- This trend is slightly less pronounced in the central part (especially FC, but also FE, RW and partly W1).
- The behaviour is about the same for the two components of motion, except on the edges (BR, W2, E2), where limited contrasts also significantly contribute to the last decile for the in-plane motion case: this probably corresponds to the contribution of reflected or transmitted P-waves, with larger incidence angles, especially in the case of limited contrast.

Plots for other GMIP are not shown here, but grossly exhibit a similar behaviour, with some tiny changes however depending on the selected parameter.

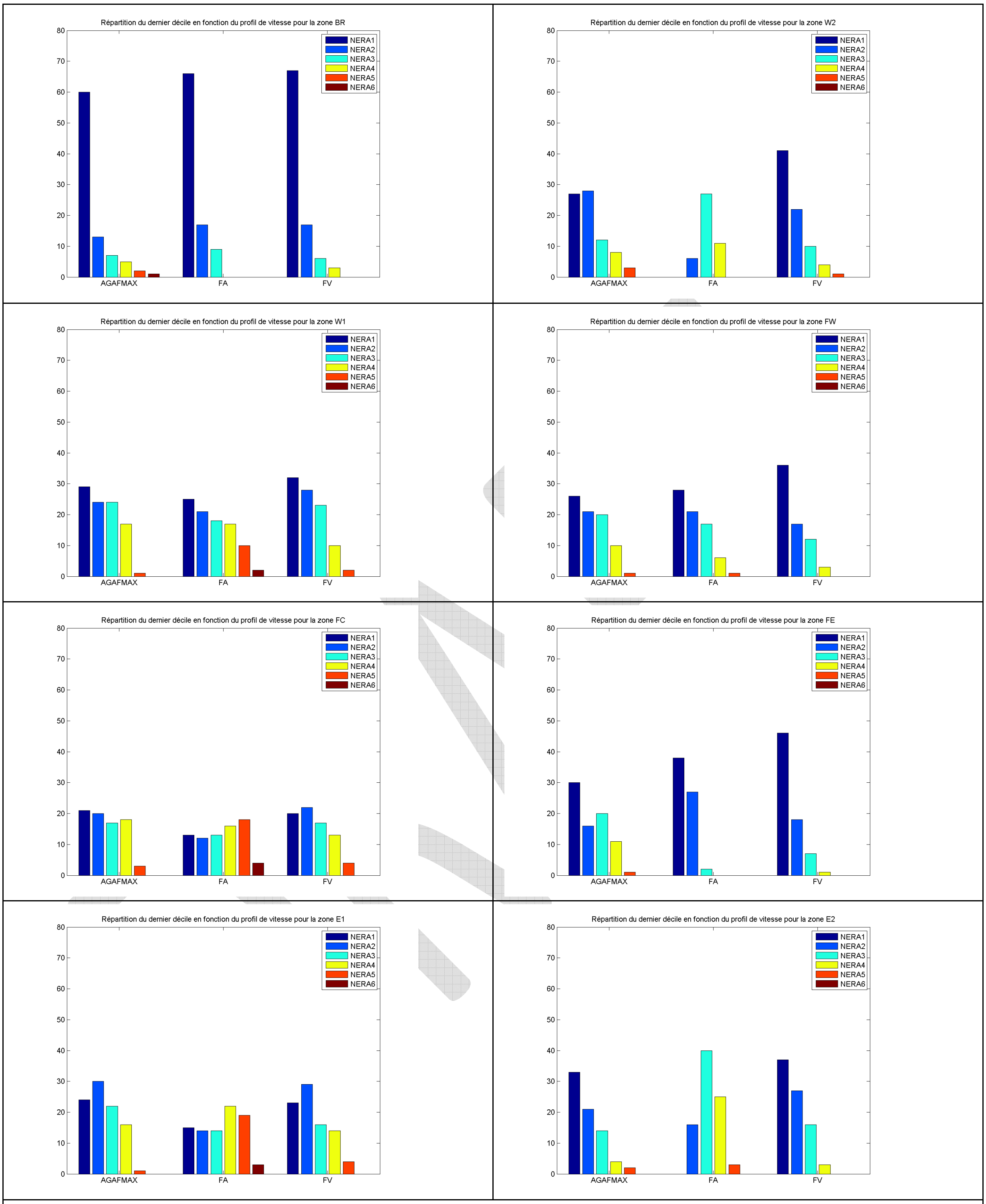

Fig. 8.19. Influence of the velocity contrast on the aggravation factor for the three "frequency domain" amplification factors (the peak one AGAFMAX, and the average short period – FA, around 0.1s) and long period (FV, around 1 s) , for the out-of-plane (SH) case. For each zone (BR, W2, W1, FW, FC, FE, E1 and E2, from left to right and top to bottom), the histograms display the number of cases corresponding to each velocity profile in the last decile. NERA profiles 1 to 6 correspond to VS30 values of 125, 167, 200, 250, 333 and 500 m/s, respectively

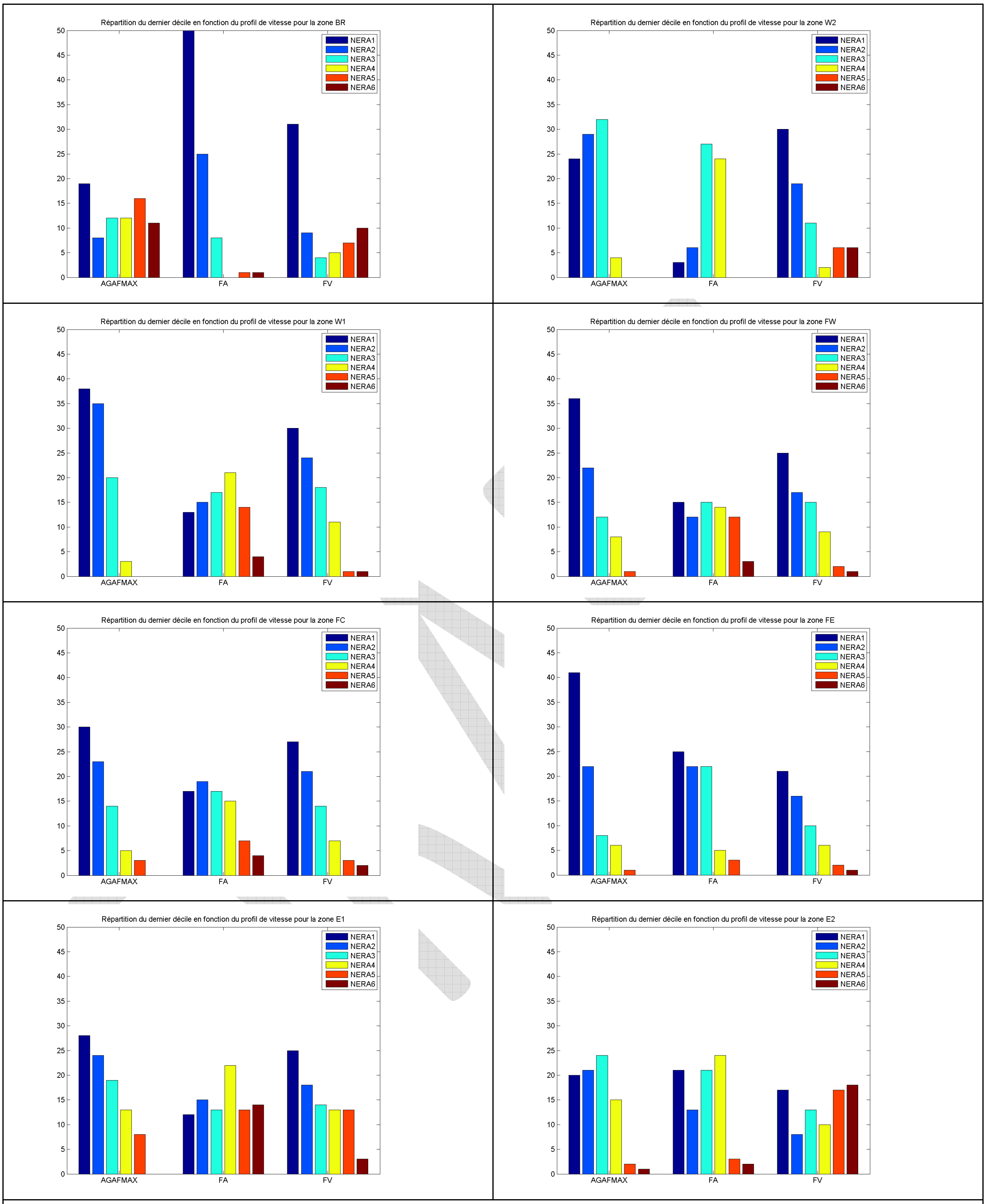

Fig. 8.20. Influence of the velocity contrast on the aggravation factor for the three "frequency domain" amplification factors (the peak one AGAFMAX, and the average short period – FA, around 0.1s) and long period (FV, around 1 s) , for the in-plane (SV) case. For each zone (BR, W2, W1, FW, FC, FE, E1 and E2, from left to right and top to bottom), the histograms display the number of cases corresponding to each velocity profile in the last decile. NERA profiles 1 to 6 correspond to VS30 values of 125, 167, 200, 250, 333 and 500 m/s, respectively

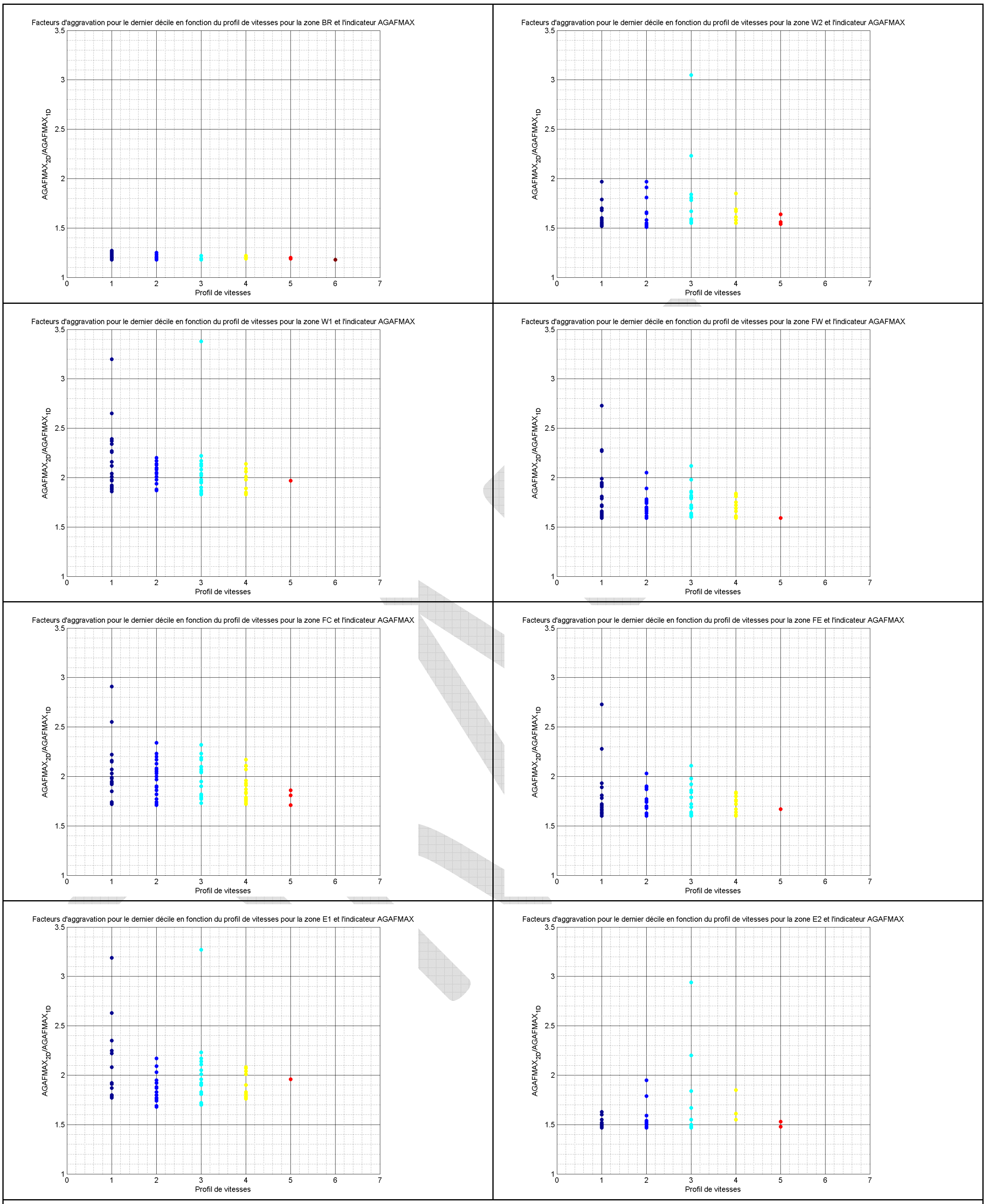

Fig. 8.21. Influence of the velocity contrast on the aggravation factor for the maximum "frequency domain" amplification factor (the peak one AGAFMAX), for the out-of-plane (SH) case. For each zone (BR, W2, W1, FW, FC, FE, E1 and E2, from left to right and top to bottom), the plots show the values of the last decile peak spectral amplification factors. As a function of the NERA profile 1 to 6(VS30 values of 125, 167, 200, 250, 333 and 500 m/s, respectively)

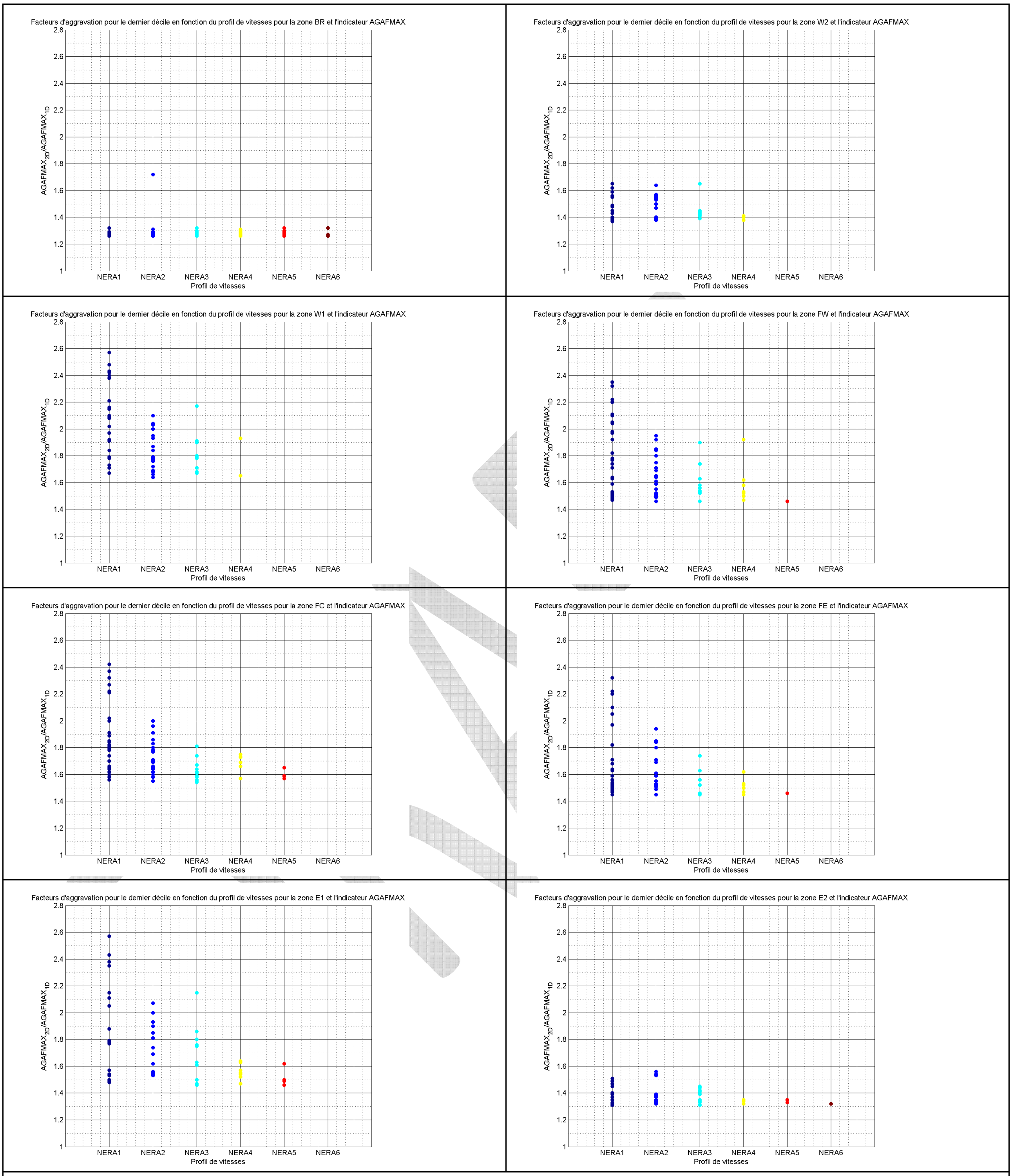

Fig. 8.22. Influence of the velocity contrast on the aggravation factor for the maximum "frequency domain" amplification factor (the peak one AGAFMAX), for the in-plane (SV) case. For each zone (BR, W2, W1, FW, FC, FE, E1 and E2, from left to right and top to bottom), the plots show the values of the last decile peak spectral amplification factors. As a function of the NERA profile 1 to 6(VS30 values of 125, 167, 200, 250, 333 and 500 m/s, respectively)

8.4.3.2 Shape ratio

As shown in Fig. 8.1 the shape ratios (i.e. ratio of maximum thickness Z_{max} over total valley width w) span a wide range from 0.012 to 0.5. Similarly to the previous section, we have considered the last decile of each zone (i.e. the 10% of cases with the largest aggravation factors), and investigated the corresponding aggravation factors and their relation to shape ratio. The results are displayed in Fig. 8.23 and Fig. 8.24 for the peak aggravation factors in the frequency domain, in the out-of-plane and in plane cases, respectively.

Even though a complete picture of the effects of shape ratio should also include the results for other GMIP, together with a closer look at the effect of the geometrical shape of the valley (trapezoidal or triangular, slope angles), we may however propose the following comments

- Large shape ratios favour large aggravation factors, especially in the case of large contrasts.
- The aggravation factor may exceed a factor of 2 for shape ratios as low as 0.08 (i.e., a 80 m thick deposit in a 1km wide valley); in that case, the location of the maximum aggravation factor is in zones W1 or E1, i.e., not in the central "flat" part, but on the "inner part" of valley edges
- There is a large scatter in the values, and the shape ratio cannot be taken as a unique explanatory variable for the aggravation factor : it should be coupled with other geometrical and/or mechanical characteristics
- The "side effects" on the outcropping bedrock are independent of the shape ratio: deep, embanked valleys do not contaminate their rocky edges more than shallow, wide valleys

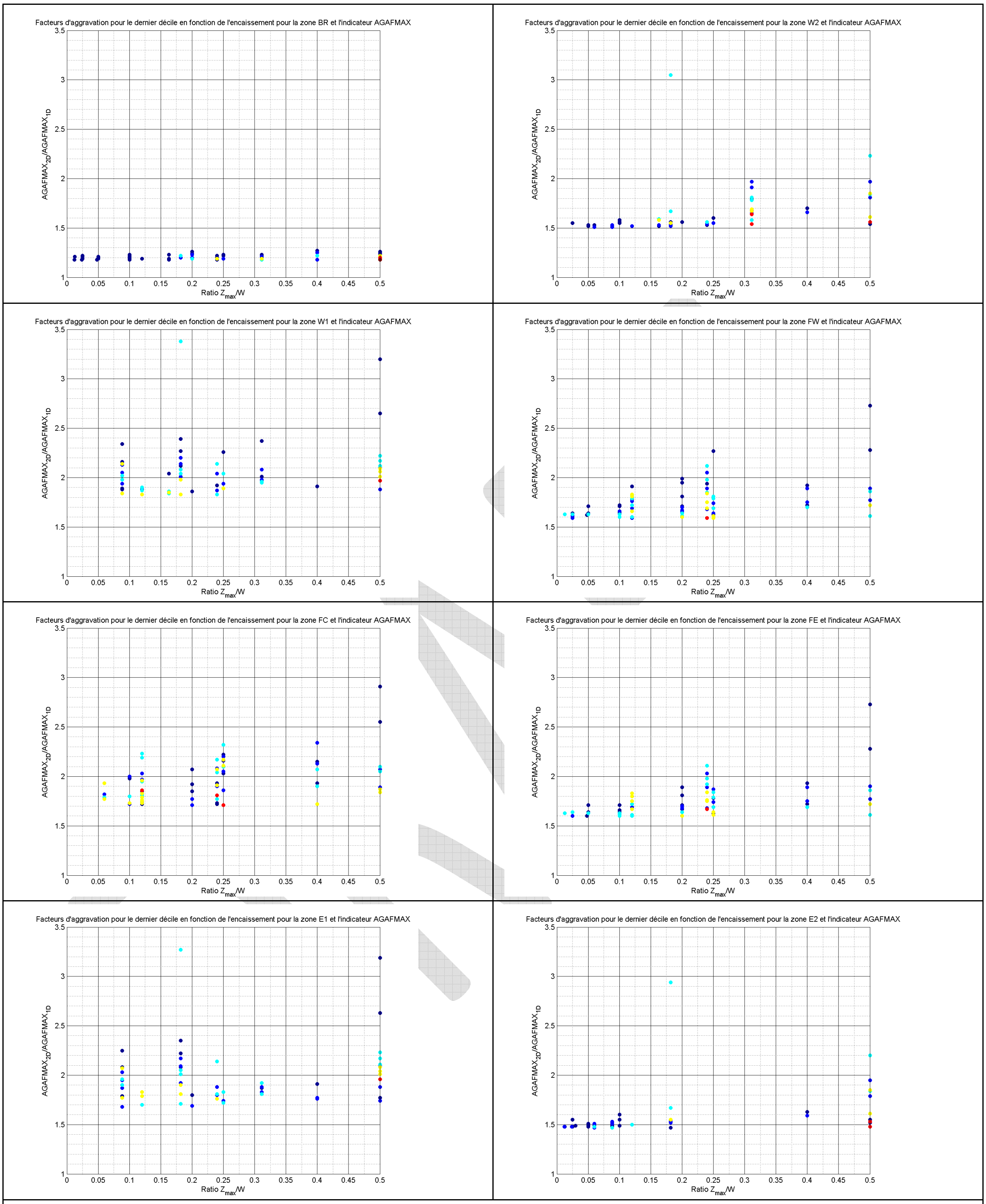

Fig. 8.23. Influence of the shape ratio on the aggravation factor for the maximum "frequency domain" amplification factors (the peak one AGAFMAX), for the out-of-plane (SH) case. For each zone (BR, W2, W1, FW, FC, FE, E1 and E2, from left to right and top to bottom), the plots show the values of the last decile peak spectral amplification factors as a function of the shape ratio Zmax/w. The colour code corresponds to the NERA profile 1 to 6 as in Fig. 8.19 (VS30 values of 125, 167, 200, 250, 333 and 500 m/s, respectively)

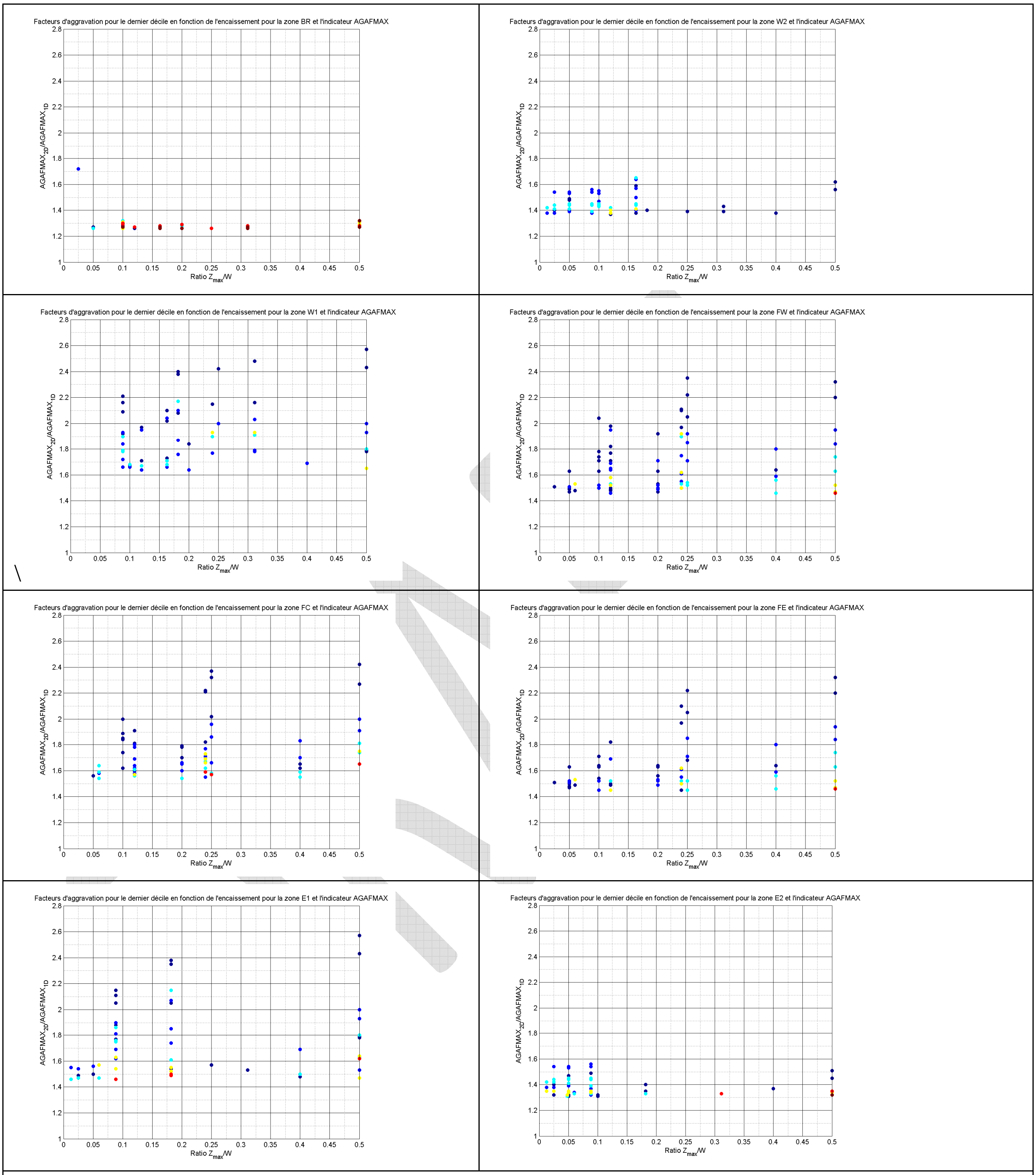

Fig. 8.24. Influence of the shape ratio on the aggravation factor for the maximum "frequency domain" amplification factors (the peak one AGAFMAX), for the in-plane (SV) case. For each zone (BR, W2, W1, FW, FC, FE, E1 and E2, from left to right and top to bottom), the plots show the values of the last decile peak spectral amplification factors as a function of the shape ratio Zmax/w. The colour code corresponds to the NERA profile 1 to 6 as in Fig. 8.19 (VS30 values of 125, 167, 200, 250, 333 and 500 m/s, respectively)

8.4.3.3 Edge slope angles

The effects of edge slope angles are investigated in a similar way as those of the velocity contrast in section 8.4.3.1. A first insight is obtained by looking at the contribution of each of the six sets of slope angle values to the last 90-100% decile (Fig. 8.25 and Fig. 8.26), for the same set of three GMIP (AGAFMAX, AGFA, AGFV), and then the corresponding values of AGAFMAX are displayed in Fig. 8.27 and Fig. 8.28 to possibly identify the most "critical" geomechanical configurations.

Grossly speaking, out-of-plane and in-plane cases exhibit similar features:

- As expected, the largest effects on the rocky edges (BR zone) predominantly correspond to the larger edge slopes, with aggravation factors up to 20-30%. These effects are slightly larger for the SV case, in probable link with the outward reflection of S and P waves from the edge slope (the latter being up-going in the cases of 45° and 65° slope angles).
- Conversely, on the edges within the valley (zones W2, W1, E1 and E2, there is a very significant contribution of the low angle cases (10° or 20°); actually, steep angles are associated with low aggravation factors (below 1 : reduction of ground motion), while gently sloping angles allow the progressive building of surface waves which contribute to the increase of ground motion
- In the central part (zones FW, FC and FE), the predominant contribution is associated with large slope angles; this is probably associated with significant shape ratios and/or Lobé-like valley edge effects

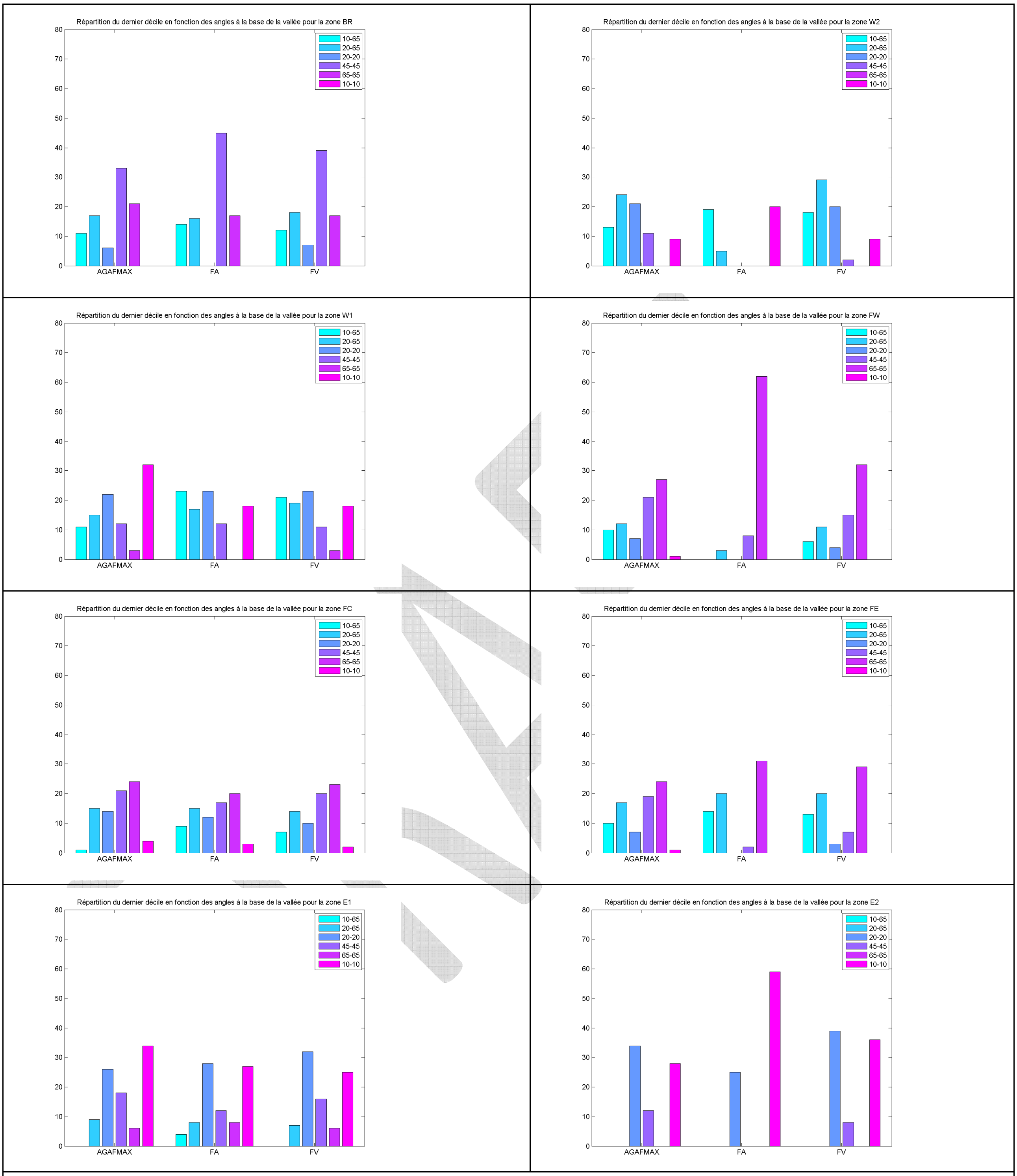

Fig. 8.25. Influence of the slope angles on the aggravation factor for the three "frequency domain" amplification factors (the peak one AGAFMAX, and the average short period – FA, around 0.1s) and long period (FV, around 1 s), for the out-of-plane (SV) case. For each zone (BR, W2, W1, FW, FC, FE, E1 and E2, from left to right and top to bottom), the histograms display the number of cases in the last decile corresponding to each of the six sets of slope angle values, starting with the dissymmetric ones (10°-65° and 20-65°), and going one with the 4 symmetrical ones (20°-20°, 45°-45°, 65-65° and 10-10°, from left to right and light blue to magenta).

Fig. 8.26. Influence of the slope angles on the aggravation factor for the three "frequency domain" amplification factors (the peak one AGAFMAX, and the average short period – FA, around 0.1s) and long period (FV, around 1 s), for the in-plane (SV) case. For each zone (BR, W2, W1, FW, FC, FE, E1 and E2, from left to right and top to bottom), the histograms display the number of cases in the last decile corresponding to each of the six sets of slope angle values. , starting with the dissymmetric ones (10°-65° and 20-65°), and going one with the 4 symmetrical ones (20°-20°, 45°-45°, 65-65° and 10-10°, from left to right and light blue to magenta).

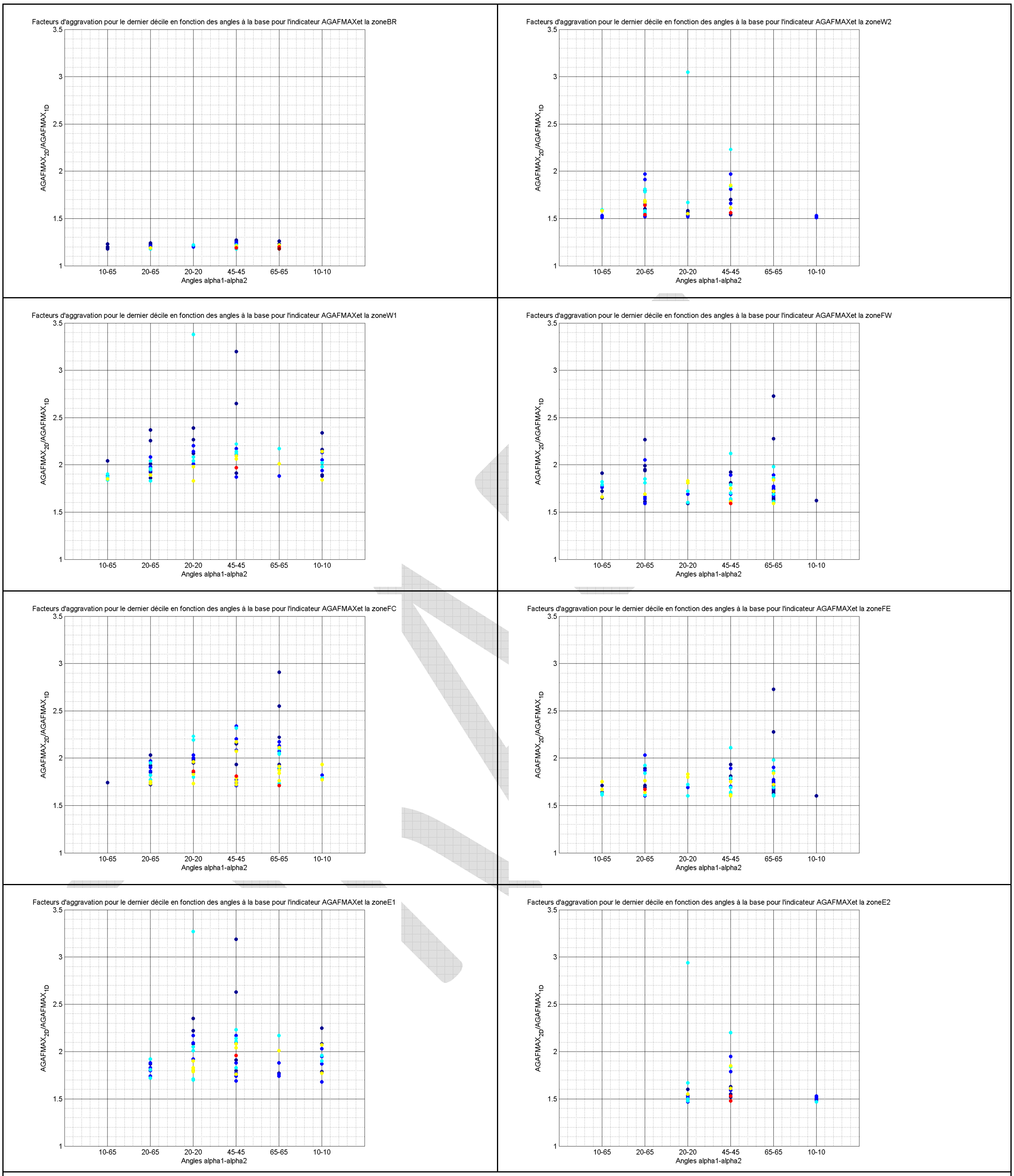

Fig. 8.27. Influence of the slope angles on the aggravation factor for the three "frequency domain" amplification factors (the peak one AGAFMAX, and the average short period – FA, around 0.1s) and long period (FV, around 1 s), for the out-of-plane (SH) case. For each zone (BR, W2, W1, FW, FC, FE, E1 and E2, from left to right and top to bottom), the histograms display the number of cases in the last decile corresponding to each of the six sets of slope angle values, starting with the dissymmetric ones (10°-65° and 20-65°), and going one with the 4 symmetrical ones (20°-20°, 45°-45°, 65-65° and 10-10°, from left to right and light blue to magenta).

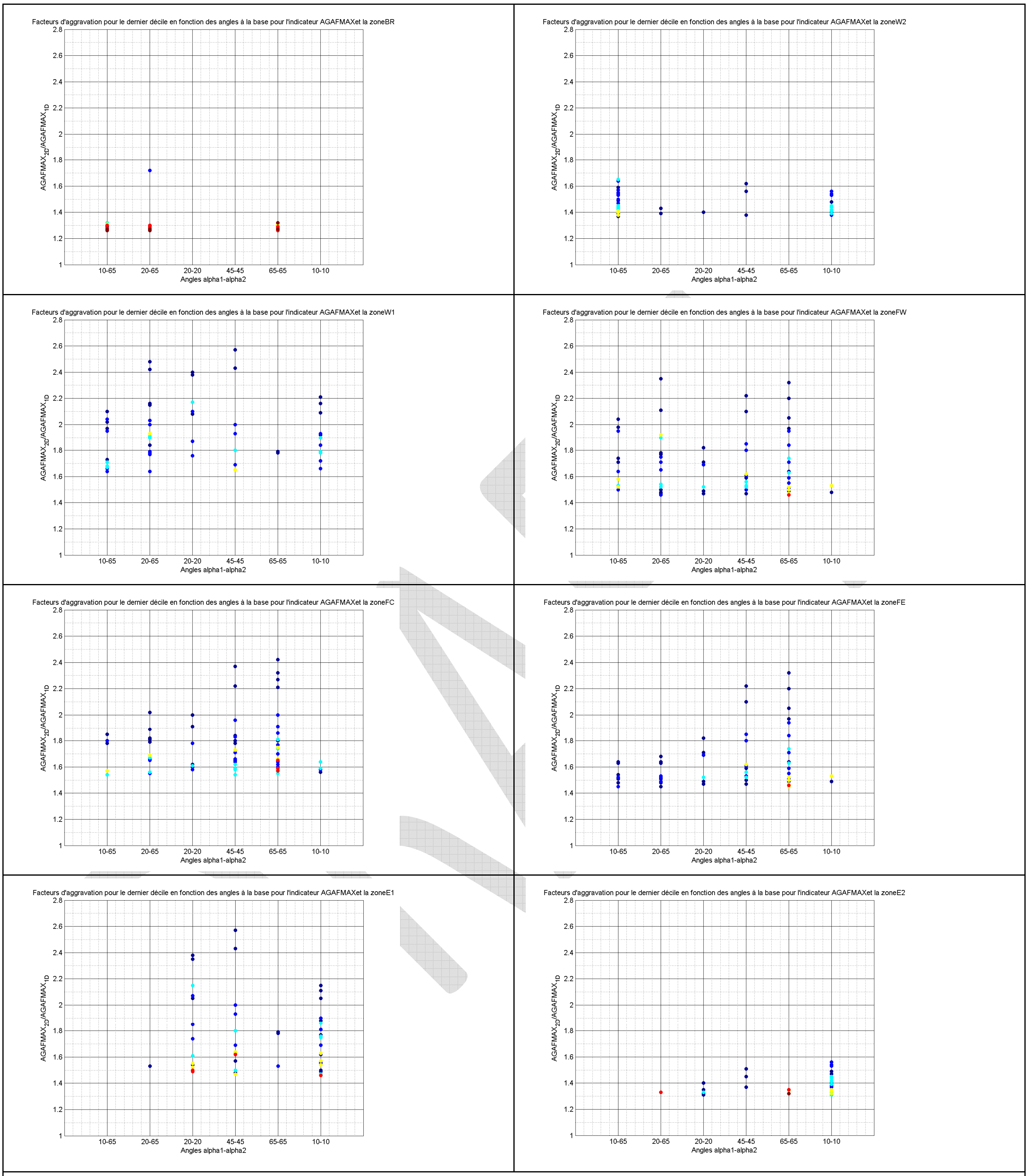

Fig. 8.28. Influence of the slope angles on the aggravation factor for the three "frequency domain" amplification factors (the peak one AGAFMAX, and the average short period – FA, around 0.1s) and long period (FV, around 1 s), for the in-plane (SV) case. For each zone (BR, W2, W1, FW, FC, FE, E1 and E2, from left to right and top to bottom), the histograms display the number of cases in the last decile corresponding to each of the six sets of slope angle values. , starting with the dissymmetric ones (10°-65° and 20-65°), and going one with the 4 symmetrical ones (20°-20°, 45°-45°, 65-65° and 10-10°, from left to right and light blue to magenta).

8.4.3.4 Position

For each zone and each ground motion intensity parameter, we also kept track of the corresponding location within the valley. It is uneasy to plot the results in a summary way: the absolute location in m from the western valley edge in varying from 0 to 20 km; normalizing it with respect to the valley width only does not fully take into account the geometrical characteristics, especially the edge slope angles. We thus arbitrarily decided to normalize the position within zones W2 and W1 from western edge and with respect to the width of the western sloping part (wwe), which provides a normalized position between 0 and 1 ([0. - 0.5] for W2 and ([0.5 – 1.0] for W1). The position within zones FW, FC and FE was then counted from the western end of the flat part of the valley, and normalized with respect to the width of the central, equal-thickness part (wfc). Zones FW, FC and FE correspond to normalized positions in the ranges [1-2], [2-3] and [3-4], respectively. Then, the position within zones E1 and E2 position was counted from the eastern end of the central flat part, and normalized with respect to the width of the eastern edge (wee). Zones E1 and E2 correspond to normalized positions in the ranges [4-4.5] and [4.5 – 5], respectively.
The corresponding equations for the normalized positions are detailed below

- W2 and W1 : xnorm = xwe / wee
- FW, FC and FE : xnorm = 1 + 3*(xwe-wee)/wfc
- E1 and E2 : xnorm = 4 + (xwe-wee-wfc)/wee

(Note that zones FW, FC and FE do not exist for triangular valleys: for such valleys, the thickest site corresponds to the normalized location xnorm = 1)

The results for the last decile of the three, frequency domain aggravation factors AFMAX, FA and FV are displayed in Fig. 8.29, Fig. 8.30 and Fig. 8.31, respectively. For each zone, the whole series of values for the last corresponding decile is considered, i.e., up to 97 values. The colour code used in these Figures correspond to the velocity profile, as shown in Fig. 8.19 and Fig. 8.20.
The most salient features of these results are the following

- The largest aggravation factors often correspond to either the valley centre (xnorm = 2.5) because of symmetry effects, or the boundaries between edge slopes and the central flat part (xnorm =1 or xnorm = 4).

- The long period aggravation factors follow the valley dissymmetry and are larger on gently sloping edges
- As already indicated, large velocity contrast lead to largest aggravation factors , in probable link with the more efficient wave trapping
- When valleys are neither symmetric nor characterized by sharp lateral changes of the sediment-bedrock interface, the peak value may occur anywhere in the central zone

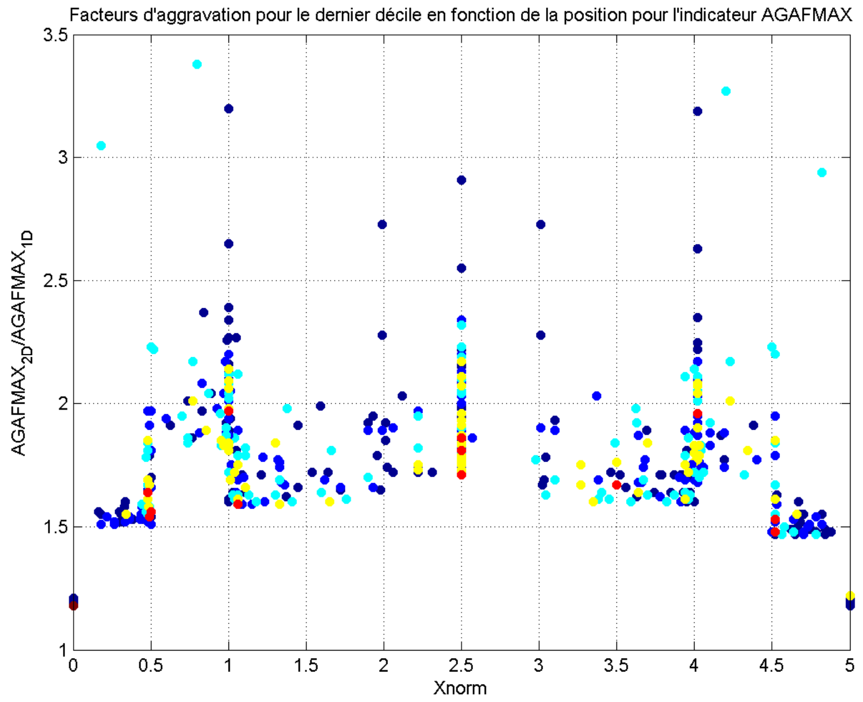

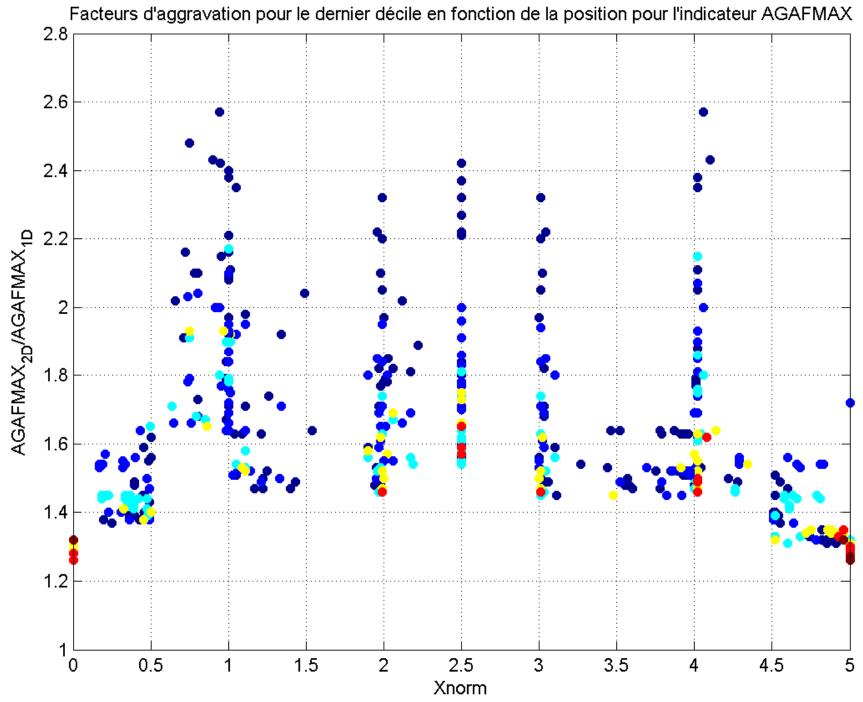

Fig. 8.29. Normalized location of the valley sites exhibiting the peak aggravation factors (last decile) on the amplification factor (AFMAX) for out-of-plane (SH, top) and in-plane (SV, bottom) motion. The colour code corresponds to the velocity profile. The vertical scales are different as SH aggravation factors are larger.

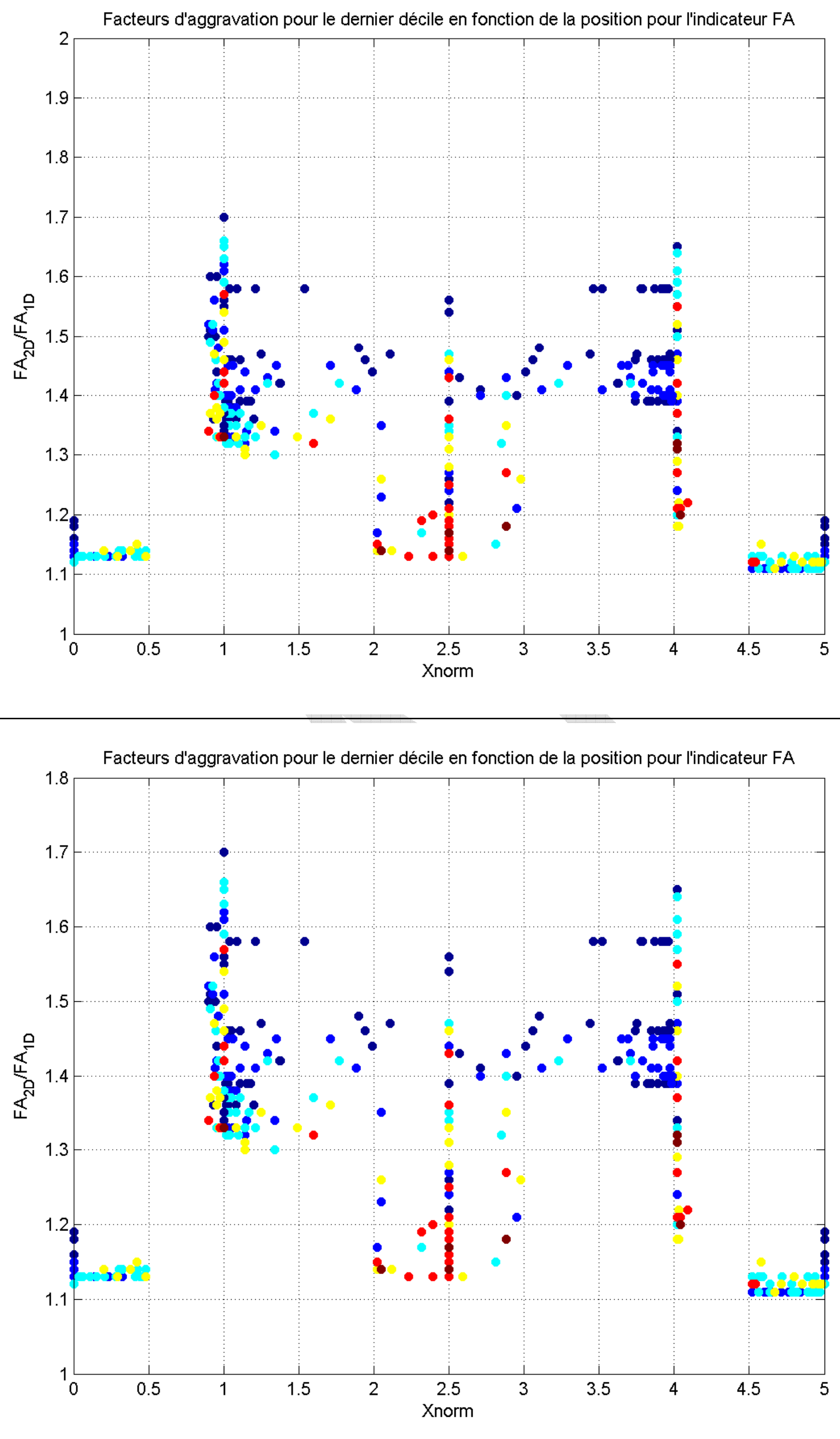

Fig. 8.30. Normalized location of the valley sites exhibiting the peak aggravation factors (last decile) on the average short period amplification factor (FA, around 0.1 s) for out-of-plane (SH, top) and in-plane (SV, bottom) motion. The colour code corresponds to the velocity profile. The vertical scales are different as SH aggravation factors are larger.

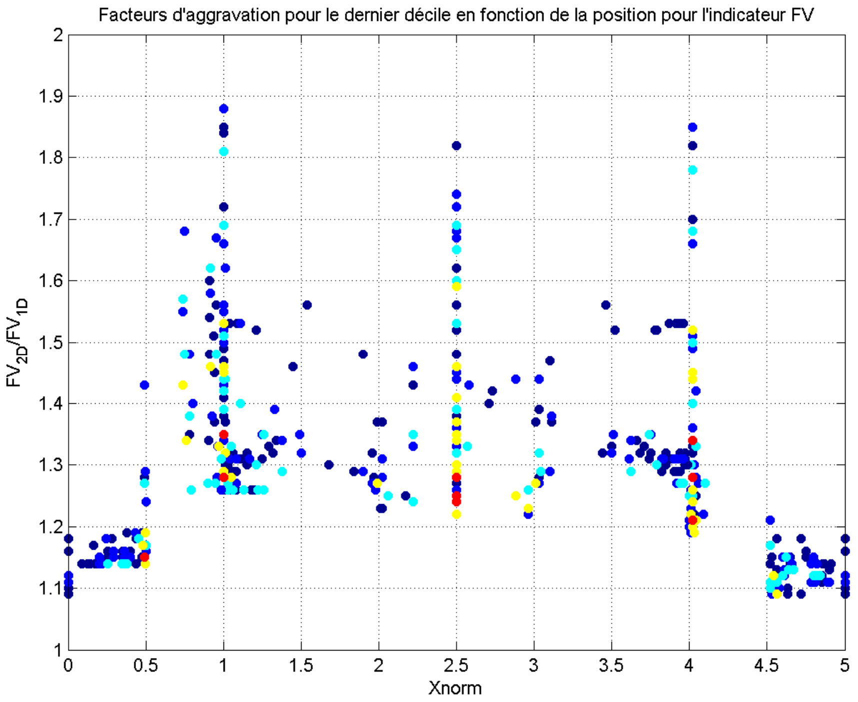

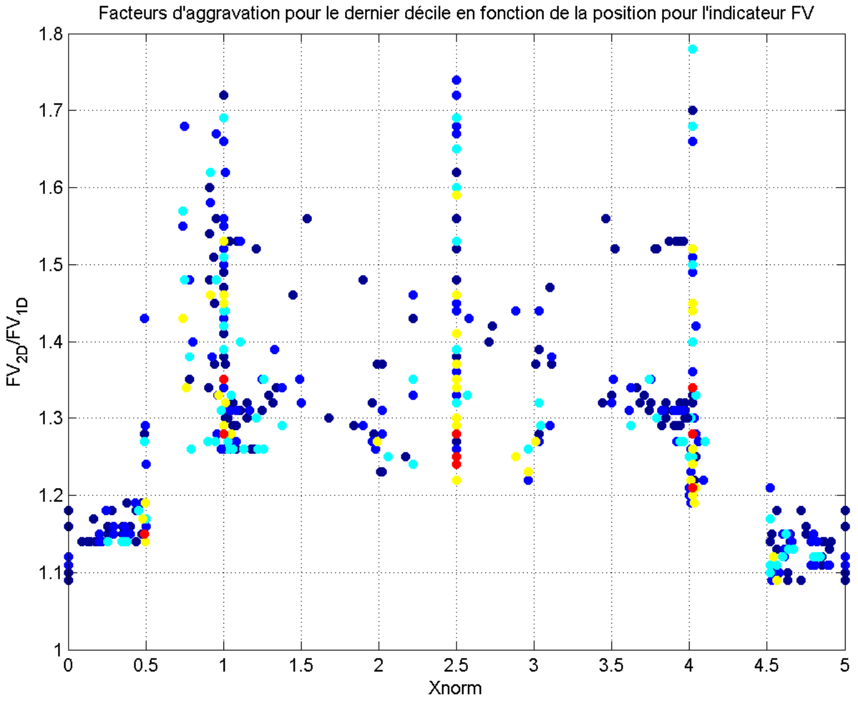

Fig. 8.31. Normalized location of the valley sites exhibiting the peak aggravation factors (last decile) on the average long period amplification factor (FV, around 1 s) for out-of-plane (SH, top) and in-plane (SV, bottom) motion. The colour code corresponds to the velocity profile. The vertical scales are different as SH aggravation factors are larger.

8.4.3.5 Polarization of motion

Fig. 8.32 and Fig. 8.33 compare the aggravation factors in the SH and SV case for the three same spectral GMIP previously considered (AGAFMAX, AGFA, AGFV) for the whole set of 972 valleys. Also indicated is the corresponding normalized position of the maximum aggravation factor in each zone. Similar results were obtained for other GMIPs.

Even though there are a few cases with lower aggravation factors in the SH case, the largely predominant situation is a larger out-of-plane aggravation factor, especially on the edge zones W1 and E1. We interpret this difference as due to the coupling, in the in-plane SV case, between horizontal and vertical motion. While the vertical component of motion was actually computed in the simulations (see Fig. 8.9 to Fig. 8.12), it was not considered in the present computation of single-component aggravation factors. The present SIGMA results for the 7 virtual sites and their variants are certainly more relevant as to the comparison between in-plane and out-of-plane results, but the large aggravation factors found for the vertical components are linked to the transfer of energy from the horizontal, in-plane component, to the vertical (in-plane) component.

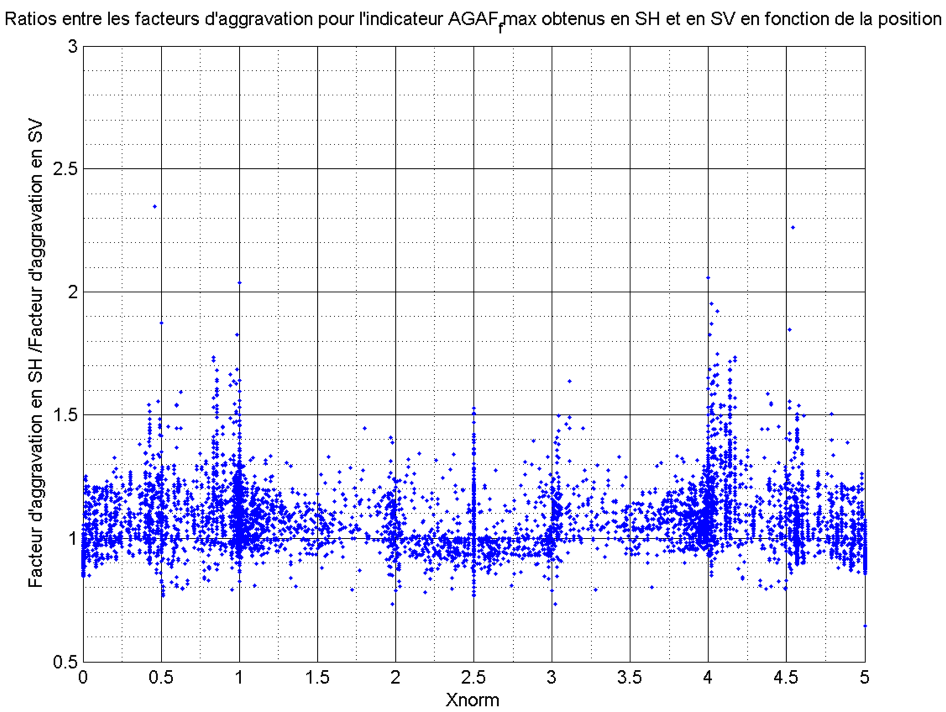

Fig. 8.32. Ratios between SH (out-of-pane) and SV (in-pane) aggravation factors for the whole set of results on the spectral amplification factor (AGAFMAX). The horizontal axis corresponds to the associated normalized location (xnorm) within the valley.

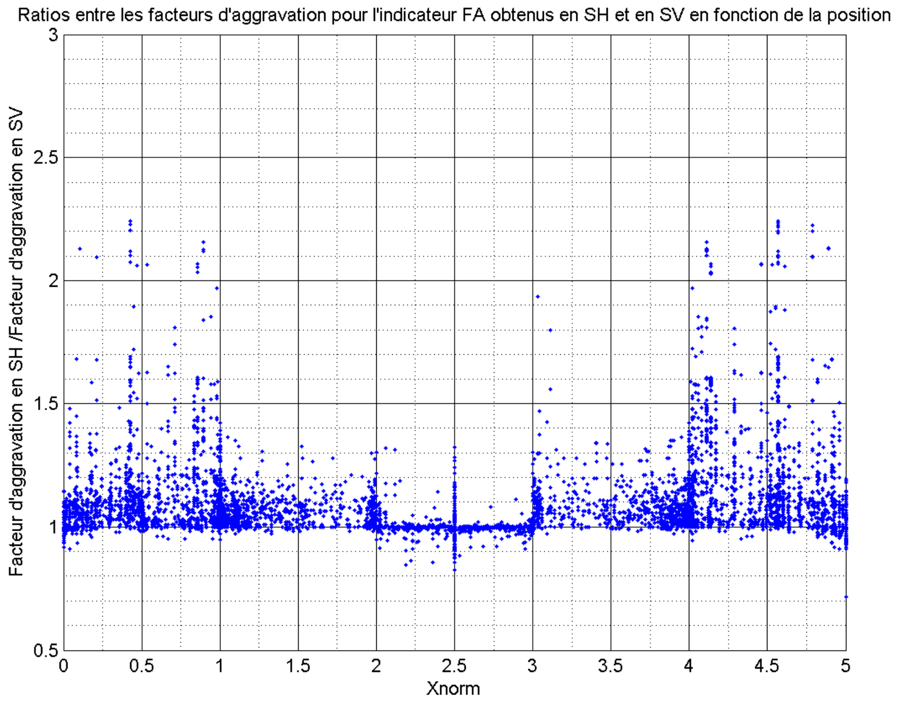

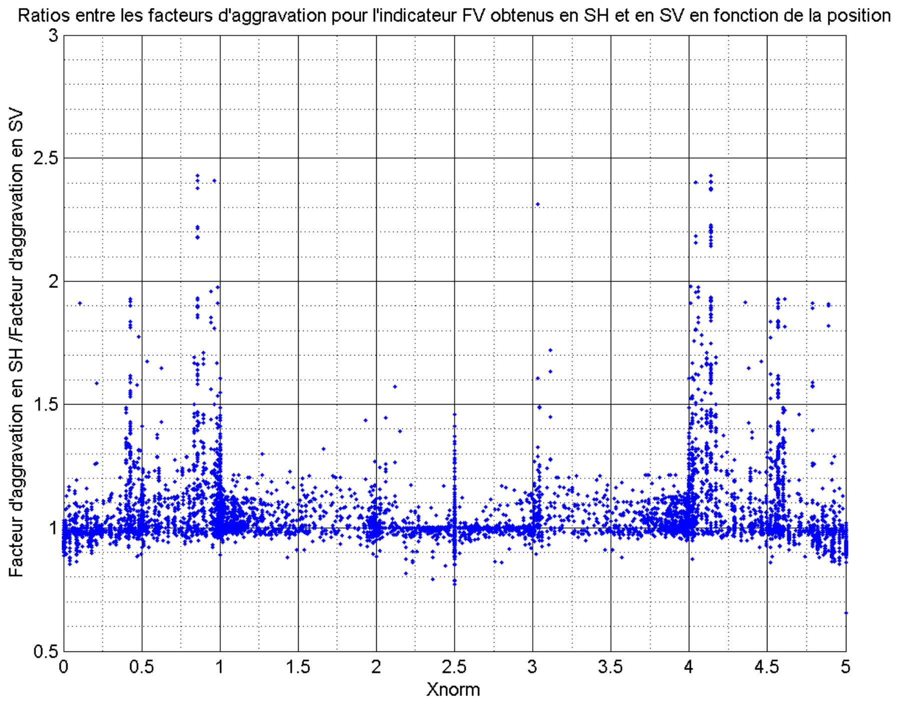

Fig. 8.33. Ratios between SH (out-of-pane) and SV (in-pane) aggravation factors for the whole set of results on the average short (Fa, top) and long period amplification factor (Fv, bottom). The horizontal axis corresponds to the associated normalized location (xnorm) within the valley.

8.5 Conclusions

The results from this comprehensive set of NERA computations have not yet been fully analysed. At this stage, a series of semi-qualitative semi-quantitative conclusions can be derived, as listed below

- The aggravation factors are component dependent, with larger values for SH, out-of-plane motion compared to SV, in-plane motion. This may be explained by the transfer of energy to the vertical component, as outlined in the other sections of this report
- The aggravation factors are parameter dependent :
    - they are generally the largest (up to 3-4) for Arias Intensity and the peak spectral amplification factor, intermediate (up to around 2-2.5) for the Cumulative Absolute Velocity, and the smallest (up to 1.5 – 2) for all the other indicators.
- The geometry has a significant control on the aggravation factor
    - For embanked valleys, the highest aggravation factors occur in the centre because of constructive interferences
    - Steep edge slopes have large effects (with aggravation factors lower than 1, i.e., deamplification effects), but only very locally just over the valley edges
    - Gentle edge slopes have significant, long distance effects because of their energetic diffraction effect
- The mechanical characteristics within the valley do affect the aggravation factor
    - The aggravation factors are generally found the largest for the largest velocity contrasts, in relation with the improved efficiency of lateral wave trapping
    - Increase in damping induce decrease of the aggravation factor, especially for high-frequency indicators (not shown here, but obtained from a small, parallel sensitivity study, and supported by the SIGMA results)
- The ground motion within the valley may be significantly prolongated, up to 10 to 15 seconds.
- The diffraction away from the lateral sloping interfaces implies a slight contamination of the motion on the rocky edges, with an increase of outcropping rock motion which may be up to 20-30%, especially in the case of steep lateral slopes. This probably contributes to the within-event aleatory variability of ground motion

Large aggravation factors (exceeding 2) in the spectral domain correspond to

- Large velocity contrasts ($V_{S,bedrock}$ /V_{S30} > 5)
- Embankment ratios Z_{max} / Width larger than 0.08
- Sites located within the central, constant thickness part of the valley (zones FW, FC and FE), or very close to it (inner parts of W1 and E1)
- Relatively steep slopes (larger than 20°) when considering sites in the central part of the valley (FW, FC, FE), and any kind of slope angles (including gentle ones) for the "inner-edge" zones W1 and E1.

The next steps are

a) to establish approximate relationship between the aggravation factors and the geo-mechanical parameters, including also the site location. This is under way through a PhD thesis, with an extensive use of the neural network approach to have a first-order estimate of the coupled effects of each parameter (velocity contrast, thickness, width, slope angles, site position)
b) to identify in tight discussion with the engineering community, some relevant threshold values for the aggravation factors on each of the various Ground Motion Intensity Parameters considered here, and to identify the geo-mechanical configurations in which one may expect such thresholds to be exceeded. This may be based on the set of NERA computations, and tested on the SIGMA computations

9 CONCLUSIONS

We

- developed methodology of calculating acceleration time histories at a site of interest assuming acceleration at a reference site for two basic configurations: a reference site is a part of the model, a reference site is not part of the model; for each of the two configurations we assumed two possible wavefield excitations: a vertical plane-wave incidence and a point DC source,
- performed extensive direct finite-difference simulations for a set of defined structural models for 6 sites of interest for the WP3 of SIGMA and calculated acceleration time histories at sites of interest assuming the configuration in which the reference site is not a part of the computational model; we performed
    - 3D simulations for 3 3D structures,
    - 2D simulations for 12 2D structures (some of them being selected 2D profiles in the 3D structures),
    - 1D simulations for local 1D models in the 2D models,
- assumed a vertical plane-wave incidence for all structures,
- assumed point DC sources for one 3D structure,
- assumed a linear behaviour,
- used a set of selected reference accelerograms from the RESORCE database,
- investigated effects of uncertainty in the bedrock velocity, velocity in sediments, attenuation in sediments, interface geometry (border slope), simultaneous variations in velocity and thickness of sediments using 12 characteristics of earthquake ground motion.

The numerical simulations can be characterized by the following numbers:

60 3D simulations

305 2D a 1D simulations (the one number meaning the fact that our 2D code makes it possible to perform simultaneously all 1D simulations for one 2D profile)

Total wall time: 220 days (of errorless simulations)

Total CPU time: 37 years assuming one CPU

The synthetic seismograms and calculated EGM characteristics take approximately 3TB of disk space.

We produced

- discrete models of the defined structural models for 6 sites of interests,
- synthetic seismograms at thousands of theoretical receiver positions,
- characteristics of earthquake ground motions.

Based on the performed simulations, calculations, descriptive statistical analysis and comparisons we can draw the following conclusions:

A. For all sites there is at least one EGM characteristic with significant 2D/1D aggravation factor. All characteristics exhibit significant 2D/1D aggravation factor on the vertical component. The anti-plane and in-plane horizontal components exhibit different behaviours. The CAV 2D/1D aggravation factor is significant at all components and all sites. 1D simulations are not sufficient for any of the investigated sites. 3D effects are pronounced in the Grenoble valley (Site 2). They are most visible on the CAV 3D/2D aggravation factors (all components). The 3D effects are less visible in the Mygdonian basin (Site 1).

B. The amplification factors and aggravation factors (mainly for the vertical component) increase with the impedance contrast. This is mainly evident at frequencies close to the fundamental resonant frequency. These conclusions are valid for all models.

C. The effect of presence of the high-velocity surface layer in the Site-2 model is negligible consistently in 1D, 2D and 3D simulations. The difference between the velocity distributions in sediments in models S6h (homogeneous) and S6g (gradient) has no effect on the 2D/1D aggravation factor. The small difference in the amplification factors for S6h and S6g can be attributed to the different impedance contrast at the sediment-bedrock interface (due to different velocity distribution in sediments).

D. As expected, the effect of attenuation is more evident at higher frequencies. The amplification factor decreases with increasing attenuation. This effect is more pronounced with increasing local thickness of sediments. Values of EGM characteristics are unrealistically large if attenuation is neglected. The 2D/1D aggravation factor is rather insensitive to variations in the attenuation. The results suggest that the effect of attenuation on the amplification can be sufficiently estimated from 1D simulations.

E. The effect of the border slope is not significant away from the border. Note that this conclusion is consistent with that by Moczo et al. (1996).

F. The 3D meander-like extension of the specified 2D model does not impact much the response: 2D approach is enough - at least as long as the curvature of the meander is restricted to the type of curvature considered and for the investigated frequency range of [0.5, 7] Hz.

G. The 2D/1D aggravation factors are less sensitive to modifications of V_S and h than the amplification factors are. The least sensitivity is at receivers atop thin sediments. The increase of the amplification factors is due to the increase of the impedance contrast.

H. Vertically incident plane waves provide robust estimates of amplification factors compared with point sources with specific azimuths. The plane-wave excitations should not, however, replace a point DC source if such a source better represents a possible excitation from a known source zone. Source variability induces an additional variability in site response (± 10%) which should be considered when the knowledge about location of potential seismic sources is very poor.

We identified the following key structural parameters:

- overall geometry of the sediment-bedrock interface; detailed geometry close to margins of the basin or valley affects mainly motions close to the margins,
- impedance contrast at the sediment-bedrock interface,
- attenuation in sediments.

10 APPENDIX: METHODOLOGY

10.1 Forward numerical modelling

The numerical simulations of seismic motion are performed using the Fortran95 computer codes FDSim3D and FDSim2D. The computational algorithm is based on the (2,4) velocity-stress staggered-grid finite-difference explicit heterogeneous scheme on Cartesian discontinuous spatial grid. Here, (2,4) means the 2nd-order accuracy in time and 4th-order accuracy in space. In the finite-difference method both medium and wavefield are represented by values in the discrete space-time grid. An explicit scheme for updating a particle velocity at a spatial position is obtained by a discrete approximation of the equation of motion and linear stress-strain relation formulated in the particle velocity vector and stress tensor. The method was concisely described in deliverable D3-97 (Kristek et al. 2013). Another basic reference is the book by Moczo et al. (2014).

10.2 Characteristics of the earthquake ground motion

In the following, $s_{\xi,i}$ will denote the ξ-th component of the acceleration at site $\vec{x}$ due to the reference i-th accelerogram $\vec{a}_i$ (do not mix up "site $\vec{x}$" with the "site" used to name the investigated localities Site 1 – Site 7). The following characteristics of the earthquake ground motion will refer to the acceleration calculated by the FD method for the model-wavefield configuration shown in the upper panel of Fig. 10.1.

10.2.1 Amplification factor

The amplification factor is defined as the ratio of the relative displacement response spectra S_D of acceleration at a site of interest, $s_{\xi,i}(t)$, and acceleration taken as a reference, $a_{\xi,i}(t)$:

$$AF_{\xi,i}(f) \equiv \frac{S_D\, s_{\xi,i}(f;5\%)}{S_D\, a_{\xi,i}(f;5\%)} \qquad (10.1)$$

The amplification factor for the horizontal component may be defined as

$$AF_{h,i}(f) \equiv \sqrt{\frac{S_D\, s_{x,i}(f;5\%)\ S_D\, s_{y,i}(f;5\%)}{S_D\, a_{x,i}(f;5\%)\ S_D\, a_{y,i}(f;5\%)}} \qquad (10.2)$$

The average amplification factor for a set of n accelerograms for the ξ-component is defined as

$$\overline{AF_\xi}(f) \equiv \sqrt[n]{\prod_{i=1}^{n} AF_{\xi,i}(f)} \qquad (10.3)$$

where $AF_{\xi,i}(f)$ is the amplification factor for the i-th accelerogram and $\xi \in \{x, y, z, h\}$. The standard deviation is defined as

$$\sigma_{\log AF} \equiv \frac{\sqrt{\sum_{i=1}^{n}\left[\log AF_{\xi,i}(f) - \log \overline{AF_\xi}(f)\right]^2}}{n-1} \qquad (10.4)$$

10.2.2 Short-period average amplification factor

The average short-period average amplification factor for a set of n accelerograms for the ξ-component at a site is defined as

$$\log \overline{F_{A_\xi}} \equiv \frac{1}{\ln 4} \int_{5}^{20} \frac{\log \overline{AF_\xi}(f)\, df}{f} \qquad (10.5)$$

10.2.3 Long-period average amplification factor

The average long-period average amplification factor for a set of n accelerograms for the ξ-component at a site is defined as

$$\log \overline{F_{V_\xi}} \equiv \frac{1}{\ln 4} \int_{0.5}^{2} \frac{\log \overline{AF_\xi}(f)\, df}{f} \qquad (10.6)$$

10.2.4 Average amplification factor for [0.75, 3.0] f$_0$

The average amplification factor for [0.75, 3.0] f_0 for a set of n accelerograms for the ξ-component at a site is defined as

$$\overline{F_{L_\xi}} \equiv 10^{\frac{1}{\ln 4} \int_{0.75 f_0}^{3 f_0} \frac{\log \overline{AF_\xi}(f)\, df}{f}} \qquad (10.7)$$

where f_0 is the fundamental resonant frequency.

10.2.5 Average amplification factor for [0.75, 3.0] f_{00}

The average amplification factor for [0.75, 3.0] f_{00} for a set of n accelerograms for the ξ-component at a site is defined as

$$\overline{F_{0_\xi}} \equiv 10^{\frac{1}{\ln 4}\int_{0.75 f_{00}}^{3 f_{00}} \frac{\log \overline{AF_\xi}(f)\,df}{f}} \qquad (10.8)$$

where $f_{00} = \min_{sites}\{f_0\}$.

10.2.6 Peak ground acceleration and peak ground velocity

The peak ground acceleration at a site is defined as

$$pga_{\xi,i}(\vec{x}) \equiv \max_t\left\{\left|s_{\xi,i}(\vec{x},t)\right|\right\} \qquad (10.9)$$

and the peak ground acceleration of the i-th accelerogram is

$$pga_{\xi,i}(\vec{x}) \equiv \max_t\left\{\left|a_{\xi,i}(\vec{x},t)\right|\right\} \qquad (10.10)$$

The pga amplification factor is defined as

$$AF_{\xi,i}\{pga\} \equiv \frac{pga_{\xi,i}(\vec{x})}{pga_{\xi,i}(\vec{x})} \qquad (10.11)$$

The average pga amplification factor is defined as

$$\overline{AF_\xi}\{pga\} \equiv \sqrt[n]{\prod_{i=1}^{n} AF_{\xi,i}\{pga\}} \qquad (10.12)$$

The peak-ground-velocity characteristics are defined analogously.

10.2.7 Cumulative absolute velocity

The cumulative absolute velocity at a site is defined as

$$CAV\left(s_{\xi,i}(\vec{x})\right) \equiv \int_0^\infty \left|s_{\xi,i}(\vec{x},t)\right| dt \qquad (10.13)$$

and the cumulative absolute velocity of the i-th accelerogram is

$$CAV\left(a_{\xi,i}(\vec{x})\right) \equiv \int_0^\infty \left| a_{\xi,i}(\vec{x},t) \right| dt \tag{10.14}$$

The CAV amplification factor is defined as

$$AF_{\xi,i}\{CAV\} \equiv \frac{CAV\left(s_{\xi,i}(\vec{x})\right)}{CAV\left(a_{\xi,i}(\vec{x})\right)} \tag{10.15}$$

The average CAV amplification factor is defined as

$$\overline{AF_\xi}\{CAV\} \equiv \sqrt[n]{\prod_{i=1}^n AF_{\xi,i}\{CAV\}} \tag{10.16}$$

10.2.8 Auxiliary quantities – cumulative square acceleration

For definitions of the Arias intensity, strong ground motion duration and root-mean-square acceleration we will use the auxiliary quantities – cumulative square accelerations

$$\begin{aligned} mcsa\left(s_{\xi,i}(\vec{x})\right) &\equiv \int_0^\infty s_{\xi,i}^2(\vec{x},t)\,dt \\ csa\left(t;s_{\xi,i}(\vec{x})\right) &\equiv \int_0^t s_{\xi,i}^2(\vec{x},\tau)\,d\tau \end{aligned} \tag{10.17}$$

Analogous quantities are defined for the i-th accelerogram $a_{\xi,i}$.

10.2.9 Arias intensity

The Arias intensity at a site is defined as

$$I_A\left(s_{\xi,i}(\vec{x})\right) \equiv \frac{\pi}{2g}\,mcsa\left(s_{\xi,i}(\vec{x})\right) \tag{10.18}$$

and the Arias intensity of the i-th accelerogram is

$$I_A\left(a_{\xi,i}(\vec{x})\right) \equiv \frac{\pi}{2g}\,mcsa\left(a_{\xi,i}(\vec{x})\right) \tag{10.19}$$

The I_A amplification factor $AF_{\xi,i}\{I_A\}$ and the corresponding average amplification factor $\overline{AF_\xi}\{I_A\}$ are defined analogously to the CAV factors.

10.2.10 Duration of strong ground motion

Two durations of strong ground motion at a site are defined as

$$D_{TB}\left[5\%-95\%\,;s_{\xi,i}(\vec{x})\right] \equiv t^{95}\left(s_{\xi,i}(\vec{x})\right)-t^{5}\left(s_{\xi,i}(\vec{x})\right)$$
$$D_{TB}\left[5\%-75\%\,;s_{\xi,i}(\vec{x})\right] \equiv t^{75}\left(s_{\xi,i}(\vec{x})\right)-t^{5}\left(s_{\xi,i}(\vec{x})\right) \quad (10.20)$$

where

$$t^{95}\left(s_{\xi,i}(\vec{x})\right) \equiv t\ \left(csa\left(t;s_{\xi,i}(\vec{x})\right)=0.95\,mcsa\left(s_{\xi,i}(\vec{x})\right)\right)$$
$$t^{75}\left(s_{\xi,i}(\vec{x})\right) \equiv t\ \left(csa\left(t;s_{\xi,i}(\vec{x})\right)=0.75\,mcsa\left(s_{\xi,i}(\vec{x})\right)\right) \quad (10.21)$$
$$t^{5}\left(s_{\xi,i}(\vec{x})\right) \equiv t\ \left(csa\left(t;s_{\xi,i}(\vec{x})\right)=0.05\,mcsa\left(s_{\xi,i}(\vec{x})\right)\right)$$

Analogous quantities are defined for the i-th accelerogram $a_{\xi,i}$.

10.2.11 Prolongation factor of the strong-ground-motion duration

The prolongation factor at a site is defined as

$$PF_{\xi,i}\left\{D_{TB}\left[5\%-95\%\,;s_{\xi,i}(\vec{x})\right]\right\}$$
$$\equiv D_{TB}\left[5\%-95\%\,;s_{\xi,i}(\vec{x})\right]-D_{TB}\left[5\%-95\%\,;a_{\xi,i}(\vec{x})\right] \quad (10.22)$$

and the average prolongation factor for a set of n accelerograms is defined as

$$\overline{PF_{\xi}}\left\{D_{TB}\left[5\%-95\%\right]\right\} = \frac{1}{n}\sum_{i=1}^{n} PF_{\xi,i}\left\{D_{TB}\left[5\%-95\%\,;s_{\xi,i}(\vec{x})\right]\right\} \quad (10.23)$$

10.2.12 Root-mean-square acceleration

The root-mean-square acceleration at a site is defined as

$$a_{rms}\left(s_{\xi,i}(\vec{x})\right) = \left[\frac{0.9}{t^{95}\left(s_{\xi,i}(\vec{x})\right)-t^{5}\left(s_{\xi,i}(\vec{x})\right)}\int_{t^{5}\left(s_{\xi,i}(\vec{x})\right)}^{t^{95}\left(s_{\xi,i}(\vec{x})\right)} s_{\xi,i}^{2}(\vec{x},t)\,dt\right]^{1/2} \quad (10.24)$$

The root-mean-square acceleration for the i-th accelerogram is defined analogously. The a_{rms} amplification factor $AF_{\xi,i}\{a_{rms}\}$ and the corresponding average amplification factor $\overline{AF_{\xi}}\{a_{rms}\}$ are defined analogously to the CAV factors.

10.2.13 Spectrum intensity

The spectrum intensity at a site is defined using the pseudo-spectral velocity response spectrum PSV at a site as

$$SI\left(s_{\xi,i}\right) = \int_{0.1}^{2.5} PSV\ s_{\xi,i}\left(\mathrm{T}; 5\%\right) dT \qquad (10.25)$$

The spectrum intensity for the i -th accelerogram is defined analogously. The SI amplification factor $AF_{\xi,i}\left\{SI\right\}$ and the corresponding average amplification factor $\overline{AF_{\xi}}\left\{SI\right\}$ are defined analogously to the CAV factors.

10.2.14 Aggravation factors

For a given site we define three aggravation factors for the ξ-component

$$\begin{aligned} AGF_{\xi,32}\left(\varphi\right) &= \frac{\varphi_{\xi,3\mathrm{D}}}{\varphi_{\xi,2\mathrm{D}}} \\ AGF_{\xi,31}\left(\varphi\right) &= \frac{\varphi_{\xi,3\mathrm{D}}}{\varphi_{\xi,1\mathrm{D}}} \\ AGF_{\xi,21}\left(\varphi\right) &= \frac{\varphi_{\xi,2\mathrm{D}}}{\varphi_{\xi,1\mathrm{D}}} \end{aligned} \qquad (10.26)$$

where φ denotes an average amplification factor of a characteristic of earthquake ground motion at the site, and 3D, 2D and 1D indicate dimension of a medium-wavefield configuration.

10.3 Wavefield-model configurations

Fig. 10.1 shows two basic site configurations of a site at which we assume acceleration $\vec{a}_i$.

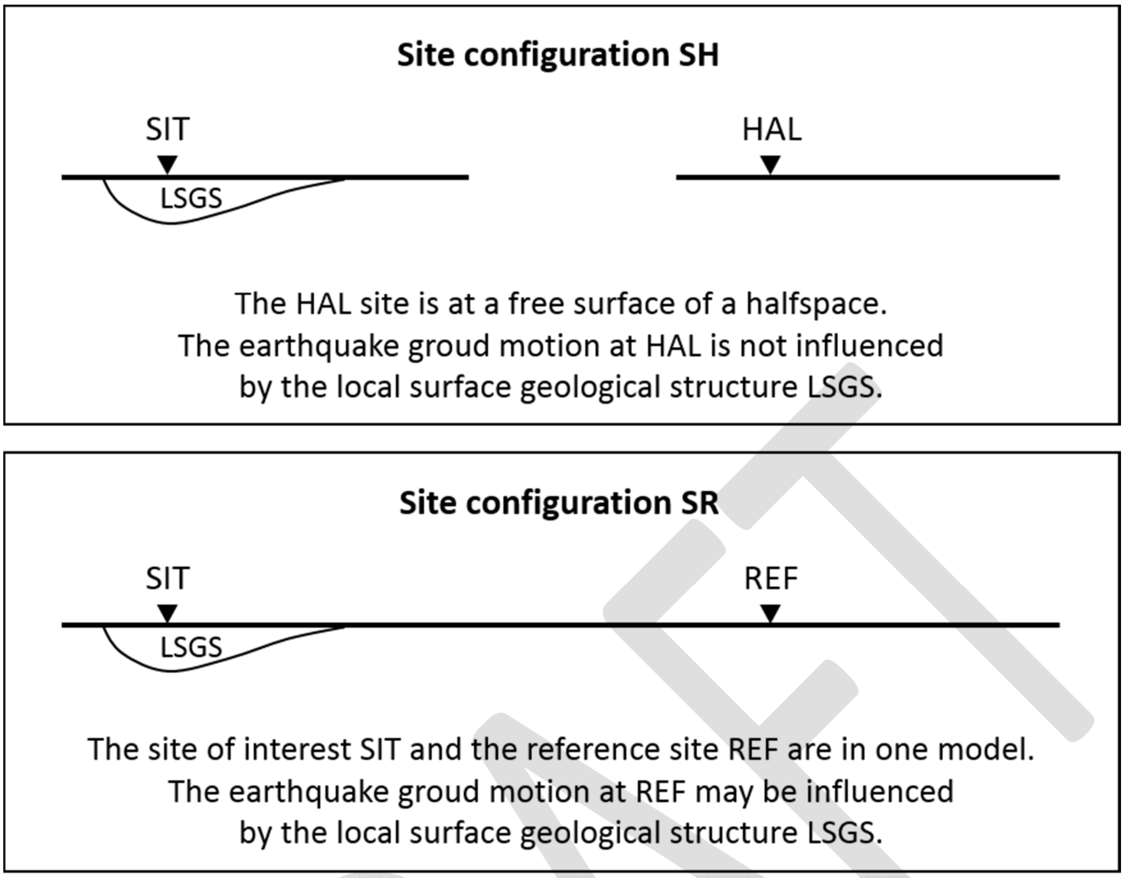

Fig. 10.1. Two site configurations considered in the analysis. S relates to site SIT, H to halfspace and thus to site HAL and R to the reference site REF. LSGS denotes the local surface geological structure.

In the SR configuration we assume that an accelerogram (from the set of selected accelerograms) represents earthquake ground motion at a site (REF) which is within the computational model comprising the local surface geological structure (LSGS). This means that the acceleration at REF may be influenced by LSGS. For given LSGS and wavefield excitation a level of influence depends on a position of REF with respect to LSGS.

In the SH configuration we assume that an accelerogram (from the set of selected accelerograms) represents earthquake ground motion at a site (HAL) which is not within the computational model comprising LSGS. This means that the acceleration at HAL is not influenced by LSGS.

If no records are available for the investigated site (represented by the computational model with LSGS) and a set of accelerograms recorded at different locations is used in order to represent variability of the earthquake ground motion, it is reasonable to assume that the records represent ground motions at a free surface of a halfspace. This corresponds to the typical situation in PSHA: the estimated characteristics of the earthquake ground motion relate to the free surface of a halfspace.

The question is then how the presence of LSGS modifies the ground motion. Therefore, we assume that the SH configuration is more appropriate for our analysis. At the same time, the SR configuration is reasonable if we are specifically interested in comparing two sites within the same site of interests. Consequently, we will develop methodology for evaluations of the amplification factors for both configurations. Later we will show results based on the two configuration assumptions.

In both two basic site configurations we may consider different types of wavefield excitation. In our analysis we will consider wavefield excitation by a vertically impinging plane wave and by a point earthquake source. Thus we will consider four model-wavefield configurations. They are shown in Fig. 10.2.

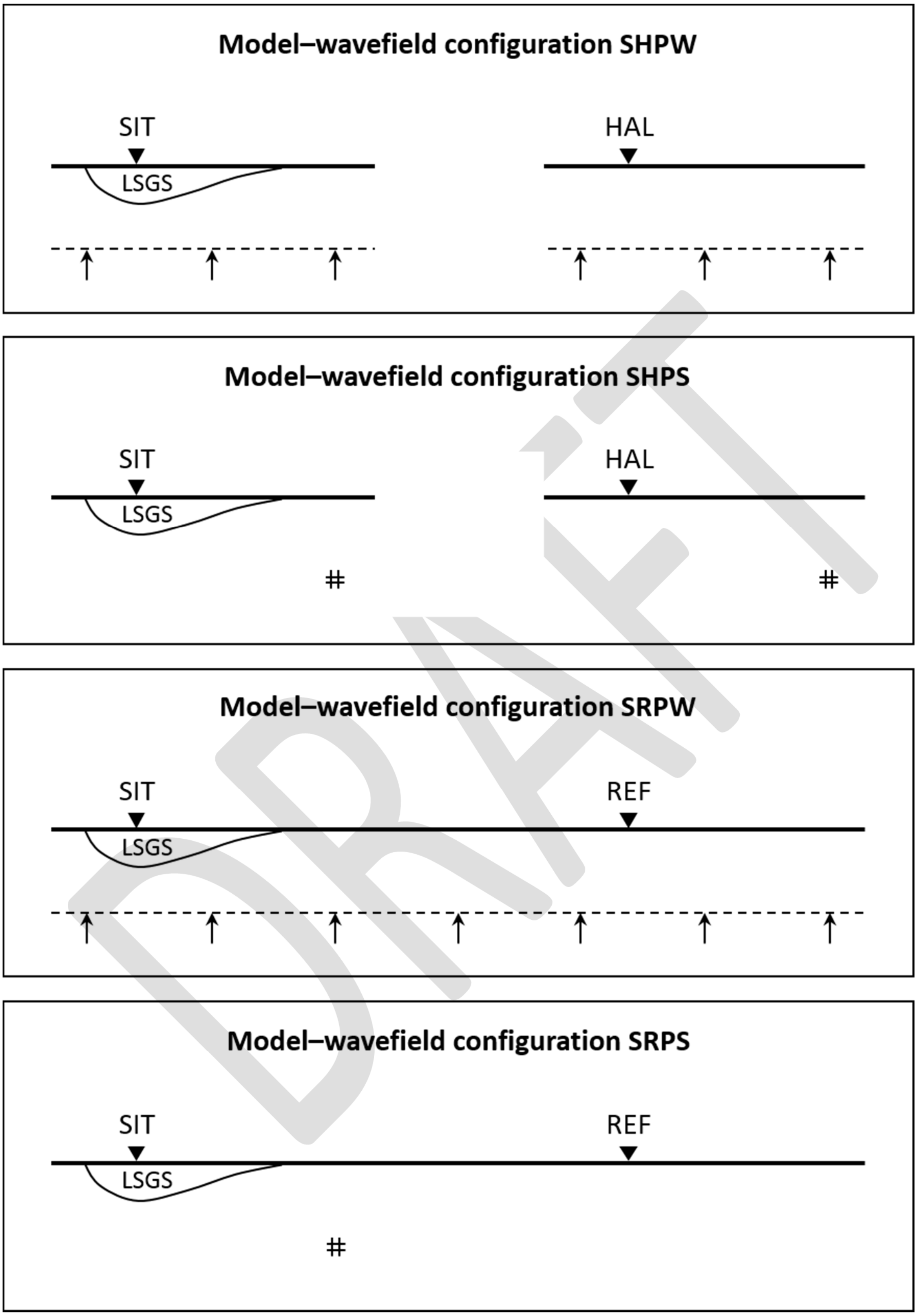

Fig. 10.2. Four model-wavefield configurations considered in the analysis. The first letter S relates to site SIT, H relates to halfspace and thus to site HAL, R to the reference site REF, PW to plane-wave, PS to point earthquake source.

10.3.1 Configuration SHPW: reference site is not in the model, plane-wave excitation

The configuration is shown in the top panel of Fig. 10.2 and detailed in Fig. 10.3.

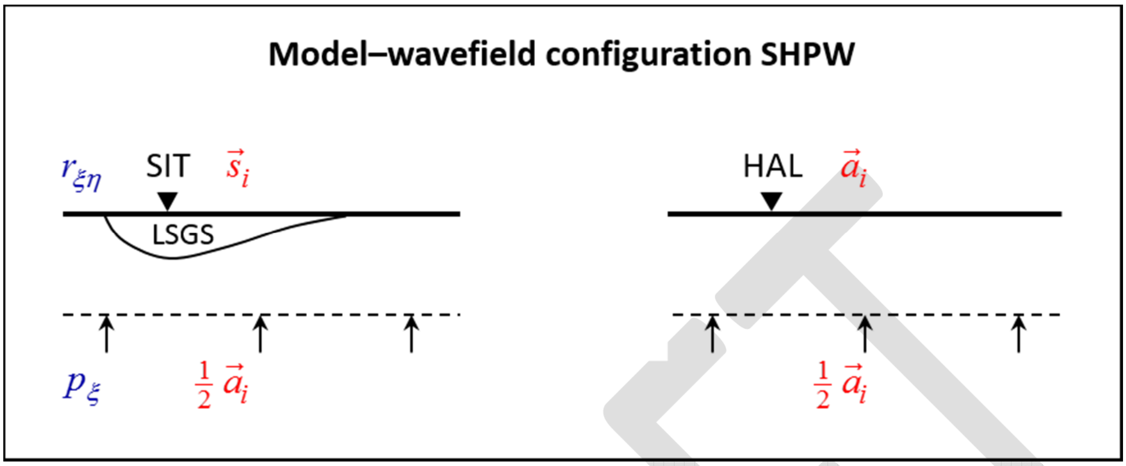

Fig. 10.3. Illustration of input and output signals. Details in the text.

In this configuration we assume a vertical incidence of a plane wave as the way of the wavefield and ground motion excitation. Define the following quantities:

Pseudoimpulse input signal. We consider the pseudoimpulse input signal in the particle velocity as the Gabor signal

$$p(t) \equiv \exp\left\{-\left[\omega_p (t - t_s)/\gamma_s\right]^2\right\} \cos\left[\omega_p (t - t_s) + \theta\right] \qquad (10.27)$$

Here $\omega_p = 2\pi f_p$, γ_s controls the width of the signal, θ is a phase shift. For this study we chose $f_p = 0.45$ Hz, $\gamma_s = 0.35$, $\theta = \pi/2$ and $t_s = 0.5$ s. (In many simulations, it is sufficient to use a smaller value determined by formula $t_s = 0.45\gamma_s / f_p$. Here we chose large t_s in order to have a smaller onset of the signal.) The signal, and its amplitude and phase Fourier spectra are shown Fig. 10.4. For obtaining the transfer properties at a site for a vertical incidence of a plane wave it is reasonable to assume

$$p_x(t) \equiv p_y(t) \equiv p_z(t) \equiv p(t) \qquad (10.28)$$

The Fourier spectrum of the input signal will be denoted by $\mathcal{F} p(f)$.

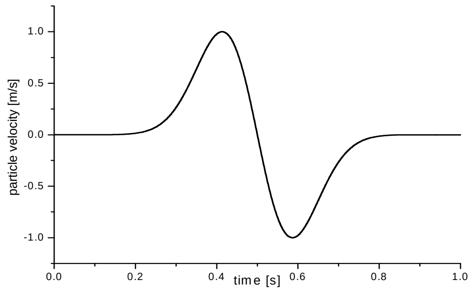

Pseudoimpulse input signal in the particle velocity

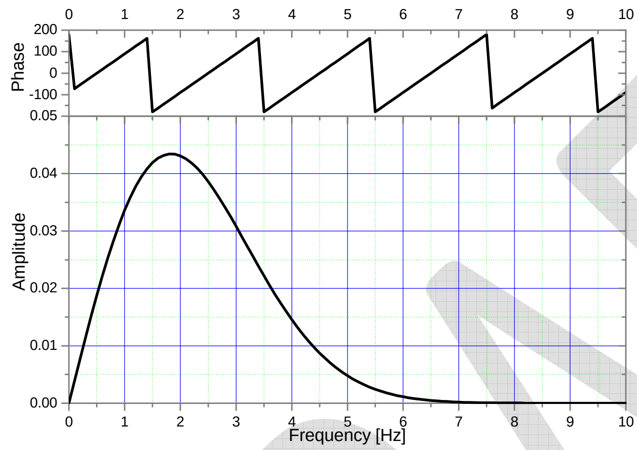

Amplitude and phase Fourier spectra of the input signal

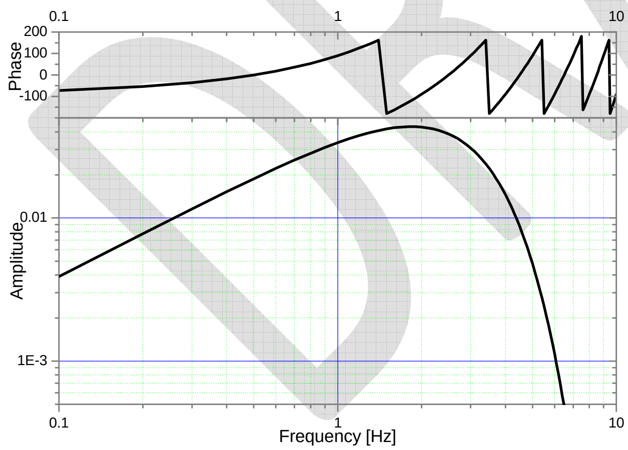

Loglog amplitude and log phase Fourier spectra of the input signal

Fig. 10.4. The input signal and its spectra

Matrix of the time-domain pseudoimpulse responses. A plane wave polarized in the x-direction results in the time-domain pseudoimpulse responses (in particle velocity) $r_{xx}(t), r_{xy}(t)$ and $r_{xz}(t)$ at site SIT. The second index indicates the component of the response. Analogously, a plane wave polarized in the y-direction results in responses $r_{yx}(t), r_{yy}(t), r_{yz}(t)$, and a plane wave polarized in the z-direction results in responses $r_{zx}(t), r_{zy}(t), r_{zz}(t)$. The matrix of the time-domain pseudoimpulse responses is then

$$\mathbf{R} \equiv \begin{bmatrix} r_{xx} & r_{yx} & r_{zx} \\ r_{xy} & r_{yy} & r_{zy} \\ r_{xz} & r_{yz} & r_{zz} \end{bmatrix} \tag{10.29}$$

and its Fourier transform is $\mathcal{F}\mathbf{R}$.

Matrix of the Fourier transfer functions. The matrix is defined as

$$\mathbf{FTF} \equiv \frac{\mathcal{F}\mathbf{R}}{\mathcal{F}p} \tag{10.30}$$

and characterizes transfer properties of the model between the horizontal plane at which the excitation by the plane wave is applied and site of interest SIT.

Acceleration at the free surface of a halfspace. Assume acceleration $\vec{a}_i(t)$ at site HAL, that is, at the free surface of a homogeneous halfspace. This means, that $\frac{1}{2}\vec{a}_i(t)$ is the acceleration of the incident plane wave. Index i denotes the i-th of n selected accelerograms.

Note, that in the numerical simulations we cannot use exactly $\frac{1}{2}\vec{a}_i(t)$ for convolution in the local structure. This is because the numerically evaluated transfer function includes effects of a discrete grid (grid dispersion). Consequently, if we replaced the local structure by a homogeneous medium (getting so the model of a homogeneous halfspace), we would not get for $\frac{1}{2}\vec{a}_i(t)$ in the incident wave exactly $\vec{a}_i(t)$ at the free surface. Therefore we apply the numerically evaluated "$\frac{1}{2}\vec{a}_i(t)$" in the convolution.

Acceleration at a site of interest SIT. If $\vec{a}_i(t)$ is the acceleration at site HAL, then the corresponding acceleration at site SIT is $\vec{s}_i(t)$. It is obtained as

$$\begin{pmatrix} s_{x,i} \\ s_{y,i} \\ s_{z,i} \end{pmatrix} = \frac{1}{2}\mathcal{F}^{-1}\left\{ \mathbf{FTF} \begin{pmatrix} a_{x,i} \\ a_{y,i} \\ a_{z,i} \end{pmatrix} \right\} \tag{10.31}$$

10.3.2 Configuration SHPS: reference site is not in the model, point earthquake source

The configuration is shown in the second panel from the top of Fig. 10.2 and detailed in Fig. 10.5. In this configuration we assume that the wavefield and ground motion are due to a point earthquake source. An arbitrary point earthquake source can be obtained by a linear combination of 6 independent elementary sources. Define the following quantities:

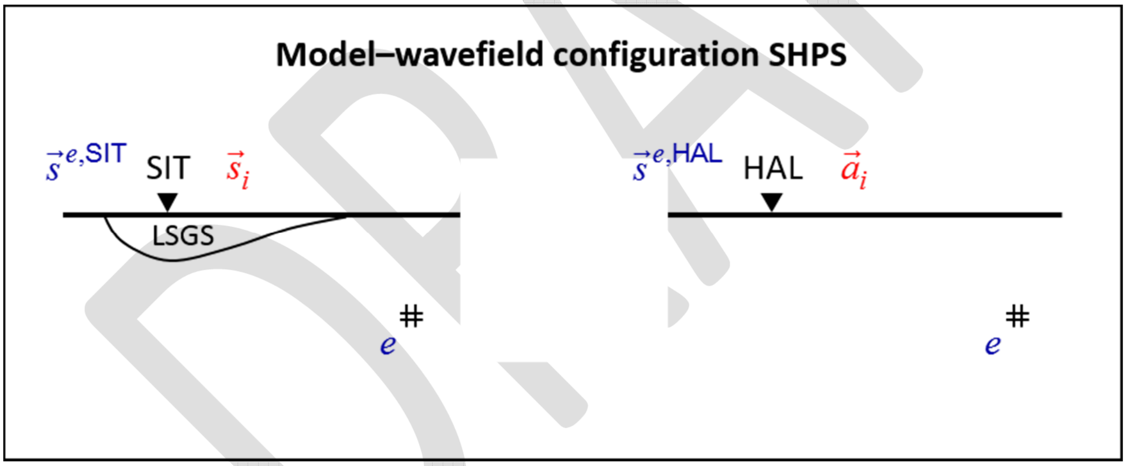

Fig. 10.5. Illustration of input and output signals. The lower-case e represents an elementary source. Details in the text.

Elementary sources e**.** 6 elementary sources comprise 3 dipoles and 3 double couples. Their moment tensors are

$$\mathbf{M}_1 \equiv M_0 \begin{bmatrix} 1 & 0 & 0 \\ 0 & 0 & 0 \\ 0 & 0 & 0 \end{bmatrix} \quad \mathbf{M}_2 \equiv M_0 \begin{bmatrix} 0 & 0 & 0 \\ 0 & 1 & 0 \\ 0 & 0 & 0 \end{bmatrix} \quad \mathbf{M}_3 \equiv M_0 \begin{bmatrix} 0 & 0 & 0 \\ 0 & 0 & 0 \\ 0 & 0 & 1 \end{bmatrix}$$
$$\mathbf{M}_4 \equiv M_0 \begin{bmatrix} 0 & 1 & 0 \\ 1 & 0 & 0 \\ 0 & 0 & 0 \end{bmatrix} \quad \mathbf{M}_5 \equiv M_0 \begin{bmatrix} 0 & 0 & 1 \\ 0 & 0 & 0 \\ 1 & 0 & 0 \end{bmatrix} \quad \mathbf{M}_6 \equiv M_0 \begin{bmatrix} 0 & 0 & 0 \\ 0 & 0 & 1 \\ 0 & 1 & 0 \end{bmatrix} \qquad (10.32)$$

Fig. 10.6 shows the normalized source-time function of slip for each of the 6 elementary sources.

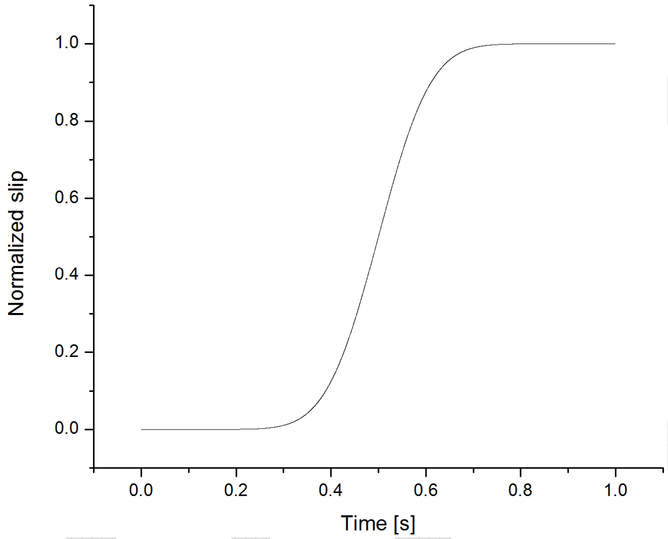

Fig. 10.6. Normalized source-time function of slip considered for each of the 6 elementary sources.

Particle velocity at HAL due to an elementary source. An elementary source e acting in the homogeneous halfspace causes particle velocity $\vec{s}^{\,e,\mathrm{HAL}}$; $e \in \{1, 2, \ldots, 6\}$ at HAL. The matrix of the elementary velocity seismograms at HAL for all 6 elementary sources is then defined as

$$\mathbf{S}_{elem}^{\mathrm{HAL}} \equiv \begin{bmatrix} s_x^{1,\mathrm{HAL}} & s_x^{2,\mathrm{HAL}} & s_x^{3,\mathrm{HAL}} & s_x^{4,\mathrm{HAL}} & s_x^{5,\mathrm{HAL}} & s_x^{6,\mathrm{HAL}} \\ s_y^{1,\mathrm{HAL}} & s_y^{2,\mathrm{HAL}} & s_y^{3,\mathrm{HAL}} & s_y^{4,\mathrm{HAL}} & s_y^{5,\mathrm{HAL}} & s_y^{6,\mathrm{HAL}} \\ s_z^{1,\mathrm{HAL}} & s_z^{2,\mathrm{HAL}} & s_z^{3,\mathrm{HAL}} & s_z^{4,\mathrm{HAL}} & s_z^{5,\mathrm{HAL}} & s_z^{6,\mathrm{HAL}} \end{bmatrix} \qquad (10.33)$$

The analogous matrix of the corresponding acceleration seismograms may be denoted as $\mathbf{A}_{elem}^{\mathrm{HAL}}$.

Particle velocity at SIT due to an elementary source. An elementary source e acting in the model with LSGS causes particle velocity $\vec{s}^{\,e,\mathrm{SIT}}$; $e \in \{1, 2, ..., 6\}$ at SIT. The matrix of the elementary velocity seismograms at SIT for all 6 elementary sources is then defined as

$$\mathbf{S}_{elem}^{\mathrm{SIT}} \equiv \begin{bmatrix} s_x^{1,\mathrm{SIT}} & s_x^{2,\mathrm{SIT}} & s_x^{3,\mathrm{SIT}} & s_x^{4,\mathrm{SIT}} & s_x^{5,\mathrm{SIT}} & s_x^{6,\mathrm{SIT}} \\ s_y^{1,\mathrm{SIT}} & s_y^{2,\mathrm{SIT}} & s_y^{3,\mathrm{SIT}} & s_y^{4,\mathrm{SIT}} & s_y^{5,\mathrm{SIT}} & s_y^{6,\mathrm{SIT}} \\ s_z^{1,\mathrm{SIT}} & s_z^{2,\mathrm{SIT}} & s_z^{3,\mathrm{SIT}} & s_z^{4,\mathrm{SIT}} & s_z^{5,\mathrm{SIT}} & s_z^{6,\mathrm{SIT}} \end{bmatrix} \qquad (10.34)$$

The analogous matrix of the corresponding acceleration seismograms may be denoted as $\mathbf{A}_{elem}^{\mathrm{SIT}}$.

Acceleration at the free surface of a halfspace. Assume acceleration $\vec{a}_i(t)$ at site HAL, that is, at the free surface of a homogeneous halfspace. This is due to some point earthquake source acting at the same position where we assumed the elementary source. We want to find coefficients $c_{1,i}$, $c_{2,i}$, $c_{3,i}$, $c_{4,i}$, $c_{5,i}$, $c_{6,i}$ of the linear combination of the elementary solutions such that

$$\begin{pmatrix} \mathcal{F} a_{x,i} \\ \mathcal{F} a_{y,i} \\ \mathcal{F} a_{z,i} \end{pmatrix} = \sum_{e=1}^{6} c_{e,i} \begin{pmatrix} \mathcal{F} a_x^{e,\mathrm{HAL}} \\ \mathcal{F} a_y^{e,\mathrm{HAL}} \\ \mathcal{F} a_z^{e,\mathrm{HAL}} \end{pmatrix} \qquad (10.35)$$

that is,

$$\begin{pmatrix} \mathcal{F} a_{x,i} \\ \mathcal{F} a_{y,i} \\ \mathcal{F} a_{z,i} \end{pmatrix} = \mathcal{F} \mathbf{A}_{elem}^{\mathrm{HAL}} \begin{pmatrix} c_{1,i} \\ c_{2,i} \\ c_{3,i} \\ c_{4,i} \\ c_{5,i} \\ c_{6,i} \end{pmatrix} \qquad (10.36)$$

If we find a pseudo-inverse matrix to $\mathcal{F} \mathbf{A}_{elem}^{\mathrm{HAL}}$ we can determine coefficients $c_{1,i}$, $c_{2,i}$, ..., $c_{6,i}$. Matrix $\mathcal{F} \mathbf{A}_{elem}^{\mathrm{HAL}}$ is the complex 3×6 matrix. It can be decomposed using the Singular Value Decomposition (SVD) method:

$$\mathcal{F} \mathbf{A}_{elem}^{\mathrm{HAL}} = \mathbf{U} \mathbf{S} \mathbf{V}^{\dagger} \qquad (10.37)$$

Here $\mathbf{U}$ is the unitary 3×3 matrix and $\mathbf{V}$ is the unitary 6×6 matrix. $\mathbf{V}^{\dagger}$ is the Hermitian conjugate (or adjoint) matrix to $\mathbf{V}$:

$$\mathbf{V}^{\dagger} = \left(\mathbf{V}^{*}\right)^{\mathrm{T}} = \left(\mathbf{V}^{\mathrm{T}}\right)^{*} \tag{10.38}$$

where * indicates complex conjugate and $^{\mathrm{T}}$ transpose. The unitary matrices satisfy relations

$$\mathbf{U}^{\dagger}\,\mathbf{U} = \mathbf{I} \quad , \quad \mathbf{V}^{\dagger}\,\mathbf{V} = \mathbf{I} \tag{10.39}$$

where $\mathbf{I}$ and $\mathbf{I}$ denote the 3×3 and 6×6 identity matrices, respectively. $\mathbf{S}$ is the diagonal 3×6 matrix in the sense that $\mathbf{S}_{ij} = 0$ if $i \neq j$. The diagonal elements may be denoted by S_j for $j = 1, 2, 3$ and are termed the singular values of matrix $\mathcal{F}\mathbf{A}_{elem}^{\mathrm{HAL}}$:

$$\mathbf{S} = \begin{bmatrix} S_1 & 0 & 0 & 0 & 0 & 0 \\ 0 & S_2 & 0 & 0 & 0 & 0 \\ 0 & 0 & S_3 & 0 & 0 & 0 \end{bmatrix} \tag{10.40}$$

Substituting $\mathcal{F}\mathbf{A}_{elem}^{\mathrm{HAL}}$ in Eq. (10.36) by the r.h.s. of Eq. (10.37), and then by sequential multiplying Eq. (10.36) by $\mathbf{U}^{\dagger}$, $\mathbf{S}^{-1}$ and $\mathbf{V}$ we obtain

$$\begin{pmatrix} c_{1,i} \\ c_{2,i} \\ c_{3,i} \\ c_{4,i} \\ c_{5,i} \\ c_{6,i} \end{pmatrix} = \mathbf{V}\,\mathbf{S}^{-1}\,\mathbf{U}^{\dagger} \begin{pmatrix} \mathcal{F}a_{x,i} \\ \mathcal{F}a_{y,i} \\ \mathcal{F}a_{z,i} \end{pmatrix} \tag{10.41}$$

where

$$\mathbf{S}^{-1} = \begin{bmatrix} S_1^{-1} & 0 & 0 \\ 0 & S_2^{-1} & 0 \\ 0 & 0 & S_3^{-1} \\ 0 & 0 & 0 \\ 0 & 0 & 0 \\ 0 & 0 & 0 \end{bmatrix} \tag{10.42}$$

Acceleration at a site of interest SIT. If $\vec{a}_i(t)$ is the acceleration at site HAL, then the corresponding acceleration at site SIT is $\vec{s}_i(t)$. As $\vec{a}_i(t)$ is the linear combination of the elementary solutions, Eq. (10.35) or (10.36), in the homogeneous halfspace, analogously $\vec{s}_i(t)$ is the same linear combination of the elementary solutions in the model with LSGS

$$\begin{pmatrix} \mathcal{F} s_{x,i} \\ \mathcal{F} s_{y,i} \\ \mathcal{F} s_{z,i} \end{pmatrix} = \mathcal{F} \mathbf{A}_{elem}^{\text{SIT}} \begin{pmatrix} c_{1,i} \\ c_{2,i} \\ c_{3,i} \\ c_{4,i} \\ c_{5,i} \\ c_{6,i} \end{pmatrix} \tag{10.43}$$

Substituting the vector of the coefficients in Eq. (10.43) by the r.h.s. of Eq. (10.41) we obtain

$$\begin{pmatrix} \mathcal{F} s_{x,i} \\ \mathcal{F} s_{y,i} \\ \mathcal{F} s_{z,i} \end{pmatrix} = \mathcal{F} \mathbf{A}_{elem}^{\text{SIT}} \ \mathbf{V}\,\mathbf{S}^{-1}\,\mathbf{U}^{\dagger} \begin{pmatrix} \mathcal{F} a_{x,i} \\ \mathcal{F} a_{y,i} \\ \mathcal{F} a_{z,i} \end{pmatrix} \tag{10.44}$$

Define matrix $\mathbf{MESH}$:

$$\mathbf{MESH} \equiv \mathcal{F} \mathbf{A}_{elem}^{\text{SIT}} \ \mathbf{V}\,\mathbf{S}^{-1}\,\mathbf{U}^{\dagger} \tag{10.45}$$

$\mathbf{M}$, $\mathbf{E}$, $\mathbf{S}$ and $\mathbf{H}$ stand for ‚matrix', ‚elementary', ‚SIT' and ‚HAL', respectively. Using $\mathbf{MESH}$ in Eq. (10.44) we obtain for the desired acceleration at SIT:

$$\begin{pmatrix} s_{x,i} \\ s_{y,i} \\ s_{z,i} \end{pmatrix} = \mathcal{F}^{-1} \left\{ \mathbf{MESH} \begin{pmatrix} \mathcal{F} a_{x,i} \\ \mathcal{F} a_{y,i} \\ \mathcal{F} a_{z,i} \end{pmatrix} \right\} \tag{10.46}$$

It is clear from the latter relation that matrix $\mathbf{MESH}$ represents relation between ground motion at HAL and SIT assuming that the wavefield and ground motion were generated by a point earthquake source. The matrix has the meaning of the spectral matrix ratio $\mathcal{F} \mathbf{A}_{elem}^{\text{SIT}} \left[\mathcal{F} \mathbf{A}_{elem}^{\text{HAL}} \right]^{-1}$. Therefore it is equivalent to the analogous spectral matrix ratio $\mathcal{F} \mathbf{S}_{elem}^{\text{SIT}} \left[\mathcal{F} \mathbf{S}_{elem}^{\text{HAL}} \right]^{-1}$. Consequently,

$$\mathbf{MESH} \equiv \mathcal{F}\mathbf{A}_{elem}^{\mathrm{SIT}} \ \mathbf{V}_S \ \mathbf{S}_S^{-1} \ \mathbf{U}_S^{\dagger} \qquad (10.47)$$

where subscript $_S$ indicates that the three matrices relate to decomposition

$$\mathcal{F}\mathbf{S}_{elem}^{\mathrm{HAL}} = \mathbf{U}_S \ \mathbf{S}_S \ \mathbf{V}_S^{\dagger} \qquad (10.48)$$

In fact, given our numerical-modelling method, that is, the velocity-stress finite-difference scheme, we primarily obtain $\mathcal{F}\mathbf{S}_{elem}^{\mathrm{HAL}}$ and $\mathcal{F}\mathbf{S}_{elem}^{\mathrm{SIT}}$ and therefore we make use of relation (10.47) for determining matrix $\mathbf{MESH}$.

10.3.3 Configuration SRPW: reference site is in the model, plane-wave excitation

The configuration is shown in the second panel from the bottom of Fig. 10.2 and detailed in Fig. 10.7.

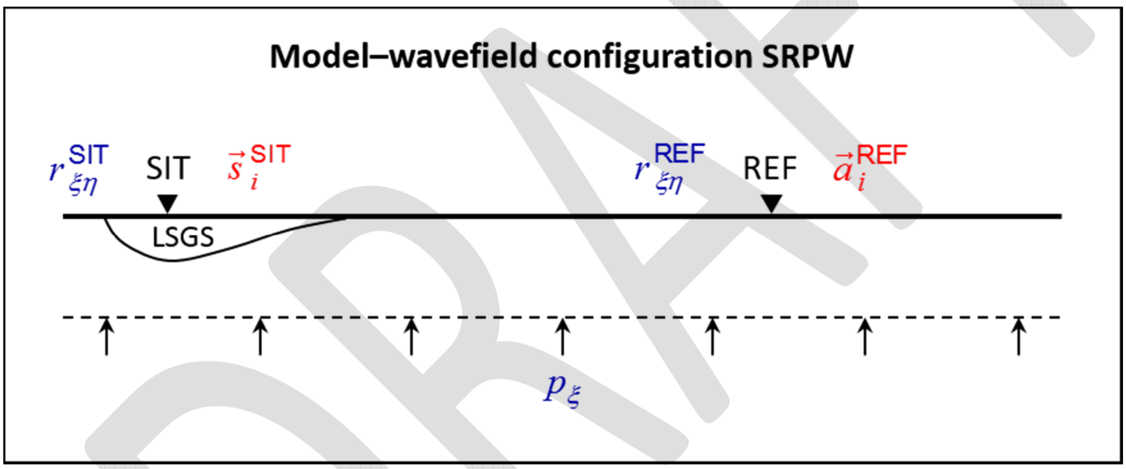

Fig. 10.7. Illustration of input and output signals. Details in the text.

In this configuration we assume a vertical incidence of a plane wave as the way of the wavefield and ground motion excitation. Both the site of interest SIT and the reference site REF are in one model comprising LSGS. Define the following quantities:

Pseudoimpulse input signal. We consider the same pseudoimpulse input signal in the particle velocity as defined by Eq. (10.27) and excitations as defined by Eq. (10.28).

Matrix of the time-domain pseudoimpulse responses at REF. A plane wave polarized in the x-direction results in the time-domain pseudoimpulse responses (in particle velocity) $r_{xx}^{\mathrm{REF}}(t), r_{xy}^{\mathrm{REF}}(t)$

and $r_{xz}^{\mathrm{REF}}(t)$ at site REF. The second index indicates the component of the response. Analogously, a plane wave polarized in the y-direction results in responses $r_{yx}^{\mathrm{REF}}(t), r_{yy}^{\mathrm{REF}}(t), r_{yz}^{\mathrm{REF}}(t)$, and a plane wave polarized in the z-direction results in responses $r_{zx}^{\mathrm{REF}}(t), r_{zy}^{\mathrm{REF}}(t), r_{zz}^{\mathrm{REF}}(t)$. The matrix of the time-domain pseudoimpulse responses at REF is then

$$\mathbf{R}_{\mathrm{REF}} \equiv \begin{bmatrix} r_{xx}^{\mathrm{REF}} & r_{yx}^{\mathrm{REF}} & r_{zx}^{\mathrm{REF}} \\ r_{xy}^{\mathrm{REF}} & r_{yy}^{\mathrm{REF}} & r_{zy}^{\mathrm{REF}} \\ r_{xz}^{\mathrm{REF}} & r_{yz}^{\mathrm{REF}} & r_{zz}^{\mathrm{REF}} \end{bmatrix} \tag{10.49}$$

and its Fourier transform is $\mathcal{F}\mathbf{R}_{\mathrm{REF}}$.

Matrix of the time-domain pseudoimpulse responses at SIT. Analogously to $\mathbf{R}_{\mathrm{REF}}$, the matrix of the time-domain pseudoimpulse responses at SIT is

$$\mathbf{R}_{\mathrm{SIT}} \equiv \begin{bmatrix} r_{xx}^{\mathrm{SIT}} & r_{yx}^{\mathrm{SIT}} & r_{zx}^{\mathrm{SIT}} \\ r_{xy}^{\mathrm{SIT}} & r_{yy}^{\mathrm{SIT}} & r_{zy}^{\mathrm{SIT}} \\ r_{xz}^{\mathrm{SIT}} & r_{yz}^{\mathrm{SIT}} & r_{zz}^{\mathrm{SIT}} \end{bmatrix} \tag{10.50}$$

Matrix of the Fourier transfer functions for REF. The matrix is defined as

$$\mathbf{FTF}_{\mathrm{REF}} \equiv \frac{\mathcal{F}\mathbf{R}_{\mathrm{REF}}}{\mathcal{F}p} \tag{10.51}$$

and characterizes transfer properties of the model between the horizontal plane at which the excitation by the plane wave is applied and the reference site REF.

Matrix of the Fourier transfer functions for SIT. The matrix is defined as

$$\mathbf{FTF}_{\mathrm{SIT}} \equiv \frac{\mathcal{F}\mathbf{R}_{\mathrm{SIT}}}{\mathcal{F}p} \tag{10.52}$$

and characterizes transfer properties of the model between the horizontal plane at which the excitation by the plane wave is applied and the site of interest SIT.

Matrix of the spectral ratios between SIT and REF.

From Eq. (10.51) we have

$$\mathcal{F}p\ \mathbf{I} = [\mathbf{FTF}_{\mathsf{REF}}]^{-1} \mathcal{F}\mathbf{R}_{\mathsf{REF}} \qquad (10.53)$$

and from Eq. (10.52)

$$\mathcal{F}\mathbf{R}_{\mathsf{SIT}} = \mathbf{FTF}_{\mathsf{SIT}}\ \mathcal{F}p \qquad (10.54)$$

Then

$$\mathcal{F}\mathbf{R}_{\mathsf{SIT}} = \mathbf{FTF}_{\mathsf{SIT}}\ [\mathbf{FTF}_{\mathsf{REF}}]^{-1} \mathcal{F}\mathbf{R}_{\mathsf{REF}} \qquad (10.55)$$

The matrix of the spectral ratios between SIT and REF may be then defined as

$$\mathbf{MSR} \equiv \mathbf{FTF}_{\mathsf{SIT}}\ [\mathbf{FTF}_{\mathsf{REF}}]^{-1} \qquad (10.56)$$

and

$$\mathcal{F}\mathbf{R}_{\mathsf{SIT}} = \mathbf{MSR}\ \mathcal{F}\mathbf{R}_{\mathsf{REF}} \qquad (10.57)$$

Acceleration at the reference site REF. Assume acceleration $\vec{a}_i(t)$ at site REF due to a vertical incidence of a plane wave with acceleration, say, $\vec{a}_i^{INC}(t)$. (Recall that subscript i denotes the i-th of n selected accelerograms.)

Acceleration at a site of interest SIT. If $\vec{a}_i^{\mathsf{REF}}(t)$ is the acceleration at site REF, then the corresponding acceleration at site SIT is $\vec{s}_i^{\mathsf{SIT}}(t)$. It is obtained as

$$\begin{pmatrix} s_{x\ \ ,i}^{\mathsf{SIT}} \\ s_{y\ \ ,i}^{\mathsf{SIT}} \\ s_{z\ \ ,i}^{\mathsf{SIT}} \end{pmatrix} = \mathcal{F}^{-1}\left\{ \mathbf{MSR} \begin{pmatrix} a_{x\ \ ,i}^{\mathsf{REF}} \\ a_{y\ \ ,i}^{\mathsf{REF}} \\ a_{z\ \ ,i}^{\mathsf{REF}} \end{pmatrix} \right\} \tag{10.58}$$

10.3.4 Configuration SRPS: reference site is in the model, point earthquake source

The configuration is shown in the bottom panel of Fig. 10.2 and detailed in Fig. 10.8.

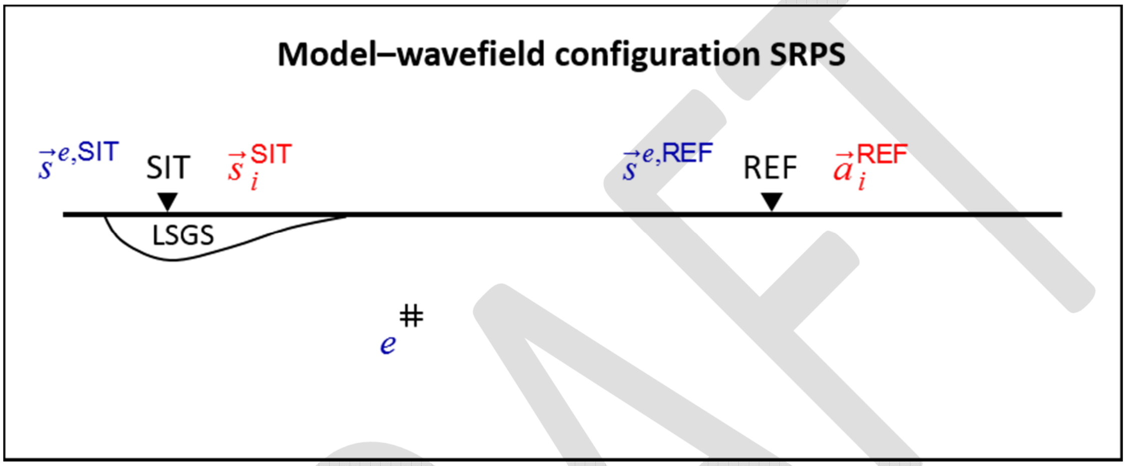

Fig. 10.8. Illustration of input and output signals. The lower-case e represents an elementary source. Details in the text.

In this configuration we assume that the wavefield and ground motion are due to a point earthquake source. An arbitrary point earthquake source can be obtained by a linear combination of 6 independent elementary sources. Both the site of interest SIT and the reference site REF are in one model comprising LSGS. Define the following quantities:

Elementary sources e**.** We consider the elementary sources by Eq. (10.32).

Particle velocity at REF due to an elementary source. An elementary source e acting in the model with LSGS causes particle velocity $\vec{s}^{\,e,\mathsf{REF}}$; $e \in \{1, 2, ..., 6\}$ at REF. The matrix of the elementary velocity seismograms at REF for all 6 elementary sources is then defined as

$$\mathbf{S}_{elem}^{\mathrm{REF}} \equiv \begin{bmatrix} s_x^{1,\mathrm{REF}} & s_x^{2,\mathrm{REF}} & s_x^{3,\mathrm{REF}} & s_x^{4,\mathrm{REF}} & s_x^{5,\mathrm{REF}} & s_x^{6,\mathrm{REF}} \\ s_y^{1,\mathrm{REF}} & s_y^{2,\mathrm{REF}} & s_y^{3,\mathrm{REF}} & s_y^{4,\mathrm{REF}} & s_y^{5,\mathrm{REF}} & s_y^{6,\mathrm{REF}} \\ s_z^{1,\mathrm{REF}} & s_z^{2,\mathrm{REF}} & s_z^{3,\mathrm{REF}} & s_z^{4,\mathrm{REF}} & s_z^{5,\mathrm{REF}} & s_z^{6,\mathrm{REF}} \end{bmatrix} \tag{10.59}$$

The analogous matrix of the corresponding acceleration seismograms may be denoted as $\mathbf{A}_{elem}^{\mathrm{REF}}$.

Particle velocity at SIT due to an elementary source. An elementary source e acting in the model with LSGS causes particle velocity $\vec{s}^{\,e,\mathrm{SIT}}$; $e \in \{1,2,...,6\}$ at SIT. The matrix of the elementary velocity seismograms at SIT for all 6 elementary sources is then defined as

$$\mathbf{S}_{elem}^{\mathrm{SIT}} \equiv \begin{bmatrix} s_x^{1,\mathrm{SIT}} & s_x^{2,\mathrm{SIT}} & s_x^{3,\mathrm{SIT}} & s_x^{4,\mathrm{SIT}} & s_x^{5,\mathrm{SIT}} & s_x^{6,\mathrm{SIT}} \\ s_y^{1,\mathrm{SIT}} & s_y^{2,\mathrm{SIT}} & s_y^{3,\mathrm{SIT}} & s_y^{4,\mathrm{SIT}} & s_y^{5,\mathrm{SIT}} & s_y^{6,\mathrm{SIT}} \\ s_z^{1,\mathrm{SIT}} & s_z^{2,\mathrm{SIT}} & s_z^{3,\mathrm{SIT}} & s_z^{4,\mathrm{SIT}} & s_z^{5,\mathrm{SIT}} & s_z^{6,\mathrm{SIT}} \end{bmatrix} \tag{10.60}$$

The analogous matrix of the corresponding acceleration seismograms may be denoted as $\mathbf{A}_{elem}^{\mathrm{SIT}}$.

Acceleration at the reference site REF. Assume acceleration $\vec{a}_i^{\,\mathrm{REF}}(t)$ at the reference site REF. This is due to some point earthquake source acting at the same position where we assumed the elementary source. Analogously to relation (10.36) we may write

$$\begin{pmatrix} \mathcal{F} a_{x,i}^{\mathrm{REF}} \\ \mathcal{F} a_{y,i}^{\mathrm{REF}} \\ \mathcal{F} a_{z,i}^{\mathrm{REF}} \end{pmatrix} = \mathcal{F}\mathbf{A}_{elem}^{\mathrm{REF}} \begin{pmatrix} c_{1,i} \\ c_{2,i} \\ c_{3,i} \\ c_{4,i} \\ c_{5,i} \\ c_{6,i} \end{pmatrix} \tag{10.61}$$

As in the case of the SRPS configuration, the complex 3×6 matrix $\mathcal{F}\mathbf{A}_{elem}^{\mathrm{REF}}$ can be decomposed using the SVD method,

$$\mathcal{F}\mathbf{A}_{elem}^{\mathrm{REF}} = \mathbf{U}\mathbf{S}\mathbf{V}^{\dagger} \tag{10.62}$$

and coefficients $c_{1,i}$, $c_{2,i}$, ..., $c_{6,i}$ can be determined using

$$\begin{pmatrix} c_{1,i} \\ c_{2,i} \\ c_{3,i} \\ c_{4,i} \\ c_{5,i} \\ c_{6,i} \end{pmatrix} = \mathbf{V}\,\mathbf{S}^{-1}\,\mathbf{U}^{\dagger} \begin{pmatrix} \mathcal{F} a_{x,i}^{\mathsf{REF}} \\ \mathcal{F} a_{y,i}^{\mathsf{REF}} \\ \mathcal{F} a_{z,i}^{\mathsf{REF}} \end{pmatrix} \qquad (10.63)$$

Acceleration at a site of interest SIT. If $\vec{a}_i^{\mathsf{REF}}(t)$ is the acceleration at the reference site REF, then the corresponding acceleration at SIT is $\vec{s}_i^{\mathsf{SIT}}(t)$. As $\vec{a}_i^{\mathsf{REF}}(t)$ is the linear combination of the elementary solutions at REF in the model comprising LSGS, Eq. (10.61), analogously $\vec{s}_i^{\mathsf{SIT}}(t)$ is the same linear combination of the elementary solutions at SIT in the same model:

$$\begin{pmatrix} \mathcal{F} s_{x,i}^{\mathsf{SIT}} \\ \mathcal{F} s_{y,i}^{\mathsf{SIT}} \\ \mathcal{F} s_{z,i}^{\mathsf{SIT}} \end{pmatrix} = \mathcal{F}\mathbf{A}_{elem}^{\mathsf{SIT}} \begin{pmatrix} c_{1,i} \\ c_{2,i} \\ c_{3,i} \\ c_{4,i} \\ c_{5,i} \\ c_{6,i} \end{pmatrix} \qquad (10.64)$$

Substituting the vector of the coefficients in Eq. (10.64) by the r.h.s. of Eq. (10.63) we obtain

$$\begin{pmatrix} \mathcal{F} s_{x,i}^{\mathsf{SIT}} \\ \mathcal{F} s_{y,i}^{\mathsf{SIT}} \\ \mathcal{F} s_{z,i}^{\mathsf{SIT}} \end{pmatrix} = \mathcal{F}\mathbf{A}_{elem}^{\mathsf{SIT}}\;\mathbf{V}\,\mathbf{S}^{-1}\,\mathbf{U}^{\dagger} \begin{pmatrix} \mathcal{F} a_{x,i}^{\mathsf{REF}} \\ \mathcal{F} a_{y,i}^{\mathsf{REF}} \\ \mathcal{F} a_{z,i}^{\mathsf{REF}} \end{pmatrix} \qquad (10.65)$$

Define matrix $\mathbf{MESR}$:

$$\mathbf{MESR} \equiv \mathcal{F}\mathbf{A}_{elem}^{\mathsf{SIT}}\;\mathbf{V}\,\mathbf{S}^{-1}\,\mathbf{U}^{\dagger} \qquad (10.66)$$

$\mathbf{M}$, $\mathbf{E}$, $\mathbf{S}$ and $\mathbf{R}$ stand for ‚matrix', ‚elementary', ‚SIT' and ‚REF', respectively, and quantities on the r.h.s. relate to Eqs. (10.62) and (10.64), that is, they should not be mixed with quantities on the r.h.s. of Eq. (10.45). Using $\mathbf{MESR}$ in Eq. (10.65) we obtain for the desired acceleration at SIT:

$$\begin{pmatrix} s_{x,i}^{\mathrm{SIT}} \\ s_{y,i}^{\mathrm{SIT}} \\ s_{z,i}^{\mathrm{SIT}} \end{pmatrix} = \mathcal{F}^{-1}\left\{ \mathbf{MESR} \begin{pmatrix} \mathcal{F}a_{x,i}^{\mathrm{REF}} \\ \mathcal{F}a_{y,i}^{\mathrm{REF}} \\ \mathcal{F}a_{z,i}^{\mathrm{REF}} \end{pmatrix} \right\} \tag{10.67}$$

Matrix $\mathbf{MESR}$ represents relation between ground motion at the reference site REF and site of interest SIT in the model comprising LSGS, assuming that the wavefield and ground motion were generated by a point earthquake source. The matrix has the meaning of the spectral matrix ratio $\mathcal{F}\mathbf{A}_{elem}^{\mathrm{SIT}} \left[\mathcal{F}\mathbf{A}_{elem}^{\mathrm{REF}}\right]^{-1}$. Therefore it is equivalent to the analogous spectral matrix ratio $\mathcal{F}\mathbf{S}_{elem}^{\mathrm{SIT}} \left[\mathcal{F}\mathbf{S}_{elem}^{\mathrm{REF}}\right]^{-1}$. Consequently,

$$\mathbf{MESR} \equiv \mathcal{F}\mathbf{A}_{elem}^{\mathrm{SIT}} \; \mathbf{V}_S \; \mathbf{S}_S^{-1} \; \mathbf{U}_S^{\dagger} \tag{10.68}$$

where subscript $_S$ indicates that the three matrices relate to decomposition

$$\mathcal{F}\mathbf{S}_{elem}^{\mathrm{REF}} = \mathbf{U}_S \; \mathbf{S}_S \; \mathbf{V}_S^{\dagger} \tag{10.69}$$

Analogously to the case of configuration SHPS we use Eq. (10.68) for determining matrix $\mathbf{MESR}$.

11 APPENDIX: FIGURES AND TABLES FOR CHAPTER 8 (LINK WITH NERA)

Tab. 1. Statistics for the aggravation factor on the peak spectral amplification factor (for each zone and each kind of input motion (SH-SV), are listed the minimum and maximum values for all the 972 valleys, the 10% and 90% fractals, the mean and the median.

AGAFMAX Zone		Min	F10	Mean	Median	F90	Max
BR	SH	1,06	1,07	1,1196	1,12	1,17	1,27
	SV	1,05	1,08	1,1537	1,15	1,25	1,72
W2	SH	0,872	1,07	1,2789	1,29	1,5	3,05
	SV	0,674	1,059	1,1828	1,18	1,36	1,65
W1	SY	0,888	1,07	1,3388	1,31	1,82	3,38
	Sv	0,6	0,9605	1,2049	1,16	1,635	2,57
FW	SH	1,03	1,09	1,3396	1,36	1,58	2,73
	SV	1,02	1,08	1,2565	1,25	1,459	2,35
FC	SH	0,99	1	1,2055	1,09	1,709	2,91
	SV	0,996	1,01	1,1978	1,14	1,53	2,42
FE	SH	1,03	1,131	1,3786	1,39	1,59	2,73
	SV	1,02	1,13	1,2744	1,27	1,44	2,32
E1	SH	0,888	1,03	1,2677	1,22	1,67	3,27
	SV	0,599	0,8463	1,0905	1,08	1,45	2,57
E2	SH	0,865	0,9757	1,1803	1,13	1,46	2,94
	SV	0,668	0,9414	1,1186	1,13	1,3	1,56

Tab. 2. Statistics for the aggravation factor on the short period amplification factor (for each zone and each kind of input motion (SH-SV), are listed the minimum and maximum values for all the 972 valleys, the 10% and 90% fractals, the mean and the median.

AG-FA Zone, wave		Min	F10	Mean	Median	F90	Max
BR	SH	0,996	1,02	1,0538	1,04	1,11	1,19
	SV	0,93	1,01	1,058	1,06	1,1	1,52
W2	SH	0,633	0,8335	1,0068	1,05	1,12	1,15
	SV	0,377	0,671	0,91311	0,99	1,06	1,11
W1	SH	0,681	0,9165	1,0646	1,05	1,29	1,7
	SV	0,39	0,695	0,95328	1,01	1,18	1,49
FW	SH	0,995	1,03	1,1324	1,12	1,29	1,58
	SV	0,977	1	1,0688	1,05	1,18	1,47
FC	SH	0,946	0,976	1,0225	0,994	1,12	1,56
	SV	0,962	0,982	1,0221	0,996	1,119	1,46
FE	SH	0,995	1,04	1,1806	1,16	1,38	1,58
	SV	0,63	1,02	1,096	1,06	1,24	1,47
E1	SH	0,681	0,7951	0,9932	1,01	1,17	1,65
	SV	0,39	0,547	0,83048	0,906	1,11	1,44
E2	SH	0,633	0,748	0,91906	0,9405	1,1	1,15
	SV	0,377	0,536	0,78482	0,855	1,03	1,08

Tab. 3. Statistics for the aggravation factor on the intermediate period amplification factor (for each zone and each kind of input motion (SH-SV), are listed the minimum and maximum values for all the 972 valleys, the 10% and 90% fractals, the mean and the median.

AG-FV Zone, wave		Min	F10	Mean	Median	F90	Max
BR	SH	1	1,017	1,0433	1,03	1,08	1,2
	SV	0,979	1,03	1,0822	1,07	1,15	1,63
W2	SH	0,492	0,8787	1,0049	1,02	1,13	1,43
	SV	0,418	0,7775	0,97239	1,03	1,1	1,25
W1	SH	0,532	0,8975	1,0582	1,04	1,25	1,88
	SV	0,369	0,6935	0,95093	1,01	1,17	1,53
FW	SH	0,965	1	1,1067	1,09	1,25	1,62
	SV	0,886	1,01	1,0707	1,05	1,17	1,42
FC	SH	0,923	0,9921	1,051	1	1,21	1,82
	SV	0,86	0,994	1,045	1,01	1,18	1,62
FE	SH	0,907	1,01	1,1221	1,11	1,26	1,56
	SV	0,601	1,01	1,0772	1,07	1,18	1,42
E1	SH	0,532	0,7651	0,99442	1,02	1,18	1,85
	SV	0,369	0,5592	0,83881	0,917	1,1	1,4
E2	SH	0,491	0,702	0,93167	1	1,08	1,21
	SV	0,418	0,561	0,86946	1,01	1,08	1,21

Tab. 4. Statistics for the aggravation factor on the peak ground acceleration (for each zone and each kind of input motion (SH-SV), are listed the minimum and maximum values for all the 972 valleys, the 10% and 90% fractals, the mean and the median

AG-PGA Zone, wave		Min	F10	Mean	Median	F90	Max
BR	SH	0,999	1,02	1,0471	1,04	1,09	1,19
	SV	0,879	1,02	1,0621	1,06	1,11	1,55
W2	SH	0,62	0,8249	1,0019	1,04	1,12	1,16
	SV	0,381	0,6975	0,91339	0,9865	1,05	1,11
W1	SH	0,635	0,919	1,0581	1,05	1,26	1,68
	SV	0,383	0,684	0,94329	1,01	1,15	1,45
FW	SH	0,997	1,02	1,1176	1,11	1,24	1,58
	SV	0,982	1,01	1,0613	1,05	1,139	1,46
FC	SH	0,946	0,9811	1,0268	0,997	1,13	1,6
	SV	0,965	0,985	1,0273	1	1,12	1,47
FE	SH	0,997	1,03	1,1546	1,14	1,35	1,58
	SV	0,59	1,01	1,0765	1,06	1,19	1,46
E1	SH	0,634	0,815	0,98936	1,01	1,159	1,65
	SV	0,383	0,541	0,82364	0,894	1,09	1,39
E2	SH	0,619	0,7387	0,91243	0,936	1,11	1,13
	SV	0,381	0,538	0,79649	0,8705	1,03	1,1

Tab. 5. Statistics for the aggravation factor on the root mean square acceleration (for each zone and each kind of input motion (SH-SV), are listed the minimum and maximum values for all the 972 valleys, the 10% and 90% fractals, the mean and the median

AG-PGV Zone, wave		Min	F10	Mean	Median	F90	Max
BR	SH	1,01	1,02	1,0512	1,05	1,08	1,18
	SV	0,978	1,01	1,069	1,06	1,14	1,44
W2	SH	0,68	0,9018	1,0046	1,03	1,07	1,53
	SV	0,486	0,8378	0,96874	1,01	1,05	1,1
W1	SH	0,71	0,9175	1,0236	1,02	1,14	1,67
	SV	0,468	0,7645	0,94808	0,994	1,07	1,29
FW	SH	0,97	1	1,0581	1,05	1,12	1,38
	SV	0,933	1	1,0399	1,04	1,08	1,28
FC	SH	0,914	0,987	1,0249	1,01	1,08	1,71
	SV	0,882	0,989	1,0315	1,02	1,09	1,37
FE	SH	0,974	1,01	1,072	1,06	1,15	1,38
	SV	0,681	1	1,039	1,04	1,08	1,28
E1	SH	0,711	0,8371	0,97565	1	1,07	1,65
	SV	0,468	0,6251	0,85634	0,9165	1,03	1,26
E2	SH	0,679	0,7847	0,94682	0,9795	1,06	1,53
	SV	0,486	0,6711	0,89691	0,9695	1,04	1,09

Tab. 6. Statistics for the aggravation factor on the Housner spectral intensity (for each zone and each kind of input motion (SH-SV), are listed the minimum and maximum values for all the 972 valleys, the 10% and 90% fractals, the mean and the median

AG-SI Zone, wave		Min	F10	Mean	Median	F90	Max
BR	SH	0,998	1,01	1,0366	1,03	1,08	1,18
	SV	0,976	1,03	1,0769	1,07	1,14	1,64
W2	SH	0,522	0,8499	0,99975	1,01	1,14	1,38
	SV	0,382	0,8008	0,95078	1,01	1,07	1,21
W1	SH	0,561	0,887	1,0605	1,04	1,29	1,8
	SV	0,4	0,7005	0,95084	1	1,155	1,55
FW	SH	0,966	1,01	1,1089	1,09	1,25	1,57
	SV	0,92	1,01	1,0687	1,05	1,15	1,5
FC	SH	0,929	0,993	1,0503	1	1,21	1,72
	SV	0,898	0,994	1,0437	1,01	1,16	1,69
FE	SH	0,924	1,02	1,1247	1,11	1,28	1,57
	SV	0,608	1,01	1,0747	1,07	1,16	1,5
E1	SH	0,561	0,7831	0,99273	1,01	1,199	1,79
	SV	0,4	0,5671	0,83994	0,9035	1,1	1,5
E2	SH	0,521	0,723	0,91914	0,975	1,08	1,25
	SV	0,382	0,5428	0,84857	0,949	1,05	1,2

Tab. 7. Statistics for the aggravation factor on the root mean square acceleration (for each zone and each kind of input motion (SH-SV), are listed the minimum and maximum values for all the 972 valleys, the 10% and 90% fractals, the mean and the median

AGCAV Zone, wave		Min	F10	Mean	Median	F90	Max
BR	SH	1,01	1,02	1,0713	1,06	1,13	1,24
	SV	0,998	1,02	1,0815	1,08	1,14	1,64
W2	SH	0,531	0,842	1,073	1,07	1,351	1,7
	SV	0,34	0,7249	0,95268	0,998	1,21	1,51
W1	SH	0,564	0,9075	1,194	1,19	1,6	2,32
	SV	0,358	0,726	1,0233	1,05	1,36	1,82
FW	SH	1,01	1,09	1,2711	1,26	1,5	1,91
	SV	1	1,04	1,1688	1,16	1,31	1,67
FC	SH	0,979	1,05	1,2682	1,23	1,6	2,13
	SV	0,996	1,04	1,1882	1,18	1,38	1,86
FE	SH	1	1,09	1,2684	1,26	1,509	1,88
	SV	0,851	1,03	1,164	1,15	1,32	1,67
E1	SH	0,564	0,7724	1,0959	1,1	1,5	2,27
	SV	0,355	0,5872	0,9017	0,946	1,28	1,75
E2	SH	0,531	0,7117	0,96999	0,99	1,28	1,64
	SV	0,337	0,5837	0,84219	0,886	1,14	1,4

Tab. 8. Statistics for the aggravation factor on the Arias intensity (for each zone and each kind of input motion (SH-SV), are listed the minimum and maximum values for all the 972 valleys, the 10% and 90% fractals, the mean and the median

AG-IA Zone, wave		Min	F10	Mean	Median	F90	Max
BR	SH	1,01	1,04	1,1082	1,09	1,21	1,43
	SV	0,926	1,06	1,1521	1,15	1,26	2,55
W2	SH	0,329	0,6479	1,0273	1,07	1,39	1,89
	SV	0,119	0,4739	0,83496	0,96	1,2	1,53
W1	SH	0,351	0,8015	1,2307	1,21	1,965	3,97
	SV	0,135	0,474	0,93877	1,03	1,595	2,54
FW	SH	1,01	1,101	1,375	1,375	1,699	2,64
	SV	1,01	1,07	1,2165	1,19	1,42	2,35
FC	SH	0,872	1,01	1,2356	1,13	1,75	3,19
	SV	0,943	1,02	1,1789	1,11	1,53	2,66
FE	SH	1,01	1,12	1,4072	1,41	1,759	2,63
	SV	0,65	1,07	1,2234	1,2	1,43	2,35
E1	SH	0,351	0,584	1,0539	1,09	1,66	3,82
	SV	0,135	0,3092	0,72135	0,813	1,36	2,46
E2	SH	0,329	0,4987	0,83831	0,8955	1,313	1,77
	SV	0,119	0,2827	0,63866	0,737	1,1	1,48

Tab. 9. Statistics for the aggravation factor on the root mean square acceleration (for each zone and each kind of input motion (SH-SV), are listed the minimum and maximum values for all the 972 valleys, the 10% and 90% fractals, the mean and the median

AGARMS Zone		Min	F10	Mean	Median	F90	Max
BR	SH	0,933	0,991	1,0241	1,02	1,07	1,19
	SV	0,803	1	1,0523	1,05	1,11	1,56
W2	SH	0,559	0,827	1,014	1,01	1,25	1,76
	SV	0,312	0,6375	0,9087	0,9605	1,16	1,46
W1	SH	0,752	0,913	1,0714	1,08	1,24	1,78
	SV	0,796	0,944	1,0374	1,03	1,13	1,61
FW	SH	0,683	0,8321	0,96559	0,963	1,14	1,57
	SV	0,785	0,8931	0,99373	0,98	1,13	1,45
FC	SH	0,753	0,966	1,1048	1,1	1,27	1,78
	SV	0,676	0,9621	1,0483	1,04	1,14	1,62
FE	SH	0,532	0,7111	0,94095	0,948	1,16	1,72
	SV	0,308	0,5021	0,78763	0,8405	1,1	1,42
E1	SH	0,514	0,6311	0,8622	0,888	1,1	1,19
	SV	0,269	0,4594	0,7474	0,833	1,02	1,16
E2	SH	0,933	0,991	1,0241	1,02	1,07	1,19
	SV	0,803	1	1,0523	1,05	1,11	1,56

Tab. 10. Statistics for the aggravation factor on the 10-95% Trifunac-Brady duration (for each zone and each kind of input motion (SH-SV), are listed the minimum and maximum values for all the 972 valleys, the 10% and 90% fractals, the mean and the median

AG-DTB1 Zone, wave		Min (s)	F10	Mean	Median	F90	Max
BR	SH	0,0736	0,146	0,38376	0,249	0,8029	2,02
	SV	-0,104	0,05798	0,47363	0,299	1,133	3,41
W2	SH	-2,32	-0,004257	1,7226	0,7865	5,14	10,8
	SV	-2,28	0,1748	1,4662	0,752	4,25	11,4
W1	SH	-1,95	-0,0921	2,1932	1,17	6,14	12,3
	SV	-1,89	0,04635	1,678	0,971	4,735	13,3
FW	SH	-0,0315	0,4792	3,484	2,46	7,908	12,4
	SV	-0,502	0,2201	2,0368	1,435	4,759	11,6
FC	SH	-0,072	0,4207	3,9588	2,375	10,29	18,5
	SV	-0,91	0,2074	2,49	1,675	6,398	12,9
FE	SH	-0,0322	0,4642	3,3788	2,46	7,459	12,4
	SV	-0,438	0,2231	2,1849	1,5	4,96	17,6
E1	SH	-1,98	-0,364	2,0958	0,9805	6,519	15
	SV	-1,91	-0,03462	1,8113	0,999	5,045	16
E2	SH	-2,32	-0,2625	1,7921	0,906	5,807	13,3
	SV	-2,28	0,2015	1,784	0,9765	4,613	14,9

Tab. 11. Statistics for the aggravation factor on the 10-75% Trifunac-Brady duration (for each zone and each kind of input motion (SH-SV), are listed the minimum and maximum values for all the 972 valleys, the 10% and 90% fractals, the mean and the median

AG-DTB2 Zone, wave		Min	F10	Mean	Median	F90	Max
BR	SH	0,0125	0,0419	0,099206	0,081	0,189	0,546
	SV	-0,00139	0,0551	0,12232	0,0912	0,2383	0,552
W2	SH	-1,25	-0,1584	0,57197	0,2455	1,902	4,75
	SV	-1,09	-0,1595	0,33375	0,114	1,22	5,72
W1	SH	-1,33	-0,159	0,90518	0,495	2,48	6,65
	SV	-1,04	-0,1705	0,56823	0,234	1,675	8,72
FW	SH	0,0431	0,2323	1,3001	1,035	2,78	5,36
	SV	-0,0955	0,107	0,72435	0,4785	1,609	6,18
FC	SH	0,0363	0,123	1,3382	0,7455	3,639	9,42
	SV	-0,0983	0,09967	0,77846	0,47	1,847	6,69
FE	SH	-0,00348	0,2311	1,2225	1,015	2,51	8,55
	SV	-0,0981	0,1082	0,76093	0,484	1,599	8,93
E1	SH	-1,33	-0,3687	0,73686	0,292	2,37	8,54
	SV	-1,04	-0,3059	0,55399	0,167	1,89	9,29
E2	SH	-1,24	-0,3473	0,49427	0,142	1,936	6,23
	SV	-1,09	-0,25	0,40536	0,111	1,54	9

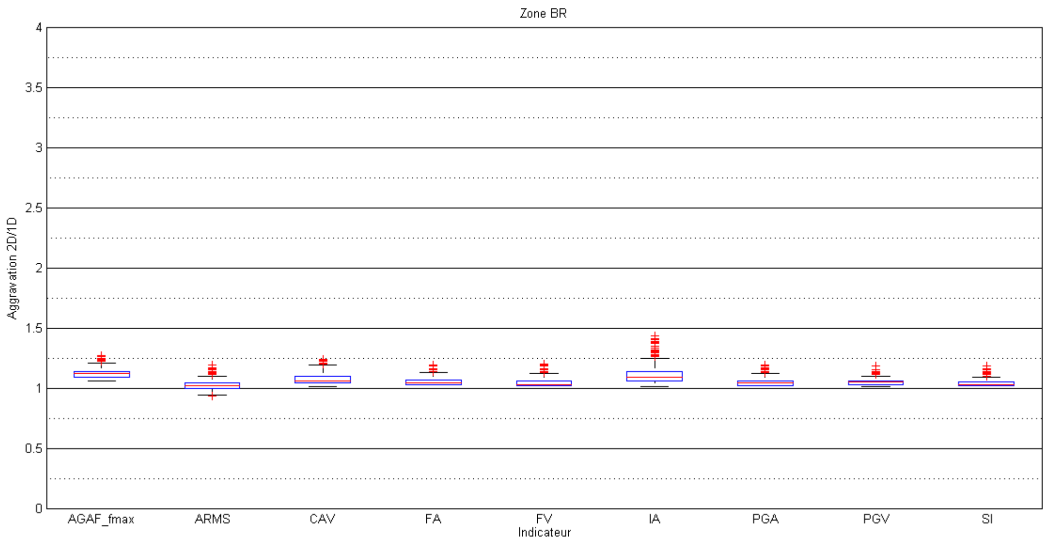

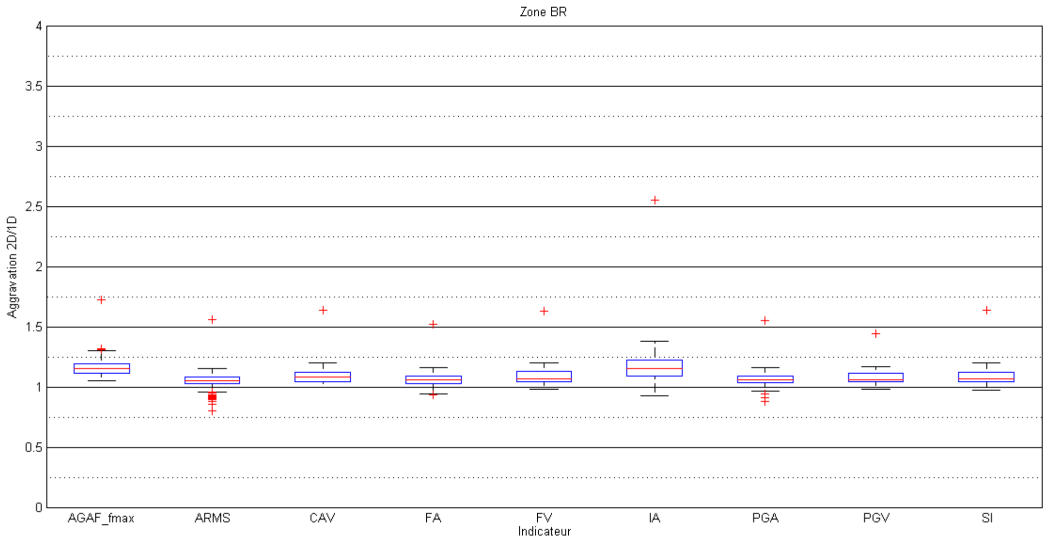

Fig. 1. BR zone statistics for the various ground motion intensity parameters. Top : Out-of-plane motion; bottom in-plane motion For each GMIP, the values of the median, 25-75% fractals (box), together with the extreme values beyond the theoretical ±2.7 σ interval, are displayed.

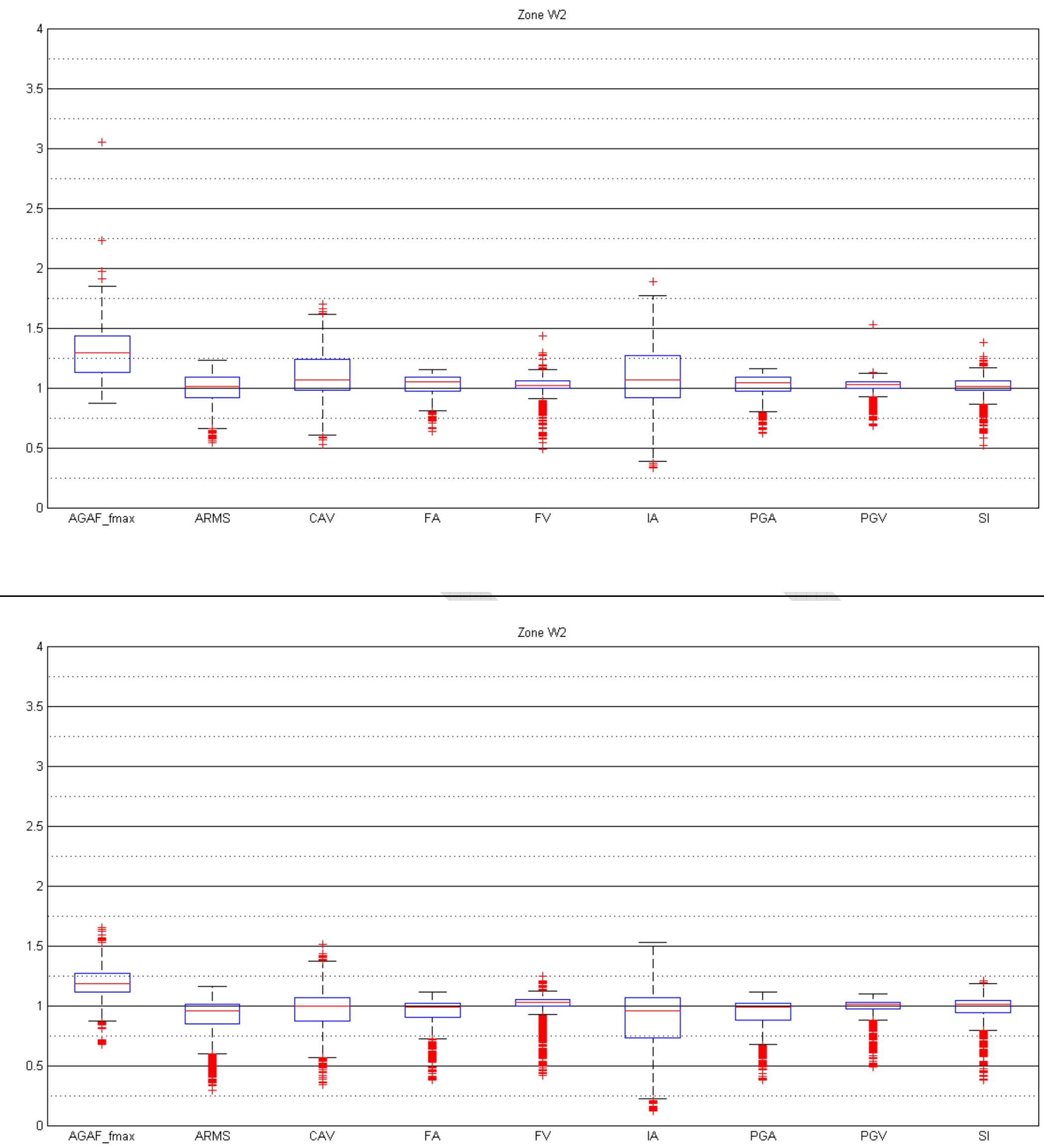

Fig. 2. W2 zone statistics for the various ground motion intensity parameters. Top : Out-of-plane motion; bottom in-plane motion. For each GMIP, the values of the median, 25-75% fractals (box), together with the extreme values beyond the theoretical ±2.7 σ interval, are displayed.

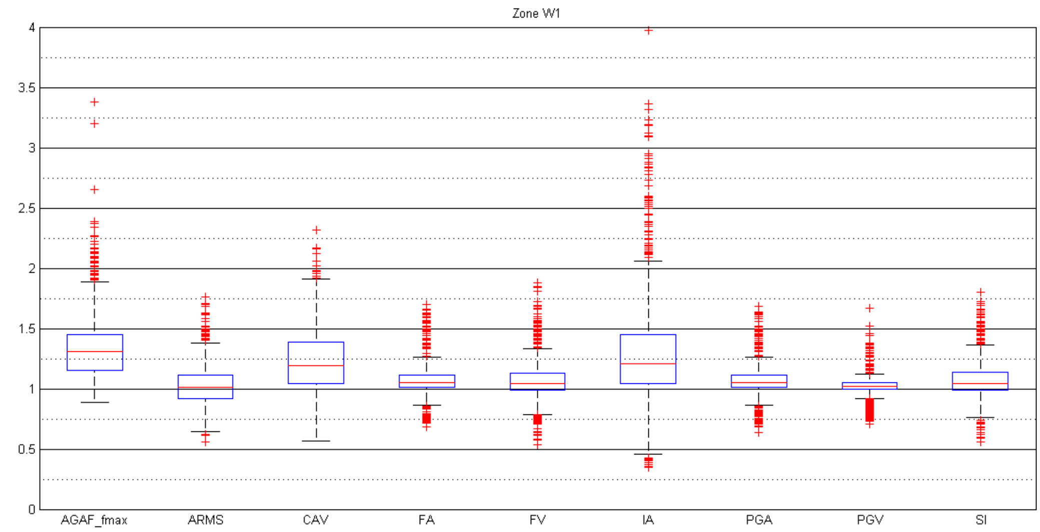

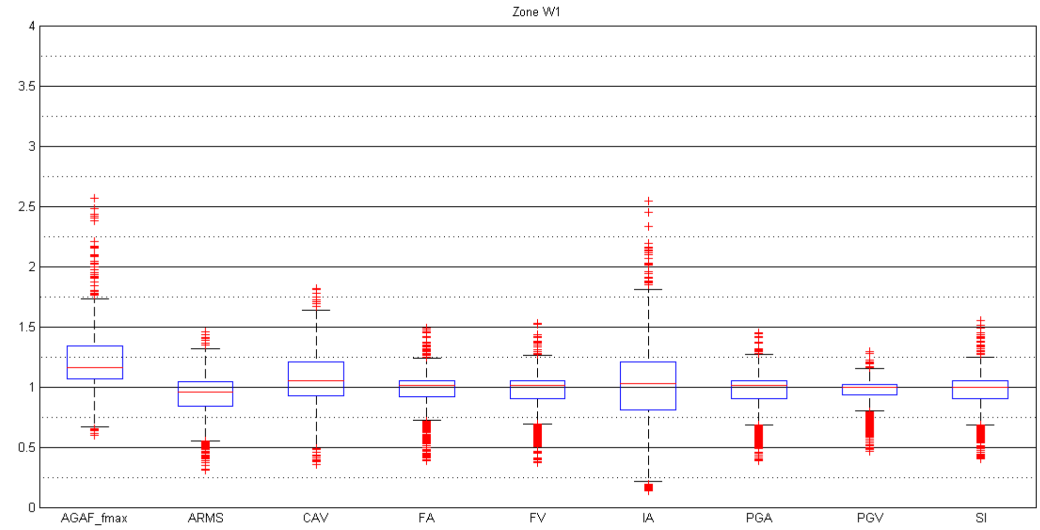

Fig. 3. W1 zone statistics for the various ground motion intensity parameters. Top : Out-of-plane motion; bottom in-plane motion For each GMIP, the values of the median, 25-75% fractals (box), together with the extreme values beyond the theoretical ±2.7 σ interval, are displayed.

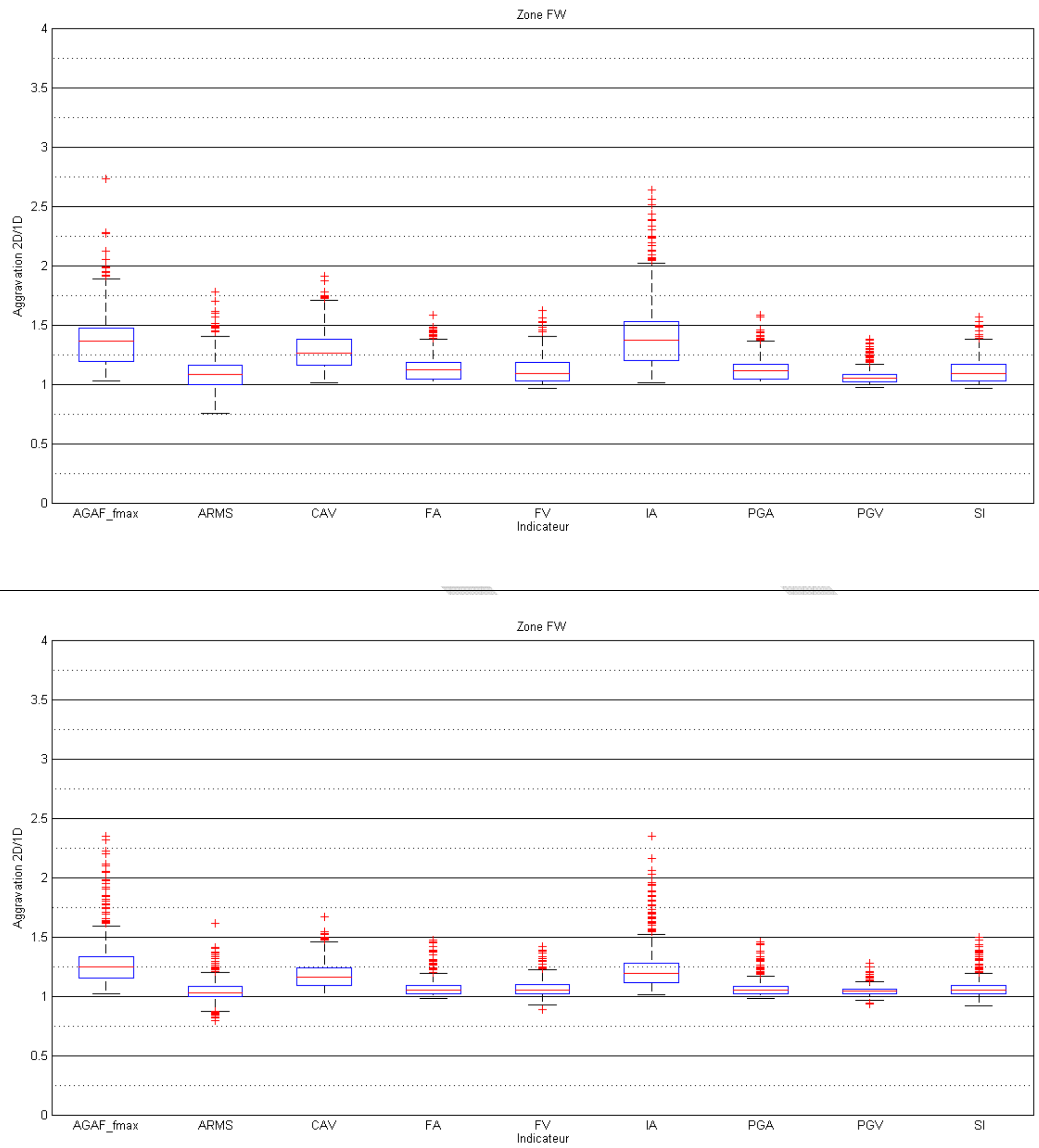

Fig. 4. FW zone statistics for the various ground motion intensity parameters. Top: Out-of-plane motion; bottom in-plane motion. For each GMIP, the values of the median, 25-75% fractals (box), together with the extreme values beyond the theoretical ±2.7 σ interval, are displayed.

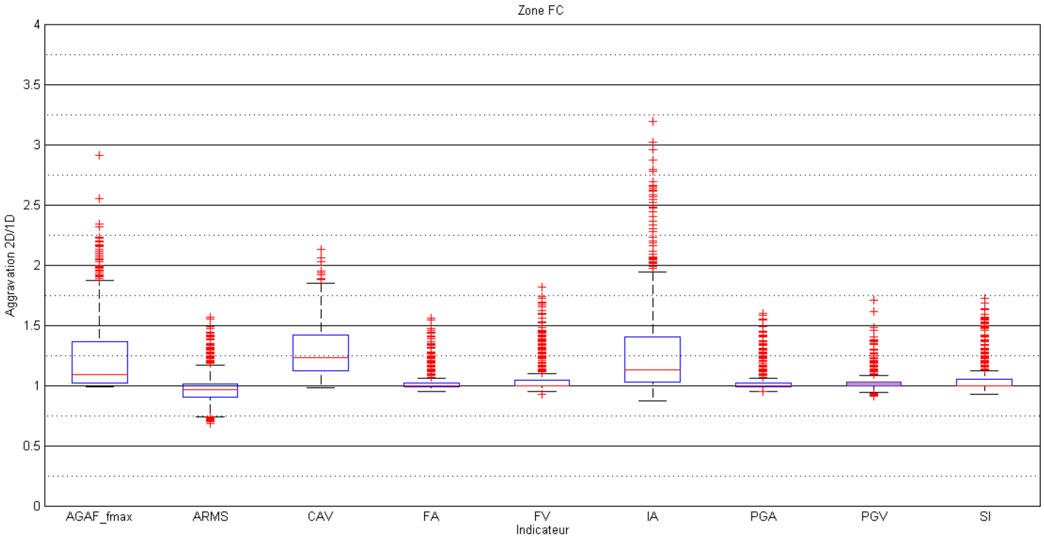

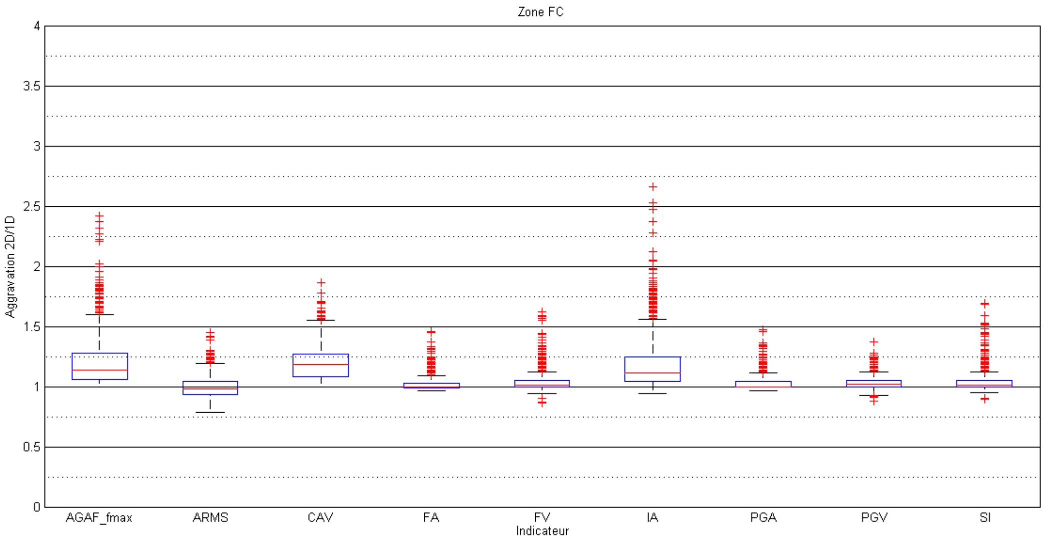

Fig. 5. FC zone statistics for the various ground motion intensity parameters. Top: Out-of-plane motion; bottom in-plane motion. For each GMIP, the values of the median, 25-75% fractals (box), together with the extreme values beyond the theoretical ±2.7 σ interval, are displayed.

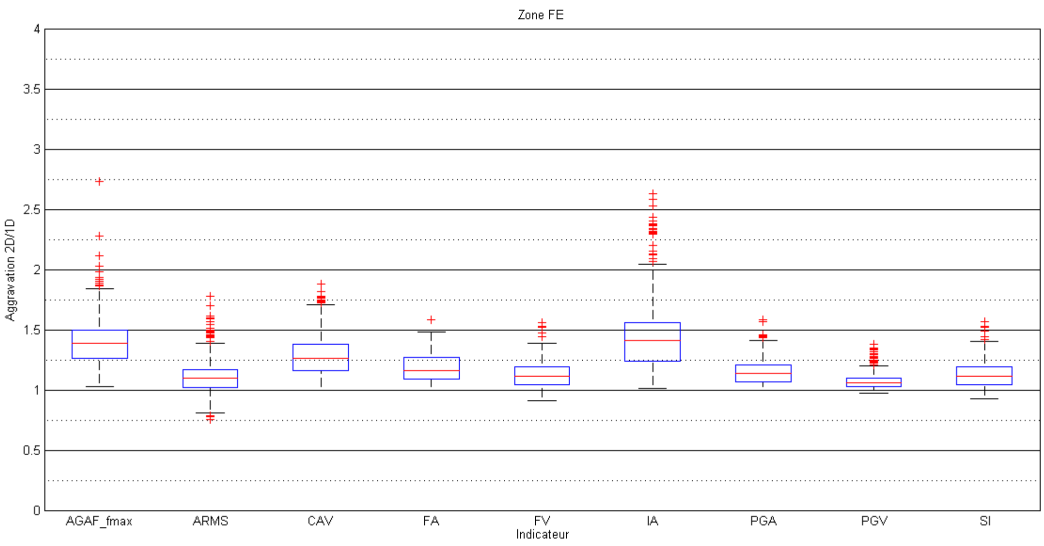

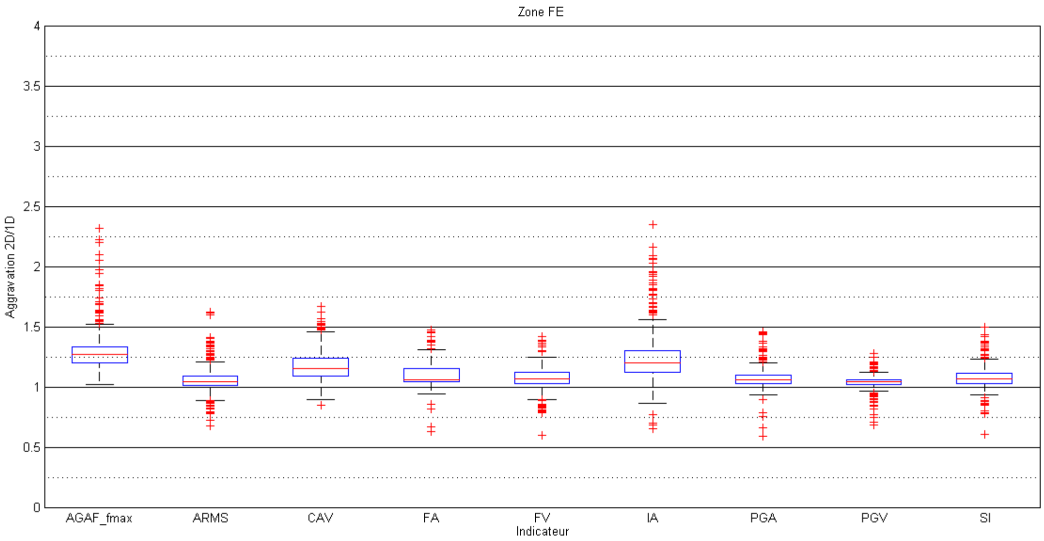

Fig. 6. FE zone statistics for the various ground motion intensity parameters. Top: Out-of-plane motion; bottom in-plane motion. For each GMIP, the values of the median, 25-75% fractals (box), together with the extreme values beyond the theoretical ±2.7 σ interval, are displayed

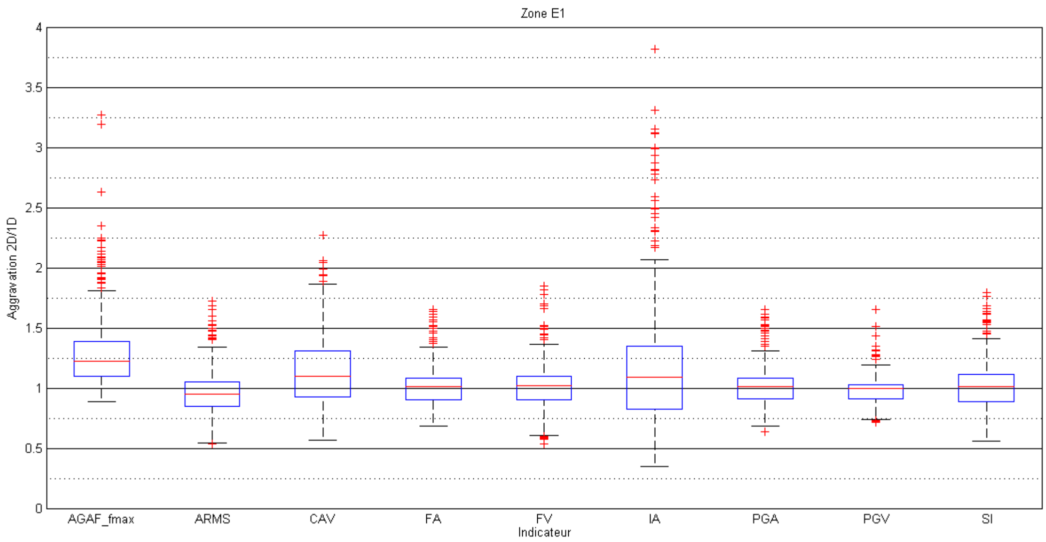

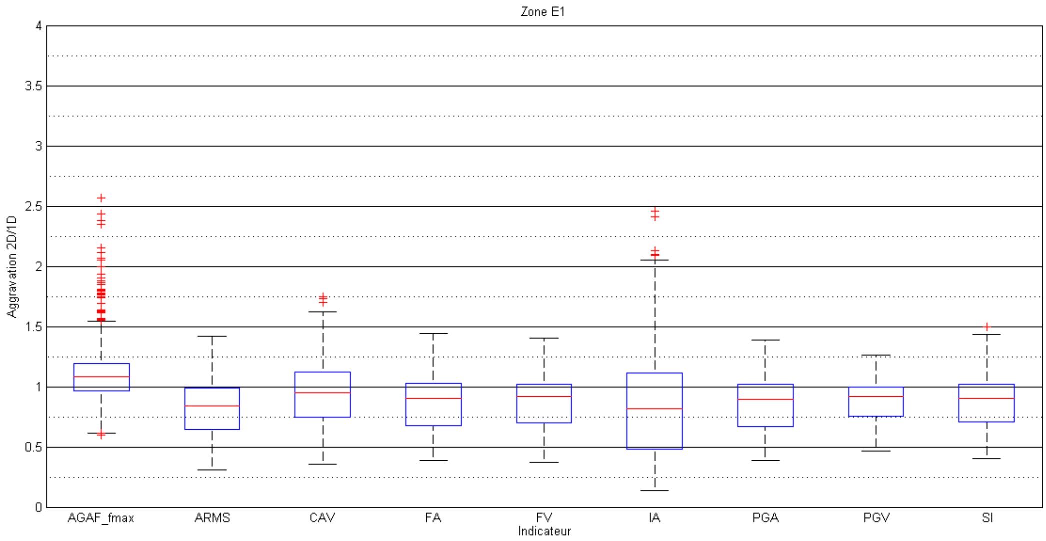

Fig. 7. E1 zone statistics for the various ground motion intensity parameters. Top: Out-of-plane motion; bottom in-plane motion. For each GMIP, the values of the median, 25-75% fractals (box), together with the extreme values beyond the theoretical ±2.7 σ interval, are displayed

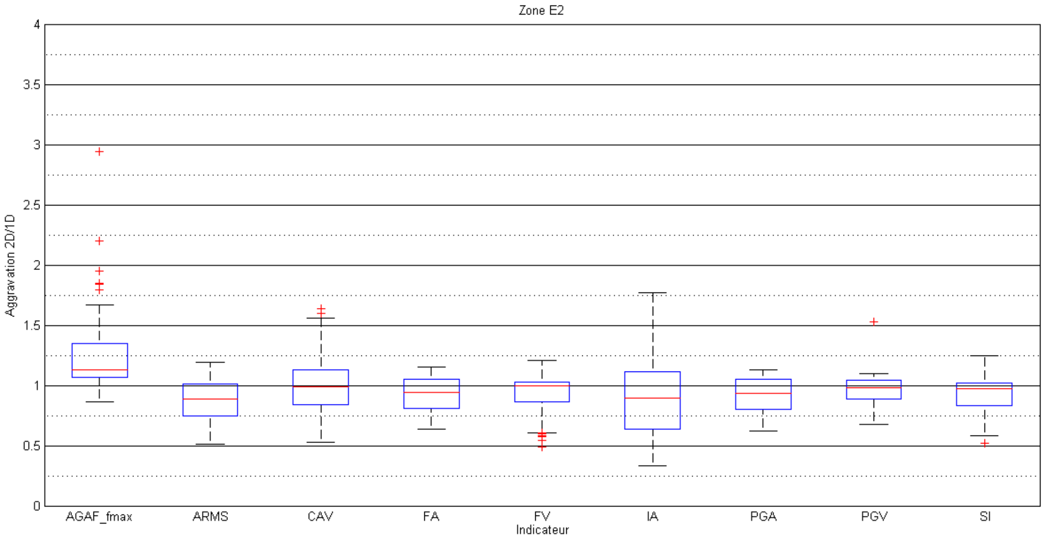

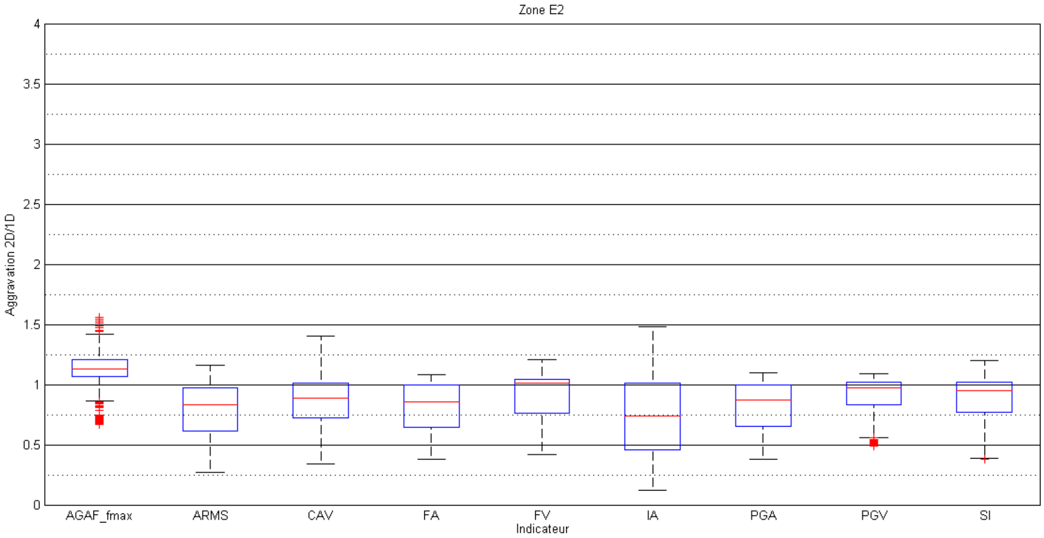

Fig. 8. E2 zone statistics for the various ground motion intensity parameters. Top: Out-of-plane motion; bottom in-plane motion. For each GMIP, the values of the median, 25-75% fractals (box), together with the extreme values beyond the theoretical ±2.7 σ interval, are displayed.

12 REFERENCES

Akkar, S., M.A. Sandikkaya, M. Senyurt, A.A. Sisi, B.O. Ay, P. Traversa, J. Douglas, F. Cotton, L. Luzi, B. Hernandez, S. Godey 2014. Reference database for seismic ground-motion in Europe (RESORCE). *Bull. Earthq. Eng.* 12, 311-339.

Chaljub, E., P.-Y. Bard, P. Moczo, J. Kristek 2012. Definition of verification cases for the NERA/JRA1 working group.

Chaljub, E., E. Maufroy, P. Moczo, J. Kristek, F. Hollender, P.-Y. Bard, E. Priolo, P. Klin, F. de Martin, Z. Zhang, W. Zhang, X. Chen 2015. 3-D numerical simulations of earthquake ground motion in sedimentary basins: testing accuracy through stringent models. *Geophys. J. Int.*, 90-111.

Chaljub, E., P. Moczo, S. Tsuno, P.-Y. Bard, J. Kristek, M. Kaser, M. Stupazzini, M. Kristeková 2010. Quantitative Comparison of Four Numerical Predictions of 3D Ground Motion in the Grenoble Valley, France. *Bull. Seism. Soc. Am.* 100, 1427-1455.

Chávez-García, F.J. 2007. Site effects: from observation and modelling to accounting for them in building codes. In: Pitilakis, K.D. (Ed.), Earthquake Geotechnical Engineering. Springer, 53-72.

Chávez-García, F.J., E. Faccioli 2000. Complex site effects and building codes: Making the leap. *Journal of Seismology* 4, 23-40.

Chávez-García, F.J., D. Raptakis, K. Makra, K. Pitilakis 2000. Site effects at Euroseistest -II. Results from 2D numerical modeling and comparison with observations. *Soil Dyn. Earthq. Eng.* 19, 23-39.

Derras, B., P.-Y. Bard, F. Cotton 2014. Towards fully data driven ground-motion prediction models for Europe. *Bull. Earthq. Eng.* 12 495-516.

Derras, B., P.-Y. Bard, F. Cotton, A. Bekkouche 2012. Adapting the Neural Network Approach to PGA Prediction: An Example Based on the KiK-net Data. *Bull. Seism. Soc. Am.* 102, 1446-1461.

Kristek, J., P. Moczo, F. Hollender 2013. Characterization of classes of sites with a large potential to cause site effects taking into account the geological heterogeneities (methodological approach). *Deliverable D3-97*.

Makra, K., F.J. Chávez-García, D. Raptakis, K. Pitilakis 2005. Parametric analysis of the seismic response of a 2D sedimentary valley: implications for code implementations of complex site effects. *Soil Dyn. Earthq. Eng.* 25, 303-315.

Makra, K., D. Raptakis, F.J. Chávez-García, K. Pitilakis 2001. Site effects and design provisions: the case of Euroseistest. *PAGEOPH* 158.

Manakou, M. 2007. Contribution of the determination of a 3D soil model for the site response study. Application to the sedimentary Mygdonian basin. PhD. Thesis (in Greek, with English summary), Department of Civil Engineering, Aristotle University of Thessaloniki.

Manakou, M., F.J. Chávez-García, K. Pitilakis 2007. The 3D geological structure of the Mygdonian sedimentary basin (Greece). *4th International Conference on Earthquake Geotechnical Engineering, June 25-28, 2007, Paper No. 1686.*

Manakou, M., D. Raptakis, F.J. Chávez-García, P.I. Apostolidis, K. Pitilakis 2010. 3D soil structure of the Mygdonian basin for site response analysis. *Soil Dyn. Earthq. Eng.* 30, 1198-1211.

Moczo, P. 1989. Finite-difference technique for SH-waves in 2-D media using irregular grids - application to the seismic response problem. *Geophys. J. Int.* 99, 321-329.

Moczo, P., J. Kristek, M. Gális 2014. The Finite-Difference Modelling of Earthquake Motions: Waves and Ruptures. Cambridge University Press.

Moczo, P., P. Labák, J. Kristek, F. Hron 1996. Amplification and differential motion due to an antiplane 2D resonance in the sediment valleys embedded in a layer over the half-space. *Bull. Seism. Soc. Am.* 86, 1434-1446.

Niccoli, M. 2014. Geophysical tutorial. How to evaluate and compare color maps. *The Leading Edge* 33, 910-912.

Pitilakis, K., D. Raptakis, K. Lontzetidis, T. Tika-Vassilikou 1999. Geotechnical and geophysical description of euro-seistest, using field, laboratory tests and moderate strong motion recordings. *J. Earthq. Engng.* 3, 381-409.

Pitilakis, K., D. Raptakis, K. Makra, M. Manakou, F.J. Chávez-García 2011. Euroseistest 3D array for the study of complex site effects, Earthquake Data in Engineering Seismology. *Geot. Geol. Earthquake Eng.* 14, 145-166.

Pitilakis, K., Z. Roumelioti, D. Raptakis, M. Manakou, K. Liakakis, A. Anastasiadis, D. Pitilakis 2013. The EUROSEISTEST strong ground motion database and web portal. *Seism. Res. Lett.* 84, 796-804.

Raptakis, D., F.J. Chávez-García, K. Makra, K. Pitilakis 2000. Site effects at Euroseistest—I. Determination of the valley structure and confrontation of observations with 1D analysis. *Soil Dyn. Earthq. Eng.* 19, 1–22.

Raptakis, D., M. Manakou, F.J. Chávez-García, K. Makra, K. Pitilakis 2005. 3D configuration of Mygdonian basin and preliminary estimate of its site response. *Soil Dyn. Earthq. Eng.* 25, 871–887.

Raptakis, D., N.P. Theodulidis, K. Pitilakis 1998. Data Analysis of the Euroseistest Strong Motion Array in Volvi (Greece): Standard and Horizontal-to-vertical Spectral Ratio techniques. *Earthquake Spectra* 14, 203-223.

Soufleris, C., J.A. Jackson, G.C.P. King, C.P. Spencer, C.H. Scholz 1982. The 1978 earthquake sequence near Thessaloniki (Northern Greece). *Geophys. J. R. Astron. Soc* 68, 429-458.

Theodulidis, N., Z. Roumelioti, A.A. Panou, A. Savvaidis, A. Kiratzi, V. Grigoriadis, P. Dimitriou, T. Chatzigogos 2006. Retrospective prediction of macroseismic intensities using strong ground motion simulation: the case of the 1978 Thessaloniki (Greece) earthquake (M6.5). *Bull. Earthq. Eng.* 4, 101-103.

Tsuno, S., E. Chaljub, P.-Y. Bard 2009. Grenoble simulation benchmark: comparison of results and main learnings In: Bard, P.-Y., Chaljub, E., Cornou, C., Cotton, F., Guéguen, P. (Eds.), ESG2006 Proceedings. LCPC Editions ISSN 1628-4704, 1377-1433.1436.